INVESTIGATION OF INERTER-BASED VIBRATION ABSORBERS FOR MACHINING CHATTER STABILITY

Hakan Doğan

Supervisors: Prof. N.D. Sims

Prof. D.J. Wagg

Department of Mechanical Engineering

The University of Sheffield

This dissertation is submitted for the degree of

Doctor of Philosophy

October 2021

Acknowledgements

Summary

Regenerative chatter, which is unstable vibration, is one of the most important issues that limit milling operations' productivity. One way to suppress the regenerative chatter is to utilise passive control methods such as tuned mass dampers (TMDs). However, the performance of passive control devices that use traditional elements (e.g. spring and dampers) is generally limited. The inerter, is a relatively new mechanical element, has been explored to improve dynamic performance of passive control systems in a wide range of engineering fields. However, it has not been examined for machining chatter stability as yet. Hence, this thesis investigates possible performance improvement using inerters in milling operations, develops an inerter design integrated into a passive device as a localised addition, and presents experimental validations of the effectiveness of the developed device.

The potential benefits of using inerters are initially shown by numerical evaluations considering only simple inerter-based layouts. These layouts are considered localised additions to provide a more versatile solution similar to a traditional TMD. Optimal design parameters of the elements in the layouts are numerically determined by performing computations witht the self-adaptive differential evolution (SaDE) algorithm. The numerical simulation results indicate that the layouts can significantly improve milling stability by up to 40% in some cases.

Milling operations generally need small-scale passive control applications due to the limited space. Furthermore, numerical evaluations indicate that the inerter requires producing small inertance due to the optimal inertance values obtained. Therefore, design studies are presented to meet the design criteria without performance loss. The developed inerter is capable of producing small inertance. Moreover, it allows the small adjustment of inertance for fine tuning by simply attaching additional lumped masses to the inerter. Using the developed inerter and a gel damper which provides hysteretic damping, an inerter-based passive device is proposed with the advantage of being applicable into small-scale applications without the need for a grounded connection like a traditional TMD.

A prototype of the proposed device is manufactured for experimental validations. The dynamic behaviour of the prototype is initially tested by impact hammer tests. These initial tests also indicate the effectiveness of the prototype in a vibration suppression case. Finally, the functionality and stability improvement of the prototype are examined and validated under real cutting conditions.

Table of contents

List of figures

List of tables

Chapter 1

Introduction

1.1 Background

Milling operations, where material is removed from a workpiece by a rotating cutting tool, represent of an important portion of the all manufacturing techniques applied in industry. Chatter is a major problem which limits the productivity of milling operations, especially in aerospace, automotive, and mould industries [1]. Excessive vibration due to chatter might lead to undesired results such as low surface quality, low material removal rate (productivity), unacceptable accuracy, loud noise and machine tool damage or even breakage.

Chatter is generally classified in two groups: primary and secondary chatter. The former is induced by friction in the cutting region, thermo-mechanical effects on the chip formation or mode coupling. The latter, secondary chatter, is caused by the regeneration effect and it is more commonly referred to as regenerative chatter.

Regenerative chatter is more detrimental and the most commonly seen chatter in machining. Therefore, the focus of this thesis is on regenerative chatter and the term 'chatter' is used to describe the regenerative chatter throughout the thesis. Regenerative chatter is induced by regeneration of waviness on the workpiece's surface. It is a type of self-excited vibration and different from forced vibration. It is a stability problem and it is therefore related to whether the vibrations grow with time or not. If a cutting operation is stable, it is dominated by forced vibration. In the case of chatter, the cutting is unstable and it is dominated by the self-excited vibration.

The basic regenerative mechanism of chatter was first explained by Tobias and Fischwick [2], and Tlusty and Polacek [3]. Tobias and Fishwick [2] introduced the concept of the stability lobe diagram by evaluating the phase shift of the waviness between two subsequent cuts, which indicates stability limit of depth of cut against spindle speed as present in Figure 1.1. The chatter vibrations can reach a detrimental level in a very short time beyond the stability border. The growth of the vibration level decreases near the stability border and chatter vibrations might be acceptable. However, the surface quality will be still affected by the chatter vibration. Stability chart in Figure 1.1 is commonly used for the evaluation of the stable region in machining operations. The productivity of a cutting operation is proportional to the material removal rate, which can be defined as the amount of material removed from the workpiece per second. A cutting operation with a high depth of cut and high spindle speed is generally favourable as it provides a high material removal rate (or productivity). Thus, enhancement of the stability limit at higher spindle speed is important to improve the productivity of cutting operations.

Proper selection of the spindle speed and the depth of cut can be used to avoid unstable cuts. However, whilst this method makes the most of the stability lobe diagram, it

Figure 1.1 Stability lobe diagram where stability limit of machining operation is shown using depth of cut versus spindle speed.

does not improve the stability limit. It is also possible to manipulate the stability limit to enhance the stable region in a desired way. One way to achieve this is to improve the structural dynamics of the milling system through passive control devices. Chatter can be induced by the dynamic flexibilities of structural mode of the machine, spindle, tool or workpiece. Application of passive control devices such as tuned mass dampers can increase the chatter resistance of the milling.

The inerter, is a relatively new mechanical device, has been increasingly studied by the vibration community to improve the performance of passive control devices in a wide range of engineering vibration problems. The concept of the inerter was first introduced by Smith [4] as a new mechanical device to complete the missing two terminals element in the standard analogy between mechanical and electrical networks. An inerter generates a force proportional to the relative acceleration between its two terminals. It corresponds to an ungrounded capacitor in an electrical network. It has been shown benefit the behaviour of the dynamic system in many applications as reviewed in Chapter 2. However, to the date, there has been no comprehensive

study in the literature that focuses on the use of the inerter to improve the chatter performance of the machining system. To the author's knowledge, the only study related to application of the inerter in milling is the work of Wang et al. [5], who examined the use of the inerter for vibration mitigation of a milling machine. However, they considered the vibration problem as forced vibration rather than the chatter stability problem. The main issue in milling operations that limits productivity is chatter. A great majority of machining research that address undesirable vibrations during cutting operation focus on the chatter problem. Hence, the investigation of the benefits of the use of inerter in chatter stability has remained a research gap in the literature.

This thesis investigates the benefits of the use of inerter-based passive control devices in improving chatter stability of milling. The integration of the inerter is considered as a localised addition [6] in a similar manner to a classical tuned mass damper in order to present more versatile solution with no (or minimum) structural modification of the milling machine.

1.2   Motivation and objectives

The aim of the current research is to investigate improvement of the chatter stability of milling, using an inerter as a localised addition. To achieve this, the main objectives are follows:

1. Numerically evaluate the performance of possible layouts of inerter-based passive control device as localised additions in milling.

2. Develop an inerter device which is applicable to small-scale small-amplitude applications such as milling operations.

3. Design an inerter-based passive control device which can be applied as a localised addition (without the need for ground connection or deployment between two parts of the controlled structure) in a similar manner to a classical TMD.

4. Manufacture a prototype and test the dynamic behaviour of the device via experiments.

5. Validate the functionality of the absorber and the stability improvement under real cutting conditions.

1.3 Thesis outline

The rest of the thesis is organised as follows:

Chapter 2 presents the literature review in two sections. In the first section, the machining chatter stability, including the stability prediction, chatter avoidance and mitigation methods are discussed. The main focus of the review is passive control methods applied in chatter stability improvement. The second section of the literature review evaluates the inerter. In this section, the physical realisation of the inerter, its performance improvement and its application are discussed.

Chapter 3 introduces the theoretical background by explaining the basic regenerative mechanism with a simplified example. It is then extended to the stability analysis of milling, which is more complex due to the rotating tool. The concept of the stability lobe diagram is also briefly explained in this chapter.

Chapter 4 performs numerical evaluations of chatter stability improvements of four different inerter-based layouts attached to the milling system. To avoid unnecessary complexity, the milling system considered in this chapter is reduced to a single degree-of-freedom (SDOF). The evaluation of the layouts is mostly conducted focusing on the absolute stability limit of milling. The sensitivity analysis of the design parameters for the layouts with best performances is also presented.

Chapter 5 involves design studies for the physical realisation of one of the layouts. The physical realisation of the layouts evaluated in Chapter 4 might not be possible as presented in ideal form due to some factors such as parasitic mass effect and realisation of the damping. Therefore, this chapter first presents a practical approach to the layout considering the parasitic mass effect as well as relatively simple realisation of the damping mechanism with hysteretic damping. Then, the chapter describes the development of a mechanical inerter with living-hinges, which is applicable to small-scale small-amplitude application, with the advantage of adjustment of the inertance for fine tuning. Using the developed inerter, the prototype of the inerter-based absorber that requires no grounded connection or deployment of two components of the host structure is presented.

Chapter 6 experimentally validates both the functionality of the prototype as an inerter-based absorber with modal tests and the improvement of milling stability through milling tests. A number of modal tests for different cases, including the evaluation of the vibration suppression performance, is utilised to test its functionality. Furthermore, the functionality and the chatter performance are evaluated under real cutting conditions applying milling tests in this chapter. Chapter 7 draws conclusions and discusses limitations and possible future works.

Chapter 2

Literature Review

This chapter presents a literature review of machining chatter and inerter. In the first part of this chapter, the literature related to the machining chatter research, including stability prediction, chatter avoidance and mitigation methods, is discussed. In the second part, the literature review of the inerter considering its concept, the physical realisation of the inerter device, its performance and applications are presented.

2.1 Machining chatter research

2.1.1 Introduction

Research studies of machine tool chatter date back to as early as the 19th century. The earlier studies were mostly based on empirical data and models, and were mostly led by industrial initiatives [7]. Among them, the most famous one is the research programme

of F. W. Taylor. One of the general conclusions of twenty-six years of factory-based research arrived about the chatter of the tool as stated in the published work entitled "On the art of cutting metals" in 1906 [8]

> Chatter is the most obscure and delicate of all problems facing the machinist, and in the case of castings and forgings of miscellaneous shapes *probably no rules or formulæ can be devised* which will accurately guide the machinist in taking the maximum cuts and speeds possible without producing chatter.

Taylor stated that no rules or formula could be devised for a general understanding of the chatter. Earlier attempts were limited for the specific cutting processes, and no comprehensive mathematical model and explanation were expressed for the chatter mechanism.

Research in the field of machining has shown a rapid development starting from the middle of the 1940s. Some of the important works which accelerated the development in the field of machining research were the works of Merchant [9–11]. He developed a steady-state orthogonal cutting force model for the metal cutting process by assuming a continuous chip (Type 2) of Ernst [12]. The mechanism underlying the regenerative chatter was first given by Tobias and Fishwick [2], and Tlusty and Polacek [3]. It was extended to multipoint cutting with the contribution of the studies of Sridhar et al. [13–15], Altintas and Budak [16–20], Insperger and Stépán [21–24], and *et alia.*

More than a hundred years after Taylor's statement, which forecast no accurate rules or formula for the accurate prediction of chatter, a good understanding of the chatter mechanism has been established by bringing the gaps between practice and theory. In parallel to this understanding, advanced methods for the prediction of the occurrence of

machine tool chatter and the mitigation of the chatter mechanism have been developed by many researchers in the field of machine tool chatter.

The ultimate aim in the research of machine tool chatter is to increase the productivity of the cutting process and/or increase the quality of the surface finishing. Different methods have been proposed to avoid regenerative chatter or increase the machining chatter stability since the establishment of the regenerative chatter theory. The advancements in machining chatter research can be classified into three groups as given in Fig. 2.1. The first group is chatter avoidance which relies on an accurate prediction of the occurrence of chatter. This group accepts the machine tool dynamic as it is, and chatter is avoided by changing the cutting parameters (e.g. depth cut and spindle speed) in the process or out-of-the-process. Therefore, progresses in analytical or numerical prediction of the chatter stability limits or the online chatter detection methods contribute to the first group. The second group involves disturbing the delay term by continuously changing the spindle speed or using special tool geometries. The last group relies on the manipulation of the structural dynamics. Higher chatter stability can be provided by modifying the components of the machine, using passive or active control devices, or utilizing special tool geometries.
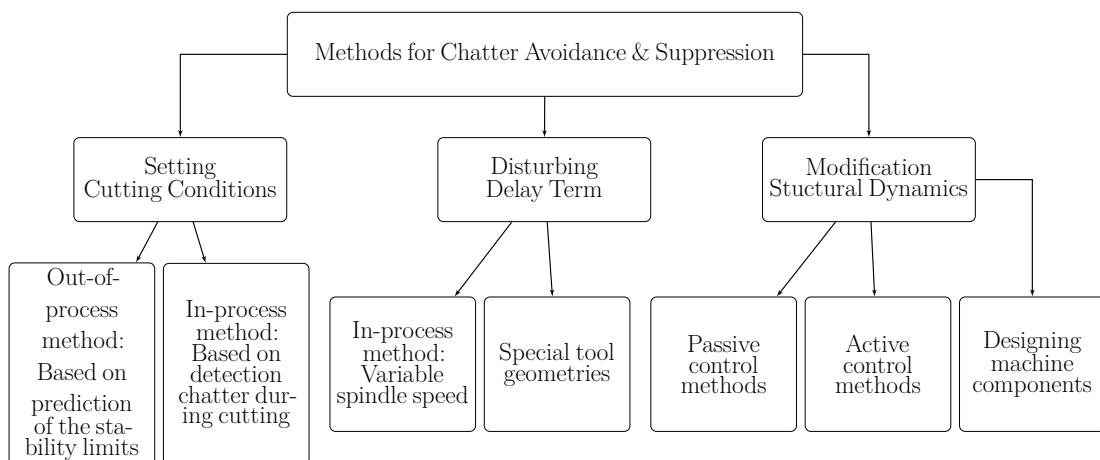
Figure 2.1 A classification of methods for chatter avoidance and suppression

The methods in the first two groups mostly depend on the advancement of the regenerative chatter model, while the methods given in the last group depends on both the advancement of the regenerative chatter model and the structural dynamics. Hence, a literature review of the studies which have been contributed to the understanding of the chatter mechanism will be given first. Following this, the methods for chatter mitigation will be presented.

2.1.2 Chatter prediction

Initial efforts focusing on chatter were made by Arnold [25], Hahn [26], and Doi and Kato [27]. However, the first satisfactory analysis for the chatter was presented by Tobias and Fishwick [2], and Tlusty and Polacek [3] almost at the same time but independently of each other. Their works have constructed the fundamental basis of our understanding of the chatter mechanism. Assuming a continuous single-point cutting, Tlusty and Polacek [3] showed that the critical depth of cut for the absolute stability was proportional to the dynamic stiffness of the machine. Tobias and Fishwick [2] presented a similar relation and also showed that the stability limit for the depth of cut in their conclusion was a function of the time delay between the inner and outer modulation of the surface with the inclusion of the rotational frequency in their model. This approach brought the establishment of the stability pockets (or lobes) in the stability charts, the so-called stability lobe diagram. Tobias [2] utilised a velocity-dependent factor, additional to the orthogonal cutting force, in order to express the effect of the dynamic cutting force. Tlusty and Polacek [3] neglected this velocity-dependency due to the lack of sufficient evidence of its existence and its small effect on the cutting force. Merritt [28] in 1965 represented the regenerative chatter of Tobias and Tlusty as a closed-loop system and applied Nyquist stability criterion for

the stability analysis. Merritt also employed an orthogonal cutting force and neglected the velocity-dependent term. He indicated the process damping for the contribution of this term [29], which occurs due to rubbing of the flank face to the wavy surface of the workpiece at lower cutting speeds. The three linear stability theories of chatter suggested to that date assumed a continuous cutting operation where the directions of the cutting force terms do not change as it is turning.

Milling operations involve a multi-point and interrupted cutting where one or more teeth may remove material at the same time depending on the start and exit angles of the teeth. The stability analysis of milling is more complicated than turning due to the rotating tool. Sridhar et al. [13, 14] and Hohn et al. [15] developed a two-DOF mathematical model for the milling process and determined the stability limits using numerical evaluation of the dynamic milling system's state transition matrix. The force coefficients in the model were time-periodic because of the rotation of the cutter. By preserving the linear assumptions, these time-periodic cutting force coefficients converts the equation of motion into a linear periodic time-delay differential equation and make the stability analysis more complex due to the infinite number of characteristic multipliers [30]. An average value of the periodic cutting coefficients was utilised to simplify the stability analysis considering the direction of the average of the total cutting force caused by teeth in cut [31] and the time-averaged values of the directional force coefficient [32, 33]. It has shown that this method causes inaccurate prediction of the stability in milling [34].

Time-domain simulations were considered as another approach to overcome the difficulty in the stability of the milling operation owing to the periodic force coefficients. Tlusty et al. [34] used time-domain simulations to assess the stability of the milling process having a two-DOF model. They also included the nonlinearity of the tool jump-out

(called the basic nonlinearity) by taking the cutting force zero when the cut leaves the workpiece surface. Later, time-domain analysis was frequently utilized to evaluate the stability limits of the milling operation [35–39]. Although time-domain simulation presents an accurate prediction of the real case and allows to be taken the nonlinearities into account, they are computationally expensive. A number of repetitive simulations need to be run to define the stability limits for a range of spindle speeds, and this number can be very high for a high-resolution picture of the stability chart.

Minis and Yanushevsky [40] showed the first analytical perspective for the stability analysis of the two-DOF dynamical milling model developed by Sridhar et al. [13]. They used Floquent's theorem and applied Fourier analysis into the solution of the milling dynamic equations to determine the characteristic equation of the system. However, their method involved the numerical evaluation of the characteristic equation to determine the stability using the Nyquist stability criterion. Budak and Altintas [17] developed an analytical method, so-called the zero-order approach (ZOA), to derive the milling stability condition. They expanded the directional milling coefficients matrix, which is periodic at tooth passing frequency, into the Fourier series and determined the stability condition analytically by considering the only constant term in the Fourier expansion. This method was extended to three-dimensional milling operations by Altintas [19]. The ZOA applied for variable pitch cutter [41, 42] and ball end mills [43]. The zero-order approach offers an accurate and fast prediction of stability limits of milling operations except cutting operations with very low radial immersions.

Although the ZOA can handle the time-periodic directional cutting coefficient by averaging and obtain the stability of milling operation with cuts with high immersion, it neglects the intermittency of the cutting process, which becomes dominant with highly intermittent cutting operations. In the earlier 2000s, some researchers [44–47]

presented the existence of additional lobes (due to period doubling bifurcations) at high speed for the cutting operations with low radial immersions. It was shown that the ZOA approach is incapable of predicting these additional lobes as the severity of the harmonics increases due to impulse-like cutting forces [48]. The first direct analytical solution to present the additional lobes was given by Davies et al. [44, 45] by considering one direction interrupted cutting operation with an extremely small ratio of time spent in cut to out of the cut. They determined the stability of the system, describing a map that consists of two stages: the solution of a free-damped system and the solution of a system forced by an impulse. The method proposed by Davies et al. [44, 45] losses its accuracy when the time spent in cut increases. In order to remove the restriction of the short time in cut, Bayly et al. [47] developed the temporal finite element analysis (TFEA) where the vibration response is obtained by the exact solution of free vibration out of the cut and approximate solution in the cut applying finite elements in time.

Insperger and Stepan [22] developed and improved [24, 49] the semi-discretization method (SDM), which is capable of the prediction of the classical Hopf instability and the period doubling instability appearing at high-speed [48]. In the SDM, the time-variant delay part of the delay differential equation is only discretised while the rest of the terms remain the same in order to obtain an approximated finite-dimensional system of the infinite-dimensional system. The effectiveness and the reliability of this method have been proved in the studies, including experimental verification [48], unstable islands [50], variable helix, and variable pitch milling tools [51, 52]. However, it requires more computational effort than direct analytical methods. It can be computationally expensive depending on the number of modes of the system and its sampling interval for accurate predictions. Moreover, the requirement of computation of modal matrices

limits its use in the industry due to the lack of robust automatic modal analysis software [53].

The establishment of the stability analysis in the frequency domain, which can predict both instabilities (Hopf and period doubling) was reported by Merdol and Altintas [20] by extending the ZOA to the multi-frequency approach (MFA). Budak and Altintas [17] had already introduced the multi-frequency approach by including the harmonics in the solution. However, they had not realised the additional lobes as they had not focused on low immersion cuts. Merdol and Altintas [20] demonstrated that the additional lobes can be predicted by considering the MFA in the stability analysis. However, the inclusion of the higher harmonics prevents a direct solution to the depth of cut. Stability analysis requires iterative eigenvalue calculations and consequently, the computational cost becomes larger compared to the ZOA. Bachrathy and Stepan [53] extended the use of this method to general tool geometries, including distributed delays.

There have been other time-domain based methods proposed to predict the stability limits of a metal cutting operation, such as the Chebyshev polynomial method [54], the Chebyshev collocation method [55] and the full-discretization method [56–58]. The accuracy of the stability prediction of metal cutting operation can be reduced due to neglecting the effects such as process damping (at low spindle speeds) and the mode coupling. Therefore, there have been efforts to increase the accuracy in the stability prediction by including the effects of process damping [59, 60] and the mode coupling into the regenerative chatter model [61, 62].

Accurate prediction of the stability limit serves to improve chatter avoidance and mitigation methods. Chatter avoidance can be simply provided by choices of the depth

of cut and spindle speed based on the prediction of the stability limits. This is known as the out-of-process method, and it completely depends on the accurate prediction of the stability limit. Alternatively, the chatter can be avoided with the in-process method based on detection of chatter during cutting. In this method, the depth of cut and/or spindle speed are set to a stable region as soon as the occurrence of the chatter is detected. Therefore, full chatter avoidance is not possible in this method as the chatter has already occurred, but its harmful effects can be attenuated.

For instance, Smith and Tlusty [63] proposed adjusting the spindle speed online by taking the tooth frequency equal to the natural frequency in high-speed milling. The speed regulation system proposed determines the Fast Fourier Transform (FFT) using the sound pressure during the cutting. If the chatter frequency starts to dominate the system, the feed is stopped and the new spindle speed is set according to the chatter frequency [64, 65]. In that way, they ensured that the spindle speed is always set to the best spindle speed without a priori knowledge of the machine tool dynamics. This method extended to a wide range of spindle speed by considering the integer fractions of the chatter frequency [66, 67]. The detection of the chatter is critical for the success of this method. Another in-process method, variable spindle speed, will be discussed in the next section.

2.1.3   Variable spindle speed

The method of variable spindle speed disturbs the regenerative chatter mechanism by continuously changing the spindle speed. In one of earlier studies, Sexton and Stone [68] investigated the effect of the spindle speed variation on chatter improvement in turning process. They showed that the improvement in stability due to the variable

spindle speed was only modest and noted that vibration induced by continuously changing spindle speed also led to poor surface finish. A turning process with a variable spindle speed is governed by a differential equation with a time-varying delay term that depends on the amplitude and frequency of the variation of the spindle speed. Jayaram et al. [69] transformed this equation into a solution of an infinite order characteristic equation applying a Fourier series expansion. They built the stability chart using the approximate solutions obtained by the truncated version of the characteristic equation. This approach allowed fast evaluation of the effect of the variable spindle speed parameters on the stability for the choice of the optimal values. Sastry et al. [70] extended this method to face-milling operations which also involves time-varying periodic force coefficients. They experimentally verified stability improvement using their method.

The semi-discretisation method was also used to investigate the effect of variable spindle speed on machining chatter improvement [23, 71–74]. Insperger et al. [23] proved that variable spindle speed can cause period-one bifurcation additional to the classical Hopf and period doubling bifurcations which can occur in a machining process with constant spindle speed. Different forms of modulation including sinusoidal [75, 76, 69, 71], triangular [75, 72, 77], rectangular [68], and random [78] have been tested and sinusoidal form of modulation was found to the most favourable form [75, 1]. Although it was shown that the technique of variable spindle speed can suppress period doubling chatter seen at high spindle speeds [72], it is known as a more effective technique at low spindle speeds, i.e. high order lobes [77, 71, 1]. For higher spindle speeds, discretely selection of spindle speed is a more favourable technique.

It is also possible to use two in-process techniques at the same time to suppress chatter in a wide range of spindle speeds. For instance, Bediaga et al. [79] proposed

an automatic spindle selection method that chooses the best suppression techniques depending on the given initial cutting conditions. The algorithm sought the best stable spindle speed for low order lobes or uses variable spindle speed for high order lobes.

Even though variable spindle speed is an easy method to implement, the performance of this method is subjected to the power and quick response of the spindle drive system. Another factor that affects the performance of this method is the selection of the parameters of the applied modulation, i.e. the amplitude and the frequency of the variation of the spindle speed. This is also one of the main difficulties that hinder the widespread use of this method in the industry. To overcome this difficulty, Al-Regib et al. [80] developed a simple formula using an energy-based method to select the optimal parameters for a sinusoidal spindle speed variation for given chatter frequency and spindle speed. However, their method does not consider machine limitations.

2.1.4   Special tools

Milling tool geometries, including variable pitch and variable helix tools, can be employed to improve regenerative chatter stability of the cutting operation. These special geometries can suppress the regenerative mechanism by disturbing the delay between adjacent cuts. Variable helix tools lead to discrete disturbance of the delay while variable helix tools cause disturbance of the delay continuously. Research focus in the use of these irregular tools in chatter suppression is mostly on accurate stability prediction considering disturbance effects and optimisation of tool geometry in a way that the best chatter suppression is obtained.

Varying pitch angle to suppress chatter was proposed by Hanh [26] as early as the 1950s. Slavicek [81] first presented the analysis of the use of variable pitch in a milling tool considering two cutting edges with an infinite tool radius. His analysis was supported with experimental verification, albeit for a limited spindle speed range. Although achievement of chatter suppression using varying pitch tools has been theoretically and experimentally presented, a random selection of the pitch angles does not guarantee stability improvement [82]. Therefore, optimisation of the tool geometry is essential to accomplish the best chatter performance.

Initially, time-domain simulations were used to seek the best pitch angles for varying pitch tools [83, 84]. Altintas et al. [41] adopted ZOA considering variation in pitch angles. This analytical approach provided fast optimisation of the pitch angles. Budak [42, 85, 86] developed and applied an analytical optimal design strategy to obtain the best pitch angles maximising the stability for a given chatter frequency, spindle speed and number of teeth. Sims et al. [51] presented semi-analytical stability prediction of milling with variable pitch and helix tools, including low radial immersion cuts. The predicted stabilities obtained by semi-discretisation [87], time-averaged semi-discretisation [41] and temporal-finite element methods [88] were compared with time-domain simulation but no experimental verification was presented. Comak and Budak [89] developed a practical design method for variable pitch tools to achieve maximum stability. As the chatter frequency and the delay changes with the pitch angle variation, the design method involves iterative solutions of time-averaged milling dynamics to determine the optimal pitch angle variation by obtaining the chatter frequency and phase difference to eliminate the delay for a given spindle speed and system's dynamics. Stepan et al. [52] proposed the Brute Force method to improve tool optimisation of the pitch angle variation by considering time-dependent milling

dynamics. The effectiveness of the method was demonstrated by Iglesias et al. [82] conducting milling experiments.

The use of variable helix tools, where the delay changes together with the axial of the tool, has been researched for the chatter resistance increment. Turner et al. [90] introduced an analytical prediction of the stability for variable helix angle. A reasonable prediction was validated for only low axial engagement. They also compared the chatter suppression performance of variable helix and variable pitch. Variable helix tools presented a better suppression performance in their experimental results. Analytical predictions of the stability of variable helix tools were also presented adopting ZOA [91] and MFA [92]. Also, Sims [93] proposed alternative MFA using the harmonic transfer function approach. This method provides an explicit appearance of the phase changing term, unlike classical MFA.

Sims et al. [51] showed that the semi discretisation method can be effectively utilised for the stability of variable helix tools. Yusoff and Sims [94] optimised the variable helix using the differential evolution algorithm integrated to the semi-discretisation method. The stability improvement provided by variable helix tools was experimentally investigated compared to the regular tool. Dombovari and Stepan [95] modelled a variable helix with weighted distributed delay and analysed the stability of milling operations with non-uniform and harmonically varied helix tool using the semi-discretisation method. The results indicated stability improvement at the lower spindle speed region.

The focus of the special tool geometry has been mostly on the variable pitch tools rather than variable helix tools. Variable pitch tools show stability improvement at higher spindle speeds compared to variable helix tools. For both tools, optimisation of

tool geometries is essential for stability improvement, which brings the necessity of fast and accurate stability prediction of milling operations with these tools.

2.1.5 Passive chatter control

Chatter stability depends on the dynamic behaviour of the structure of the machining system. Improvement of the structural dynamics of the system can increase the chatter resistance. One way to achieve this is to use passive control devices. Passive control devices generally provide inexpensive solutions with easiness of implementation. One of the most commonly applied passive control devices in vibration suppression as well as chatter mitigation is the tuned mass damper (TMD). Therefore, although some of the other passive control devices, such as friction dampers and viscoelastic dampers, are reviewed, the focus of this section is mainly on TMD applications in machining chatter suppression.

The Lanchester dampers consisting of only the damper and auxiliary mass was considered for chatter mitigation. In one of the earlier studies, Kato et al. [96] employed the Lanchester damper to increase the chatter stability in boring operations. They attached a mass to the end of the boring bar and benefited from the damping property of the thin air film surrounding the mass. They experimentally verified the chatter suppression. A similar pneumatic Lanchester damper was later developed by Gubaniv [97] improved the chatter performance in a milling operation. They used a cylindrical weight covered by a thin-walled shell, and the damping was realised with air filling the gap between the shell and the weight. Their experimental results showed a significant chatter improvement.

Impact and friction dampers have also been investigated to increase chatter resistance. Ema and Mauri [98, 99] proposed impact dampers to enhance the damping capacity of slender parts such as boring bars. Marui et al. [100] used micro-slip between the tool shank and tool post by placing a plate into a rectangular hole cut in the long

cutting tool bar. The friction between the rectangular hole and the plate increased the damping capacity of the system, and therefore, the machining stability improvement was provided. Similarly, Ziegert et al. [101] placed a multi-fingered cylindrical insert inside milling cutters to enhance the damping capacity. The damping is increased due to the bending of the milling cutter during cutting operation, which leads to friction between the milling cutter and the insert. Edhi and Hoshi [102] developed a friction damper to increase the stability of a boring operation at high frequencies. Their friction damper consists of an additional mass mounted at the end of the boring bar with a permanent magnet and needs no tuning for the parameters.

Seto and Tominari [103] used a tuned mass damper with a variable stiffness mounted on the end of a long ram and tuned the parameters of the damper using Den Hartog's method. The machining tests showed that the TMD significantly improves the limited critical depth of cut. Liu and Rouch [104] investigated the use of the TMD to increase the chatter stability in milling. They numerically obtained the optimal parameters of the TMD and showed that the TMD doubles the limited critical depth of cut. Rivin and Kang [105] presented a comprehensive study to increase the stability of boring bars in cutting operations. They proposed a tooling structure design with a light overhang section, which allows high mass ratios for TMDs. They also analysed the boring bar with a TMD, including the tuning optimal parameters and design of the TMD. Significant performance improvements in chatter stability were reported in their study. Tarng et al. [106] utilised a piezoelectric inertia actuator as a TMD for the elimination of the chatter in turning. They manually tuned the parameters by setting the natural frequency of the vibration absorber equal to the natural frequency of the cutting tool. Six time higher chatter stability in cutting tests were achieved.

Tuning of parameters is important to obtain the best performance from TMDs. Earlier studies that utilised TMDs to increase machining stability generally applied Den Hartog's method [107], numerical or manual strategies for tuning parameters. However, it was shown that the absolute stability of machining operation is inversely proportional to the negative real value of the FRF [3, 2]. Using this relation, Sims [108] suggested a new analytical tuning strategy for vibration absorbers used to improve machining stability. The author showed that three fixed-points (instead of two fixed-points in Den Hartog's method) exist in the real part of the frequency response. Following the same procedure applied in Den Hartog's method, the optimal stiffness and damping values of the absorber can be analytically obtained for equal real peaks and equal real troughs. This tuning methodology was tested in a milling time-domain simulation, and a 40-50% performance improvement was shown compared to Den Hartog's method. Analytical expressions in Sims' method, as in the case of Den Hartog's method, were derived for an undamped main system. Although they do not guarantee the best performance, they could be applicable to a lightly damped system to an extent.

The performances of TMDs in boring operations have been further evaluated by modelling the boring bar as an Euler-Bernoulli cantilever beam, including the effect of a selection of tuning strategies [109–111]. Moradi et al. [109] investigated the best position of the absorber along the boring bar to minimise the free-end deflection. They stated that the analysis results regarding the position of the absorber are valid for chatter suppression as well. Miguelez et al. [110] evaluated the chatter suppression in boring bars by modelling a bar as an Euler-Bernoulli cantilever beam and showed that Sims' method demonstrates a better performance than Den Hartog's method. They also presented a local analysis of the analytical expressions from Sims' method [108] to obtain a better tuning frequency which improves the chatter suppression performance. Rubio et al. [111] studied the parameter optimisation of TMDs to increase chatter

stability in a boring bar involving the structural damping in the bar. They showed the effectiveness of Sims' method over Den Hartog's method. They also employed a numerical optimisation method to maximise the critical depth of cut and achieved a better performance than Sims' method.

Applications of TMDs embedded in a boring bar or milling tool were also proposed. Yadav et al. [112] modelled the boring bar as an Euler-Bernoulli cantilever beam in boring operation and applied the receptance coupling method to obtain the tool-tip FRF. The optimal parameters of the absorber were obtained by numerical optimisation, and chatter stability improvement was demonstrated with experimental results. A similar analysis was conducted by Ma et al. [113] for milling tools. They also numerically obtained the optimal design parameters of the absorber by obtaining the tool-tip FRF of the milling tool with the receptance coupling method and experimentally validated the results.

Viscoelastic dampers for chatter stability have also been theoretically and experimentally studied in the literature. Kim and Ha [114] evaluated the optimal design parameters of a viscoelastic damper following Den Hartog's optimisation criteria. They implemented a viscoelastic damper mounting on a tool post of a lathe and achieved stability improvement in turning tests. Rashid and Nicolescu [115] analysed and tested a viscoelastic damper to reduce the vibrations in a milling operation. The damper mounted on the workpiece provided significant vibration suppression. However, neither of the works of Kim and Ha [114], or Rashid and Nicolescu [115] directly focused on chatter stability. Saffury and Altus [116] analysed the optimisation of a viscoelastic turning bar for chatter stability by considering the real part of the FRF. The results were given with a comparison of the tuning of an elastic turning bar with a TMD

whose parameters were obtained by Sims' method. Advantages of the viscoelastic bar in the use of different stability measures were reported.

Enhancement of chatter performance of traditional TMD was sought by investigating multiple, nonlinear and two-DOF TMDs. Yang et al. [117] employed multiple TMDs to improve the chatter stability. They analysed the effect of the number of TMDs by keeping the total mass ratio constant. It was shown that multiple TMDs provided better performance than single TMD for the same mass ratio. However, the improvement was not the same for each TMD added. For instance, there was not a significant improvement was not shown after adding three TMDs in their study. They experimentally verified their result with a turning operation. In another study, Nakano et al.[118] also employed multiple TMDs in the end milling through a collect chuck and experimentally verified chatter stability improvement compared to the uncontrolled structure.

Employment of nonlinear elements alongside linear elements has been investigated in the context of machining stability. Wang et al. [119, 120] studied nonlinear a TMD, which consists of a friction-spring element in parallel to a traditional TMD. The FRF of the machining system with the nonlinear TMD was obtained by the harmonic balance method, and the parameters were tuned to minimise the real part of the response [120]. The authors tested the nonlinear TMD manufactured in a turning operation and the experimental results showed that the limited critical depth of cut was significantly increased with the nonlinear TMD [119]. Habib et al. [121] studied a nonlinear TMD that involves a cubic stiffness in parallel to a spring-damper arrangement. A nonlinear cutting force was considered in a linear model of a turning system. Their study concluded that, unlike a linear TMD, a nonlinear TMD with a cubic stiffness can increase the robustness of the system against subcritical bifurcations for known operational spindle speed.

Further chatter stability improvement succeeded with a two-DOF TMD. Yang et al. [122] designed and implemented a two-DOF TMD in milling operation. They numerically tuned the parameters for minimum amplitude peaks and achieved more than 100% improvement in the critical limiting depth of cut. Yang et al. [123] utilised eddy current damping with two permanent magnets in a two-DOF TMD for machining vibration suppression. They applied the damper into a thin-walled workpiece in milling tests and accomplished significant vibration reduction by matching the natural frequencies of the dampers with two dominant vibration modes of the workpiece.

Thin-walled or flexible workpieces are frequently machined in especially aerospace applications. Passive control devices have been evaluated for these workpieces to increase chatter stability. Yang et al. [124] developed an eddy current damper consisting of a permanent magnet and springs. The damper was applied to a thin-walled workpiece for chatter stability improvement. They experimentally showed that the damper was effective in increasing chatter stability by enhancing the damping of the thin-walled structure. Yang et al. [125] developed a passive damper whose stiffness is adjustable by changing the rotational orientation of the damper. The device was effective against the variation in dynamic properties of the thin-walled workpiece due to the material removal. Stability improvement was also shown with machining tests. Another passive damper with variable stiffness was proposed by Yuan et al. [126]. The working range of the damper was designed by examining the effect of the material removal on the dynamic properties. Design parameters were determined following Den Hartog's methods. It was experimentally tested by mounting it on a thin-walled workpiece in a milling operation and improved the chatter stability of the cutting process. Yuan et al. [127] also developed a TMD for a milling operation of the free-end of flexible cylindrical parts. They employed a sequential quadratic programming algorithm to obtain the design parameters of TMD to improve chatter

resistance of the system. The milling tests demonstrated that the TMD designed successfully reduced the vibration and increased the stability of the milling process.

Instead of adding passive control devices to machining structure, damping increment has also been studied to improve machining chatter stability. For instance, Zhang et al. [128, 129] conducted milling cutting tests of a thin-walled workpiece in a viscous fluid (silicone oil) to suppress the chatter. They reported stability improvement due to increase of damping of the thin-walled workpiece in the viscous fluid and considerable cutting force coefficients reduction due to the lubrication effect of the viscous fluid. They also concluded that noise during the cutting operation could be reduced since the viscous fluid provides an isolated environment around the cutting area. Butt et al. [130] increased the damping in the machining by applying non-contact eddy current damping to the tip of the milling cutter. Their proposed method leads to no change in the dynamic properties due to the mass of passive control device addition. They used permanent magnets held by an apparatus whose orientation and distance to the milling cutter can be adjusted by two servo motors. They mounted the apparatus on the spindle head and experimentally showed the damping increment in the vibration response.

Passive methods to support flexible workpieces have been investigated to increase chatter resistance. Fei et al. [131] studied the use of a moving damper acting with the milling cutter to support the workpiece from its other side and increase the chatter stability. They designed the damper considering the varying dynamic properties due to material removal and experimentally verified the stability improvement. Wan et al. [132] applied pre-stress to long thin-walled workpieces to improve local stability in milling operation. They obtained the relationship between pre-stress and the natural

frequency of the workpiece. They experimentally demonstrated chatter improvement using this relationship.

It is also possible to increase the chatter stability by designing a clamping system or using a passive control device to support fixtures on which workpieces are mounted. Munoa et al. [133] designed a clamping table with adjustable stiffness and damping for milling of a thin-walled part. Milling tests proved that their design of the clamping table provides a significant stability improvement for the thin-walled workpiece. Wang et al. [5] experimentally investigated the effect of supporting the fixture using an inerter-based configuration to suppress vibration in milling. They analysed the vibration response under forced vibration by directly connecting two different inerter-based configurations to the ground. They conducted the experiments using limited components. Although both simulation and experimental results provided performance improvements in vibration suppression, the improvement ratios showed clear differences between some simulation and experimental results. Therefore, although their work was important in terms of presenting the potential benefits of the use of the inerter, a more comprehensive study is needed, analysing not only the forced vibration under the cutting force but also chatter stability improvement of the use of the inerter in a machining process.

2.1.6 Semi-active chatter control

Although passive control methods offer robust, reliable and low-cost solutions to increase regenerative chatter resistance, their performances are generally limited and only applicable to a narrow frequency band. In order to increase chatter resistance performance and broaden the frequency band, semi-active or active methods have been utilised in machining applications. External energy is introduced into the system

in both methods. However, the energy inserted into the system in an active control method acts against the disturbance in a manner of suppressing vibration while the energy in a semi-active method is used to adjust the dynamic properties of control device such that the performance is increased. The energy requirement of semi-active control applications is low as opposed to active control applications as the energy is only used to adjust the control parameters, and then it acts as a passive control device.

All passive dampers which allow variable stiffness, damping and mass can be classified as a semi-active control method. Within this context, the damper proposed by Seto and Tominari [103] where the stiffness of the damper can be adjusted by changing the position of the sliding damper mass through the overhung length of the ram can be classified as a semi-active control application. Munoa et al. [134] also proposed the use of a TMD with variable stiffness where its stiffness is set by a rotary spring. Their design aimed to suppress the chatter in heavy-duty milling operations by mounting the TMD into fixtures. They automatically tuned the stiffness of the rotary spring using a small motor to match the natural frequency of the TMD with the chatter frequency that is also automatically obtained by evaluating the FFT of the measured acceleration. They utilised eddy currents for the damping and experimentally showed the effectiveness of the proposed design by testing it on fixture systems in heavy-duty milling.

It is also possible to obtain similar natural frequency adjustment by changing the damper mass instead of changing the stiffness. Burtscher and Feischer [135] proposed a TMD with variable mass to compensate for the detuning effect stemming from the position of the machine tool in milling operations. They used a liquid tank as the damper mass, which can be filled with coolant liquid or emptied to the desired level via hydraulic connections. In that way, the natural frequency of the damper between

the natural frequencies obtained from a fully filled tank and a empty tank could be continuously adjusted. They were also experimentally tested the manufactured prototype for different positions of the machine tool by mounting the damper to the spindle head and validated its effectiveness.

Smart fluids such as Magnetorheological (MR) or Electrorheological (ER) fluids whose viscosity can be controlled applying a magnetic or an electric field, respectively, have been studied to improve the stability of machining operations. Changing elasticity with increasing magnetic or electric field leads to change in the dynamic properties of the structure interacted with or filled with MR or ER fluids, and this change has been used to increase in favour of chatter resistance in the proposed methods in the literature. Lei [136] first proposed the use of ER squeeze film damper to improve chatter performance of machining operations. In this study, only the basic principle of the application was presented without any theoretical analysis or experimental work. Aoyama and Inasaki [137] utilised an ER shear film damper into the table system in a milling operation. The damping of the table that was supported by four linear-motion bearings was increased with two ER film dampers. It was experimentally shown that the chatter vibrations which existed with zero voltage applied to ER film damper were suppressed with applied voltage. Wang and Fei [138] also showed how to improve the chatter stability using a boring bar with ER fluid.

Although both ER and MR fluids have advantageous features such as controllability, reversibility and quick response, MR fluids provide higher yield stress and operation in a wider temperature range with lower power supply [139]. Similar to ER dampers, MR dampers were also investigated to increase chatter resistance in turning operations [140–142] and boring operation [143]. Ma et al. [144] proposed to use MR fluids to support the thin-walled workpiece in milling operation. They placed the thin-walled workpiece

in MR fluid inside a guiding block between two coils. The stability improvement was achieved by applying a magnetic field to the MR fluid through the coils during the cutting tests.

The studies of MR or ER fluids mentioned above were conducted considering a constant electric or magnetic field. Smart fluid applications with the time-varying electric or magnetic fields were also considered. It was shown that a sinusoidally varying electric field gives better chatter suppression performance for an ER fluid [145]. Mei et al. [146, 147] showed how to improve chatter stability with an MR fluid-based boring bar by applying a current in a square waveform to the coil to induce the magnetic field. They concluded that the square waveform presents the best performance compared to sinusoidal and triangular waveforms.

2.1.7   Active chatter control

Active control applications generally offer higher performance than passive and semi-active control methods. Different from semi-active applications, the actuator continuously generates force to suppress the chatter. An active control method requires an actuator to produce a counteracting force, sensors to feed the system with the measured data, a controller and other supporting equipment such as an amplifier and signal conditioner.

Earlier attempts of chatter suppression with active control methods in machining operations focused on improving the dynamic behaviour of boring bar in boring operations. Klein and Nachtigal [148, 149] actively manipulated the slope of the boring bar around a pivot by using an electrohydraulic servo to improve the chatter

stability of boring operation. The controller in their application was fed back with a torsional strain gage placed near the tool insert, and a considerable chatter suppression improvement was presented in cutting tests. Similarly, Glaser and Nachtigal [150] used a torsional strain gage for the measurement, but the actuation force was provided by a pressure difference between two hydraulic chambers inside the boring bar. Piezoelectric actuators were also implemented to create the actuation force by directly attached piezoelectric ceramic plates to the boring bar [151] and by utilising a proof mass absorber where the piezoelectric actuators move the auxiliary mass inside the boring bar [152]. In these works, the actuation force was applied uniaxially. Pratt and Nayfeh [153] proposed the use of biaxial actuator forces to obtain the best chatter performance in boring operation. The active control of the boring bar in their work was considered with a nonlinear model and applied using magnetostrictive actuators.

Active control techniques have been frequently applied to the tool-tool holder-spindle system, workpiece-fixture system or structure of the milling machine using different types of actuators. Dohner et al. [154] developed a smart spindle unit for the implementation of an active control to improve the stability of a milling operation. Four electrostrictive actuators in the spindle unit provided actuation force over the spindle through a static cartridge and ball bearings. The bending of the cutting tool was measured by the strain gages placed to the tool. The smart spindle unit was tested under real cutting conditions, and the active control method provided a higher maximum stable depth of cut of up to five times.

There are a considerable number of application that employs active tool holder-spindle systems supported by piezoelectric actuators to increase chatter resistance of milling operation. Monnin et al. analysed the use of the active control [155] implemented using a spindle shaft supported with piezoelectric actuators from its front bearing [156].

They achieved more than 50% improvement in the limited critical depth of cut using a model-based disturbance rejecting controller. The controller was fed back by data measured by the accelerometers placed near the actuators. Similar applications of smart tool systems supported by piezoelectric actuators were presented with different controllers, including an adaptive controller [157], a model-predictive controller [158], a controller based on H_∞ almost disturbance decoupling problem [159] and a robust controller [160].

Some researchers employed a piezoelectric actuator with an open-loop control approach, where the controller is not fed by a sensor, in order to reduce the complexity of the control methods and use of expensive equipment. Wang et al. [161] proposed a time-varying stiffness technique for mitigation chatter in milling operation. The control force was applied to the tool holder by a piezoelectric actuator through the rolling bearings to vary the stiffness of the machine tool system. They evaluated the effect of stiffness variation in two radial directions, including sinusoidal, square and triangular waveforms with different frequencies and amplitudes. The best chatter performance was obtained with a square waveform with small amplitudes and frequencies of 40-60 Hz. Later, they showed that multi-harmonic and random stiffness variations presented better chatter suppression than the single frequency stiffness excitation studies previously, albeit with increased computational costs to obtain optimal excitation parameters [162]. Using an identical spindle-tool holder setup with piezoelectric actuators, Li et al. [163] implemented an asymmetric stiffness in two radial directions. The analyses and experimental results showed that having a higher stiffness in one of the radial directions can help to improve the milling stability depending on the type of the milling operation (up and down).

Active magnetic bearings (AMBs) serve as non-contact supports to a spindle system by producing magnetic forces. These magnetic forces can also be used to increase chatter suppression by manipulating the spindle shaft through a control method. AMBs were frequently employed in chatter suppression of milling operation [164–168]. Chen and Knospe [165] proposed three control strategies to enhance the machining stability for spindle speed-independent, a specific spindle speed, and a given spindle speed band. Although only the controller for spindle speed-independent control was tested by a turning operation that mimicked the dynamics of a milling spindle, three control schemes showed improvements when compared to a PID controller, which was considered a standard controller for AMBs, during impact tests. Experimental cutting tests showed 63% improvement in the critical limiting depth of cut for spindle speed-independent control strategy.

Van Dijk et al. [169, 170] developed an active robust control scheme using μ-synthesis where the process parameters (spindle speed and depth of cut) were considered as uncertainties to ensure stable cut for a range of process parameters for high-speed milling. Van de Wouv et al. [171] first experimentally verified the μ-synthesis control method presented in [169, 170] using an active spindle supported by AMB. Wu et al. [167] also utilised the AMB with μ-synthesis approach but for a low immersion milling operation. Huang et al. [168] proposed an optimal controller considering rotor stability including acceleration and spindle speed variation in air cutting and an adaptive controller for chatter suppression in material cutting for a spindle supported by AMBs. In the work, only numerical simulations of milling operations were considered, and no cutting tests were conducted.

Active magnetic actuators were directly applied to the spindle shaft without using active magnetic bearings. Bickel et al. [172] developed a spindle prototype whose shaft

can be actively controlled by an electromagnetic actuator. The initial results obtained from milling tests indicated 50% improvement in the limited critical depth of cut. Similarly, Wan et al. [173] built a spindle system with a non-contact electromagnetic actuator that can generate control forces in both radial directions of the spindle shaft. The displacement sensors placed around the spindle shaft were used for the feedback signal. They conducted experimental milling tests using, first, a simple PD control [173] and later, sliding mode control [174]. Chatter suppression was verified in both control methods, but no direct comparison of experimental results was presented.

There are also considerable active control studies applied to workpieces or workpiece fixturing systems. Huyanan and Sims [175] examined three control strategies, including the virtual passive-active absorber controller, the skyhook controller, and the virtual passive absorber controller with the consideration of machining chatter performance. They employed an electromagnetic proof-mass actuator attached to the workpiece excited by a shaker to evaluate the dynamic behaviour. The results showed that the virtual passive absorber was the most favourable controller with less sensitivity to measurement noise and relatively lower control energy consumption. Although no machining test was presented and only peak magnitude of FRF was considered in this study, later, milling tests for the virtual passive absorber controller with Sims' method was presented [176]. However, the performance of the virtual passive absorber controller, like other model-based control approaches, is possibly degraded due to change in the dynamics of the workpiece during material removal or unaddressed modes. To deal with this, Beudaert et al. [177] employed a portable electromagnetic proof-mass actuator with a model-independent control scheme where parameters were automatically determined to maximise the dynamic stiffness. The effectiveness of the portable actuator with the proposed control scheme was also verified with milling tests in laboratory conditions as well as an industrial application.

Zhang and Sims [178] proposed the use of a thin piezoelectric actuator attached to the surface of the workpiece to improve the stability of a milling operation. Stability improvements were verified under real cutting conditions for both the open-loop and the closed-loop cases with a positive position feedback controller. The authors reported saturation of the piezoelectric signal observed in many tests with the closed-loop control as a possible performance reduction factor. Piezoelectric actuators integrated into workpiece holding systems were studied to mitigate specifically chatter [179, 180] and excessive vibration [181]. Brecher et al. [179] developed an active workpiece holder consisting of piezoelectric actuators and flexural guides. They achieved chatter suppression with the control strategy applied by minimising the dynamic compliance in milling tests. Sallese et al. [180] used a similar workpiece holder to suppress chatter with a high chatter frequency beyond the controllable frequency by a piezoelectric actuator. The control strategy applied for this purpose involves amplitude modulation of the piezoelectric actuation at low frequency. The preliminary results obtained from slope cutting tests verified the improvement in the absolute stability limit. Parus et al. [182] employed a piezoelectric actuator in a flexible workpiece-fixture system to address the chatter problem caused by flexible workpieces connected non-rigidly. Applying Linear Quadratic Gaussian algorithm, experimental milling tested validated improvement in the suppression performance for both chatter and forced vibration. A high voltage requirement was reported as the challenging point for the workpiece-workpiece holder system integrated with the piezoelectric actuator [181, 182].

The structure of the machine tool becomes the critical mode with its low frequencies in heavy-duty milling. It was shown that the structural mode can be actively damped using an inertial actuator and stability improvement could be achieved for heavy-duty milling operations. Chung et al. [183], for instance, experimentally evaluated the negative real response of a milling machine controlled by a magnetic inertial

actuator. The results demonstrated that a significant stability improvement in the structure modes can be achieved. Brecher et al. [184] accomplished an inertial actuator excited by an electrohydraulic system with the capability of producing large forces to suppress chatter in heavy-duty milling. The controlled structure with velocity feedback control provided more than double improvement in cutting tests. Munoa et al. [185] developed an active control by placing a biaxial inertial mass actuator on the ram of the milling machine. They compared different control strategies, including direct acceleration, velocity and position feedbacks, as well as delayed position feedback. The best performance obtained by the direct velocity feedback and the stability improvement was experimentally verified for different ram positions of the milling machine. Zaeh et al. [186] presented active chatter suppression of structure mode of milling machine using an inertial actuator. In the proposed method, the inertial actuator was used for both automatic system identification and subsequently, active control where the parameters of the controller were obtained automatically. By applying this control method, stability improvements were achieved for the direct velocity feedback and H_∞ controller under real milling operations.

2.1.8   Summary of machining chatter review

Stability prediction is an essential tool for chatter avoidance as an out-of-process technique. The zero-order approach method is a fast and accurate method for cuts with high radial immersions. One of the most frequently used methods that are accurate for both low and radial immersion cuts is the semi-discretisation method. It has been employed in the prediction of the stability of milling, even including variable spindle speed and using special tool geometries. However, this method is computationally more expensive and less suitable for industrial applications compared to the frequency-

based ZOA as well as the MFA. Utilising the ZOA is generally more preferable to the semi-discretisation method for high radial immersion cuts conducted by a standard tool with constant helix and pitch angles as it provides fast and accurate prediction. Moreover, using the ZOA provides an extra benefit since it explicitly presents the direct relationship between the system's stability and structural dynamics. Therefore, in this study, the ZOA is adopted to evaluate the performance of using inerters in milling operations.

Chatter stability improvement is possible to different extent for all chatter control methods presented above. However, each method shows different drawbacks that limit its use. Variable helix and variable pitch tools require optimisation of the tool geometries, which can be challenging due to computational cost. Variable spindle speed needs spindle drives that are capable of meeting the requirement of the amplitude and frequency variations. Also, its stability improvement is more effective at lower spindle speeds. Implementations of active, semi-active and passive control methods might need structural modifications. The performance of the passive control methods is limited compared to active control methods and they could lose their effectiveness with the change in dynamic properties. Semi-active and active controls can be adaptive and provide better performance. However, their applications are more complex and expensive compared to passive control methods so this justifies the exploration of using inerters instead. Although using inerters increases the complexity and cost of passive solution, it still offers a cheaper and simpler method than semi-active/active methods. Furthermore, it does not have disadvantages of leading to instabilities, as can occur in active control methods. However, its application requires more effort in the analysis, optimisation and analysis stages.

Finally, although applications of the passive control methods in the literature are rich, they are generally limited to traditional control elements. Integration of inerter into traditional passive control devices such as TMD could bring the improvement of chatter stability. Promising results in this direction were already presented by Wang et al. [5]. Their studies approached to the undesirable vibration in milling operation as a forced vibration problem rather than a stability problem. However, the major issue in milling operation is the stability problem, the so-called chatter. Chatter vibration is more detrimental than forced vibration as chatter is cause by instability and lead to an increase in vibration level with time. Also, they conducted the experiments with limited elements by using only available springs, dampers and inerters instead of manufacturing them in their optimal values. Therefore, this thesis provides a more comprehensive study by focusing on the chatter stability and presenting a more versatile implementation of the inerter.

2.2 Inerter review

There has been an increasing number of research activities that focus on the inerter and its application in the vibration control community. For the past two decades, the inerter has been employed in a wide range of vibratory systems. Therefore, research studies regarding the inerter and its application deserve a separate section. Having presented the literature review of machining chatter, this second section focuses on the inerter and its applications.

2.2.1 Introduction

The tuned mass damper (TMD) as an effective passive vibration control device has been frequently employed to mitigate undesirable vibrations in mechanical structures. The concept was initially introduced by Frahm [187] by adding spring and secondary mass to the vibratory system. Later, it was improved by Ormondroyd and Den Hartog [188] by including a damper in parallel to the spring. Adding a damper prompts the energy dissipation in the structure and enhances the effectiveness of the device by broadening the frequency range. The parameters of TMD are needed for tuning to obtain the best performance. For this purpose, analytical tuning strategies based on the fixed-point theory, such as Den Hartog's method [107] and Sims' method [108] aiming general vibration suppression and machining chatter suppression respectively, were presented. The TMD with a proper tuning strategy has been extensively used in a wide range of engineering applications.

The performance of a classical TMD can be further improved by integrating an inerter. The inerter is a two terminal mechanical device that generates forces proportional to the relative acceleration between its terminals. The forces in an ideal inerter are equal in magnitude and opposite in direction [189]. The concept of inerter was first introduced by Smith [4] to develop a two-terminal representation of a capacitor in a mechanical context based on the force-current analogy between mechanical and electrical contexts. A simple realisation of the inerter was presented with a rack-and-pinion inerter in his work. He also demonstrated performance improvement and possible application of the inerter in a vibration absorption and vehicle suppression systems.

Prior to Smith's study, other mechanical devices applying the same principle had been proposed under different names. In 1997, Okumura [190] patented an inerter

device named the gyro-mass. Kuroda et al. [191] and Saito et al. [192] analysed a relative-acceleration inertial mechanism, called the gyro-damper. Historical reviews of inerter and inerter-like devices were covered in more detail in [193, 194]. Following the introduction of the inerter concept in Smith's work [4], the inerter has been widely utilised in many engineering applications to improve the system performance, as it will be reviewed in the following sections.

2.2.2   Mechanical inerter devices

Different types of physical realisation of the inerter were developed to investigate the performances of the inerter and inerter-based control device in a configuration with other traditional components (e.g. spring and damper). Three types of the inerter that have been commonly employed in literature are rack-and-pinion inerters, ball-screw inerters and fluid-based inerters, as depicted in Figure 2.2. All inerter devices consist of an inertial body (e.g. flywheel or fluid) and a mechanism scaling the inertia (e.g. gears, nut/threaded rod or helical tube).

As its name shown suggests, a rack-and-pinion drives a flywheel in a rack-and-pinion inerter as shown in Figure 2.2a. The gear ratio between the gear and pinions defines the factor of inertia of the flywheel scaled. Neglecting the masses of all components but the flywheel, the inertance of the rack-and-pinion inerter is written as

$$b = m\left(\frac{\gamma_0}{r_1}\right)^2\left(\frac{r_2}{r_3}\right)^2, \tag{2.1}$$

where m is the mass of the flywheel, and r_1, r_2, r_3 and γ_0 are the radius of the flywheel pinion, the gear, the rack pinion, and the gyration of the flywheel in Figure 2.2a.
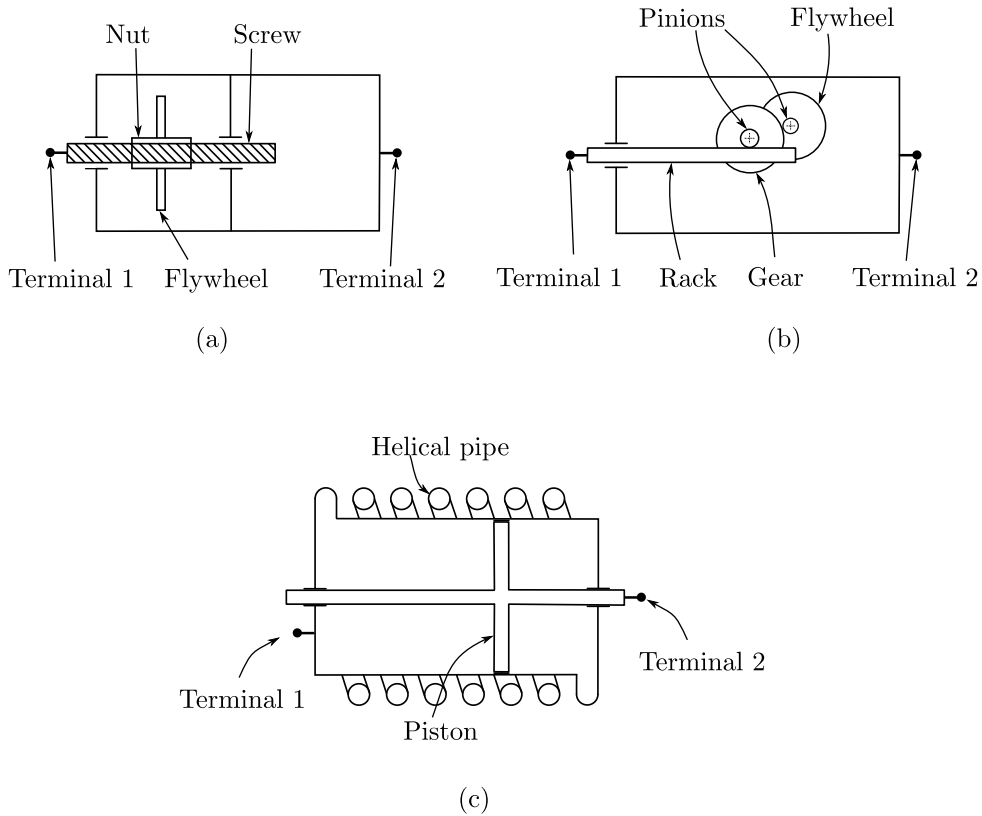
Figure 2.2 Some of possible physical realisations of mechanical inerters: Ball-screw inerter, (b) rack-and-pinion inerter and (c) helical-fluid inerter.

Papageorgiou et al. [195] presented experimental results of a rack-and-pinion inerter and a ball-screw inerter. The manufactured rack-and-pinion inerter was capable of producing an inertance of 700 kg with a mass of 3.5 kg. Although the experimental results were close to an ideal inerter, friction and backlash observed in the device were highlighted. Experimental analyses of the manufactured inerters for vehicle suspension systems were performed by Smith and Wang [196], and Wang et al. [197]. The inerter device, known as gyro-mass, patented by Okumara [190] also employed a rack-and-pinion mechanism with a spring.

The interaction between the nut and the threaded rod leads to rotation of the flywheel in a ball-screw inerter as shown schematically in Figure 2.2b. The factor that scales the inertia of the flywheel is the function of the transmission ratio of the ball-screw.

Neglecting the masses of all components except flywheel, the inertance of the ball-screw inerter is written as

$$b = m\left(\frac{2\pi\gamma_0}{p}\right)^2, \tag{2.2}$$

where m is the mass of the flywheel, γ_0 is the radius of the gyration of the flywheel, and p is the pitch of the screw with the unit of m/rev in Figure 2.2b. Earlier inerter devices named gyro-dampers [191, 192] and tuned viscous mass damper (TVMD) [198] utilised a ball-screw system to amplify the inertial effect. Wang and Su [199] experimentally evaluated a ball-screw inerter for a vehicle suspension system. The experimental results showed the existence of friction and the elastic effect in the ball-screw inerter. Even though these nonlinearities reduced the performance of the suspension system tested, their performance surpassed a conventional suspension system. Gonzalez-Buelga et al. [200] analytically and experimentally analysed a ball-screw inerter connected in series to a parallel-connected spring-damper arrangement with a dry friction model. They concluded that the detrimental effect of the friction was only apparent in low amplitude excitations and was improved by retuning parameters. However, re-tuned parameters for low amplitude excitations degraded the performance in high amplitude excitations.

In order to achieve a mechanical inerter device, the employment of a flywheel is not a necessity. A helical fluid inerter, as given in Figure 2.2c, where the inertance is provided by rotating fluid through helical channels. Neglecting the masses of all components except the fluid, the inertance of the helical fluid inerter is written as :

$$b = \rho l\left(\frac{A_1}{A_2}\right)^2, \tag{2.3}$$

where ρ, l, A_1 and A_2 are the density of the fluid, the channel length, effective cross-sectional area of the main cylinder, and the helical channel in Figure 2.2c. First

examples of the helical fluid inerters were reported in patent applications [201–203]. Swift et al. [204] first built and experimentally examined a helical fluid inerter. They considered nonlinear parasitic damping in parallel with an ideal inerter in the model to reflect the pressure drop in helical channels. Later, De Domenico et al. [205] employed a similar model for experimental investigation of a helical fluid inerter to improve seismic control of buildings. Liu et al. [206] provided a generalised model of a helical fluid inerter considering different parameters, including friction, coupler stiffness, backlash and fluid stiffness. Their proposed model was experimentally verified with different design settings.

The friction that was observed in the experimental investigations of most of the inerter devices presented above possibly cause detrimental effects. In order to eliminate friction, a pivoted flywheel with living-hinges was developed by John and Wagg [207]. Inspired by the DAVI of Flannelly [208], they employed a pivoted rotating disc as both the flywheel and a lever arm to amplify its own inertance through the distance between the pivots. In their design, living-hinges in the pivot connections provided frictionless rotation of the flywheel. The effectiveness of the device in base isolation was also demonstrated by experiments. Although the achieved inertance-to-mass ratio by their inerter device was small compared to other types of mechanical inerter devices, the potential use of the inerter such as applications with small amplitude is promising.

Types of mechanical inerter devices are not limited to the above-mentioned examples. Other types of mechanical inerter devices were also proposed in the literature including fluid-based inerter with flywheel [209], fluid inerter with a rubber membrane where the stiffness element is integrated into inerter [210], the mem-inerter [211], clutched inerters [212] and semi-active inerters [213]—see also [193, 189]. Feasibility and benefits

of inerter-based control devices with any type of mechanical inerter devices mostly depend on the layout of the elements of the control device and application.

2.2.3 Performance evaluations and applications

Inerter-based applications have been widely applied in many fields of engineering to increase the vibration performance of the system. A series of different inerter-based layouts were investigated in the vehicle suspension systems to increase the different performance measurements, including passenger comfort, handling, tyre grip, and suspension deflection [196, 214, 197, 215–218]. The inerter was employed in motorcycle steering compensator to increase the stability [219, 220] and in suspension systems of railway vehicles to enhance the ride comfort and lateral body movement [221–223]. Its application areas have been extended to aircrafts' landing gear to improve both its shimmy suppression [224] and touchdown performance [225]. There have been considerable number of studies regarding civil engineering applications including buildings suppression [198, 226–229], wind turbines [230, 231] and cables [232–234]. It was also proposed to be used for the vibration reduction in milling machines [5]. Besides these application-based studies, a more general investigation was also conducted. For instance, Chen et al. [235] theoretically showed that inerter can reduce the natural frequency of a system. Hu et al. [236] also demonstrated that the natural frequencies of a mass-chain system can be designated by solely inerters and springs.

In theory, there is an infinite number of possible layouts consisting of control elements: inerters, springs and dampers. However, layouts with low complexity are preferable due to technical difficulties of physical realisation and space limitations. Thus, on one hand, researchers investigated the best simplification of the layouts by restricting the

number of elements while keeping the performance as high as possible [217, 237–240]. On the other hand, the structural-based approach where the low-complexity is already guaranteed with the predefinition of the inerter-based layout was widely applied. Three well-known layouts utilised in vibration suppression and isolation systems are the tuned inerter damper (TID), the tuned mass damper inerter (TMDI) and the tuned viscous mass damper (TVMD) as illustrated in Figure 2.3.
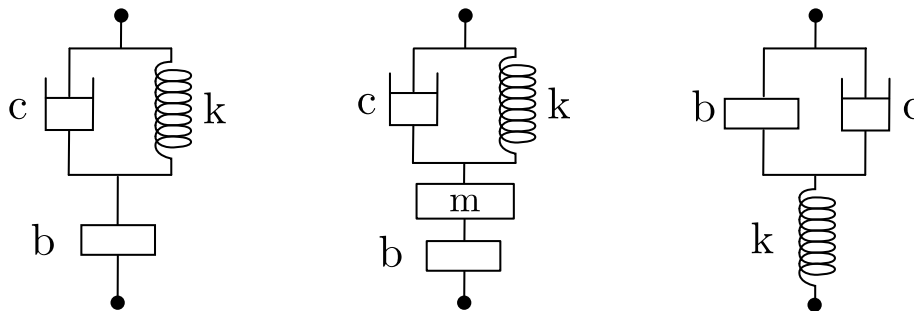
Figure 2.3 Three well-known layouts of the inerter: (a) Tuned inerter damper (TID), (b) Tuned mass damper inerter (TMDI), and (c) Tuned viscous mass damper (TVMD).

An inerter is in series with a parallel-connected spring-damper arrangement in a TID as shown in Figure 2.3a. Lazar et al. [226] proposed a TID to mitigate the vibration of a multi-storey building. They employed an iterative optimisation process based on Den Hartog's method to obtain the optimal design parameters. It was shown that the TID provided the same performance as a TMD for the same mass ratio but a lighter device's mass. Also, the best performance was obtained when the TID was located at the bottom storey, which reduces the structural loads at higher floors. They also studied the TID attached to ground from its one terminal for the suppression of vibration of cables [232]. Sun et al. [233] considered the use of a TID by interconnecting cables. The TID showed superior performance over traditional passive methods. This layout was also evaluated for seismic control of structures [241, 242] considering the effect of the soil type [243] and structural damping [244].

The TMDI layout is similar to a TID but with a secondary mass between the series-connected elements as present in Figure 2.3b. In this respect, a TID can be accepted as a special form of the TMDI with zero secondary mass. Marian and Giaralis [245] proposed a TMDI by attaching an inerter to a classical TMD to suppress vibrations of SDOF and MDOF structures induced by stochastic base excitation. Optimal design parameters were also analytically obtained for an undamped SDOF main system. They concluded that a TMDI can achieve better performance than a TMD with the same auxiliary mass or provide the same performance as a TMD but with lighter mass. Later, they also considered harmonic base and forced excitations for an undamped SDOF system and obtained analytical closed-form solutions for the optimal design parameters [246]. In this study, the energy harvesting performance of TMDI was also investigated by replacing the damper with an electromagnetic motor.

Giaralis and Taflanidis [247] enhanced the optimal design strategy involving high-order modes and uncertainties for the seismic control of MDOF structures. The authors also considered inertance as a design parameter in the optimisation process, and TID as a special case of a TMDI. They concluded that the TMDI showed a better performance than a TMD, including the higher modes. It was also added from the results that the TMDI exhibited robustness against both uncertainties in excitation and structure. Matteo et al. [248] investigated the TMDI for base isolated MDOF systems to suppress the seismic vibrations. They developed an analytical formula for the optimal design parameters. Although their formula involves some assumptions, its effectiveness was proven by testing with real earthquake data and the comparison with the design parameters obtained by numerical optimisation.

Wang and Giaralis [249] examined the performance of the TMDI attached to the free end of cantilever-like structures with different shapes for the effect of the location

of the inerter's connection. It was found that the best performance was obtained when the inerter was grounded. They also noted that the control of the shape of the structure with a more flexible upper part than the lower part requires less secondary mass or shorter connection distance for the inerter, which means cost reduction in the implementation. TMDI were further studied to suppress the vibration induced by wind in tall buildings [250, 251] and vortex-induced vibration in long-span bridges [252].

De Angelis et al. [253] evaluated the seismic control performances of a TMD, a TID, and a TMDI together with a base isolation system considering a generic model. Both inerters in the TID and the TMDI were grounded in their study. They showed that both the TMDI and the TID have better performance than the TMD. However, the performances of all control devices, including TMD, lose their effectiveness with increasing damping in the base isolation system. Deastra et al. [254] utilised a linear hysteretic damping in a TMDI and a TID, instead of linear viscous damping. Behaviours of both hysteretic devices differed from the TMDI and TID at higher frequencies. In addition to frequency domain analysis, they also evaluated time-domain response of the hysteretic devices via their developed time domain method based on the time-reversal technique.

A TVMD consists of a spring in series to a parallel-connected a viscous damper and an inerter as given in Figure 2.3c. Ikago et al. [198] analysed the use of the TVMD for the control of an SDOF structure for seismic control. They also obtained a closed-form solution for optimal design parameters for harmonic base excitation using fixed-point theory. The TVMD exhibited a better performance than a classical TMD in shaker table tests conducted with real earthquake data. Pan et al. [255] also studied a TVMD (named as parallel-layout viscous inerter damper in their study) for the control of a damped SDOF. Instead of using fixed-point theory, they proposed a numerical design

strategy where both the displacement response of the structure and the damping force are taken into consideration. Later, Pan and Zhang [256] proposed a more practical method for the designs of both the TVMD and TID as well as the series layout inerter system (that consists of a series-connection of an inerter, a spring and a damper) for the mitigation of seismic response. Their method employed the closed-form solution of stochastic mitigation ratio as the design indicator considering structural damping in the main system under white-noise excitations.

Hu et al. [257] derived the closed-form solutions for optimal design parameters of five different layouts of isolator system, including a TID and TVMD. They considered both H_∞ and H_2 optimisations, where the design parameters were optimised for minimisation of the maximum amplitude of the system under harmonic excitation and minimisation of the mean squared displacement of the main system under random excitation, respectively. The authors highlighted the potential benefits of the inerter-based isolators due to the obtainability of large inertance with small physical mass. The results demonstrated that some layouts can achieve better H_∞ and H_2 performances with the same inertance-to-mass ratio compared to a classical TMD. Zhang et al. [258] presented the relationship between the energy dissipated and the vibration suppression by evaluating the stochastic response of the damping elements in a TVMD and TID. Using this relationship, they proposed a design strategy where both the vibration suppression and the damping enhancement are taken into consideration as objectives to be satisfied.

Vibration absorption of an SDOF system where the inerter-based device is attached in a similar way to a classical TMD was considered by Hu and Chen [259]. They analysed performances of inerter-based dynamic vibration absorbers (IDVAs) where the damper in a classical TMD is replaced with six different inerter-based layouts.

The IDVAs were mounted on an undamped SDOF main system subjected to force excitation. The optimal design parameters were numerically determined for the H_∞ and H_2 performances (except the Layout C3 analytically derived for H_2 performance). The results showed that connecting only an inerter in series or parallel to the damper of a classical TMD presented no increase in the suppression in both performances while the layouts which added a spring, such as a TID or TVMD (C4 and C6 in their work), can improve the H_∞ and H_2 performances by 20% and 10%, respectively, compared to a TMD. Analytical expressions for the optimal design parameters of layouts with the best performance (C3, C4 and C6) were presented by Barredo et al. [260] by extending the fixed-point theory. Javidialesaadi and Wierschem [261] derived the closed-form solution of the design parameters of a TVMD (named the rotational inertial double tuned mass damper in their work or C6 in [259]) for random base and force excitations. The researchers noted that the optimal design parameters for the two excitation types exhibited significant differences. The implementation of IDVAs (C3, C4 and C6) with an additional damper connected in parallel was also theoretically examined for an off-shore wind turbine to reduce loads induced by wind and wave [262]. The results obtained from numerical H_2 optimisation for a simplified linear model showed an increment in the performance in general.

The performance of the layouts were further increased by adding more elements. For instance, Javidialesaadi and Wierschem [263] proposed to attached a spring in series with the TMDI's damper to enhance the performance of the TMDI. Nontraditional IDVAs attached to an SDOF main system whose one or more elements are directly connected to ground [264–266], even including negative stiffness [267, 268], were also investigated to further increase vibration suppression performances of IDVAs. Moreover, designated nonlinearity in the inerter element and/or the stiffness element in the control system have been examined to enhance the system performance. A nonlinear energy

sink was improved by an inerter by replacing the linear stiffness with a cubic stiffness in the TID [269] and TMDI [270]. Both studies reported the performance increment and the reduction in the mass of the control device compared to their linear counterparts. Hua et al. [271] achieved to increase the vibration performance and robustness of an isolation system by applying a friction element in parallel to the TID. Moraes et al. [272] geometrically applied nonlinear inerter by horizontally attaching an inerter to the vertical spring-damper isolation system. Numerical results showed better performance at higher frequencies due to the shift of the anti-resonance. Moreover, Yang et al. [273] considered the geometrically nonlinear inerter to improve the performance of the quasi-zero stiffness isolator. The nonlinear inerter enhanced the frequency band for the overall performance and lowered peak in the force transmissibility. Even though complex inerter-based layouts and the inclusion of the nonlinear elements generally showed better performance compared to simple and linear layouts, the physical realisation of these layouts is challenging.

2.2.4   Summary of inerter review

The inerter has been increasingly studied to enhance dynamic response of system in the last two decades. Among different possible realisations of the inerter, the most common types of mechanical inerter device are the rack-and-pinion inerters, ball-screw inerters and fluid-based inerters. The implementation of these devices could involve some nonlinearities such as friction and backlash. Moreover, inerter devices are generally designated for relatively large applications such as building isolation or vehicle suspension systems. The implementation of them into small-scale small-amplitude applications can be problematic except the living-hinge inerter [207], which was proposed as a small-scale inerter. Therefore, in this thesis, the living-hinge inerter

forms the basis of the inerter design. It is modified for being capable of producing small inertance and integration into localised additions.

There have been different inerter-based layouts proposed in the literature. Applications have been mostly focused on civil engineering applications or vehicle suspension systems where the inerter-based layout is grounded or deployed between two parts of the primary structure. IDVAs, on the other hand, can be applied without need for such connection limitations. However, it was only studied theoretically. Physical implementations of IDVAs, especially in small scales, have not been presented yet. Therefore, the experimental validation of the study in this thesis considers such implementation in Chapter 4.

Finally, although inerters have been utilised a wide range of engineering applications, there has been no study of inerter regarding machining chatter stability as discussed in the summary of machining chatter review. This thesis address this gap in the literature.

Chapter 3

Theoretical Background

3.1 Introduction

This chapter introduces the theoretical background of machining stability analysis applied in the following chapters of this thesis. The mechanism underlying the regenerative chatter has differences from the classical vibration theory of free/forced vibrations utilised in the analysis of the general vibratory problem. It is induced by instabilities due to the waviness of the cut surface. In Section 3.2, a basic understanding of the regenerative chatter mechanism established by Tobias and Fishwick [2], and Tlusty and Polacek [3] is presented considering a continuous single-point cutting operation. The introduction of the concept of the stability lobe diagram is also given in the same section. Section 3.3 extends the theory to stability analysis of milling through the zero-order approach (ZOA) proposed by Budak and Altintas [17]. This approach enables the analytical stability analysis involving the Fourier expansion of time-periodic coefficients to obtain averaged time-invariant coefficients. The details of the method

are presented for a general two-DOF milling system. Then, the stability criterion is reduced to the milling of an SDOF structure for the milling application in the following chapters.

3.2 Theory of regenerative chatter

Regenerative chatter is a self-excited vibration caused by the waviness of the cutting surface on the workpiece. In a cutting process, the tool indented to the workpiece induces cutting forces during the material removal. The flexible cutting tool and workpiece excited by these cutting forces lead to waviness imprinted on the surface of the workpiece in each cut. The total contribution of the waviness remained from the previous cut and vibration in the current cuts can increase the chip thickness removed, which results in high cutting forces. These high forces again cause higher chip thickness and higher cutting forces. Consequently, the amplitude of the vibrations continuously grows. This regenerative mechanism is known as chatter. The analysis of the regenerative chatter mechanism was first presented by Tobias and Fishwick [2], and Tlusty and Polacek [3]. Here, it is explained with a simplified example of turning where a continuous single-point cut is considered.

A schematic view of turning operation with a rigid rotating workpiece and flexible cutting tool in the y-direction is illustrated in Figure 3.1a. There is no vibration considered in x-direction as both the cutting tool and the workpiece are assumed to be rigid in this direction. Considering an orthogonal cutting operation where the cutting edge is perpendicular to the cutting velocity, the cutting tool fed in the workpiece's radial direction generates two cutting forces with constant directions: tangential
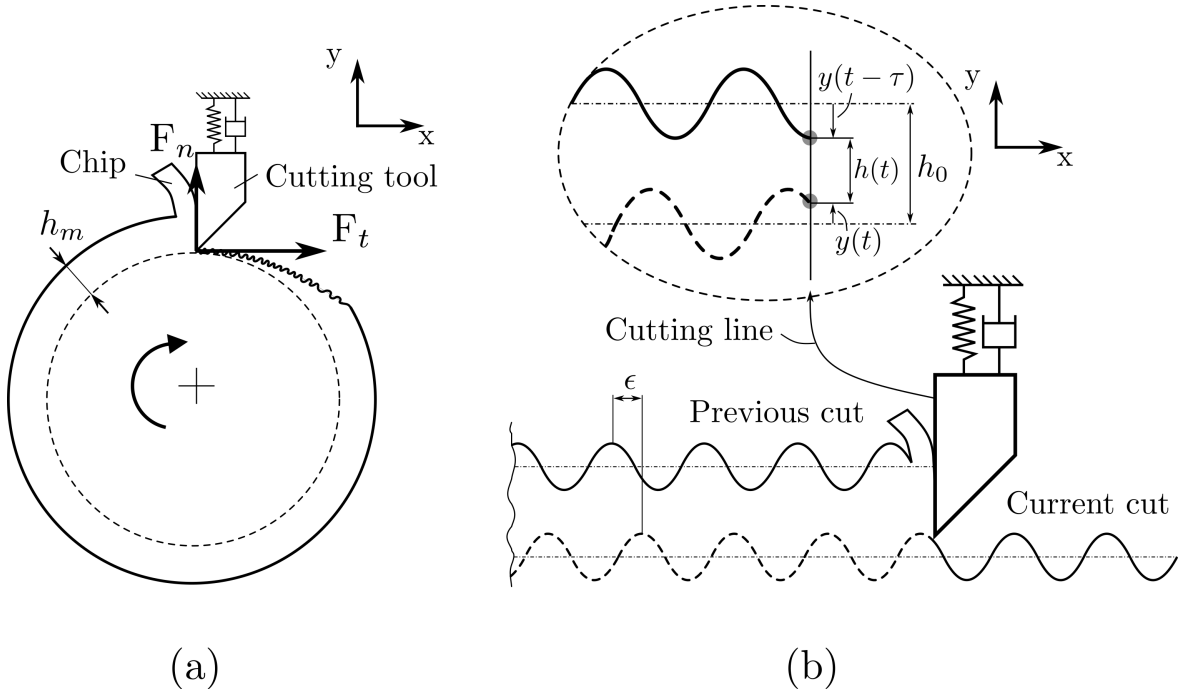
Figure 3.1 Schematic view of turning operation in (a) where a continuous single-point cutting is considered with (b) the phase and modulation of chip thickness due to the undulations of surface in previous and current cuts. The figure is adopted from [274].

cutting force, F_t and normal cutting force, F_n. The cutting forces can be assumed to be proportional to a cutting coefficient, and chip area [275]. Therefore, the cutting forces can be written as

$$F(t) = K_c a h(t), \tag{3.1}$$

where K_c is the cutting stiffness in unit N/m² and determined separately for each direction. The chip area is the product of the chip thickness $h(t)$, and the axial depth of cut a. A flattened view of the surface of the cylindrical workpiece after several rotations of the workpiece in the cut is depicted in Figure 3.1b. The flexible cutting tool under the cutting force causes undulations on the surface of the workpiece in each cut. Due to the phase difference between the successive cuts, the chip thickness varies from the desired chip thickness h_0 as shown in Figure 3.1b. The instantaneous chip

thickness is written as

$$h(t) = h_0 + \Big(y(t - \tau) - y(t)\Big) \tag{3.2}$$

where $y(t)$ is the vibration of the tool in the current cut while $y(t - \tau)$ is the vibration of the tool in the previous cut with the time delay τ due to workpiece rotation.

The dynamic cutting force leads to vibration of the cutting tool that causes the surface waviness. The vibration of the cutting tool can be written in the Laplace domain:

$$Y(s) = F(s)G(s) \tag{3.3}$$

where $G(s)$ is the transfer function of the system in the Laplace domain. $F(s)$ is the cutting force in Equation 3.1 in the Laplace domain, which is expressed:

$$F(s) = K_c a H(s). \tag{3.4}$$

Noting that the Laplace transform of the vibration in the previous cut is $\mathscr{L}\{y(t-\tau)\} = e^{-sT}Y(s)$ and taking the Laplace transform of Equation 3.2, the dynamic chip thickness in the Laplace domain is written

$$H(s) = H_0 + \Big(e^{-s\tau} - 1\Big)Y(s). \tag{3.5}$$

Substituting Equation 3.4 into Equation 3.3 and thereafter, Equation 3.3 into Equation 3.5 yields:

$$H(s) = H_0 + \Big(e^{-s\tau} - 1\Big)K_c a H(s)G(s). \tag{3.6}$$

Equation 3.6 presents a mathematical relationship between the instantaneous chip thickness and the desired chip thickness, which can be expressed:

$$\frac{H(s)}{H_0} = \frac{1}{1 + (1 - e^{-s\tau})K_c aG(s)}.$$
(3.7)

Equation 3.7 is in the form of a closed-loop transfer function. Thus, it is possible to consider the regenerative chatter mechanism as a closed-loop system shown in Figure 3.2a. The stability analysis of Equation 3.7 determines whether the chatter occurs or not in the cutting operation. The denominator of Equation 3.7 is defined as the closed-loop characteristic equation and the stability of the system is identified by its roots, $s = \sigma + j\omega_c$. The system is stable if the real part is larger than zero ($\sigma > 0$). The system is unstable if the real part is smaller than zero ($\sigma < 0$). Finally, the system is critically stable in the case that real part equals zero ($\sigma = 0$). The stability border can be determined by considering the critical stable case and equalling the characteristic equation zero for $s = j\omega_c$. Alternatively, the stability can be determined by the Nyquist criterion for $s = j\omega_c$:

$$K_c a_{cr} G(j\omega_c)(1 - e^{-j\omega_c\tau}) = -1.$$
(3.8)

where a_{cr} is the critical axial depth of cut, which defines the stability border, ω_c is the chatter frequency, and the phase between subsequent cuts can be given by $\epsilon = \omega_c\tau$. Equation 3.8 can be rewritten by defining the critical axial depth of cut:

$$a_{cr} = -\frac{1}{K_c G(j\omega_c)(1 - e^{-j\epsilon})}$$
(3.9)

Since both the axial depth of cut and the cutting stiffness are physical quantities with real and positive values, $G(j\omega_c)(1 - e^{-j\epsilon})$ requires a real and negative value for a legitimate stability limit. This condition is only satisfied with a complex conjugate
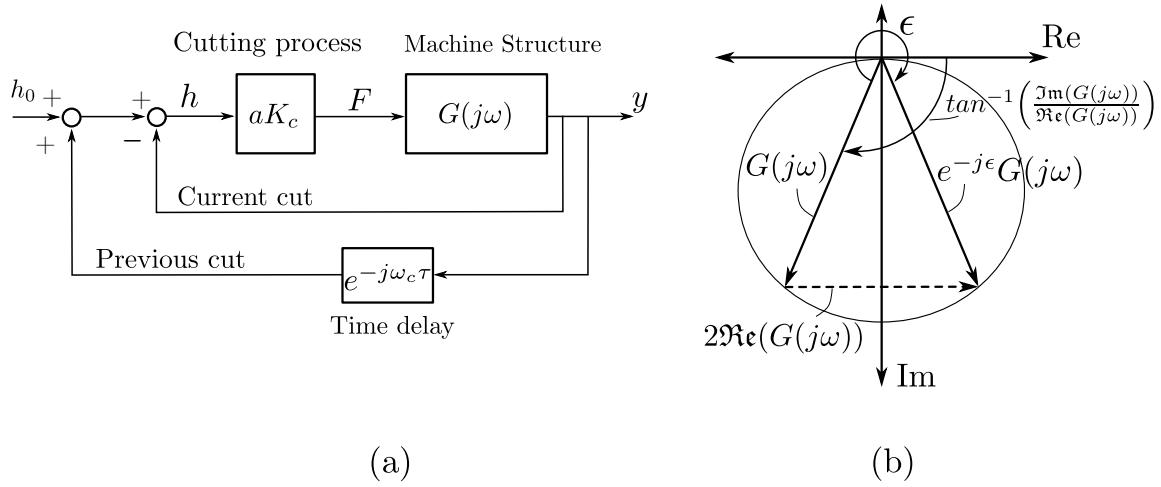
Figure 3.2 (a) Closed-loop block diagram representation of regenerative chatter mechanism and (b) vectorial representation $G(j\omega)(1 - e^{-j\epsilon})$ of Equation 3.10 in Nyquist diagram. The figure is adopted from [275].

pair of $G(j\omega_c)$ and $e^{-j\epsilon}G(j\omega_c)$ as illustrated in the Nyquist diagram in Figure 3.2b:

$$G(j\omega_c)(1 - e^{-j\epsilon}) = 2\mathfrak{Re}\Big(G(j\omega_c)\Big). \tag{3.10}$$

Substituting Equation 3.10 into Equation 3.9 gives:

$$a_{cr} = -\frac{1}{2K_c\mathfrak{Re}\Big(G(j\omega_c)\Big)}. \tag{3.11}$$

It should be noted that $\mathfrak{Re}\Big(G(j\omega_c)\Big)$ still needs to have a negative sign for a physically meaningful depth of cut value. Equation 3.11 shows that the stability limit is inversely proportional to the negative real part of the system's response and the cutting stiffness.

There is a relation between the chatter frequency ω_c ($f_c = 2\pi\omega_c$), and the rotational frequency of the workpiece n (rev/s), which can be given as:

$$\frac{f_c}{n} = k + \frac{\epsilon}{2\pi} \tag{3.12}$$
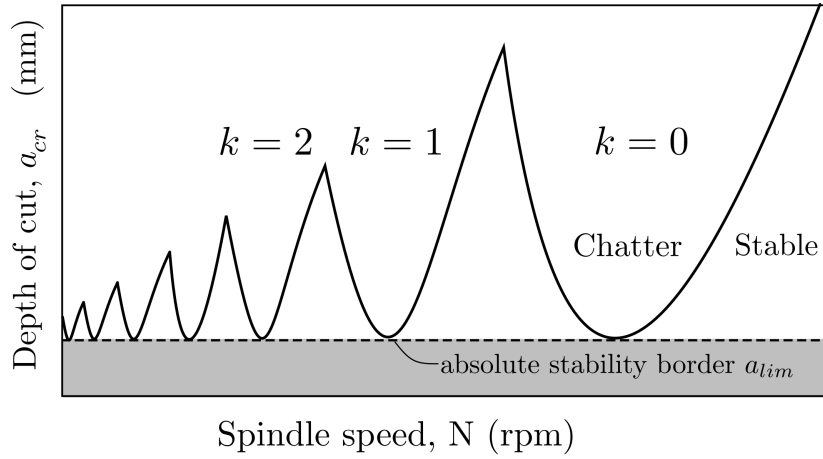
Figure 3.3 Stability lobe diagram with its absolute stability region highlighted (grey region).

where k is the integer number of waves and

$$\epsilon = 2\pi - 2\tan^{-1}\left(\frac{\mathfrak{Re}\big(G(j\omega_c)\big)}{\mathfrak{Im}\big(G(j\omega_c)\big)}\right). \tag{3.13}$$

The real part of the transfer function is a function of chatter frequency. Choice of different a chatter frequency ω_c not only changes the rotational frequency of the workpiece due to the relationship given in Equation 3.12 but also affects the stability limit a_{cr} in Equation 3.11 due to change in the corresponding real part value. Therefore, the stability of a cutting process is generally obtained for a set of chatter frequencies at the negative real part of the transfer function. For different integer values of k in Equation 3.12, the stability limit of a cutting operation is presented with the so-called *stability lobe diagram* as shown in Figure 3.3. In a stability lobe diagram, the region below the stability limit shows the stable cuts while the above region indicates chatter.

Finally, the absolute stability of the cutting process is obtained by the most negative real part of the transfer function. It is defined by the limited critical axial depth of cut

as

$$a_{lim} = -\frac{1}{2K_c min\big(\mathfrak{Re}\big(G(j\omega_c)\big)\big)} \tag{3.14}$$

where $min\big(\mathfrak{Re}\big(G(j\omega_c)\big)\big)$ represents for the most negative real part of the frequency response of the cutting system. The limited critical axial depth of cut a_{lim} indicates the absolute stability limit and ensures limit of stable cut regardless of the rotational speed of the workpiece (or spindle speed in milling operation) as indicated in grey in Figure 3.3.

Improving the stability limit increases the material removal rate, which turns into an increase in productivity. Therefore, the stability analysis presented in this section demonstrates the relation between the productivity and the structural dynamics of a cutting system.

3.3 Stability analysis of milling

Milling operation involves material removal from a stationary workpiece by a rotating cutting tool. The cutting tool generally has multiple teeth and material removal can be succeeded by one or multiple teeth at the same time, depending on the milling parameters. Unlike the turning operation, cutting forces continuously vary with the rotation of the tool. The basic theory of regenerative chatter presented for turning operations generally remains insufficient for an accurate stability prediction of milling operations. It requires a more advanced stability analysis approach where the varying cutting forces, multiple teeth engagement and intermittency of cutting are involved in the dynamic model.

Although a comprehensive dynamic milling model was developed as early as the 1960s [13], its stability analysis suffered from difficulties due to the time-periodic force coefficient induced by the rotation of the cutting tool. Therefore, the stability analysis of the model was restricted to inaccurate methods based on the averaged time-varying constants [31, 32] or time-consuming methods (e.g. time-domain simulations [34, 35] or iterative technique [40]). Fast and accurate stability analysis for cutting operations, ZOA, was developed by Budak and Altintas [17], where the stability limits of a milling operation can be obtained in seconds. This approach is utilised in the evaluations of the stability analyses of milling scenarios in this thesis.

3.3.1   Milling stability analysis

A milling operation where a flexible cutting tool removes material from a rigid workpiece is presented in Figure 3.4a. The cutting forces vary in both direction and magnitude with rotation of the cutting tool $\theta_j(t)$. The cutting forces induced by tooth j act on the radial (r) and tangential (u) directions while the cutting tool vibrates in x- and y-directions. Since the cutting force is a function of the instantaneous chip thickness that depends on the tool vibration, the projection of the vibration in x- and y-directions on the radial direction is first determined by:

$$r = -x \ \sin(\theta_j) - y \ \cos(\theta_j). \tag{3.15}$$

It should be noted that the intended chip thickness, as shown in Figure 3.4b is a function of the tool rotation $h_0 = f_t \sin(\theta_j)$ where f_t is the feed of the cutting tool.

The instantaneous chip thickness is written:

$$h(\theta_j) = \Big(f_t \, \sin(\theta_j) + r_{j-1} - r_j\Big)g(\theta_j) \tag{3.16}$$

where the index j represents for the current cut and $j-1$ indicates the previous cut. $g(\theta_j)$ is the switching function which defines whether tooth j is in cut or not. It is written:

$$g(\theta_j) = \begin{cases} 1 & \text{for} \quad \theta_s \leq \theta_j \leq \theta_e \\ 0 & \text{for} \quad \theta_j < \theta_s, \ \theta_j > \theta_e \end{cases} \tag{3.17}$$

where θ_s and θ_e indicate the angles of the tool j when it starts and exits the cut. The static part $f_t \sin(\theta_j)$ can be neglected as there is no contribution to the dynamic chip load regeneration mechanism. Substituting Equation 3.15 into Equation 3.16 and neglecting the static part, the dynamic instantaneous chip thickness can be rewritten:

$$h(\theta_j) = \Big(\Delta x \, \sin(\theta_j) + \Delta y \, \cos(\theta_j)\Big)g(\theta_j) \tag{3.18}$$

where $\Delta x = x_j - x_{j-1}$ and $\Delta y = y_j - y_{j-1}$. Assuming that the cutting force is proportional to the chip area and the cutting stiffness, the tangential and the radial cutting force is written:

$$F_{t,j} = K_t a h(\theta_j)$$
$$F_{r,j} = K_r a h(\theta_j) \tag{3.19}$$

where K_t and K_r are the cutting stiffnesses. The cutting stiffnesses describe the required force to remove a unit chip area and are determined by the material, geometry of the tool and the friction between the tool and the chip. Therefore, the cutting forces obtained by using Equation 3.19 are highly realistic as long as the axial depth of cut a and the cutting stiffnesses K_t and K_r remain constant. However, any variation in the cutting stiffnesses (e.g. wearing in tool) or the axial depth of cut due to the vibration

of the tool in axial direction leads to deviation in the cutting force. In order to obtain the vibration of the tool caused by the cutting force, the cutting forces are projected to x and y directions:

$$
\begin{aligned}
F_{x,j} &= -F_{t,j} \, \cos(\theta_j) - F_{n,j} \, \sin(\theta_j), \\
F_{y,j} &= F_{t,j} \, \sin(\theta_j) - F_{n,j} \, \cos(\theta_j).
\end{aligned}
\tag{3.20}
$$

Combining Equations 3.18, 3.19 and 3.20, and applying trigonometric identities, the cutting forces in x- and y-directions are rewritten:

$$
\begin{aligned}
F_{x,j} &= -\frac{1}{2}K_t a g(\theta_j)\Big[\Delta x\Big(\sin(2\theta_j) + K_n\big(1 - \cos(2\theta_j)\big)\Big) + \Delta y\Big(1 + \cos(2\theta_j) + K_n \, \sin(2\theta_j)\Big)\Big], \\
F_{y,j} &= -\frac{1}{2}K_t a g(\theta_j)\Big[\Delta x\Big(\big(1 - \cos(2\theta_j)\big) - K_n \, \sin(2\theta_j)\Big) + \Delta y\Big(\sin(2\theta_j) - K_n\big(1 + \cos(2\theta_j)\big)\Big)\Big].
\end{aligned}
\tag{3.21}
$$

The cutting forces presented here involve only the contribution of one tooth in the cut. Contribution of all teeth in the cut is given:

$$
F_x = \sum_{j=1}^{N_t} F_{x,j} \quad \text{and} \quad F_y = \sum_{j=1}^{N_t} F_{y,j}
\tag{3.22}
$$

where N_t is the number of teeth of the cutting tool. The cutting forces can be expressed in the matrix form:

$$
\mathbf{F} = \frac{1}{2}aK_t[\mathbf{A}(\theta)](\mathbf{\Delta})
\tag{3.23}
$$

where

$$
\mathbf{F} = \begin{pmatrix} F_x \\ F_y \end{pmatrix}, \quad \mathbf{A}(t) = \begin{bmatrix} a_{xx}(\theta) & a_{xy}(\theta) \\ a_{yx}(\theta) & a_{yy}(\theta) \end{bmatrix} \quad \text{and} \quad \mathbf{\Delta} = \begin{pmatrix} \Delta x \\ \Delta y \end{pmatrix}
\tag{3.24}
$$

where $\mathbf{A}(\theta(t))$ is the time-dependent matrix, which is referred to as the directional dynamics force coefficient matrix. The forces in Equation 3.21 are a function of time as the rotation of the cutting tool $\theta_j(t)$ is time-dependent. Thus, all time-dependent

(a)

(b)
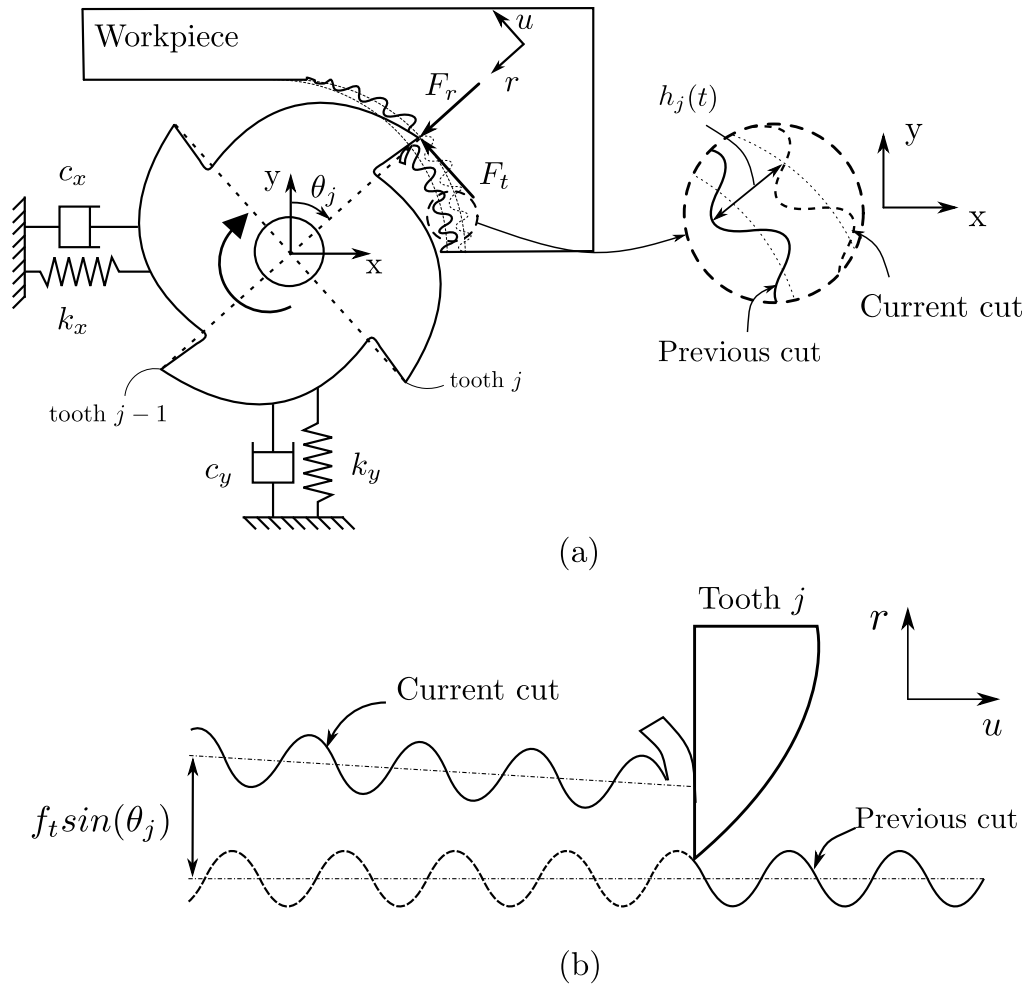
Figure 3.4 (a) Schematic view of milling operation with multiple teeth and (b) the change in the intended chip thickness $h_0 = f_t sin(\theta_j)$ due to rotation of the cutting tool.

terms of $\mathbf{A}(t)$ result from the rotation of the cutting tool. The matrix $\mathbf{A}(t)$ is periodic at the tooth passing frequency $f_{tp} = N_t N/60$ (where N is the spindle speed in unit of rev/min). Budak and Altintas [17] expanded $\mathbf{A}(t)$ into Fourier series and only considered the zeroth harmonic term with a time-invariant average component. By doing so, time-varying matrix $\mathbf{A}(t)$ is reduced to a time-invariant form in which the analytical solution is possible. The zeroth harmonic term can be obtained:

$$\left[\boldsymbol{A_0}\right] = \frac{N_t}{2\pi} \begin{bmatrix} \alpha_{xx} & \alpha_{xy} \\ \alpha_{yx} & \alpha_{yy} \end{bmatrix} \tag{3.25}$$

where

$$\begin{aligned}
\alpha_{xx} &= \frac{1}{2}\Big(\cos(2\theta) - 2K_n\theta + K_n\sin(2\theta)\Big)\Big|_{\theta_s}^{\theta_e}, \\
\alpha_{xy} &= \frac{1}{2}\Big(-\sin(2\theta) - 2\theta + K_n\cos(2\theta)\Big)\Big|_{\theta_s}^{\theta_e}, \\
\alpha_{yx} &= \frac{1}{2}\Big(-\sin(2\theta) + 2\theta + K_n\cos(2\theta)\Big)\Big|_{\theta_s}^{\theta_e}, \\
\alpha_{yy} &= \frac{1}{2}\Big(-\cos(2\theta) - 2K_n\theta - K_n\sin(2\theta)\Big)\Big|_{\theta_s}^{\theta_e}.
\end{aligned} \tag{3.26}$$

Substituting Equation 3.25 into Equation 3.23, the time-varying directional dynamic force is averaged based on the Fourier series expansion involving the contributions of all teeth in the cut.

The vibration differences in the x- and y-directions of subsequent teeth can be written in the frequency domain using the transfer function of the flexible structure $[\boldsymbol{G}(j\omega_c)]$:

$$\begin{pmatrix} \Delta X \\ \Delta Y \end{pmatrix} = (1 - e^{-j\omega_c\tau}) \begin{bmatrix} G_{xx} & G_{xy} \\ G_{yx} & G_{yy} \end{bmatrix} \begin{pmatrix} F_x \\ F_y \end{pmatrix} \tag{3.27}$$

where $e^{-j\omega_c\tau}$ is the delay term with a period of tooth passing frequency and $G_{xy} = G_{yx} = 0$ assuming that x- and y-directions are orthogonal. Replacing Equations 3.25 and 3.27 into Equation 3.23, the dynamic milling force equation is rearranged in the frequency domain:

$$\boldsymbol{F} = \frac{1}{2}aK_t[\boldsymbol{A_0}](1 - e^{-j\omega_c\tau})[\boldsymbol{G}(j\omega_c)]\boldsymbol{F}. \qquad (3.28)$$

For critically stable system, its nontrivial solution is obtained by equalling the determinant zero:

$$\det\left([\boldsymbol{I}] - \frac{1}{2}K_ta(1 - e^{-j\omega_c\tau})[\boldsymbol{A_0}][\boldsymbol{G}(j\omega_c)]\right) = 0, \qquad (3.29)$$

which is the characteristic equation. It can be simplified by expressing the product of $[\boldsymbol{A_0}][\boldsymbol{G}(j\omega_c)]$ with the oriented FRF:

$$[\boldsymbol{A_0}][\boldsymbol{G}(j\omega_c)] = \frac{N_t}{2\pi}[\boldsymbol{G_{or}}(j\omega_c)] \qquad (3.30)$$

where

$$[\boldsymbol{G_{or}}(j\omega_c)] = \begin{bmatrix} \alpha_{xx}G_{xx}(j\omega_c) & \alpha_{xy}G_{yy}(j\omega_c) \\ \alpha_{yx}G_{xx}(j\omega_c) & \alpha_{yy}G_{yy}(j\omega_c) \end{bmatrix}. \qquad (3.31)$$

Giving the eigenvalue of the characteristic equation as

$$\Lambda = -\frac{N_t}{4\pi}aK_t(1 - e^{-j\omega_c\tau}) \qquad (3.32)$$

results in the characteristic equation as

$$\det\left([\boldsymbol{I}] + \Lambda[\boldsymbol{G_{or}}(j\omega_c)]\right) = 0 \qquad (3.33)$$

where it is straightforward to obtain the eigenvalue for given chatter frequency ω_c, cutting coefficients K_t and K_n, start and exit angles (θ_s, θ_e) which are defined by the milling type and the radial immersion, and the FRF of the milling system. The

assumption of no cross-talk between directions leads to a quadratic form of the characteristic equation, which can be easily solved. Using the eigenvalue, the critical axial depth of cut a_{cr} and the spindle speed N are found as

$$a_{cr} = -\frac{2\pi\mathfrak{Re}(\Lambda)}{N_t K_t}\left(1 + \left(\frac{\mathfrak{Im}(\Lambda)}{\mathfrak{Re}(\Lambda)}\right)^2\right) \tag{3.34}$$

$$N = \frac{60}{N_t \tau} \tag{3.35}$$

where τ is the tooth passing period as given

$$f_c \tau = k + \frac{\epsilon}{2\pi} \tag{3.36}$$

where k indicates the integer number of waves between subsequent cuts and $\epsilon/2\pi$ is the fractional wave. The phase angle is written:

$$\epsilon = \pi - 2\tan^{-1}\left(\frac{\mathfrak{Im}(\Lambda)}{\mathfrak{Re}(\Lambda)}\right). \tag{3.37}$$

Using Equations 3.34 and 3.35, the stability limits of milling operations can be analytically predicted. The stability limits are generally presented in stability lobe diagrams.

The milling type (up or down milling as given in Figure 3.5) and radial immersion of the cutting tool into the workpiece affect the averaged time-invariant $[\boldsymbol{A_0}]$ as they specify the start and exit angles θ_s and θ_e. This method is also independent of the helix angle of teeth since the helix angle only reduces the harmonics of the cutting force and does not change the average of the force [275, 134]. Although the ZOA is an accurate method for cuts with high radial immersions, it could show inaccuracy for the stability prediction of highly intermittent milling with low radial immersion (e.g. less than 10%

[48]) due to the increasing number of harmonics of the cutting forces . However, the method of zero-order approach is assumed to be an accurate method since only milling operations with high radial immersions (50%) will be considered throughout this thesis. Also, its advantage of being a fast method will be greatly benefited by the optimisation process to reduce the computational cost.
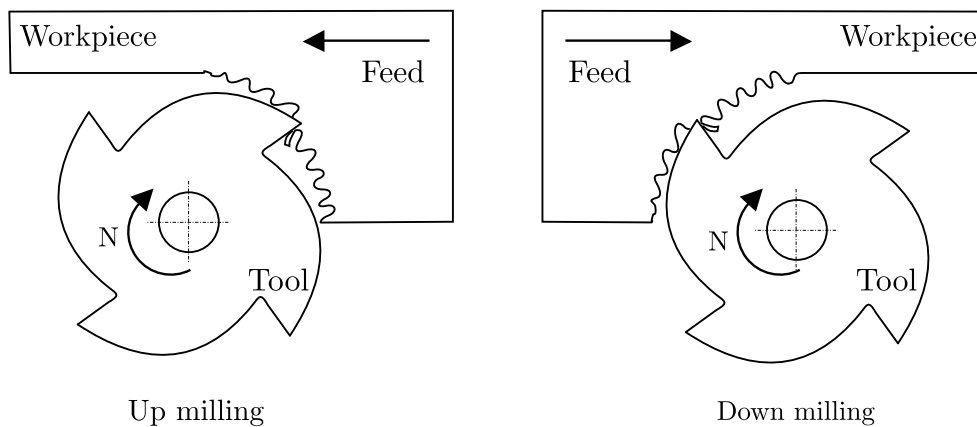
Figure 3.5 Schematic views of up milling where the cutting tool rotates against the feed and down milling where the cutting tool rotates together with the feed.

3.3.2   Stability of milling of SDOF structure

The focus in this thesis will be the stability improvement of milling of an SDOF structure (the most flexible mode) as similar to most of the inerter-based applications in the literature. A milling system involves different vibration modes related to machine tool structure, the spindle, the tool and the workpiece. The most critical mode in terms of chatter stability is the most flexible mode or modes. In order to consider a milling system as a SDOF, only one mode must be the most flexible and adequately far away from the other modes. This can be the case in milling a thin-walled workpiece while it cannot be appropriate, for instance, if the most flexible mode is related to the tool as tools have similar flexibilities in two directions due to its cylinder geometry.

The mechanical model of the milling system in Figure 3.4 assumes that the tool is flexible while the workpiece is rigid. However, it is worth noting that this model is exactly applicable for the reverse case, where the tool is rigid and the workpiece is flexible as the relative compliance between the tool and the workpiece does not change.

The milling system in Figure 3.4 is considered to be allowed to vibrate only in the y-direction. The characteristic equation in Equation 3.29 reduces to:

$$1 - \frac{1}{2}aK_t(1 - e^{-j\omega_c\tau})\frac{N_t}{2\pi}\alpha_{yy}G_{yy}(j\omega_c) = 0 \tag{3.38}$$

where α_{yy} is the zeroth-order harmonic given in Equation 3.26 and $G_{yy}(j\omega_c)$ is the transfer function of the SDOF structure. The critical axial depth of cut a_{cr} can be written:

$$a_{cr} = \frac{1}{2K_tN_tU\mathfrak{Re}\big(G_{yy}(j\omega_c)\big)} \tag{3.39}$$

where N_t is the number of teeth, and U involves the averaged force term due to rotating cutting tool:

$$U = \frac{\alpha_{yy}}{4\pi}. \tag{3.40}$$

The critical axial depth of cut in Equation 3.39 is in a similar form of the stability limit of the turning operation (as described in Section 3.2 and Equation 3.11) but the inclusion of the number of teeth and a cutting force coefficient that depends on immersion and milling type. The spindle speed is obtained from:

$$N = \frac{60}{N_t\tau} \quad \text{where} \quad f_c\tau = k + \frac{\epsilon}{2pi}, \tag{3.41}$$

and the phase angle is found:

$$\epsilon = 2\pi - 2\tan^{-1}\left(\frac{\Re\big(G_{yy}(j\omega_c)\big)}{\Im\big(G_{yy}(j\omega_c)\big)}\right). \tag{3.42}$$

Equation 3.39 indicates that the critical depth of cut a_{cr} is inversely proportional to the real part of the transfer function and the cutting stiffness as in the turning operation. Additionally, it is inversely proportional to the number of teeth N_t and α_{yy}. α_{yy} represents the effect of the average cutting force. Therefore, it depends on the type of milling and radial immersion for given a tool diameter as they define the start and exit angle of the cut (θ_s, θ_e). Whether the stability limit is defined by the negative or the positive real part of the transfer function depends on the milling type (up or down milling) as it changes the sign of α_{yy}. For instance, in the case of a down milling operation, the sign of α_{yy} becomes negative, and thus the stability limit is defined by the negative real part. In that case, the absolute stability limit a_{lim} equals the most negative real part of the transfer function.

The study in this thesis focuses on the structural dynamics part of the stability analysis. Employment of an inerter either as a localised addition or integrating into one of the parts of the machine (machine structure, spindle-tool holder system or workpiece holder) only improves the transfer function of the structure. Therefore, the interest of this study is the structural dynamics part of Equation 3.39, which is the real part of the transfer function. Other parameters of Equation 3.39 K_t, α_{yy} and N_t defines by the specifications related to the material and the cutting conditions. They will be mostly excluded in the evaluation of the performance analysis.

3.4 Summary

The theoretical background of the stability analysis of milling has been presented in this chapter. The theory of regenerative chatter was first explained for a continuous single-point cutting operation, and the concept of the stability lobe diagram was presented. Next, the stability analysis was extended to milling operations where intermittent cuts with multiple teeth involved. The stability limit of the milling operation a_{cr} was derived for a general two-DOF milling and reduced to the milling of an SDOF structure. The stability limit derived was finally discussed in respect to the structural dynamics.

Chapter 4

Chatter Stability Analysis of Inerter-based Vibration Absorbers

This chapter introduces the analysis of the use of inerter-based absorbers in milling operations to increase regenerative chatter. The application of the inerter is considered in a localised addition, and performances of different inerter-based layouts are investigated. Selection of optimal design parameters to obtain the best performance is discussed, and numerical optimisation based on a genetic algorithm is presented. Using the optimal design parameters obtained, the performance of each layout is evaluated with the frequency response functions and stability lobe diagrams considering a milling scenario. Finally, global sensitivity analysis is conducted to examine the sensitivities of the design parameters on the chatter performance.

4.1 Introduction

The inerter element has been frequently studied to improve the dynamic performance of systems. It has been employed in vibratory systems in different fields of engineering. However, the author's knowledge, it has never been examined for machining applications with a particular emphasis on chatter stability. The only study which investigates the use of the inerter in machining application is the work of Wang [5], but this study focuses on the vibration suppression in milling machines rather than the stability of a cutting process. It presents a simpler investigation to show the benefits of the use of the inerter in milling operation. It lacks detailed and comprehensive analysis considering the regenerative chatter, which is the major problem in milling operation. Instead, this study examines the analysis of inerter-based dynamic vibration absorbers considering regenerative chatter stability.

A milling operation can be modelled as an SDOF system. The chatter problem can be modelled similar to the vibration absorption of the primary system under forced excitation but the interest is in chatter stability rather than forced vibration. The grounded connection of a passive control device or deployment between two components of the machine is also restricted due to constructional limitations. Therefore, the application of the inerter-based passive control device in a milling operation is considered as a localised addition [6]. This approach provides a more versatile solution similar to a classical TMD application where no grounded connection or attachment between two components is needed. It also saves the milling structure from requiring major modifications.

The complexity of the layouts is kept as low as possible considering its physical realisation and limited-space that milling application generally has. Layouts are formed

by replacing the damper in the TMD with all possible networks consisting of an inerter, a spring and a damper. These layouts, named inerter-based dynamic vibration absorber (IDVA), have been studied by Hu and Chen [259] for vibration suppression analysis. It has been shown that the layout without an extra stiffness element provides no improvement in comparison to a TMD. Therefore, these layouts consisting of two springs, an inerter, a damper and an auxiliary mass are evaluated for chatter stability performance in this chapter. The selection of the design parameters are obtained by performing self-adaptive differential evaluation (SaDE) algorithm. The performance of each configuration is evaluated considering the real part of the frequency response and the stability lobe diagram for milling. Also, a global sensitivity analysis is conducted to assess the effect of the change in each design parameter on the performance.

4.2   Layouts and transfer functions

A SDOF milling system controlled with an IDVA is given in Figure 4.1a. The milling system is subject to unwanted vibrations, which cause poor surface quality, noise, breakage or failure of the cutting tool. It has parameters mass M (kg), spring stiffness K (N/m), and viscous damping C (Ns/m.) Although these parameters are defined by the contribution of all components of the milling system, they are dominated by the most flexible part of the milling (such as the tool or workpiece). The IDVA is mounted on the most flexible part of the machine as the localised addition in order to increase regenerative chatter stability. In practice, mounting the IDVA to a rotating tool is not possible due to practical limitations. Therefore, it is designed and applied to the workpiece in Chapters 5 and 6. Each IDVA has an auxiliary mass m_a (kg), two springs

k_o and k_i (N/m), inerter b (kg), and viscous damper c (Ns/m), as shown in Figure 4.1b.
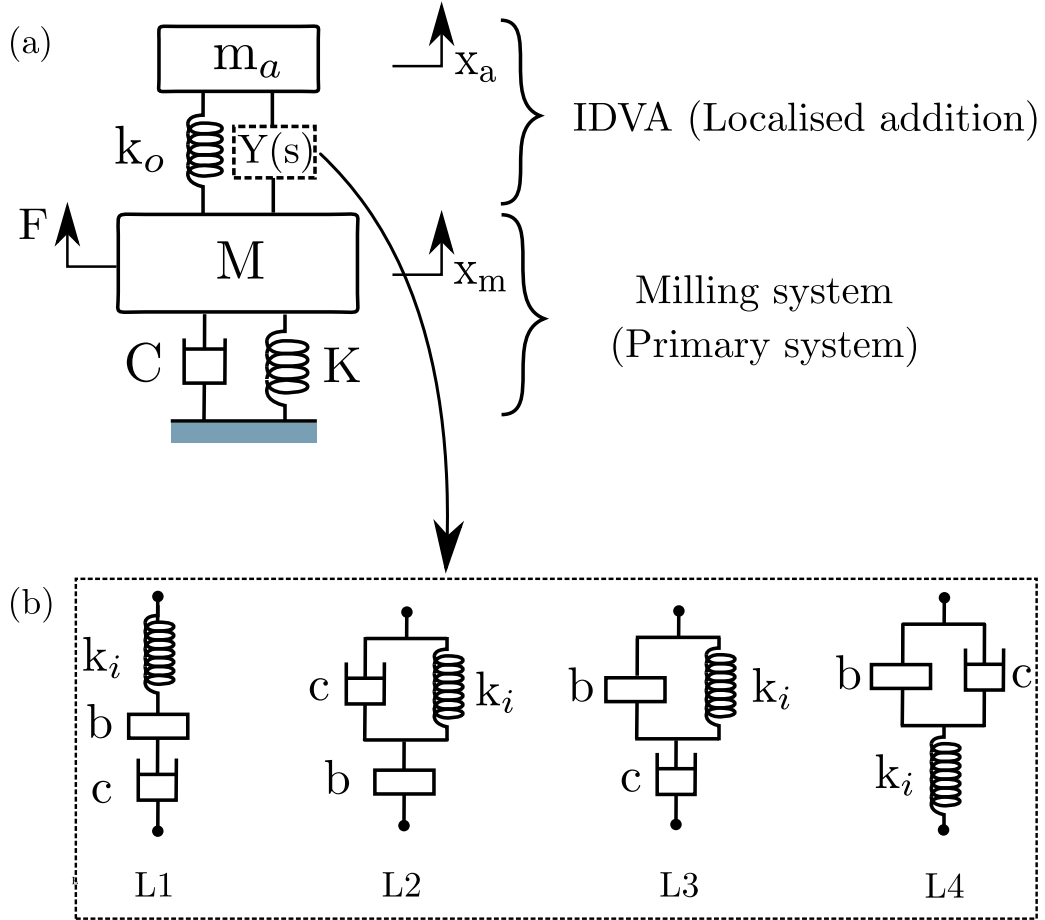
Figure 4.1 (a) A SDOF milling system with the IDVAs where (b) four different inerter-based layouts are considered by replacing the damper in TMD with networks consisting of an inerter, a spring and a damper.

Stability analysis of milling requires the transfer function of the system. The transfer function of the machining system with the IDVA can be derived by writing the equations of motion. The equations of motion of the SDOF system controlled with the IDVA in Figure 4.1 can be written in the Laplace domain:

$$Ms^2 X_m(s) + CsX_m(s) + KX_m(s) - F_c(s) = F(s),$$
$$m_a s^2 X_a(s) + F_c(s) = 0,$$

(4.1)

Table 4.1 Impedances Y(s) of the networks consisting of an inerter, a spring and a damper in Figure 4.1.

L_1	L_2	L_3	L_4
$\dfrac{1}{\frac{s}{k_i}+\frac{1}{c}+\frac{1}{bs}}$	$\dfrac{1}{\frac{1}{\frac{k_i}{s}+c}+\frac{1}{bs}}$	$\dfrac{1}{\frac{1}{\frac{k_i}{s}+bs}+\frac{1}{c}}$	$\dfrac{1}{\frac{1}{bs+c}+\frac{s}{k_i}}$

where $X_m(s)$ and $X_a(s)$ are the Laplace transforms of the displacements of the primary and auxiliary masses, respectively. M, m_a are the modal mass of the primary system and auxiliary mass of the absorber, K and C are the stiffness and damping of the primary system, k_o, k_i, c and b are the stiffnesses of the outer spring and the inner spring, damping of the absorber and the inertance of the inerter, respectively. $F(s)$ and $F_c(s)$ are the Laplace transforms of cutting and control forces. The control force written as

$$F_c = \Big(k_o + sY(s)\Big)\Big(X_a(s) - X_m(s)\Big) \tag{4.2}$$

where $Y(s)$ is the impedance[1] of each layout in Figure 4.1b as given in Table 4.1. Substituting Equation 4.2 into Equation 4.1 and applying algebraic manipulations, the transfer function of the system in Figure 4.1a can be written in the Laplace domain:

$$G(s) = \frac{X_m(s)}{F(s)} = \frac{m_a s^2 + sY(s) + k_o}{\Big(Ms^2 + Cs + K\Big)\Big(m_a s^2 + sY(s) + k_o\Big) + m_a s^2\Big(sY(s) + k_o\Big)} \tag{4.3}$$

where transition from the Laplace domain to frequency domain is made by replacing $s = j\omega$.

---

[1]Here, the impedance is defined as

$$F(s) = Y(s)v(s)$$

where $F(s)$ is force, $Y(s)$ is impedance and $v(s)$ is velocity [259, 276].

Using the following dimensionless parameters:

$$\mu = \frac{m_a}{M}, \qquad \delta = \frac{b}{m_a}, \qquad \Omega = \frac{\omega}{\omega_n}, \qquad \gamma = \frac{\omega_a}{\omega_n},$$
$$\alpha = \frac{\omega_b}{\omega_a}, \qquad \zeta_m = \frac{C}{2\sqrt{KM}}, \qquad \zeta_a = \frac{c}{2\sqrt{k_o m_a}}, \tag{4.4}$$

where ω is the forcing frequency and ω_n, ω_a and ω_p can be expressed as

$$\omega_n = \sqrt{\frac{K}{M}}, \qquad \omega_a = \sqrt{\frac{k_o}{m_a}}, \qquad \omega_b = \sqrt{\frac{k_i}{b}}.$$

the dimensionless transfer function can be found in this form:

$$\tilde{G}_i = \frac{X_m}{F/K} = \frac{A_i(\Omega, \delta, \gamma, \alpha, \zeta_a) + jB_i(\Omega, \delta, \gamma, \alpha)}{C_i(\Omega, \mu, \delta, \gamma, \alpha, \zeta_m, \zeta_a) + jD_i(\Omega, \mu, \delta, \gamma, \alpha, \zeta_m)} \tag{4.5}$$

Full expressions for A_i, B_i, C_i, and D_i are presented in Appendix A. The stability limit of an SDOF structure is inversely proportional to the real part of the transfer function. Optimal dimensionless design parameters that provide the best stability performance can be obtained from using Equation 4.5.

4.3   Optimisation/tuning parameters

The selection of the design parameters has an important effect on the performance of the absorber. Tuning parameters can be done manually (e.g. setting the natural frequency of the absorber to the natural frequency of the main system), iteratively, numerically or analytically. The analytical method, which provides a set of generic formulas for the values of the optimal design parameters, is the most sophisticated method among them. For instance, Den Hartog [107] and Sims [108] derived analytical

expressions that give the optimal design parameters considering amplitude peak in the FRF for a vibratory system and the real part of the FRF for a machining operation, respectively. However, such analytical expressions involve assumption of undamped primary systems in the derivation. The optimal design parameters vary on the level of damping when the damping exists in the primary system.

Numerical optimisation strategies, on the other hand, are capable of dealing with the damping in the main system. Although they could be computationally costly, they could provide accurate values for the optimal design parameters. With the advent of computing speed and cost-effective computational algorithms, the numerical optimisation method has become a powerful method for the obtainment of the design parameters. In this thesis, a self-adaptive differential evolution algorithm is applied for numerical optimisation to obtain the optimal design parameters of the IDVA. In this section, before the details of the numerical optimisation, fixed-points technique as a possible analytical tuning method will be discussed. Then, objective functions, a brief explanation of SaDE and finally, the optimal design parameters obtained by performing SaDE will be presented in the following sections.

4.3.1 Identification of the fixed points

Den Hartog's method [107] uses the damping-ratio-invariant points, the so-called fixed points, for H$_\infty$ optimisation for a TMD. In this method, the amplitudes at two fixed point frequencies are first set to be equal by frequency ratio. Then, the damping ratio is obtained considering the slope of the amplitude at the fixed point frequencies. Sims' method applies the same criteria but is interested in the real part of the FRF, where three fixed points appear. Only two of the existing three fixed points are considered to

provide equal peaks or troughs depending on the cutting parameters. Barredo et al. [260] demonstrated that there exist four fixed points for the magnitude of the FRF for the IDVAs. They can be employed for analytical expressions for the optimal design parameters by applying a similar scheme to Den Hartog's. Although this approach provides only quasi-optimal design parameters, using the analytical expressions are more convenient and sufficiently effective.

The use of the fixed points to obtain the optimal design parameters for the IDVAs in Figure 4.1b can also be considered for machining chatter stability which is defined by the real part of the FRF as discussed in Chapter 3. There are four dimensionless design parameters γ, ζ_a, δ, and α. For constant γ, δ, α and undamped main system $\zeta_m = 0$, there are five fixed-points identified in the real part response for each layout which is obtained by using Equation 4.5. An example that indicates the fixed points for L1 is given in Figure 4.2 and the fixed points for other layouts are presented in Appendix B. Moreover, numerical evaluations showed that values for γ, δ and α that make the fixed points equal provide slightly better performance than a classical TMD for L1, L2 and L4 as long as the damping ratio is properly chosen. However, the fixed points technique could not provide better performance than the numerical optimisation method as presented in Appendix B. The evaluation to obtain the analytical expressions was conducted in Maple software. Even though it was straightforward to obtain the frequencies of the fixed points, it was challenging to obtain expressions for the optimal design parameters due to the excessive number of terms. This is because the solution involves the roots of cubic equations.

Besides the difficulty in obtaining analytical expressions due to the excessive number of terms and lower performance obtained compared to numerical optimisation, the fixed points technique is only valid for an undamped primary system. Therefore, numerical
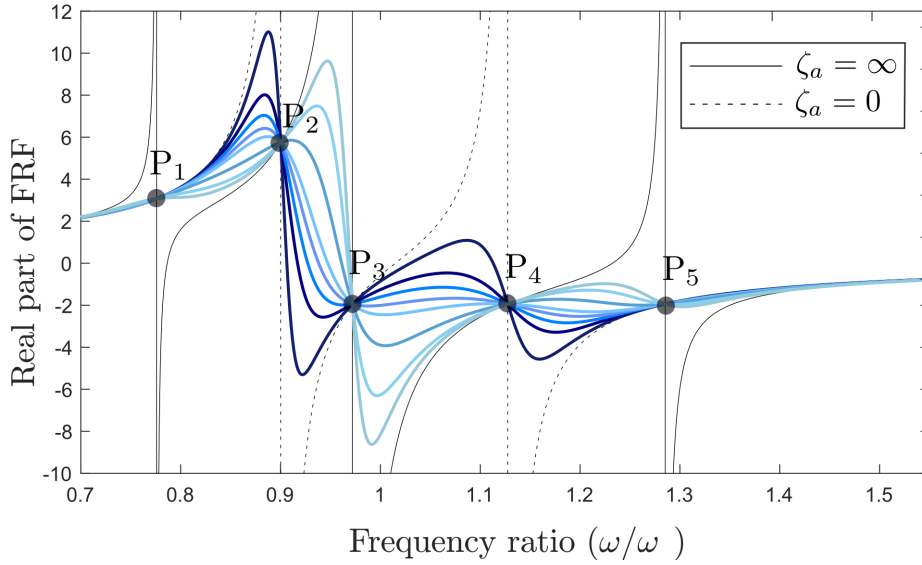
Figure 4.2 Five the damping-ratio-invariant fixed points in the Layout L1. The values of the real part at frequencies from P1 to P5 are fixed for different damping ratios ζ_a but constant values for the rest of the design parameters γ, δ and α. Zero and infinitely large damping ratios are shown in the legend. Other lines represent different values of the damping ratio in $0 < \zeta_a < \infty$.

optimisation is considered as a more suitable method for the applications in this thesis. The evaluation regarding the fixed points is kept limited with only this subsection, and the rest of the chapter focuses on numerical optimisation to acquire optimal design parameters.

4.3.2   Optimisation problems

Four dimensionless design parameters γ, ζ_a, δ, and α are the inputs of the optimisation for given mass ratio μ and structural damping in the primary system ζ_m. The optimisation algorithm attempts to minimise or maximise the output value of the objective function by searching the pool of the input values. Three objectives are defined in this study for the evaluation of chatter stability. The first and main objective

is to maximise the limited critical depth of cut a_{lim} so that chatter-free depth of cut is increased regardless of the spindle speed. The second objective is to maximise the largest stable depth of cut value as possible. However, this objective could end up a deep but narrow stable region in the stability chart since it does not consider a spindle speed band. Thus, the third objective is to enhance the deep stability region in the first stability pocket (between the first and second stability lobes). This objective aims to increase the stable area between predefined spindle speeds instead of maximisation of the largest stable point.

The stability limit of milling with an SDOF structure was determined in Section 3.3.2 as:

$$a_{cr} = \frac{1}{2K_t N_t U \mathfrak{Re}\big(G(j\omega)\big)} \tag{4.6}$$

where U is defined by the milling type and radial immersion, N_t is the number of teeth, and K_t is the tangential cutting coefficient. Substitution of the dimensionless transfer function Equation 4.5 into Equation 4.6 yields the critical depth of cut expressed as follows:

$$a_{cr} = \frac{K}{2K_t N_t U \mathfrak{Re}\big(\tilde{G}(j\Omega)\big)} \tag{4.7}$$

where K is the stiffness of the primary system and $\Omega = \omega/\omega_n$. As the dimensionless analysis is employed, K is here just a scaling factor (or gain) like the milling parameters K_t, N_t and U. With this approach, the stability performance only depends on the dimensionless real part response, which is defined by the dynamic behaviour of the inerter-based layouts. The rest of the parameters only scale the stability limits and can be excluded from the analysis from the structural dynamics point of view. Non-dimensional spindle speed is given by the frequency ratio $\tilde{N} = N_t N/(60 f_n)$ where N is the spindle speed as discussed in Equation 3.35.
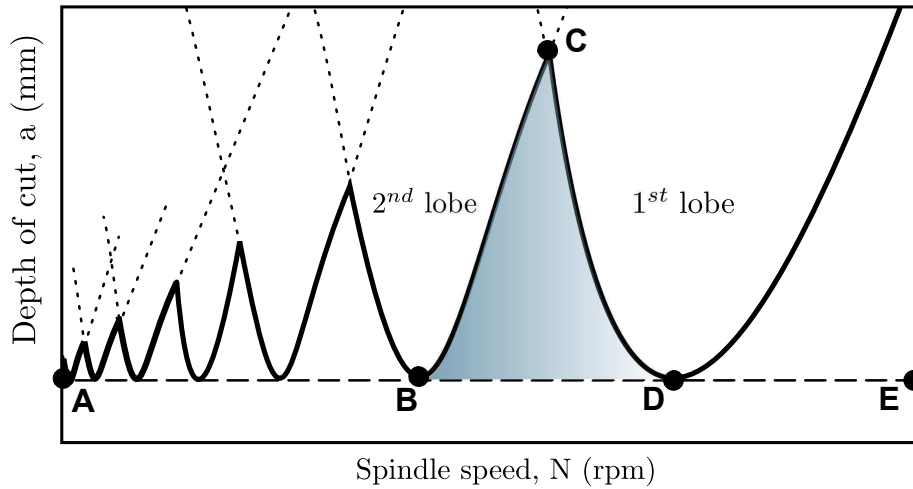
Figure 4.3 Stability lobe diagram where the absolute stability (a_{lim}) is shown with the dashed line $\overline{AE}$. Point C indicates the largest stable depth of cut, whose maximisation is the second optimisation objective. The third objective of the optimisation is the enhancement of the first stability pocket (blue region).

The limited critical depth of cut a_{lim}, which indicates the absolute stability limit, depends on the negative or positive real part and it is independent of the spindle speed. However, the optimisations for the maximisation of the largest depth of cut and the maximisation of the stability pocket have to consider spindle speeds due to overlaps of the lobes (as shown with black dotted line in Figure 4.3). These lobes are caused by different integer k in Equation 3.12 as discussed in Section 3.2. There can be more than one critical depth of cut values yielded by different k for the same spindle speed. The stability border for that spindle speed is defined with the lowest critical depth of cut value. In order to achieve the optimisations of the maximisations of the largest depth of cut and the stable area, the stability limit is expressed as an one data set (bold black line in Figure 4.3) by eliminating higher critical depth of cut in the overlapped areas. The three objectives are presented in detail below:

Objective 1: Maximisation of limited critical depth of cut

The first objective of the numerical optimisation is to maximise the limited critical depth of cut in the stability lobe diagram. It defines the absolute stability limit of the cutting operation, as illustrated with the dashed line $(\overline{AE})$ in Figure 4.3. For given mass ratio μ and structural damping ζ_m, the objective function can be written as

$$J_1 = -max_\Omega\Big(\big|\mathfrak{Re}(\tilde{G}_i(j\tilde{\omega}))\big|\Big), \qquad i = L_1, \ldots, L_4 \tag{4.8}$$

subject to

$$\begin{cases} \mathfrak{Re}(\tilde{G}_i(j\tilde{\omega})) < 0 & \text{for down milling} \\ \mathfrak{Re}(\tilde{G}_i(j\tilde{\omega})) > 0 & \text{for up milling} \end{cases}$$

where $\tilde{G}$ is the transfer function of the controlled structure. For the consistency with the following optimisation objectives, a negatives sign is assigned to perform the optimisation for the maximisation of the objective value.

Objective 2: Maximisation of largest stable depth of cut

The second objective of the numerical optimisation is to maximise the largest stable point in the stability chart. In that way, the cutting operation can be conducted at the spindle speed where the largest stability point is obtained. The largest stable point in a stability lobe diagram considering the machine limit is generally obtained between the first and second lobes, as shown with Point C in Figure 4.3. The design parameters that give the largest stable depth of cut are sought in this optimisation. For given mass ratio μ, structural damping ζ_m and the milling parameters, the problem formulation

can be established as

$$J_2 = max\Big(\boldsymbol{a}_{cr}\Big) \tag{4.9}$$

where a_{cr} is the critical depth of cut vector that contains all critical depth of cut values in the combined stability lobe diagram (bold black line in Figure 4.3). Due to the machine limitation, ultra-high speed zone ($k < 0.5$ in Equation 3.12) is excluded in the optimisation.

Objective 3: Maximisation of the stability pocket

It is possible that the maximisation of the stable depth of cut at one spindle speed in the previous optimisation could lead to a stable region with a high limiting depth of cut but narrow spindle speed band. If the spindle speed of the stable region is too narrow, the cutting operation can easily shift to the unstable region even with a small change in the spindle speed (e.g. spindle speed uncertainties). Furthermore, this stable region with a narrow spindle speed band might not be seen in practice as theoretical stability analysis contains assumptions such as linear cutting force and linear system behaviour. Therefore, the third objective of the numerical optimisation is to increase the stable region between two chosen spindle speeds, instead of increasing the stability at one chosen spindle speed. As the most stable region in a stability lobe diagram occurs between the first and second lobes, the area of the stable region between these two lobes is aimed to enhance the stability. This region is illustrated in blue colour between Points B and D in Figure 4.3. For given mass ratio μ, structural damping ζ_m and the milling parameters, the problem formulation can be established as

$$J_3 = \frac{1}{(N_D - N_B) + 1} \sum_{i=N_B}^{N_D} a_{cr,i} \tag{4.10}$$

where $((N_D - N_B) + 1)$ is the total number of spindle speed points between two chosen spindle speeds. a_{cr} represents each critical depth of cut in the range of $[N_B, N_D]$.

All three optimisations are performed for the maximisation of the objective values by utilising the SaDE algorithm.

4.3.3   Self-adaptive differential evolution (SaDE) algorithm

The self-adaptive differential evolution algorithm is a differential evolution algorithm with the capability of adapting its control parameters after a pre-defined learning period. Differential evolution (DE) algorithm is a simple and powerful population-based stochastic search method, which is capable of handling non-differentiable, nonlinear and multimodal functions [277, 278]. Traditional DE requires four control parameters that needs to be defined: Mutation strategy, scaling factor F, crossover ratio CR, and population size. The control parameters have an important effect on the performance and the convergence speed of the optimisation.

The optimisation algorithm of DE is illustrated in Figure 4.4. DE searches the parameters which give the best objective value in a population pool. In each generation, this population pool is updated applying three operations called mutation operation, crossover operation and selection operation, respectively. The initial pool population is constructed by uniformly distributed values from constrained vectors which define upper and lower boundaries for each design parameter. The set of design parameters in the initial population is named as target vectors $\mathbf{X}$ and the objective value for

each target vector is determined. Mutation operation uses mutation strategies, which involves the manipulations of target vectors, including multiplication by scaling factor F, to obtain a mutant vector $\mathbf{V}$. Each mutation strategy has different strong sides (e.g. fast converge, strong exploration capability [278]) and thus, it is important to choose a suitable mutation strategy depending on the optimisation problem. Crossover operation generates a trial vector $\mathbf{U}$ utilising the binomial crossover:

$$
u_{n,G}^m = \begin{cases} v_{n,G}^m, & \text{if} \quad (\text{rand}[0,1] \leq \text{CR}) \\ x_{n,G}^m, & \text{otherwise} \end{cases} \quad , \qquad m = \gamma, \zeta_a, \delta, \alpha \qquad (4.11)
$$

where CR is the crossover rate and its range is $[0,1]$.

The objective value of each trial vector created in the crossover operation is compared with the corresponding target vector in the selection operation. If the target vector has a better objective value, the target vector is transferred to the next generation and placed into the new population pool. Otherwise, the trial vector is moved to the next generation.

Instead of manually specifying the control parameters as in traditional DE, SaDE adaptively determines the mutation strategy, scaling factor F, and crossover ratio CR by learning from the previous generation. This self-adaptation during the optimisation allows a suitable choice of the control parameters for not only overall search space but also different sections in the search space [278]. Settings for the self-adaptive part of the algorithm are established by following the implementation in [279]. Four mutation strategies chosen to obtain the mutant vector are:

1. rand1: $\mathbf{V}_n = \mathbf{X}_{r_a} + F\left(\mathbf{X}_{r_b} - \mathbf{X}_{r_c}\right)$
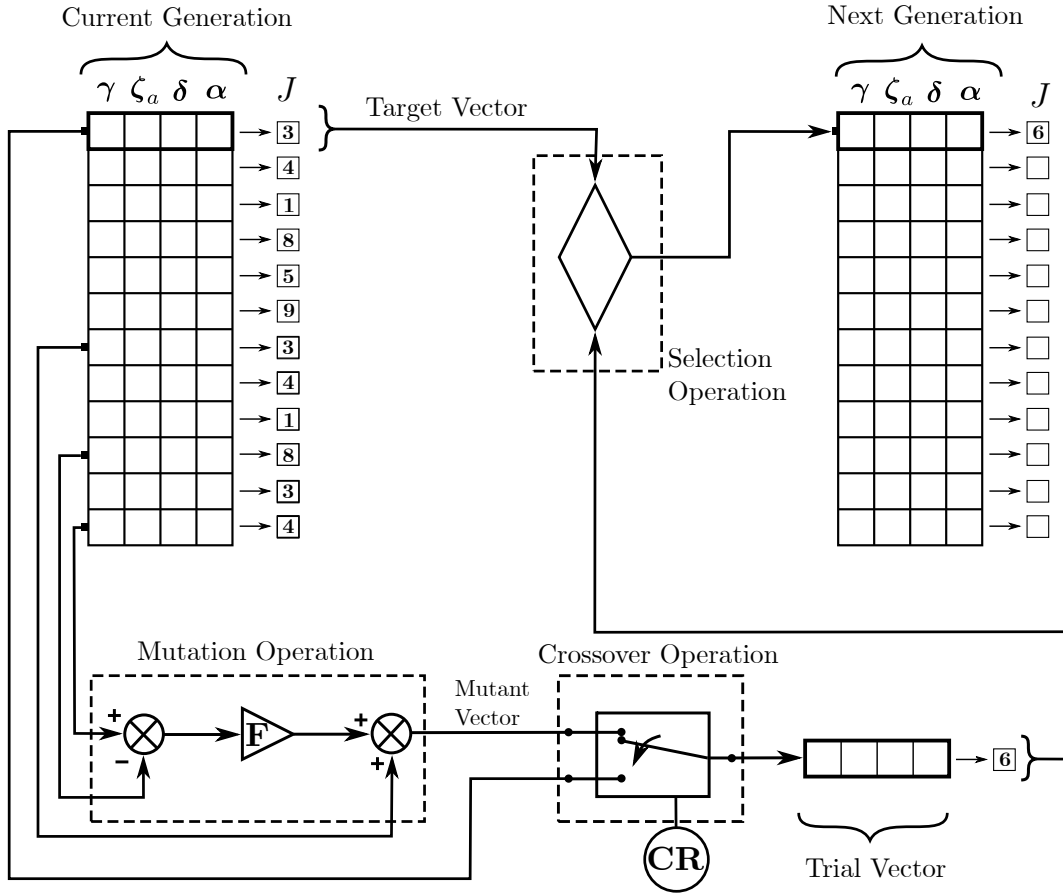
Figure 4.4 Schematic illustration of the SaDE algorithm where the next generation is obtained through mutation operation, crossover operation and selection operation.

2. current-to-best2: $\mathbf{V}_n = \mathbf{X}_n + F\big(\mathbf{X}_{best} - \mathbf{X}_n\big) + F\big(\mathbf{X}_{r_a} - \mathbf{X}_{r_b}\big) + F\big(\mathbf{X}_{r_c} - \mathbf{X}_{r_d}\big)$

3. rand2: $\mathbf{V}_n = \mathbf{X}_{r_a} + F\big(\mathbf{X}_{r_b} - \mathbf{X}_{r_c}\big) + F\big(\mathbf{X}_{r_d} - \mathbf{X}_{r_e}\big)$

4. current-to-rand1: $\mathbf{V}_n = \mathbf{X}_n + F\big(\mathbf{X}_{r_a} - \mathbf{X}_n\big) + F\big(\mathbf{X}_{r_b} - \mathbf{X}_{r_c}\big)$

where $\mathbf{X}_{r_a}$, $\mathbf{X}_{r_b}$, $\mathbf{X}_{r_c}$, $\mathbf{X}_{r_d}$, and $\mathbf{X}_{r_e}$ are randomly chosen target vectors while $\mathbf{X}_n$ and $\mathbf{X}_{best}$ are the current target vector and the target vector with the best objective value, respectively. F is scaling factor. The mutation strategy is chosen from the four predefined strategies according to probabilities which are determined considering success rate. Initially, the probability for selection of each strategy is equal: $\mathbf{P} =$

$\{0.25, 0.25, 0.25, 0.25\}$. The numbers of trial vectors that are transformed and discarded in the next generation are stored in the first generations, the so-called learning period. At the end of the learning period, the selection probabilities are updated according to the ratio of the number of successful trial vectors to all trial vectors, including successfully transformed and discarded for each mutation strategy. After the learning period, the probabilities are updated for every generation by considering only the last generation.

Scaling factor F and crossover ratio CR are normally distributed with $\mathcal{N}(\overline{F}, 0.3)$ and $\mathcal{N}(\overline{CR}, 0.1)$, respectively. Initially, both $\overline{F}$ and $\overline{CR}$ are considered as 0.5 in the learning period. They are updated through the same method as the selection probabilities of the mutation strategies by taking the averages of the F and CR values of trial vectors which are transformed to the next generation. Adaptation of the F and CR is carried out individually for each mutation strategy as each mutation strategy could require different optimal values for F and CR for the best performance. The range of scaling factor F is taken $[0, 2]$ and it is kept in its range by considering the closest boundary if it exceeds its range. Similarly, each parameter in the trial vector during the mutation operation is forced to remain in its range $[\mathbf{X}_{min}, \mathbf{X}_{max}]$.

Having explained the key points of SaDE, four design parameters $\mathbf{X} = \{\gamma, \zeta_a, \delta, \eta\}$ were optimised through optimisation problems defined by performing the SaDE algorithm. Initially, different values were tested for upper and lower boundaries of the initial population pool. After the initial runs, it was observed that the objective value settled after 250 generations, and it did not show significant improvement, as presented for the absolute stability in Appendix C. For given mass ratio μ, structural damping ζ_m and the milling parameters (for the second and third optimisation objectives), the optimisation using SaDE was conducted for 500 generations for each configuration and

each optimisation problem defined above. Since DE is a stochastic method to seek the global maximum, each case was repeated several times to assure the achievement of the best objective value. The optimal design parameters obtained are presented in the next section.

4.3.4   Optimal design parameters

Optimal design parameters for four layouts for three optimisation problems were obtained by performing the SaDE algorithm. For the first objective aiming the maximisation of the limited critical depth of cut, optimal dimensionless design parameters for down milling were found for the mass ratios of 0.01, 0.05 and 0.2 considering three different structural dampings of 0, 0.01 and 0.023. The optimal design parameters for all cases evaluated for down milling were also determined for up milling. In the optimal design parameters, only the frequency ratio γ showed differences between up and down milling. The rest of the design parameters were very close in both milling types. The dimensionless optimal design parameters are given in Table 4.3 for the down milling for the three mass ratios and structural damping values. For the up milling, the parameters are presented for only one case in Table 4.4. The objective value J_1, which is the most negative/positive real part, is given with J_1 in the tables.

The absolute limits were also evaluated considering a milling scenario. The parameters obtained for the milling scenario are presented in Table 4.2. It should be noted that there is no effect of these milling parameters on the dimensionless design parameters for given modal parameters (M, f_n and ζ_m). Although stability limit a_{cr} is the function of these parameters in Table 4.2, the non-dimensional transfer function $\tilde{G}(j\Omega)$ is independent of these parameters. The analysis with the dimensionless design parameters maintain

its validity for the same milling type with different milling parameters. Considering the milling scenario, the limited critical depth of cut (a_{lim}) and stability improvement (Imp.) of each layout for each case compared to the TMD are also given in Table 4.3. The TMDs were tuned using the same objective functions for the reference values.

Table 4.2 Milling simulation parameters

Main stiffness, K	5.8122 x 10^6 N/m
Tangential cutting coefficient, K_t	796.1 N/mm^2
Radial cutting coefficient, K_r	168.8 N/mm^2
Tool diameter	16 mm
Radial immersion	8 mm
Number of teeth	4

The same milling scenarios were also utilised for the second and third objectives of the optimisation, where the maximisation of the largest stable point and the first stability pocket are considered. It is known that the largest stable point occurs in a stability lobe diagram when the machining system is excited at its natural frequency since the value of the real part approaches zero. Therefore, the required spindle speed range for the third objective was chosen as $[0.9\tilde{N}_{f_n}, 1.4\tilde{N}_{f_n}]$ where $\tilde{N}_{f_n}$ corresponds to non-dimensional spindle speed for $f_c=f_n$ and $k = 0$. The optimal design parameters for both objectives are presented in Tables 4.5 and 4.6 for $\mu = 0.05$ and $\zeta_m = 0.023$. For these optimisations, only the down milling was considered and the performance of the TMD tuned for the same objectives was used as the benchmark for the performance evaluations.

Table 4.3 Optimal design parameters obtained for the absolute stability of down milling (a_{lim}). Improvements (Imp.) are calculated, taking the performance of TMD tuned for the same objective as reference.

	ζ_m	μ	γ	ζ_a	δ	α	J_1	a_{lim} (mm)	Imp. (%)
TMD			1.0269	0.0629*	-	-	-6.59	1.30	-
L1			1.0383	0.0546	0.0238	1.0050	-5.01	1.70	30.3
L2	0	0.01	1.0442	0.0026	0.0241	0.9853	-5.04	1.69	29.8
L3			1.0101	0.0665	2.1306	1.1273	-5.95	1.44	10.3
L4			1.0319	0.0026	0.0232	1.0251	-5.01	1.70	31.0
TMD			1.0369	0.1322*	-	-	-2.71	3.18	-
L1			1.0640	0.1199	0.1146	1.0241	-2.01	4.28	34.7
L2	0	0.05	1.0883	0.0219	0.1057	0.9430	-2.06	4.17	31.4
L3			0.9975	0.1504	1.7337	1.3330	-2.40	3.58	12.8
L4			1.0346	0.0253	0.0965	1.1222	-2.01	4.28	34.7
TMD			0.9967	0.2502*	-	-	-1.16	7.39	-
L1			1.0537	0.2244	0.4085	1.0943	-0.83	10.39	40.6
L2	0	0.2	1.1157	0.0999	0.3249	0.8510	-0.90	9.55	29.1
L3			0.9230	0.2929	1.1307	1.8812	-0.99	8.66	17.1
L4			0.9642	0.1324	0.2190	1.4890	-0.83	10.39	40.6
TMD			1.0348	0.0641*	-	-	-5.25	1.64	-
L1			1.0459	0.0562	0.0255	1.0058	-4.18	2.05	25.0
L2	0.01	0.01	1.0516	0.0025	0.0240	0.9867	-4.20	2.03	23.9
L3			1.0175	0.0679	2.1405	1.1319	-4.82	1.78	8.6
L4			1.0392	0.0028	0.0245	1.0260	-4.18	2.05	25.0
TMD			1.0433	0.1346*	-	-	-2.42	3.56	-
L1			1.0702	0.1214	0.1190	1.0248	-1.84	4.68	31.7
L2	0.01	0.05	1.0956	0.0230	0.1091	0.9409	-1.88	4.57	28.5
L3			1.0027	0.1526	1.7076	1.3411	-2.17	3.97	11.7
L4			1.0400	0.0263	0.0988	1.1248	-1.84	4.68	31.7
TMD			1.0006	0.2538*	-	-	-1.10	7.85	-
L1			1.0580	0.2255	0.4090	1.0953	-0.79	10.90	38.8
L2	0.01	0.2	1.1204	0.1006	0.3271	0.8506	-0.86	10.05	27.9
L3			0.9279	0.2925	1.1239	1.8882	-0.94	9.15	16.5
L4			0.9661	0.1356	0.2207	1.4980	-0.79	10.90	38.8
TMD			1.0452	0.0629*	-	-	-4.11	2.09	-
L1			1.0559	0.0581	0.0270	1.0054	-3.41	2.51	20.1
L2	0.023	0.01	1.0626	0.0030	0.0267	0.9847	-3.43	2.50	19.4
L3			1.0261	0.0705	2.0360	1.1402	-3.84	2.24	7.1
L4			1.0488	0.0031	0.0260	1.0270	-3.41	2.51	20.1
TMD			1.0517	0.1356*	-	-	-2.12	4.06	-
L1			1.0784	0.1232	0.1227	1.0256	-1.65	5.21	28.3
L2	0.023	0.05	1.1045	0.0237	0.1116	0.9403	-1.69	5.08	25.1
L3			1.0115	0.1529	1.7014	1.3473	-1.92	4.35	7.0
L4			1.0475	0.0270	0.1005	1.1285	-1.65	5.21	28.3
TMD			1.0062	0.2547*	-	-	-1.02	8.46	-
L1			1.0633	0.2270	0.4160	1.0958	-0.74	11.58	36.9
L2	0.023	0.2	1.1260	0.1014	0.3294	0.8519	-0.80	10.69	26.5
L3			0.9316	0.2951	1.1052	1.9045	-0.89	9.79	15.8
L4			0.9698	0.1380	0.2222	1.5055	-0.74	11.59	37.1

* $\zeta_a = \frac{c}{2\sqrt{k_o m_a}}$ for TMD, where c is the damping of the damper in parallel to the spring.

Table 4.4 Optimal design parameters obtained for the absolute stability of up milling (a_{lim}). Improvements (Imp.) are calculated, taking the performance of TMD tuned for the same objective as reference.

	ζ_m	μ	γ	ζ_a	δ	α	J_1	a_{lim} (mm)	Imp. (%)
L1			0.8693	0.1199	0.1142	1.0250	3.01	-5.72	23.1
L2	0	0.05	0.8926	0.0216	0.1050	0.9441	3.06	-5.61	21.0
L3			0.8382	0.1500	1.7258	1.3331	3.40	-5.05	8.9
L4			0.8449	0.0257	0.0972	1.1231	3.01	-5.2	23.1

Table 4.5 Optimal design parameters obtained for the maximisation of the largest stable depth of cut for down milling.

	ζ_m	μ	γ	ζ_a	δ	α	Imp. (%)
TMD			1.6420	0.0618	-	-	-
L1			1.6433	0.0614	1.4160	1.0442	2.8
L2	0.023	0.05	1.6396	0.0619	16.2429	0.0147	0.2
L3			1.6296	0.0599	5.8019	1.0815	3.5
L4			1.5491	0.1151	0.0155	4.0203	4.4

Table 4.6 Optimal design parameters obtained for the enhancement of the first stability pocket for $[0.9\tilde{N}_{f_n}, 1.4\tilde{N}_{f_n}]$ for down milling.

	ζ_m	μ	γ	ζ_a	δ	α	Imp. (%)
TMD			0.9894	0.1208	-	-	-
L1			1.2303	0.6344	0.3005	1.0402	15.2
L2	0.023	0.05	1.3089	0.0288	0.3019	0.8811	11.4
L3			0.9003	0.1798	7.6489	1.1849	-0.2
L4			1.1309	0.0297	0.2119	1.2746	15.6

4.4   Stability performances of the layouts

The performance improvements of each layout for each case are presented with the optimal design parameters in Tables 4.3, 4.4, 4.5 and 4.6. The performances of the layouts are evaluated with different comparisons. Figure 4.5 compares the real part of the FRFs of each layout with the TMD. The comparison is given for the mass ratio of 0.05 and no structural damping ($\zeta_m = 0$). As the primary system includes no damping in this case, the TMD results are given for Sims' method [108] considering equal positive peaks (for up milling) and equal negative troughs (for down milling) of the real part. The IDVAs results are for the optimal design parameters in Tables 4.3 and 4.4 for the down and up milling, respectively. It should be noted that the optimal design parameters obtained from numerical optimisation for TMD were almost identical with the values obtained from Sims' method [108] for undamped structure.

The comparisons of real parts of the FRFs of the four layouts with the uncontrolled case and TMD are presented in Figure 4.6. The results were obtained for down milling with the structural damping of 0.023 in the main system and the mass ratio of 0.05. These real parts were used to obtain the stability lobe diagram as given in Figure 4.7. The results demonstrate that all layouts for undamped and damped primary systems indicated better performance in improving the absolute stability limit by improving the most negative/positive real part. More than 25% improvement was provided in the limited critical depth of cut for L1, L2 and L4.

As for the maximisation of the largest stable depth of cut, IDVAs with the design parameters in Table 4.5 are compared with TMD tuned for the same objective. The largest stable depth of cut showed a significant increment with this tuning. However, all IDVAs showed almost identical performance with the TMD. Therefore, only the

stability limit obtained by L2 (solid orange line) and TMD (dashed black line) are presented in Figure 4.8. The third optimisation focused on the maximisation of the first stability pocket in the non-dimensional spindle speed range of $[0.9, 1.4]$. The TMD was also optimised for this objective and compared with the IDVAs. This optimisation results exhibited that the L1, L2 and L4 broadened the spindle speed band for the stable cut in the pocket. Moreover, the largest stable depth of cut was comparable to the values obtained in the second optimisation. L1, L2 and L4 show similar performance improvements to each other, while L3 presented similar performance to the TMD. In Figure 4.8, only the stability limit of L2 (solid green line) compared to TMD (blue dotted dash line) for this optimisation is presented. Both TMD or L2 improved stability limits of more than 12 mm. However, the IDVA-L2 provided two times higher spindle speed band where 12 mm depth of cut is stable, compared to the TMD.

4.5   Discussion

The optimisation results showed that all layouts improved the absolute stability performance compared to a classical TMD for the same mass ratio. The best performances were obtained for L1, L2 and L4. L1 and L4 showed almost identical improvement for all cases while L2 performed slight less. The performance improvement of L3 remained limited compared to other three layouts. The layouts for higher mass ratios and smaller structural damping generally showed greater improvement.

One of the important points from the results is that the optimal inertance-to-mass ratio values δ were quite small. For instance, for the layouts with the best performances
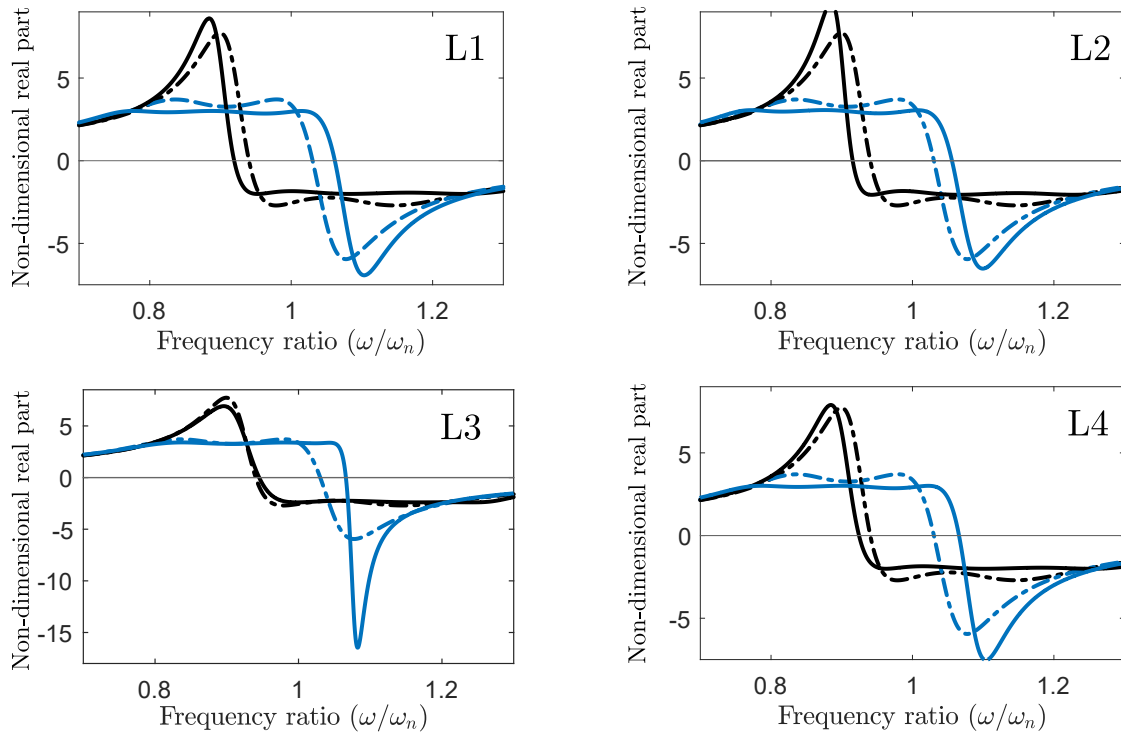
Figure 4.5 Real part responses of the IDVAs for $\mu = 0.05$ and $\zeta_m = 0$ in comparison with the TMD. The IDVAs responses are obtained from the optimal design parameters in Tables 4.3 and 4.4. The TMD responses are obtained from Sims' method [108]. (-·--·-) equal real troughs for TMD, (-·-·-) equal real peaks for TMD, (——) down milling for IDVA, (——) up milling for IDVA.
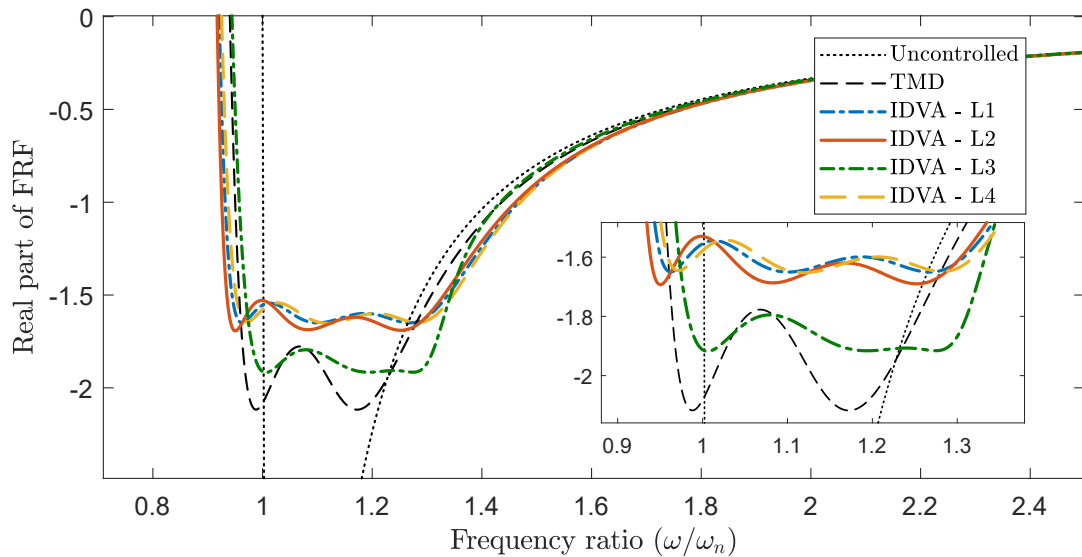

Figure 4.6 Comparisons of the real part responses of the IDVAs for down milling obtained from the design parameters for $\mu = 0.05$ and $\zeta_m = 0.023$ in Table 4.3 for milling parameters in Table 4.2.
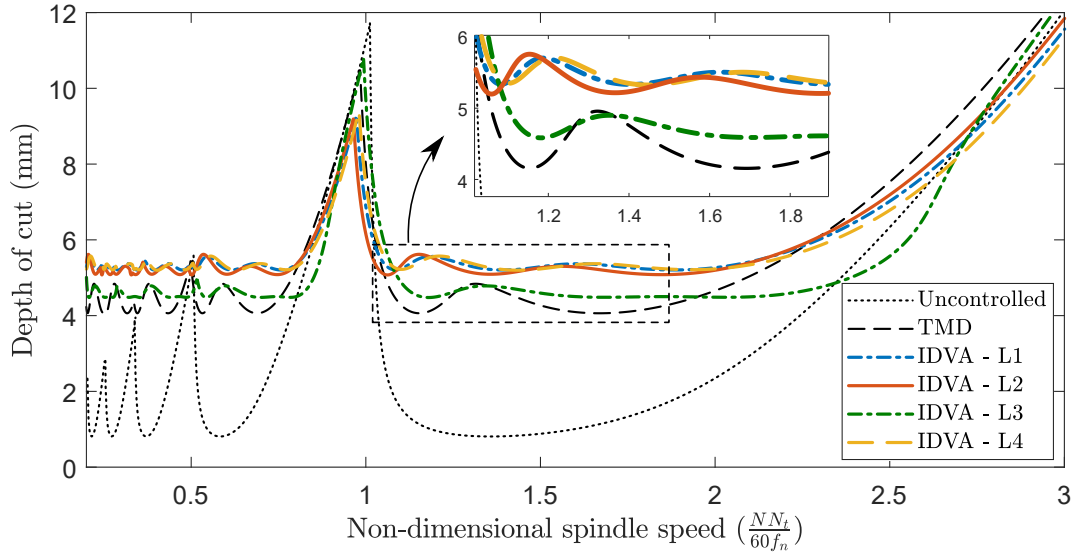
Figure 4.7 The stability lobe diagram for the structure controlled with the IDVA in comparison with the uncontrolled case and the TMD. The stability limits are obtained from the real part responses presented in Figure 4.6.
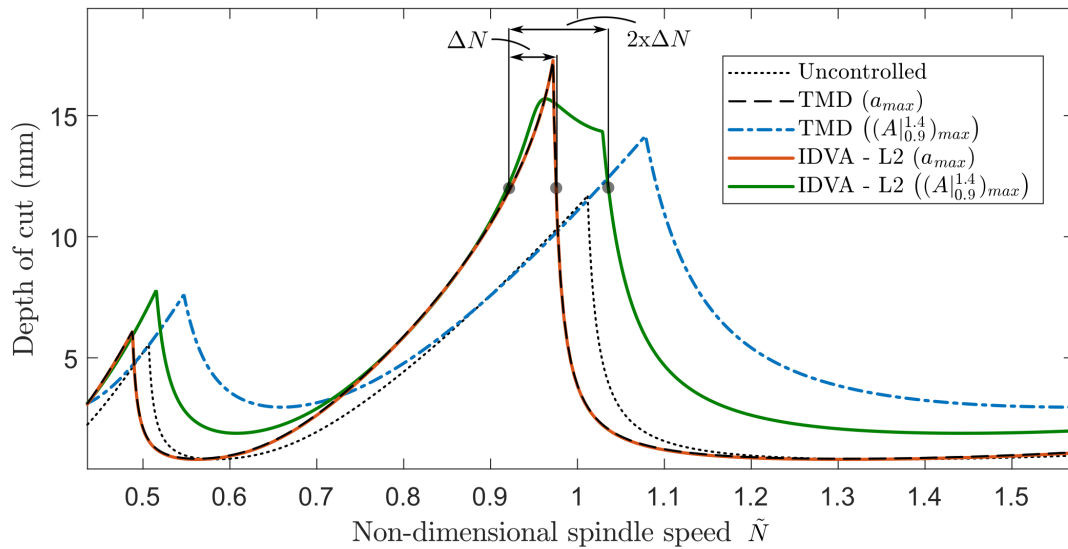

Figure 4.8 The stability lobe diagram showing the improvement for the Layout L2 obtained from the second and third optimisation objectives (J_2 and J_3). a_{max} and $(A|_{0.9}^{1.4})_{max}$ in legend represents for the maximisations of the largest stable depth of cut (J_2) and first stability pocket in $[0.9\tilde{N}_{f_n}, 1.4\tilde{N}_{f_n}]$ (J_3).

(L1, L2 and L4), the inertance-to-mass ratio values were around 0.1, which leads to inertance of 0.005 kg for the primary system with unit modal mass. This value increased for the higher mass ratios but using a high mass ratio can be problematic for the limited space applications. Therefore, the physical realisation of the inerter that can produce such small inertance should be evaluated for the limited-space applications. It is well-known that the inerter is employed to achieve a higher inertial effect with a small mass. However, having determined small inertance for the optimal value indicates that inerter functions act more like a control element that increase the order of the transfer function rather than acting like an inertial amplifier.

Comparing the up and down milling operations it can also be seen that a transition from equal real troughs to equal real peaks occurs with only a change in the optimal dimensionless design parameters, which was the frequency ratio γ. The rest of the parameters remained almost identical. This is parallel to Sims' method [108] where only the frequency ratio changes while the damping ratio remains constant during the transition from equal real troughs to equal real peaks.

It might be preferable to try and use the stability pockets for cutting with a higher depth of cut. It was shown that tuning a TMD to maximise the largest stable depth of cut provided more than 50% improvement at the maximum stable point. There was no additonal benefit exhibited presented by the IDVAs and all layouts presented TMD-like behaviour for this optimisation. One clear example of this can be seen in L2 since this layout turns into a TMD with an infinite inertance in theory. It was observed from the optimal design parameters of L2 in Table 4.5 that the behaviour of the L2 converged to a TMD by having a high optimal inertance value. However, using IDVAs (L1, L2 and L4) improved the spindle speed band where a high depth of cut is possible. High stable depth of cut with narrow spindle bands predicted in theory can

be a chatter region in practice due to assumptions made in the stability analysis and the uncertainties. Employment of the IDVAs can be beneficial by improving the spindle speed band and machining at a high depth of cut. Nonetheless, the computational cost of this optimisation is heavy as it involves interpolation and obtainment of the stability lobes.

Using an IDVA as a localised addition seems more promising for performance improvement of the absolute stability rather than the maximisation of the stability pocket. Therefore, the main focus will be the absolute stability improvement in the rest of the thesis. The following section will investigate the sensitivity of the design parameters.

4.6   Global sensitivity analysis

The milling chatter performance of different layouts of inerter-based dynamic vibration absorbers have been evaluated by directly looking at the performance outputs. Numerical simulations were conducted assuming the exact optimal value for each design parameter. However, due to assumptions made in the theoretical calculations in the design stage and manufacturing errors, it is difficult to obtain the exact optimal design parameters in practice unless elements of the control device are adaptive (e.g. variable stiffness and/or variable damping). Therefore, the analysis of the effect of each design parameter deviation from its exact optimal value on the chatter resistance performance is important, especially in a design study or in a model with multiple input factors. The importance of each input factor in terms of the effect on the chatter suppression performance can be different. Some of them can be unimportant and have a very small effect on the output, while some of them can be very influential. The sensitivity

analysis provides this information about the input factors, which can be helpful in the evaluation of the feasibility of a particular layout in the design study.

A global sensitivity analysis, where the sensitivity of the parameters is not assessed locally but over the full range of the possible values (sample space), is conducted to evaluate the sensitivity of the design parameters for the layouts with the best performances (L1, L2 and L4). Only the first optimisation case stated in the previous section is examined and thus, the limited critical depth of cut is considered as the performance output. Sobol's method—a variance-based global sensitivity method— is employed to handle the nonlinear and nonmonotonic relationship between the design parameters and the output (the limited critical depth of cut).

4.6.1   Problem foundation

Each layout of inerter-based absorber has four dimensionless design parameters γ, ζ_a, δ, and α. For given mass ratio μ and the structural damping ζ_m, the sensitivity analysis problem can be described as

$$a_{lim} = f(\gamma, \zeta_a, \delta, \alpha) \tag{4.12}$$

where a_{lim} is the output as the limited critical depth of cut and γ, ζ_a, δ and α are the input factors which defines the output. In the sense of the sensitivity analysis, Equation 4.12 is described as the model, and the sensitivity becomes the measure of how much the variation in the input parameters affects the output.

The input factors are the actual values of the control elements that cannot be changed unless they are not adaptive. It is important to assess how much the differences between the input factors and the optimal values affect the output, which eventually defines the productivity of the cutting operation. The outputs are created via Monte Carlo simulations and determined by randomly selected input factors. The variations observed in the outputs due to the change in each input factor indicates the sensitivity of the parameters. Therefore, a reasonable choice of the input factors has an essential role in the sensitivity results.

Each input factor is chosen from a pre-defined range that covers possible actual values of a control element considering its optimal value. Input factors are randomly chosen from the pre-defined range. However, complete randomness could lead to a poor representation by choosing most of the samples from the same section. Therefore, it is also important to have a representation of all sections according to the distribution function.

4.6.2   Latin hypercube sampling

The Latin Hypercube sampling (LHS), which was first developed by McKay et al. [280] in 1979, is an efficient method to generate random sampling. A simple sampling does not assure the representation of all sections of the distribution functions. The LHS defines the vectors of the input factors by dividing the range of each variable into equal intervals and chooses a value with respect to the distribution function in the interval. Therefore, the samples in this method are chosen evenly to represent its distribution function. With a fewer number of samples, it provides better coverage of the sample space of the inputs than a simple random sampling.

A simple example of the sampling for two input vectors with two elements, which are created by the LHS, is given in Figure 4.9. For a uniform distribution $U(0, 10)$, the LHS divides each input factor into 10 and chooses one random value inside that interval for both input factors as shown in Figure 4.9a. Thus, a representation of each section of the sample space is provided. The sample space for a normal distribution $N(5, 2)$ is demonstrated in Figure 4.9b. In that case, more samples are selected near the mean values of the input factor as following the distribution function.

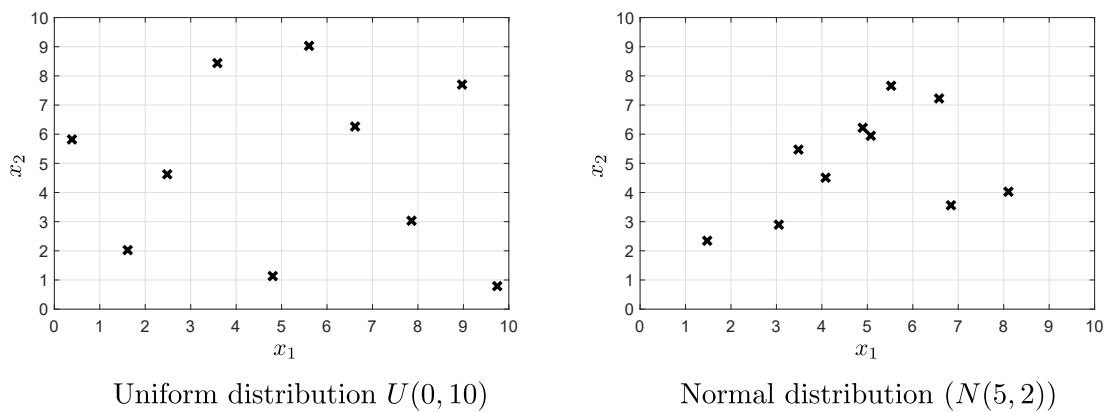Uniform distribution $U(0, 10)$ Normal distribution $(N(5, 2))$

Figure 4.9 Samples generated using the Latin Hypercube sampling

The purpose of the generation of samples for the four design parameters is to evaluate the effect of the changes in the parameters on the result. Although designs of the components are made considering the optimal design parameters obtained from the optimisation method, they are likely to have different parameters in practice due to the manufacturing process and the assumptions in the design process. Assuming that the possibility of having a large variation from the targeted design parameter is less likely than the possibility of having a small variation, samples can be chosen with a normal distribution of the samples over the sample space.

Sensitivity analysis was considered for the dimensionless design parameters obtained for down milling with $\mu = 0.05$ and $\zeta_m = 0.023$ as presented in Table 4.3. The mean values

and the standard deviations for the normal distribution are given in Table 4.7 with the optimal design parameters. The mean values are the optimal design parameters for each layout. The standard deviations were considered as 10% of the mean value for the parameters γ and α, considering that the deviations in the dimensional parameters are relaxed in these dimensionless parameters due to the square root. The standard deviations were taken 20% of the mean value for the parameters ζ_a and δ.

Table 4.7 Optimal design parameters for the three layouts for $\mu = 0.05$ and $\zeta_m = 0.023$ with the mean values and the standard deviations for a normal distribution for the Monte Carlo simulation.

	Layouts	$\gamma = \sqrt{\frac{k/m_a}{K/M}}$	$\zeta_a = \frac{c}{2\sqrt{m_a k_o}}$	$\delta = \frac{b}{m}$	$\alpha = \sqrt{\frac{k_i/b}{k_o/m_a}}$
Optimum Values	L_1	1.0784	0.1232	0.1227	1.0259
	L_2	1.1045	0.0237	0.1116	0.9403
	L_4	1.0475	0.0270	0.1005	1.1285
Mean ± Sd. dev.	L_1				
	L_2	$\gamma_{opt} \pm 10\%$	$\zeta_{a,opt} \pm 20\%$	$\delta_{opt} \pm 20\%$	$\alpha_{opt} \pm 10\%$
	L_4				

4.6.3 Sobol sensitivity analysis

Sobol's method [281, 282] is employed for the analysis of the sensitivity of parameters. It is a global sensitivity analysis method and is based on the decomposition of the variance of the output. One of the most important advantages of this method is the ability to tackle problems with a nonlinear and nonmonotonic model as it is a variance-based method, and the major drawback is its high computational cost [282]. It has been extended by Homma and Saltelli [283] to obtain the total effect sensitivity of the input factors. The first-order and total effect sensitivity indices, which are the outputs of the Sobol sensitivity analysis and its extension, are briefly explained in this section.

The changes in the influential parameters in a system cause higher variations in the output. Therefore, variance-based methods for sensitivity analysis evaluate the variance of the output by fixing one or some input factor(s). Assuming that an input factor is fixed, the variance which is taken over the rest of the factors give information about the sensitivity of that parameter on the output.

Assuming a model with an output $y = f(x_1, ... x_n)$, where $\boldsymbol{x}$ is the vector of n input factors, the first-order sensitivity index for input factor is written as [281, 282]

$$S_i = \frac{V(E(y|x_i))}{V(y)} \tag{4.13}$$

where $V(E(y|x_i))$ is the variance of the mean of y is taken over all factors but x_i by keeping x_i constant and $V(y)$ is the unconditional variance of the output. The first-order index indicates the main effect contribution of each input factor to the variance of the output.

The decomposition of the unconditional variance of the output proposed by Sobol [284] contains the conditional variances, which correspond to the first-order effects and the interactions between the input factors. The total output variance $V(y)$ for a model with n orthogonal input factors can be decomposed as [281, 282]

$$V(y) = \sum_i V_i + \sum_i \sum_{ij} V_{ij} + ... + V_{1...n} \tag{4.14}$$

where

$$V_i = V(E(y|x_i)) \tag{4.15}$$

$$V_{i,j} = V(E(y|x_i, x_j)) - V_i - V_j \tag{4.16}$$

$$V_{i,j,m} = V(E(y|x_i, x_j, x_m)) - V_{ij} - V_{im} - V_{jm} - V_i - V_j - V_m \tag{4.17}$$

where $V(E(y|x_i, j))$ and $V(E(y|x_i, x_j, x_m))$ are the joint effects and represent the interaction effects of the in put factors of (x_i, x_j) and $(x_i, x_j$ and $x_m)$, respectively.

The total effect sensitivity index, which considers both the main effect contributions and the interaction effects between the input factors, is described by Homma and Satelli [281, 283] :

$$S_{Ti} = \frac{V(y) - V(E(y|x_{-i}))}{V(y)} = \frac{E(V(y|x_{-i}))}{V(y)} \tag{4.18}$$

where $V(y) - V(E(y|\mathbf{x}_{-i}))$ is the sum of all terms in variance decomposition (Equation 4.13) which include x_i. The total effect of the first parameter for a model with four input factors can be determined as:

$$S_{T1} = S_1 + S_{12} + S_{13} + S_{14} + S_{123} + S_{124} + S_{1234} \tag{4.19}$$

From Equations 4.13 and 4.18 , the importance of an input factor is evaluated by looking at how close to 1 the first-order and the total effect sensitivity indices are since both of them are found by normalised by total variance $V(y)$. If the sensitivity index is close to 1, it is an important input factor. If it is close to 0, it is an unimportant one.

More detail for the sensitivity indices and the application of the theory into a model can be found in [281, 282]. In the following section, the total effect sensitivity indices will be evaluated for four design parameters of the absorber.

4.6.4 Total effect sensitivity indices

The sensitivity of the dimensionless design parameters was found for down milling with the parameters in Table 4.2 for the structural damping ζ_m=0.023 and different mass ratios μ from 0.01 to 0.4. The choice of structural damping value $\zeta_m = 0.023$ is not arbitrary. It is the structural damping value measured for the main system in the experimental setup as presented in Chapter 6. The output was considered as the absolute stability (a_{lim}) as presented in Equation 4.12. The LHS with a normal distribution function was utilised for the selection of the samples as given in Table 4.7. The total effect indices in Equation 4.18 were calculated for the Layouts L1, L2 and L4. The analyses were first made for the mass ratio of 0.05 for the different number of samples, and the total effect indices showed little change after the number of samples of 1000 as presented in Figure 4.10. The total effect sensitivity indices of the three layouts obtained for 25000 samples are presented in Figure 4.11 for different mass ratios. It has been found that the dimensionless parameter γ, which is associated with the outer spring stiffness for a given main structure damping ratio, is the most influential parameter on the output regardless of the layout of the absorber.
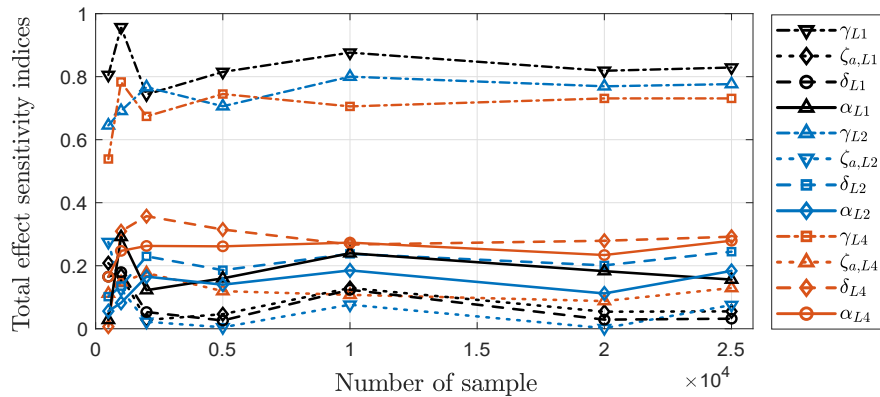
Figure 4.10 Convergence study for sensitivity indices of the Layouts L1, L2 and L4 for mass ratio of 0.05 and structural damping of 0.023.
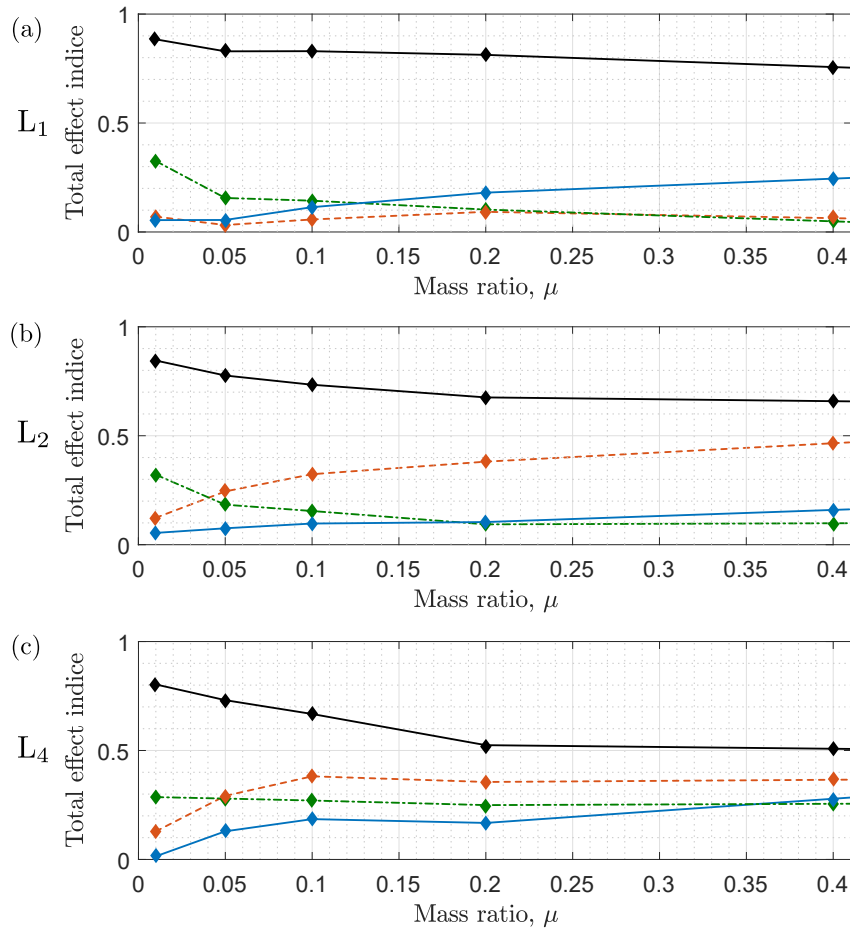

Figure 4.11 The total effect sensitivity indices of the design parameters for the Layouts L1, L2 and L4 for $\zeta_m = 0.023$ and different mass ratios. $(\text{—}\blacklozenge\text{—})\gamma = \sqrt{\frac{k/m_a}{K/M}}$, $(\text{—}\blacklozenge\text{—})\zeta_a = \frac{c}{2\sqrt{m_a k_o}}$, $(\text{--}\blacklozenge\text{--})\delta = \frac{b}{m}$, $(\text{--}\bullet\text{--})\eta = \sqrt{\frac{k_i/b}{k_o/m_a}}$.

4.6.5 Discussion

The total effect sensitivity indices S_{Ti} in Figure 4.11 reflects both the main contribution effect of each design parameter and the interaction effects between the parameters. For all three layouts, the most influential design parameter is the frequency ratio γ as the highest total effect indices value belonged this parameter. The dimensionless design parameter γ is related to the outer spring. Considering an analogy between the IDVA and the TMD, the outer spring in the IDVA directly corresponds to the spring in TMD while the whole subnetwork, consisting of the inerter, the damper and the inner spring in the IDVA, corresponds to the damper in the TMD. Hence, any change in any element in the subnetwork corresponds to a portion of the damper in the TMD. Hence, these elements have less influence compared to the outer spring. Furthermore, the outer spring defines the stiffness of the whole control device. For instance, the higher the stiffness of the outer spring is, the harder the relative motion between the two ends of the subnetwork becomes. Therefore, it is reasonable to expect that the outer spring is the most influential parameter.

The effects of the rest of the parameters vary depending on the layout and the mass ratio. For the Layout L1, the second influential parameter is η for small mass ratios and ζ_a for high mass ratios. δ, which is directly associated with the inertance for given mass ratio, becomes more influential with increasing mass ratio in the Layout L2 and the effects of the other two parameters on the performance are limited. For the Layout L4, only the influence of η seems important after the frequency ratio γ for small mass ratio. With increasing mass ratio, all design parameters become influential.

The relations between the dimensionless parameters and the dimensional parameters were given in Equation 4.4. The dimensionless design parameters γ and δ are directly

defined by the outer spring k_o and the inertance b. The change of the viscous damping c affects more the damping ratio ζ_a than the outer spring k_o since k_o involves in the square root. Therefore, the damping ratio can be mostly associated with viscous damping. It is difficult to associate the dimensionless parameter α with only one parameter as it includes all dimensional design parameters except the damping. It can only be stated that the inner spring k_i is uninfluential if the total effect index is small for α. Having considered these relations, the importance of the dimensional design parameters can be evaluated. The most critical value is the stiffness of the outer spring for all three layouts. The inertance seems an unimportant parameter for all mass ratios evaluated in the Layout L1. Similarly, the viscous damping shows no importance on the performance of the Layout L2, and the inertance becomes more influential with the increasing mass ratio in this layout. Finally, all dimensional parameters in the Layout L4 become influential on the result with increasing mass ratio.

4.7   Summary

This chapter investigated the benefits of the using an inerter as a localised addition through numerical simulations. The investigation mostly focused on the improvement of absolute stability. It was discussed that there are fixed points for the real part response for each layout, which can be employed for an analytical tuning strategy like Sims' method [108]. However, this attempt remained limited to identifying the fixed points due to the difficulty in the derivation and the limitation in the application. Numerical optimisation by performing SaDE was utilised to obtain optimal design parameters. The performances of four inerter-based layouts were evaluated from the real part of the FRF and stability lobe diagrams considering a down milling operation.

The results showed that all layouts outperformed a classical TMD. The three layouts L1, L2 and L4 achieved to enhance the stability more than 20% for almost all cases examined. The improvements extended even further for higher mass ratios. Moreover, the layouts were analysed to improve the stability pocket. For this, a classical TMD was first optimised for this objective and achieved 50% improvement in the largest stable point. Taking this result as a benchmark, it was shown that none of the layouts presented an important improvement in the largest stable depth of cut. However, they enhanced the spindle speed band at a high stable depth of cut.

The sensitivities of the design parameters were studied for only the three layouts with the best performance. Instead of applying local sensitivity analysis, global sensitivity analysis was conducted by applying Sobol's method. Running Monte Carlo simulation, the sensitivity of the design parameters were determined by evaluating the variance of the critical limiting depth of cut against the change of the design parameters. Results showed that the most influential design parameter is the outer spring k_o in all layouts studied. This indicates that the most of the care in the experimental design should be given to the outer spring to achieve an actual stiffness as close to its optimal value as possible.

The novelty in the study presented in this chapter is that the benefits of using inerters in machining operations were investigated, focusing on the machining chatter stability for the first time. Numerical evaluations showed that the chatter stability could be improved by using inerters. The improvement can only be achieved with the proper choice of design parameters. For this, even the inertance was included optimisation as a design parameter instead of considering it as a given parameter. This approach indicated that choosing a high inertance value does not guarantee performance improvement, and there was an optimal inertance value. It was seen that the optimal inertance values

were generally small for small mass ratios. Therefore, the physical implementation of the IDVAs in a milling operation requires to be in small scale and capable of producing small inertance values. The direct implementation of the idealised layouts in such a small scale might not be possible due to the constructional limitations. Also, nonlinearities such as friction and backlash can be more problematic in small scale applications. Thus, experimental validation of the results obtained in this chapter becomes an important part of this thesis.

Chapter 5

Design Study

5.1 Introduction

All layouts in the previous chapter were analysed by assuming idealised (i.e. theoretical) IDVAs without physical implementation. Milling operations generally have limited spaces for passive control devices. Therefore, one of the main challenges in using IDVA in milling operations is that the physical realisation of an idealised IDVA can be impracticable for relatively small scale applications. This chapter investigates the practical application of the Layout L2, updating the mechanical model and presents the absorber's design study including a new mechanical design of the inerter and the realisation of the damping mechanism. Among the layouts which provide the best performance in the previous chapter, L2 is chosen for the design study since its realisation is more straightforward than the others. Although only one layout is considered throughout the chapter, the design studies presented in this chapter can be used as a base study for the other layouts.

The main difficulty in realising the idealised L2 that could reduce the performance improvement achieved in Chapter 4 is the parasitic mass effect caused by structural masses of absorber elements. In Chapter 4, the optimal design parameters were obtained for idealised configurations where no parasitic mass was considered. The parasitic mass effect, which is likely to be encountered in any real system could lead to a detuning effect and reduce the chatter resistance performance of the absorber. Therefore, this chapter first evaluates the structural masses of the elements in L2 in terms of whether they create a parasitic mass effect in the system or not. Secondly, a hysteretic gel damper is considered for the practical design of L2 based on its simplicity and easiness of implementation. Having considered the parasitic mass and the linear hsyteretic damping, an updated model of the idealised L2 is presented with the performance analysis.

The physical design of the inerter and L2 is then studied in order to verify the performance improvement in milling operations. Although applications of the inerter have been widely studied in the vibration community, most of the works either presented a theoretical analysis of the performance or focused on relatively large scale applications such as building vibration suppression, or vehicle suspension systems. The use of mechanical inerter devices developed in those studies in small-scale applications could be problematic due to the backlash and friction between mechanical parts and flow losses (for fluid-based inerters) that become prominent on small scales. Moreover, most inerter implementation in the literature needs a grounded connection of the passive control device or its deployment between different structural parts. Milling operations generally have limited spaces and no availability of a grounded connection to apply to a passive control device. Implementing the IDVAs as a localised addition in a milling operation requires a small-scale design of the IDVAs without the need for inertial ground. To the author's knowledge, the only inerter which is applicable for the

small scale application is frictionless living-hinge inerter proposed by John and Wagg [207]. Based on their design concept, a pivoted-bar inerter device with living-hinges is developed in this chapter. Also, the implementation of the gel damper is presented. Using the developed inerter and the gel damper, a new mechanical design of IDVA can be applied to the limited-space applications without the requirement of inertial ground or deployment between two parts of the host structure.

The chapter is organised as follows. Section 5.2 assesses the influence of the parasitic mass on the chatter performance. Section 5.3 updates the idealised L2, including the parasitic mass and the hysteretic damping to the model and examines the performance of the updated model. Section 5.4 introduces the pivoted-bar inerter with living hinges. This section also discusses the stiffness effect in the inerter due to the living hinges and analysis the fatigue life cycle of the inerter. The implementation of the gel damper is presented in Section 5.5. The final design of the absorber is demonstrated in Section 5.6. After discussion in Section 5.7, a summary of the chapter is given in the last section.

5.2   Parasitic mass effect

5.2.1   Influence of parasitic mass on IDVA-L2

The Layout L2 is constructed with a spring in series to an inerter network consisting of a parallel-connected spring and damper arrangement in series to an inerter (also known as a TID). It has a relatively complex layout compared to a classical TMD consisting of a spring and a damper in parallel. It is vital to assess the possible parasitic mass effect

due to the structural masses of the element in a complex layout as it can degrade the performance. The structural masses of the elements in a TMD generally do not cause a problem as they can mainly be compensated for. Masses of the spring, damper and connection elements, for instance, can be counted to either the main mass or auxiliary mass. However, for L2, this cannot be possible because of the serial-connected elements. As a result, the inertial effect of some elements or the connection elements becomes unavoidable between the absorber components. If the influence of this parasitic mass acting in the system is large, it leads to a detuning effect and reduces the performance of the IDVA-L2.

The influence of the parasitic mass acting between the components can be evaluated by deriving the equations of motion of the IDVA-L2 with a parasitic mass. A schematic representation of an IDVA-L2 with a parasitic mass mounted on an SDOF milling system is illustrated in Figure 5.1. The parasitic mass is considered to act between the serial-connected element; the inerter and the spring-damper arrangement. Depending on the orientation of the IDVA, there are two possible connections; one of terminals of the inerter is directly connected to the primary system (named in this study as *icms*) as shown in Figure 5.1a and one of the terminals of the inerter is directly connected to the auxiliary mass (named in this study as *icma*) as shown in Figure 5.1b.

The equations of the motion for the *icms* case in Figure 5.1a is written as

$$
\begin{aligned}
& M\ddot{x}_m(t) + C\dot{x}_m(t) + Kx_m(t) - b\big(\ddot{x}_p(t) - \ddot{x}_m(t)\big) - k_o\big(x_a(t) - x_m(t)\big) = F(t), \\
& m_p\ddot{x}_p(t) + b\big(\ddot{x}_p(t) - \ddot{x}_m(t)\big) - c\big(\dot{x}_a(t) - \dot{x}_p(t)\big) - k_i\big(x_a(t) - x_p(t)\big) = 0, \\
& m_a\ddot{x}_a(t) + k_o\big(x_a(t) - x_m(t)\big) + c\big(\dot{x}_a(t) - \dot{x}_p(t)\big) + k_i\big(x_a(t) - x_p(t)\big) = 0,
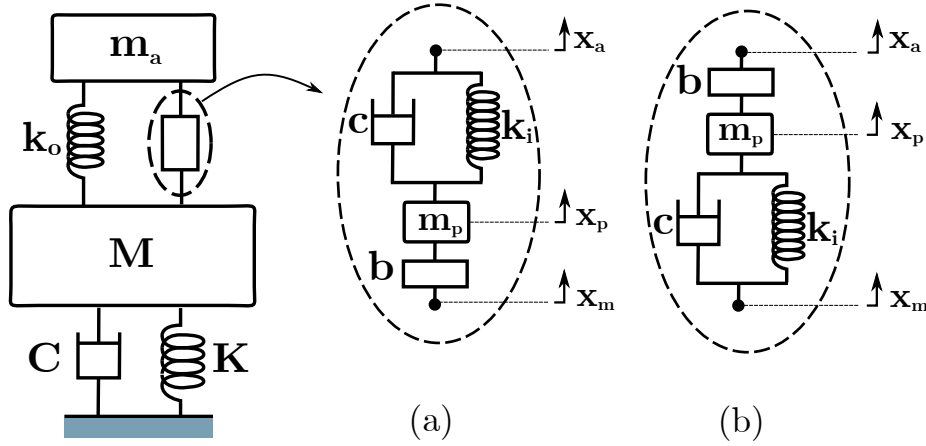\end{aligned}
\tag{5.1}
$$

Figure 5.1 Mechanical models of the idealised IDVA-L2 with parasitic mass between the series-connected elements: (a) the *icms* case where the inerter is positioned close to the machining system, and (b) the *icma* case where the inerter is positioned close to the auxiliary mass m_a.

where m_p is the parasitic mass, and $x_p(t)$ is the displacement of the parasitic mass. If the inerter is connected between the parasitic mass and the auxiliary mass m_a, the equations of motion differ from the *icms* case. The equations of the motion for the case *icma* case in Figure 5.1b is written as

$$M\ddot{x}_m(t) + C\dot{x}_m(t) + Kx_m(t) - c\big(\dot{x}_p(t) - \dot{x}_m(t)\big) - k_i\big(x_p(t) - x_m(t)\big) - k_o\big(x_a(t) - x_m(t)\big) = F(t),$$

$$m_p\ddot{x}_p(t) - b\big(\ddot{x}_a(t) - \ddot{x}_p(t)\big) + c\big(\dot{x}_p(t) - \dot{x}_m(t)\big) + k_i\big(x_p(t) - x_m(t)\big) = 0, \qquad (5.2)$$

$$m_a\ddot{x}_a(t) + b\big(\ddot{x}_a(t) - \ddot{x}_p(t)\big) + k_o\big(x_a(t) - x_m(t)\big) = 0.$$

Additional to the dimensionless parameters presented in Equation 4.4, the dimensionless parameter $\beta = m_p/m_a$ for the parasitic mass is introduced for the dimensionless analysis. Taking the Laplace transform and replacing $s = j\omega$ into Equations 5.1 and 5.2, the equations of motion with dimensionless parameters can be written for the *icms* and

the *icma* cases, respectively:

$$\left[-(1+\delta\mu)\Omega^2 + j2\zeta_m\Omega + 1 + \gamma^2\mu\right]X_m + (\delta\mu\Omega^2)X_p - (\gamma^2\mu)X_a = \Delta,$$

$$(\delta\Omega^2)X_m + \left[-(\delta+\beta)\Omega^2 + j2\zeta_a\gamma\Omega + \alpha^2\gamma^2\delta\right]X_p - (j2\zeta_a\gamma\Omega + \alpha^2\gamma^2\delta)X_a = 0, \quad (5.3)$$

$$-(\gamma^2)X_m - (j2\zeta_a\gamma\Omega + \alpha^2\gamma^2\delta)X_p + (-\Omega^2 + j2\zeta_a\gamma\Omega + \alpha^2\gamma^2\delta + \gamma^2)X_a = 0,$$

and

$$\left[-\Omega^2 + j2(\zeta_m + \zeta_a\gamma\mu)\Omega + \gamma^2\mu(\alpha^2\delta+1) + 1\right]X_m - (j2\zeta_a\gamma\mu\Omega + \alpha^2\gamma^2\delta\mu)X_p - (\gamma^2\mu)X_a = \Delta,$$

$$-(j2\zeta_a\gamma\Omega + \alpha^2\gamma^2\delta)X_m + \left[-(\beta+\delta)\Omega^2 + j2\zeta_a\gamma\Omega + \alpha^2\gamma^2\delta\right]X_p + (\delta\Omega^2)X_a = 0, \quad (5.4)$$

$$-(\gamma^2)X_m + (\delta\Omega^2)X_p + \left[-(1+\delta)\Omega^2 + \gamma^2\right]X_a = 0,$$

where X represents the Laplace transform of the displacement with indices for the corresponding masses M, m_p and m_a. $\Delta = \mathcal{L}\{F(t)\}/K$ is the scaled excitation signal in the Laplace domain. It is noted that both equations of motions give identical results when reduced to the idealised IDVA-L2 which corresponds to the case when $\beta = 0$.

The dimensionless parasitic mass β is always coupled with the dimensionless inerter term ($\delta = \frac{b}{m_a}$) as given in Equations 5.3 and 5.4. If δ is big enough than β, the influence of the parasitic mass in the system diminishes as δ in the governing equations always appears as being summed by β. However, adjusting the inertance to eliminate the parasitic effect is not possible since all inertance terms in the governing equations are not coupled with the parasitic mass.

The parasitic mass m_p is defined by the structural mass of the element that creates the parasitic mass effect. It is directly related to the size of the element, while the inertance is obtained by the optimisation. For instance, Table 5.1 gives the selected optimal inertance values from Table 4.3 for a down-milling operation. Assuming the

Table 5.1 Selected optimal design parameters for down-milling operation from Table 4.3.

ζ_m	$\mu = \left(\frac{m_a}{M}\right)$	$\delta = \left(\frac{b}{m_a}\right)$	$\mu\delta = \left(\frac{b}{M}\right)$
0	0.05	0.1056	0.0053
0	0.20	0.3249	0.0650
0.023	0.05	0.1116	0.0056
0.023	0.20	0.3294	0.0659

primary system with a modal mass of 10 kg and damping ratio of 0.023, the parasitic mass of 33 grams corresponds to 5% of the optimal inertance for the mass ratio of 0.2. This value decreases to 2.8 grams as the mass ratio decreases to 0.05. This means even a relatively small structural mass between the elements connected in series (e.g. mass of the connection part between the damper and the terminal of the inerter) presents an influential parasitic mass effect.

The influence of the parasitic mass on the chatter performance of IDVA-L2 can be evaluated from the real part response. Manipulating Equation 5.3 and 5.4 (in Maple symbolic computation software), the dimensionless transfer function for the *icms* and the *icma* cases in Figure 5.1 are written in the following form:

$$\tilde{G}_i = \frac{X_m}{\Delta} \tag{5.5}$$

where i represents either the *icms* or the *icma* case.

The influence of the parasitic mass on the real part response for a mass ratio of 0.05 and structural damping of 0.023 is shown in Figure 5.2. The results are obtained from the design parameter given in Table 4.3. The effects of a parasitic mass of 5% of the inertance are considered for both the *icms* and the *icma* cases. The figure indicates
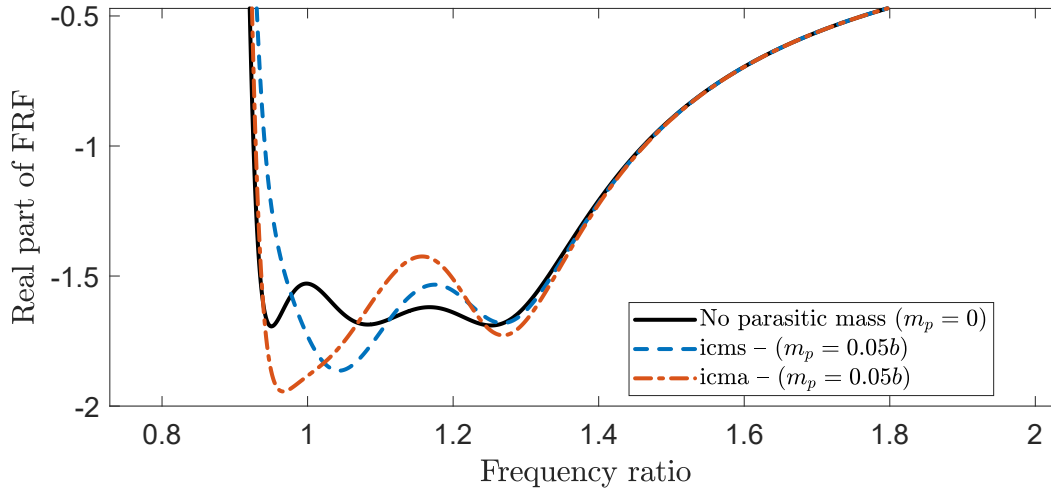
Figure 5.2 A visual example that shows the effect of the parasitic mass on the real part of the response for the *icms* and the *icma* cases. The result for no parasitic mass is obtained from the optimal design parameters considering the idealised IDVA-L2 for the mass ratio of 0.05 and the damping of 0.023. The *icms* and the *icma* are obtained using the optimal design parameters for no parasitic mass but considering a parasitic mass of 5% of the inertance.

that the parasitic mass leads to a detuning effect and decreases the most negative real part values in both cases. It is observed from the figure that the deterioration of the performance is higher in the *icma* case.

5.2.2   Retuning design parameters

Even a small parasitic mass leads to a detuning effect and decreases the cutting stability, as the previous numerical example suggests. In order to avoid the detuning effect induced by a parasitic mass, the mechanical model with the parasitic mass must be employed in tuning the parameters instead using of the idealised model. For the mechanical model presented in Figure 5.1, the design parameters were retuned via SaDE. The objective for the optimisation was the minimisation of the most negative real part, which refers to the same optimisation problem given in Equation 4.8. The real
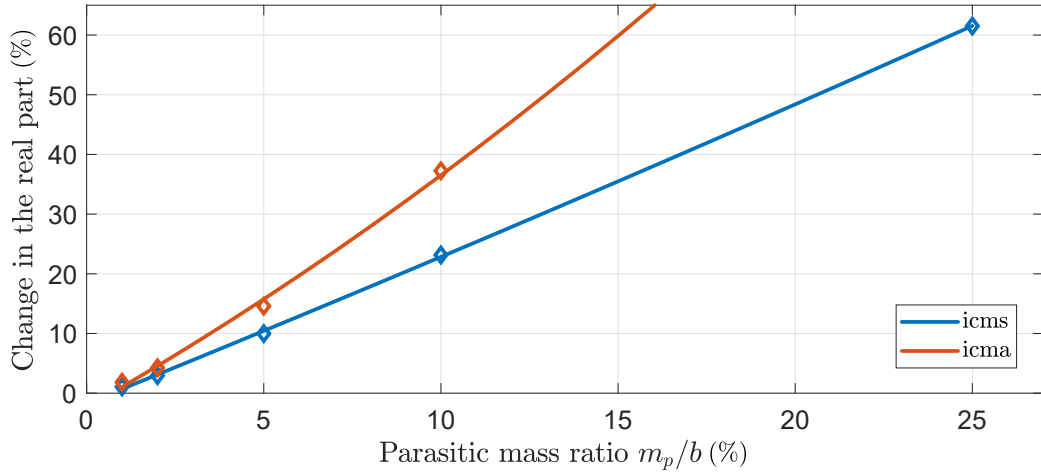
Figure 5.3 Change in the real part of the response from the optimal result for different parasitic mass ratios. The result for no parasitic mass is obtained from the optimal design parameters considering the idealised IDVA-L2 for the mass ratio of 0.05 and the damping of 0.023. The *icms* and the *icma* are obtained using the optimal design parameters for no parasitic mass but different parasitic mass ratios m_p/b.

Table 5.2 Optimal design parameters, where $\beta = m_p/m_a$, for $\mu = 0.05$ and $\zeta_m = 0.023$ after tuning parameters considering the parasitic mass of 5% of the optimal inertance that was obtained for no parasitic mass case as shown in Figure 5.1.

Case	β	γ	ζ	δ	η
No parasitic mass	$-$	1.1045	0.0237	0.1116	0.9403
icms	0.0053	0.9027	0.0236	0.1063	0.9625
icma	0.0058	0.9058	0.0258	0.1166	0.9623

part response was determined from Equation 5.5 and the optimal design parameters found are given in Table 5.2. Figure 5.4 demonstrates the results with the new optimal design parameters. Using the new optimal design parameters, identical real part response to the idealised IDVA-L2 was obtained for both the *icms* and the *icma* cases.

It is important to include the parasitic mass effect, especially for small-scale small-inertance applications as even small parasitic mass can easily lead to a detuning effect. In L2, the parasitic mass effect occurs due to the series-connected element, and a
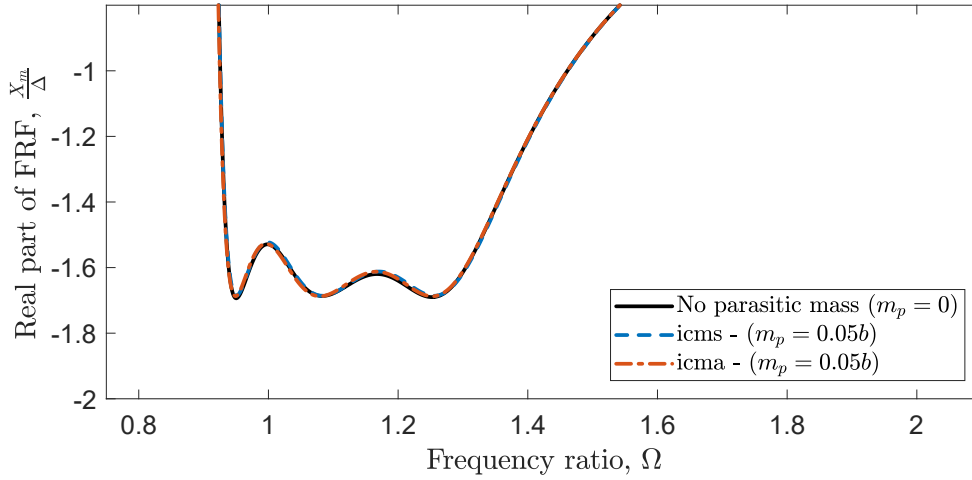
Figure 5.4 Real part responses of the *icms* and the *icma* after their re-tuning considering the parasitic mass.

more accurate model should reflect a mass between elements in series. It was observed from the analysis that the reason for the performance loss is not the L2 with parasitic mass but the change in the optimal design parameters. Identical performance to the idealised L2 was achieved by updating the optimal design parameters.

5.3   Model update with complex stiffness

The previous section presented results that showed that the implementation of the idealised L2 can be impractical due to the parasitic mass effect. Therefore, the mechanical model was updated by considering the parasitic mass and the tuning parameters were obtained using the updated model. Similar consideration for the design of the damping in the L2 in practice is presented in this section. A hysteretic gel damper, which is modelled as a complex stiffness, is considered to be employed for the physical realisation of the spring-damper arrangement. In that way, the inner stiffness element and the damping can be easily implemented as one component. The

implementation and the dynamic properties of the gel will be presented in detail in Section 5.5. This section further updates the mechanical model with the parasitic mass in the previous section employing a complex stiffness as the inner spring-damping arrangement. It evaluates the update model's performance in terms of stability of milling operation by comparing with the idealised L2 and the L2 with the parasitic mass. To make the notation clearer, the L2 with parasitic mass in the previous section will be named D1. The L2 involving both the parasitic mass and hysteretic damping will be named D2, while the idealised L2 will be called just L2 in the rest of the thesis.

The dynamic behaviour of the gel damper can be modelled with the complex stiffness $k(1 + j\eta)$, where η is the loss factor and $j = \sqrt{-1}$. Assuming time and frequency invariant damping coefficient, the force dissipated through the hysteretic damping $(k\eta)$ is independent of the forcing frequency while the force dissipated through viscous damping $(c\omega)$ is proportional to the forcing frequency. Although equivalent viscous damping can be represent the loss factor for a certain frequency, this method will lose its effectiveness for applications with a wide range of working frequency bands. Chatter frequency varies with the changing spindle speed in cutting operations. Hence, the optimal loss factor will be directly obtained by SaDE instead of using equivalent viscous damping.

A schematic representation of the L2 with complex stiffness and parasitic mass (named D2 in this study) is illustrated in Figure 5.5. The equations of motion of the updated mechanical model with the complex stiffness are written as

$$
\begin{aligned}
&M\ddot{x}_m(t) + C\dot{x}_m(t) + Kx_m(t) - b\big(\ddot{x}_p(t) - \ddot{x}_m(t)\big) - k_o\big(x_a(t) - x_m(t)\big) = F(t), \\
&m_p\ddot{x}_p(t) + b\big(\ddot{x}_p(t) - \ddot{x}_m(t)\big) - k_i\big(1 + j\eta\big)\big(x_a(t) - x_p(t)\big) = 0, \\
&m_a\ddot{x}_a(t) + k_o\big(x_a(t) - x_m(t)\big) + k_i\big(1 + j\eta\big)(x_a(t) - x_p(t)) = 0.
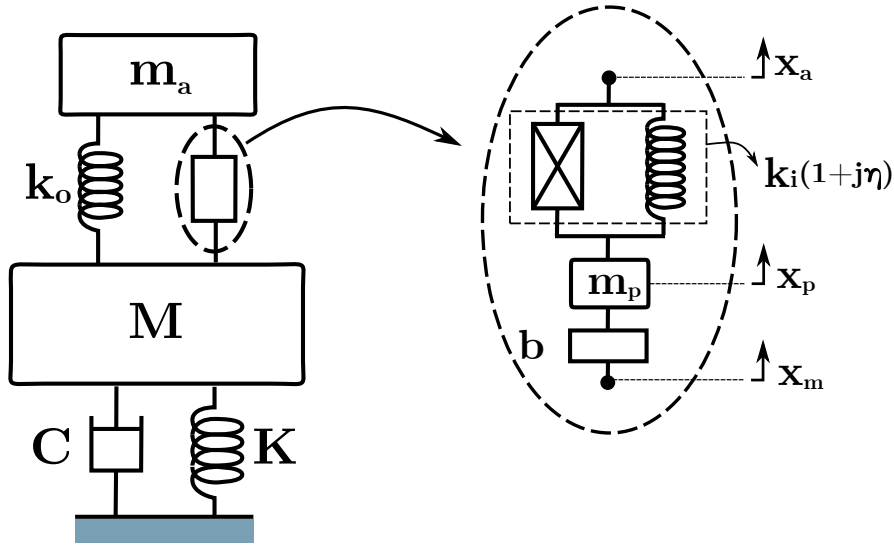\end{aligned}
\tag{5.6}
$$

Figure 5.5 Updated mechanical model with both parasitic mass and complex stiffness which employs loss factor (η) instead of viscous damping.

where k_i and η are the stiffness of the gel damper and the loss factor, respectively. It should be noted that the loss factor is a dimensionless coefficient which is the measure of the level of damping dissipated at each cycle. Using the dimensionless design parameter defined in Equation 4.4 and parasitic-mass-to-auxiliary-mass ratio $\beta = m_p/m_a$, taking the Laplace transform and replacing $s = j\omega$, the equations of motion with the dimensionless parameters are derived as

$$[(-1 - \delta\mu)\Omega^2 + j2\zeta_m\Omega + 1 + \gamma^2\mu]X_m + (\delta\mu\Omega^2)X_p - (\gamma^2\mu)X_a = \Delta,$$

$$(\delta\Omega^2)X_m + [(-\delta - \beta)\Omega^2 + \alpha^2\gamma^2\delta(1 + j\eta)]X_p - [\alpha^2\gamma^2\delta(1 + j\eta)]X_a = 0, \qquad (5.7)$$

$$(-\gamma^2)X_m - [\alpha^2\gamma^2\delta(1 + j\eta)]X_p + [-\Omega^2 + \gamma^2 + \alpha^2\gamma^2\delta(1 + j\eta)]X_a = 0.$$

where $\Delta = \mathcal{L}\{F(t)\}/K$ is the scaled excitation signal in the Laplace domain.

Table 5.3 Optimal dimensionless design parameters of D2 in comparison with optimal design parameters for the TMD, L2 and D1. All parameters are obtained for $\mu = 0.5$ and $\zeta = 0.023$.

	β	γ	α	δ	ζ_a	η
TMD	–	1.0517	–	–	0.1356	–
IDVA-L2	–	1.1045	0.9403	0.1116	0.0237	–
IDVA-D1	0.05	1.1361	1.1999	0.0704	0.0253	–
IDVA-D2	0.05	1.1214	1.1447	0.0803	–	0.5385

Using Maple symbolic computation software, the dimensionless transfer function is written in the form:

$$\tilde{G}_i = \frac{X_m}{\Delta} \tag{5.8}$$

where i stands for IDVA-D2.

For a down-milling operation, the optimisation's objective is to maximise the most negative real part of the FRF. For $\mu = 0.05$, $\beta = 0.05$ and $\zeta_m = 0.023$, the optimal design parameters obtained via SaDE are given in Table 5.3 in comparison with the optimal design parameters for a classical TMD, IDVA-L2 and IDVA-D1. Using the optimal design parameters in Table 5.3, the real part responses are shown in Figure 5.6. Assuming a down-milling operation with the same milling parameters in Table 4.2, the stability lobe diagrams obtained from the real parts of the responses in Figure 5.6 are also demonstrated in Figure 5.7. All three layouts: L2, D1 and D2, showed identical stability performance.

The L2 has evolved the D1 with consideration of the parasitic mass, and then the D2 replacing the viscous damping with the hysteretic damping. D2 is more feasible in practice than either L2 or D1 since it considers both the parasitic mass effect and

the damping solution, which offers a more compact physical design and easiness in its implementation. Furthermore, it shows no performance loss in the chatter stability in terms of the absolute stability of the milling operation (a_{lim}). The following sections will conduct physical design studies of the absorber components, including the inerter and the gel damper.
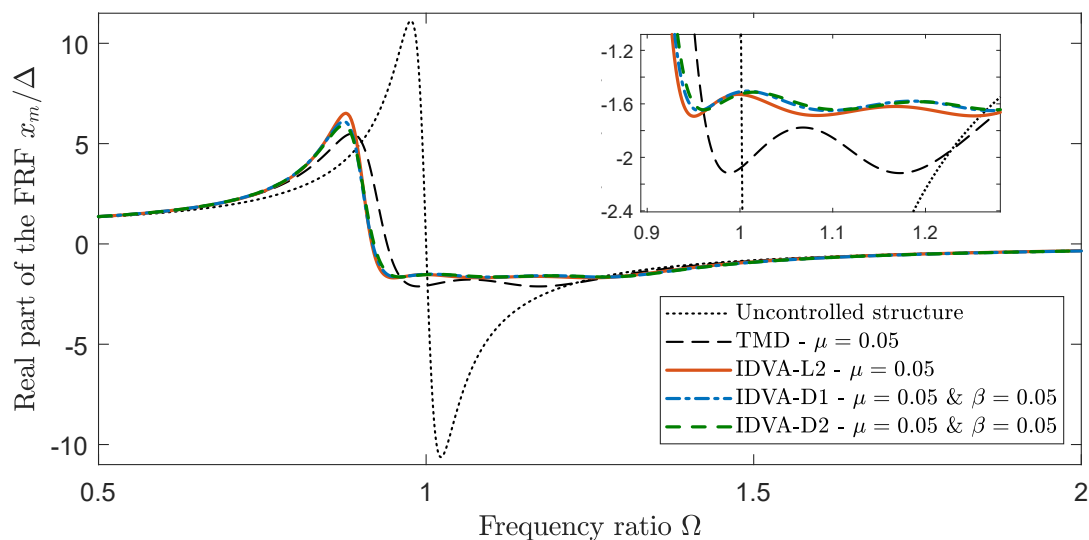

Figure 5.6 Negative real part of the FRFs of D2 in comparison with the uncontrolled system response, the TMD, L2 and D1 as a performance indicator of the chatter stability. The design parameters in Table 5.3 were used for the controlled systems.
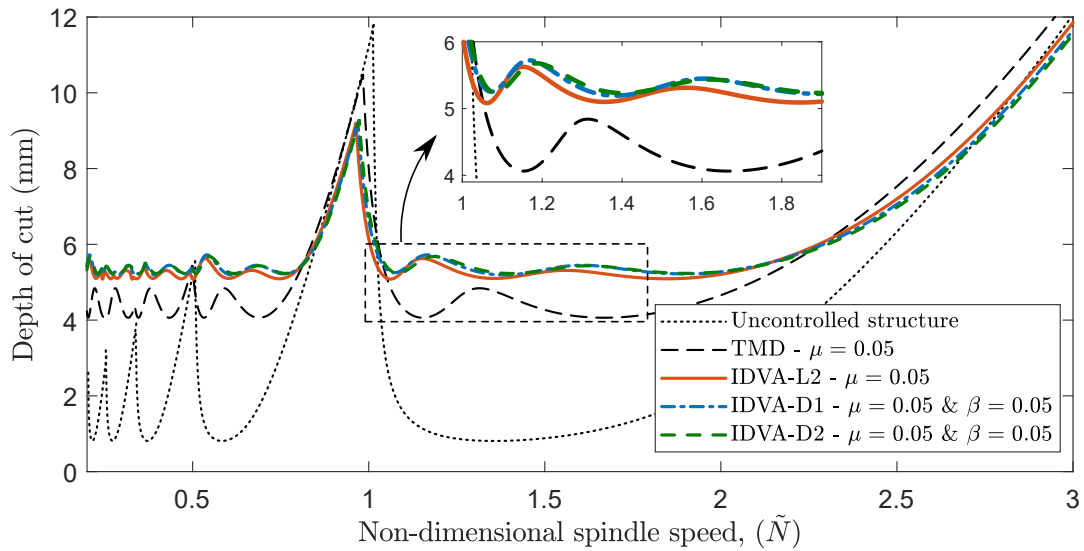
Figure 5.7 Stability performance of D2 in the stability lobe diagram of a down-milling operation with 4 flutes and half-immersion in comparison with the uncontrolled system response, the TMD, L2 and D1.

5.4   Inerter design

The most important part of the absorber in terms of its design and manufacture is
the inerter since it is a relatively new mechanical device and has a relatively more
complex structure than the other conventional components such as spring and damper.
This section aims to achieve a design of inerter that can be applicable to milling
operations. It thereby presents a pivoted-bar inerter with living hinges, including
design studies that investigate the effect of the stiffness of the living hinges on the
inerter's performance and the fatigue life cycle of the inerter.

The inerter concept was introduced by Smith [4] with the rack-pinion inerter as an
example of the physical realisation of the inerter device. Following that, different types
of inerter including ball-screw inerter [198, 199] and helical fluid inerters [201–203] were
further proposed as possible realisations of the inerter. However, most of the inerters
proposed as yet have been developed for relatively large structural applications. Using
of these inerters in small-size applications could be ineffective since the friction and
backlash between the mechanical parts and flow losses in fluid-based inerters could
become an important issue as the size of the mechanical device shrinks. Therefore, the
implementation of one of these inerters into a milling operation as part of localised
addition would not be feasible.

To the author's knowledge, the only inerter device that is applicable into small-scale
applications was proposed by John and Wagg [207], which is a pivoted flywheel inerter
with living hinges. Inspiring the DAVI of Flannelly [208], they developed their inerter
device by introducing a rotating disc as a flywheel instead of the lever-arm mechanism
in the DAVI and rearranging the pivot position in a way that balanced forces are
generated as expected from an inerter. They also added living hinges in the pivots

to eliminate friction. The inerter design presented in this section is the synthesis of the DAVI and the living-hinge inerter of John and Wagg [207]. A pivoted-bar with additional lumped masses is arranged so that it acts as an inerter. The additional lumped masses placed to the bar provides easy adjustment of the inertance even after its establishment.

The DAVI works as an isolator to suppress the vibration caused by a base excitation. It consists of a lever-arm and an auxiliary mass connected to the end of the lever-arm as shown in Figure 5.8a. It can produce unbalanced forces as it was not specifically designed to behave as an inerter. The inerter of John and Wagg [207] uses a rotational disc as a flywheel shown in Figure 5.8b. The relative acceleration between the pivot points is transformed into a rotational acceleration of the flywheel and therefore, an inertial force proportional to the relative acceleration is produced. The factor of the relative acceleration, named inertance, is determined as

$$b = \frac{I}{l_a^2} \tag{5.9}$$

where l_a is the distance between the pivots, and I is the moment of inertia of the flywheel disc.

Inerters are inherently designed to amplify the inertial effect. For instance, the ball-screw inerter in [285] is able to produce $60 - 240$ kg inertance with its structural mass of 1 kg. Similarly, the living-hinge inerter [207] succeeded at producing almost six times amplification of the inerter device's mass. However, the optimal inertance values for IDVA can be very small for a small mass ratio, as shown in the optimisation results in Chapter 4. If the inerter device with a disc flywheel is considered to have small inertance, either the moment of the inertia I should be small or the distance between
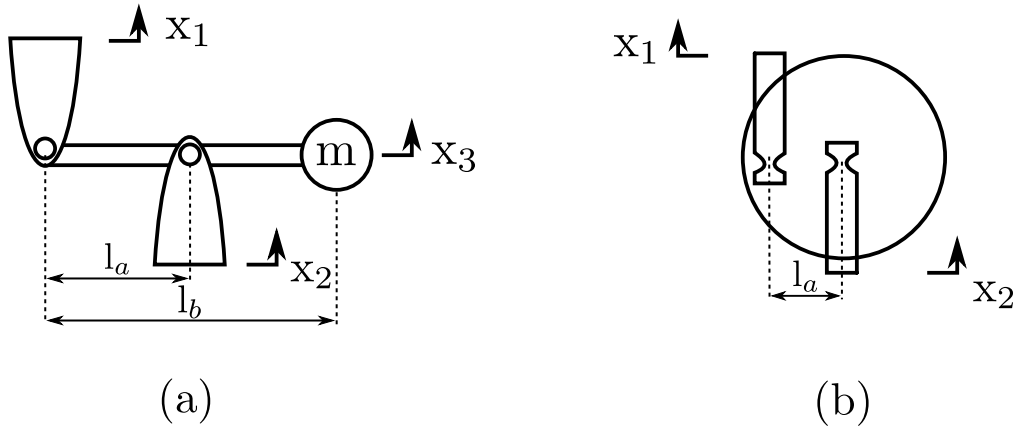
Figure 5.8 Schematic views of (a) the DAVI of Flannelly [208], and (b) the living-hinge inerter proposed by John and Wagg [207].

the pivot points l_a should be chosen largely as Equation 5.9 suggests. However, the maximum l_a is limited to the radius of the disc. This means that if the radius of the flywheel disc is getting smaller to reduce the moment of inertia to have small inertance, l_a is also getting smaller, which increases the inertance. The minimum inertance of an inerter device with the disc flywheel is $\frac{m_{disc}}{2}$ taking the moment of inertia $I = \frac{1}{2}m_{disc}r^2$ and $l_a = r^2$, where r and m_{disc} are the radius of the disc and the mass of the disc. It can be possible to obtain a small inertance by choosing a small radius but this could lead to very limited space on the flywheel for the connection of the living hinges.

A bar design can be more favourable in terms of having a smaller moment of inertia and their assembly to the other elements. The moment of the inertia of a bar rotating around its center of mass is $I = \frac{1}{12}m_{bar}l_{bar}^2$ and the inertance of the inerter device with a bar flywheel becomes $\frac{m_{bar}}{3}$ considering a distance between the pivots $l_a = \frac{l_{bar}}{2}$. A bar-type flywheel has a smaller moment of inertia than the disc type flywheel for the same structural mass of the flywheels, assuming that both flywheels are homogeneous and rotate about their centre of mass. From the above discussion, it is considered that the pivoted-bar design is preferable for the inerter device with small inertance.
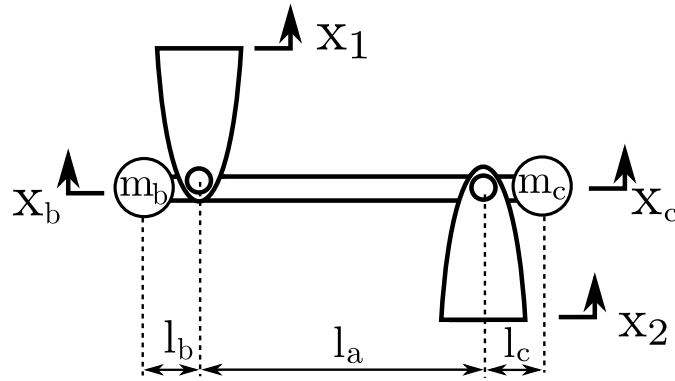
Figure 5.9 Generic model of a pivoted-bar with two additional lumped masses m_b and m_c where l_b and l_c are the distances of the additional masses to the closest pivot, and l_a is the distance between two pivots. The pivoted-bar freely rotates around its pivots.

5.4.1 Pivoted-bar design as an inerter

The position of the pivots along the bar is the key parameter to enable a pivoted-bar that acts as an inerter. For the investigation of the different arrangements, a generic model of the pivoted-bar, on which different locations of the pivots and additional two small masses for fine tuning can be set, is given in Figure 5.9. The pivoted-bar can freely rotate around the pivots. It is assumed that the pivoted-bar consists of all inertial elements (lumped masses and a rigid bar). The equations of motion are derived by using Lagrage's equation to find the inertial terms in the system, and they are classified as the relative inertial and the non-relative inertial terms. The relative inertial term refers to the factor of the relative acceleration term that exists in both equations of the motion. The rest of the terms (e.g. factors of $\ddot{x}_1$, $\ddot{x}_2$ and $\ddot{x}_1 + \ddot{x}_2$) are named non-relative inertial term. As an ideal inerter produces equal but opposite forces at its terminals, the aim is to eliminate or minimise the non-relative inertance terms in the equations of motion to have a system acting as close to a pure inerter as possible.

Related parameters are shown in Figure 5.9 where m_b, m_c and m_{bar} are the masses added to the leftmost and the rightmost points of the bar and the mass of the inerter bar, respectively. l_b, l_c and l_a are the distances between the first pivot and m_b, the second pivot and m_c and the two pivots. x_1 and x_2 are the displacements of the first pivot and the second pivot. The displacements of m_b and m_c and the angular displacement of the inerter bar are defined as x_b, x_c and θ, respectively. The masses of the legs connected to the pivots are neglected.

Assuming that the bar is homogeneous, the kinetic energy of the system depicted in Figure 5.9 can be written as

$$T = \frac{1}{2}m_b\dot{x}_b^2 + \frac{1}{2}m_c\dot{x}_c^2 + \frac{1}{2}I\dot{\theta}^2 + \frac{1}{2}m_{bar}\dot{x}_{cm}^2 \tag{5.10}$$

where x_{cm} is the displacement of the centre of the inerter bar. I is the moment of inertia of the bar. x_3, x_4, θ and x_{cm} can be described with x_1 and x_2 by assuming the small-angle approximation in the inerter bar as

$$x_c = x_2(\frac{l_a + l_c}{l_a}) - x_1(\frac{l_c}{l_a}), \qquad x_b = x_1(\frac{l_a + l_b}{l_a}) - x_2(\frac{l_b}{l_a}),$$
$$\theta = \frac{x_1 - x_2}{l_a}, \qquad x_{cm} = \frac{x_1}{l_a}(l_a - \frac{l_{bar}}{2} + l_b) + \frac{x_2}{l_a}(l_a - \frac{l_{bar}}{2} + l_c) \tag{5.11}$$

where l_{bar} is the length of the bar.

Substituting the first derivative of the expressions in Equation 5.11 into Equation 5.10 yields:

$$
\begin{aligned}
T ={}& \frac{1}{2}m_b[(1+\beta_b)^2\dot{x}_1^2 + \beta_b^2\dot{x}_2^2 - 2\beta_b(1+\beta_b)\dot{x}_1\dot{x}_2] \\
&+ \frac{1}{2}m_c[\beta_c^2\dot{x}_1^2 + (1+\beta_c)^2\dot{x}_2^2 - 2\beta_c(1+\beta_c)\dot{x}_1\dot{x}_2] \\
&+ \frac{I}{2l_a^2}[\dot{x}_1^2 + \dot{x}_2^2 - 2\dot{x}_1\dot{x}_2] \\
&+ \frac{1}{2}m_{bar}[\dot{x}_1^2(1-\beta_a+\beta_b)^2 + \dot{x}_2^2(1-\beta_a+\beta_c)^2 + 2(1-\beta_a+\beta_b)(1-\beta_a+\beta_c)\dot{x}_1\dot{x}_2]
\end{aligned}
$$

$$(5.12)$$

where $\beta_a = l_{bar}/2l_a$, $\beta_b = l_b/l_a$ and $\beta_c = l_c/l_a$. There is no potential energy, V, in the system as it consists of only inertial elements. The Lagrange's equation for the pivoted-bar system is written as

$$
\frac{d}{dt}\frac{\partial T}{\partial \dot{q}_n} - \frac{\partial T}{\partial q_n} + \frac{\partial V}{\partial q_n} = Q_n \tag{5.13}
$$

where $V = 0$ and $Q_n = 0$ as there are no dissipative or external forces acting on the system. n represents the number of degrees of freedom. q_n is the generalised coordinates, which are x_1 and x_2 for the system in Figure 5.9. Therefore, two equations of motion are obtained with respect to x_1 and x_2. Substituting the kinetic energy T

and the potential energy V into Equation 5.13, the equations of motion are found as:

With respect to x_1:

$$m_c[\beta_c^2\ddot{x}_1 - \beta_c(1+\beta_c)\ddot{x}_2] + m_b[(1+\beta_b)^2\ddot{x}_1 - \beta_b(1+\beta_b)\ddot{x}_2] + \frac{I}{l_a^2}(\ddot{x}_1 - \ddot{x}_2)$$
$$+ m_{bar}[(1-\beta_a+\beta_b)^2\ddot{x}_1 + (1-\beta_a+\beta_b)(1-\beta_a+\beta_c)\ddot{x}_2] = 0$$

(5.14a)

With respect to x_2:

$$m_c[(1+\beta_c)^2\ddot{x}_2 - \beta_c(1+\beta_c)\ddot{x}_1] + m_b[\beta_b^2\ddot{x}_2 - \beta_b(1+\beta_b)\ddot{x}_1] + \frac{I}{l_a^2}(\ddot{x}_2 - \ddot{x}_1)$$
$$+ m_{bar}[(1-\beta_a+\beta_c)^2\ddot{x}_2 + (1-\beta_a+\beta_b)(1-\beta_a+\beta_c)\ddot{x}_1] = 0$$

(5.14b)

where m_{bar} is the mass of the inerter bar and I is the moment of inertia of the pivoted-bar, which is given $\frac{1}{12}m_{bar}l_{bar}^2$.

5.4.1.1 An example arrangement acting as an inerter

Equation 5.14 will be used to examine different arrangement of the pivoted-bar but an example is first presented to explain the relative inertial term and non-relative inertial term clearly. Assuming that one pivot is at the centre of the mass ($l_b = \frac{l_{bar}}{2}$) while the other pivot can be positioned freely between the centre and the rightmost end ($l_c = \frac{l_{bar}}{2} - l_a$), and two equal lumped masses of m added two end of the bar in Figure 5.9, Equations 5.14a and 5.14b yield:

$$\left[2\left(\frac{l_{bar}}{2l_a}\right)^2 m + \frac{I}{l_a^2}\right](\ddot{x}_1 - \ddot{x}_2) + (m_{bar} + 2m)\ddot{x}_1 = 0$$

(5.15a)

$$\left[2\left(\frac{l_{bar}}{2l_a}\right)^2 m + \frac{I}{l_a^2}\right](\ddot{x}_2 - \ddot{x}_1) = 0$$

(5.15b)

$m_{bar} + 2m$ is the total mass of the pivoted-bar with the two additional lumped masses (i.e. inerter). Equation 5.15a, which is related to motion with respect to x_1, consists of two terms: the relative inertial term, which expresses the inerter behaviour and the term proportional to $\ddot{x}_1$ (non-relative inertial term), which expresses the translational motion of the total system (rigid body motion). It should be noted that the rigid body motion is proportional to $\ddot{x}_1$ since the system only moves translationally with the motion of the pivot at the centre of the mass. Equation 5.15b, on the other hand, has only the relative term. Therefore, the relative inertial term defines the inertance of the pivoted-bar as

$$b = 2\left(\frac{l_{bar}}{2l_a}\right)^2 m + \frac{I}{l_a^2} \tag{5.16}$$

The form of both equations of motion is the same as the equations of motion of an inerter. The rigid body motion is neglected in an ideal inerter as the inertance of the inerter is generally much larger than the structural mass of the inerter ($b >> m_{bar} + 2m$). The inertance is proportional to the moment of the inertia of the bar and inversely proportinal to the square of the distance between the pivots. The inertance can also be adjusted by changing m in Equation 5.16, which is easily done by adding equal lumped masses to the ends of the bar. Equation 5.16 yields the same formula as the living-hinge inerter in [207] for $m = 0$.

5.4.1.2 Consideration of small inertance

One of the key criteria in the design of an inerter is to produce small inertance due to the small optimal inertance obtained in Chapter 4. From Equation 5.16, the minimum inertance can be achieved with minimum possible I and maximum possible l_a for $m = 0$. Keeping in the mind that the optimal inertance can be very small for small mass ratios, and a very small value of I is difficult due to the manufacturing limitations.

Therefore, considering the maximum possible $l_a = \frac{l_{bar}}{l_2}$ and the moment of inertia of the bar $I = \frac{1}{12}m_{bar}l_{bar}^2$, the minimum inertance is written:

$$b = \frac{m_{bar}}{3} + 2m \tag{5.17}$$

where $m = 0$ in theory but it is still shown in the formula as it might be needed in even small inertance for fine tuning.

The inertance found in Equation 5.17 is smaller the total mass of the pivoted bar $(m_{bar} + 2m)$ and thus, the non-relative inertial term in Equation 5.15a cannot be neglected. Although this non-relative term looks problematic when the inerter is analysed without attachment, it becomes negligible as the whole control system is considered. If the pivot in the centre of the mass of the pivoted-bar is connected to the primary system, the non-relative inertial term (mass of the inerter) acts with the main mass, M, as shown in Figure 5.10a. It should be noted that the mass of the inerter is directly dependent on the inertance magnitude (Equation 5.16), and the optimal dimensionless design parameters of L2 ensures that the optimal inertance values for small mass ratios are always much smaller than the main mass $M >> m_{bar} + 2m$, as discussed in Chapter 4. Therefore, the non-relative inertial term can be now regarded as negligible.

For a numerical example, a primary system with a modal mass of 1 kg is assumed. The optimal dimensionless inertance-to-mass ratio $\delta = 0.0267$, which equals b/m_a, is given in Table 4.3 for $\mu = 0.05$ and $\zeta_m = 0.023$. Ignoring the additional lumped mass m, the mass of the inerter (three times the inertance) is found to be just 0.004 kg, which is even smaller than 1% of the primary mass. This value slightly increases for

smaller structural damping. For the same system but $\zeta_m = 0$, the mass of the inerter becomes 0.016 kg, which is still smaller than 2% of the primary mass.
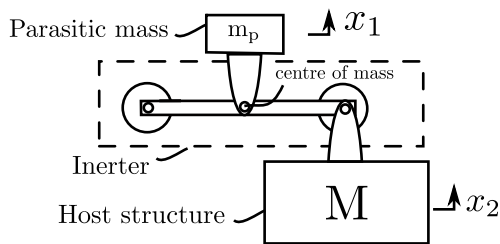
However, if the pivoted-bar is connected to the host structure from the other pivot as demonstrated in Figure 5.10b, the mass of the inerter increases the parasitic mass effect and escalates the detuning effect. Even in this scenario, chatter performance could be improved to some extend by retuning the parameters. However, this type of connection is to be avoided since even fine tuning of inertance by adding small mass requires a new optimisation due to the increase in the parasitic mass with the additional masses.
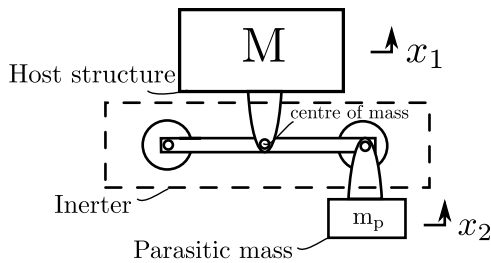
Equations of motion:

$$b\big(\ddot{x}_1 - \ddot{x}_2\big) + \big(M + m_{bar} + 2m\big)\ddot{x}_1 = 0$$
$$b\big(\ddot{x}_2 - \ddot{x}_1\big) + m_p\ddot{x}_2 = 0$$

(a)

Equations of motion:

$$b\big(\ddot{x}_1 - \ddot{x}_2\big) + \big(m_p + m_{bar} + 2m\big)\ddot{x}_1 = 0$$
$$b\big(\ddot{x}_2 - \ddot{x}_1\big) + M\ddot{x}_2 = 0$$

(b)

Figure 5.10 Connection arrangements of the inerter and the related equations of motions. The mass of the inerter is included in the mass of the host structure if the inerter is mounted to the host structure from the pivot at the centre of the mass in (a). If the inerter is connected from the other pivot, the mass of the inerter increases the parasitic mass effect by being added to the existed parasitic mass m_p in the system in (b).

5.4.1.3   Analysis of different arrangements of the pivoted-bar

Six different arrangements of the pivoted-bar are demonstrated in Figure 5.11 in order to find similar behaviour as in the above example. Using Equations 5.14a and 5.14b, the equations of motion of each arrangement were obtained and their inertial terms are presented in Table 5.4. The arrangements discussed above are illustrated in Figures 5.11a (first example) and 5.11d (example with small inertance). The results in Table 5.4 states that the three arrangements in Figures 5.11a, 5.11c and 5.11d have the relative inertial term (factor of relative acceleration) and the non-relative inertial term proportional only to $\ddot{x}_1$. Only arrangements where the first pivot is at centre of the mass of the total system consisting of the pivoted-bar and the additional lumped mass have this non-relative inertial term. Each of the three arrangements can be a candidate for the inerter design. For the other arrangement, the translational inertia of the total system is distributed over two pivots and the non-relative inertial terms in the equation of motion with respect to x_1 of these arrangements involves the factors of both $\ddot{x}_1$ and $\ddot{x}_2$. Thus, these arrangements cannot be employed as an inerter.
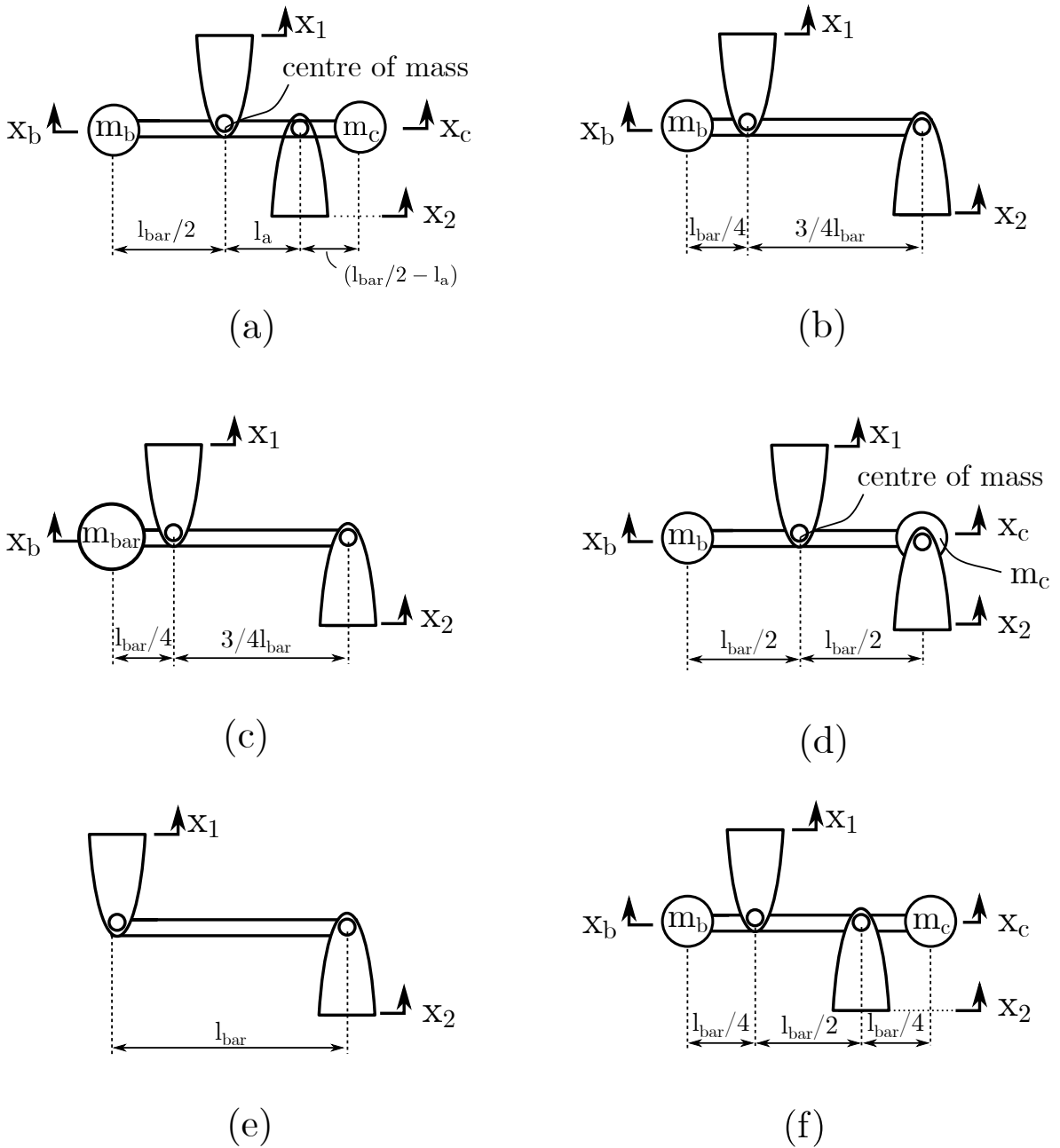
Figure 5.11 Different arrangements of the pivoted-bar with the additional lumped mass which can be derived from the generic model. Two pivots are connected from the centre of mass of the homogeneous bar in (a) and (d). (d) is a special case of (a) that considered for small inertance. (b) is the DAVI concept[208] if the second pivot is grounded. (c) is the same as (b) but the centre of the mass of the total system consisting of the pivoted-bar and the additional lumped mass coincides with one of two pivots. There are two additional lumped masses considered at the ends of the pivoted-bar in (d) and (f), while no additional lumped mass is considered in (e).

Table 5.4 Relative inertial and non-relative inertial terms for six arrangements of the pivoted-bar given in Figure 5.11, where $\beta_a = \frac{l_{bar}}{2l_a}$, $\beta_b = \frac{l_b}{l_a}$ and $\beta_c = \frac{l_c}{l_a}$.

Pivoted-bar arrangement	m_b	m_c	β_a	β_b	β_c	Relative inertial term*	Non-relative inertial term in Eq. 1.14a	Non-relative inertial term in Eq. 1.14b
Figure 5.11a	m	m	$\frac{l_{bar}}{2l_a}$	$\frac{l_{bar}}{2l_a}$	$\left(\frac{l_{bar}}{2l_a}-1\right)$	$\frac{I}{l_a^2} + 2\left(\frac{l_{bar}}{2l_a}\right)^2 m$	$(2m + m_{bar})\ddot{x}_1$	—
Figure 5.11b	m	0	0	$\frac{1}{3}$	$\frac{1}{3}$	$\frac{I}{l_a^2} + \frac{m}{9}$	$\left(\frac{2}{9}m_{bar} - \frac{1}{3}m\right)\ddot{x}_1 + \frac{m_{bar}}{9}\ddot{x}_2$	$\left(\frac{4}{9}m_{bar} - \frac{5}{3}m\right)\ddot{x}_1$ $+\left(\frac{2}{9}m_{bar} - \frac{1}{3}m\right)\ddot{x}_2$
Figure 5.11c	m_{bar}	0	$\frac{2}{3}$	$\frac{1}{3}$	0	$\frac{I}{l_a^2} + \frac{2}{9}m_{bar}$	$2m_{bar}\ddot{x}_1$	—
Figure 5.11d	m	m	1	1	0	$\frac{I}{l_a^2} + 2m$	$(2m + m_{bar})\ddot{x}_1$	—
Figure 5.11e	0	0	$\frac{1}{2}$	0	0	$\frac{I}{l_a^2}$	$\frac{1}{4}m_{bar}(\ddot{x}_1 + \ddot{x}_2)$	$\frac{1}{4}m_{bar}(\ddot{x}_1 + \ddot{x}_2)$
Figure 5.11f	m	m	1	$\frac{1}{2}$	$\frac{1}{2}$	$\frac{I}{l_a^2} + \frac{3}{2}m$	$m\ddot{x}_1 + \frac{1}{4}m_{bar}(\ddot{x}_1 + \ddot{x}_2)$	$m\ddot{x}_2 + \frac{1}{4}m_{bar}(\ddot{x}_1 + \ddot{x}_2)$

*Relative inertial terms are the factor of relative acceleration, $(\ddot{x}_1 - \ddot{x}_2)$ or $(\ddot{x}_2 - \ddot{x}_1)$, in Equations 5.14a and 5.14b.

Among arrangements, the arrangement in Figure 5.11d was chosen as the design of the inerter device due to the advantages of being capable of producing small inertance and fine tuning property. Its inertance is already derived in Equation 5.17 as

$$b = \frac{m_{bar}}{3} + 2m \tag{5.18}$$

Important points of the chosen pivoted-bar arrangement are listed following:

- *Acting as an inerter:* Although there is a non-relative inertial term proportional to the acceleration of the centre of the mass of the pivoted-bar, this term is negligible if the inerter is connected to the host structure from the pivot at the centre.

- *Generating small inertance:* One of the design objectives of the inerter is to produce small inertance due to the optimal inertance obtained from the optimisation. This can be achieved with the proposed arrangement.

- *Simple fine tuning of the inertance:* The inertance can be adjusted by simply placing two equal additional masses at the ends of the pivoted-bar. It allows the fine tuning of inertance after its establishment. This can be very helpful to eliminate performance loss due to manufacturing errors and uncertainties stemming from the primary system or the other components of the absorber.

It has been shown that the pivoted-bar in Figure 5.11d fulfils the requirements of the inerter employed in D2 to improve the chatter resistance of a milling operation. Next, the physical design of the pivoted-bar with flexure hinges will be presented and tested in the next section.
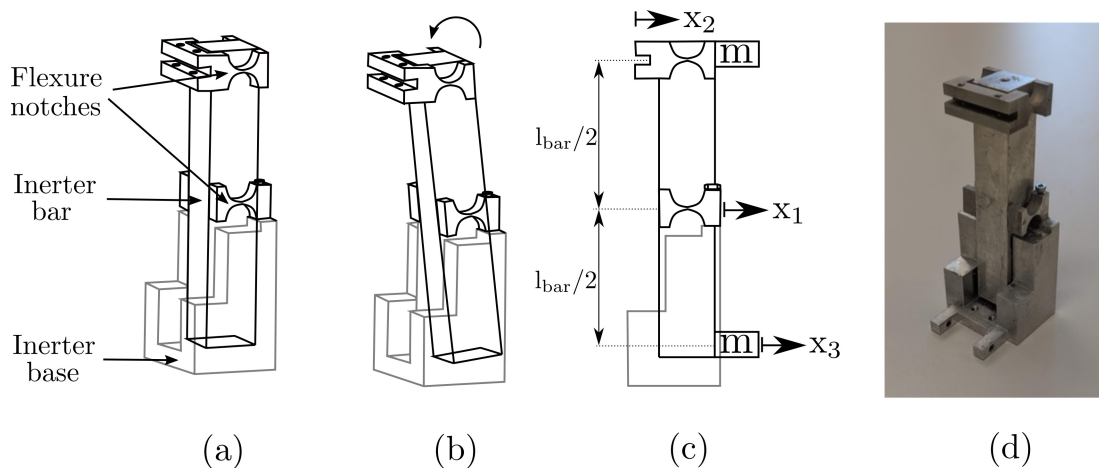
Figure 5.12 Physical realisation of the pivoted-bar as an inerter consisting of the inerter bar, flexural-hinges and the inerter base. The schematic views of the inerter are illustrated in (a) the equilibrium position and (b) rotating. The additional lumped masses for fine tuning is presented with the side view in (c). The manufactured prototype is given in (d).

5.4.2   Physical design and the test of the inerter

The pivoted-bar arrangement chosen as the inerter desing is given in in Figure 5.11a. The bar is pivoted from one of its two ends and the middle of the homogeneous inerter bar with two additional masses at the ends of the bar. The flexure notches as living hinges as shown in Figure 5.12a eliminates friction and provides low stiffness. They allow the inerter bar to rotates around only one axis as shown in Figure 5.12b. The inertance of the inerter is initially set from the mass of the inerter bar m_{bar}. After that, the fine tuning of the inertance is possible by altering the additional two equal masses at both ends of the bar as illustrated in Figure 5.12c.

For the physical parameters in Table 5.5, an aluminium inerter device was manufactured as illustrated in Figure 5.12d. It was experimentally tested to obtain dynamic properties. If the inerter is fixed from one terminal, the force generated by an ideal inerter is the function of the acceleration of the free terminal. In order to evaluate the inertance, the

Table 5.5 Physical properties of the pivoted-bar

ρ (kg/m^3)	Area (m^2)	l_a (m)	l_{bar} (m)	m_{bar} (kg)
2700	0.015 x 0.015	0.040	0.080	0.0486

inerter device was fixed from the inerter base and excited from its free terminal (upper terminal in Figure 5.12d) with an impact hammer (Dytran 5800B2). The accelerance response of the same terminal was measured by an accelerometer type PCB 3553B18 with a mass of 2 grams. The measured inertance was the sum of the inertance of the inerter and the mass of the accelerometer as the inerter device was fixed from the inerter base. The inertance was determined by taking the inverse of the accelerance since inertance is defined as

$$b = \frac{F}{\ddot{x}} \tag{5.19}$$

where $\ddot{x}$ is the acceleration of the upper terminal of the inerter and F is the applied force from the same terminal. The experiment was conducted with different additional masses used for fine tuning. The measured inertances were normalised by subtracting the mass of the accelerometer. The inertance values are presented in Figure 5.13. The intended inertance value obtained from Equation 5.18 is given with dashed line for each test.

The experimental results showed that the pivoted-bar succeeded the intended inertance value for frequencies larger than 80 Hz for each additional mass despite small fluctuations. The frequency band below 80 Hz, where the inertance varies, corresponds to resonance region of the pivoted bar occurring due to the stiffness of the flexural notch. Even though resonance region cannot be entirely eliminated as zero stiffness of the flexural notch is not possible, the natural frequency of the inerter can be as low as almost zero with a flexural notch with very small stiffness. However, this can
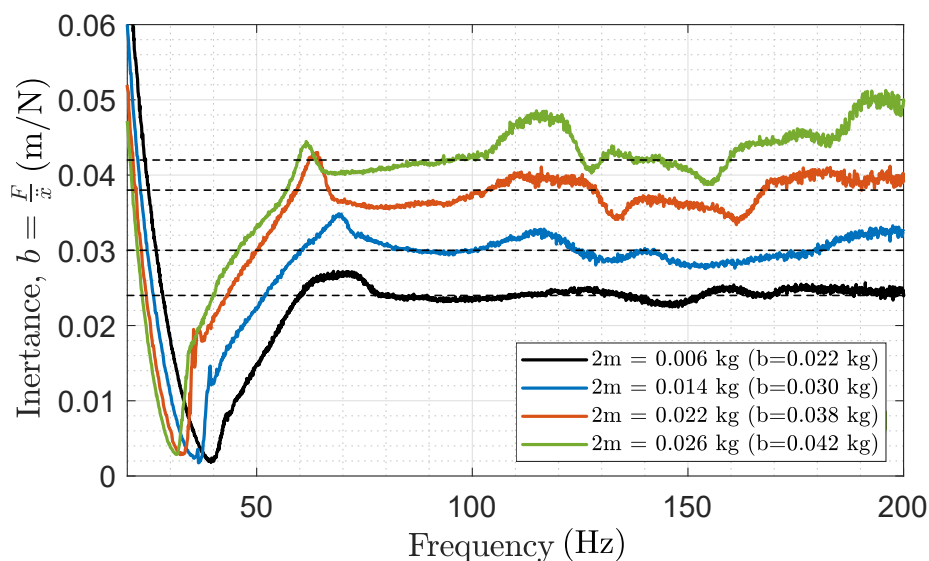
Figure 5.13 Experimental inertance of the inerter obtained for different additional lumped masses. The inerter was tested by fixing from the lower flexure via inerter base and exciting the upper flexure with an impact hammer. The acceleration was collected from the same flexure via an accelerometer. The ratio of the measured excitation force to measured acceleration is presented inertance of the pivoted-bar. The intended inertance value is shown with dashed horizontal line in each test.

also involve some difficulties, such as manufacturing flexural notches with very small thickness. Alternatively, high inertance also decreases the natural frequency of the inerter. However, the flexural notch's stiffness remains as an important factor in this case as the optimal inertance obtained from the optimisation process is small.

Although notch stiffness prevents the pivoted-bar working as an ideal inerter by generating steady inertance along with a frequency band, the pivoted-bar still operates as an ideal inerter far from the resonance region. Thus, the stiffness of the flexural hinge is an important parameter that should be considered in the design stage of the inerter. The following section will study the effect of the stiffness of the flexural hinge on the inertance performance of the inerter.

5.4.3   Design of the flexural-hinges

Flexure hinges employed in the pivoted-bar eliminate the friction at the pivots but introduce a stiffness to the inerter device. Although this stiffness can be very small, it cannot be eliminated. For especially the pivoted-bar system that produces small inertance, even small stiffness values can easily create a resonance region where the device is prevented from working effectively as an ideal inerter. Hence, the natural frequency of the inerter device consisting of the pivoted-bar and flexure hinges should be designed as far away from the operating frequencies as possible. Otherwise, the device should be modelled as a parallel-connected spring-inerter arrangement to reflect the variation in the inertance around the resonance region.

The flexure hinges used in the device are semi-circular notch type hinges as shown in Figure 5.14a, where R, t and w are the radius, thickness and width of the notch, respectively. The dashed line in the middle of the notch passes through the centre of rotation and θ indicates the rotation angle around the centre of rotation. The most influential parameter that defines the stiffness of the semi-circular notch hinge is the thickness of the notch t. The higher the thickness is, the higher the stiffness the notch hinge has. A more accurate mechanical model of the pivoted-bar with flexural-hinges is an inerter in parallel to a spring, as given in Figure 5.14b. The pivoted-bar turns into a pure inerter device for $k_{notch} = 0$, where there is no stiffness considered at the notch hinge ($t = 0$). The mechanical model turns into an inerter-spring arrangement in the existence of stiffness. However, even in cases where the stiffness exists, the device can effectively operate as an inerter by producing a constant inertance at frequencies after its resonance effect diminishes. For very small stiffness values, the natural frequency becomes very close to zero and the notch stiffness can be neglected entirely for all frequencies.
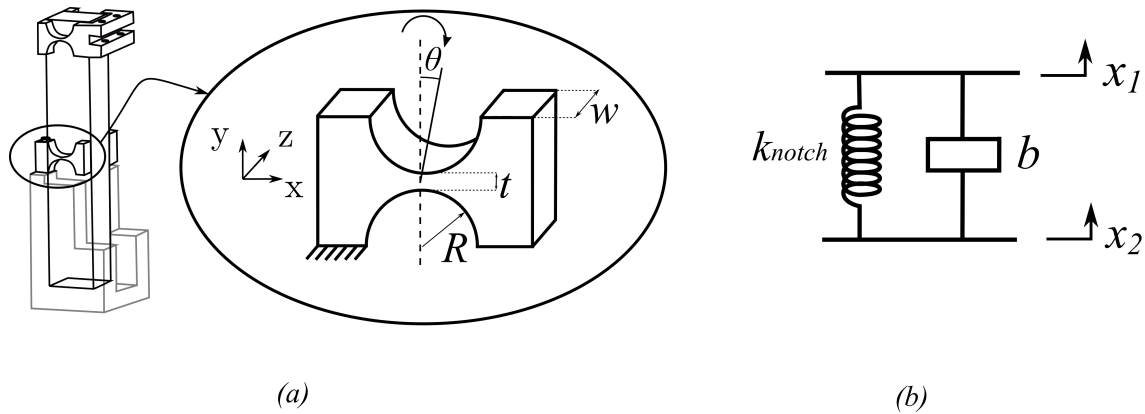
Figure 5.14 Pivoted-bar inerter with (a) semi-circular notches as flexural hinges and (b) the mechanical model of the pivoted-bar including non-zero notch stiffness.

It should be noted that an even more accurate model of the pivoted bar in Figure 5.14a would be given with the structural mass of the inerter connected to the one of the terminals of spring-inerter arrangement in Figure 5.14b. However, it can be neglected as being directly connected to the host structure as discussed in Section 5.4.1. For the same reason, there was no effect of the structural mass of the inerter grounded from the centre of mass in the experiment in the previous section. Therefore, the mass of the inerter is also neglected here in the analysis of the effect of the stiffness of the flexural hinge on the inertance performance.

The stiffness for a semi-circular notch hinge in Figure 5.14a can be predicted as [286]

$$k_{\theta_z} \approx \frac{2Ewt^{5/2}}{9\pi R^{1/2}} \tag{5.20}$$

where E, w, t and R are Young's Modulus, depth of the hinge, thickness of the flexure notch and radius of the flexure notch, respectively. k_{notch} in Figure 5.14 corresponds to total stiffness of the four flexural-hinges connected to the bar. The total translational stiffness k_{notch} is determined from the rotational stiffness in Equation 5.20 for given distance between the pivots on the bar l_a.

The relative accelerance of the inerter device is derived as

$$\frac{(\ddot{x}_1 - \ddot{x}_2)}{F} = \frac{-\omega^2}{k_{notch} - b\omega^2} \qquad (5.21)$$

where F is the amplitude of force produced by the spring-inerter arrangement, and ω is the excitation frequency. From Equation 5.19, the inertance of the system is determined by taking the inverse of the accelerance to evaluate the inerter performance of the device. As it can be seen from Equation 5.21, the accelerance becomes $\frac{1}{b}$ for $k_{notch} = 0$ and a constant inertance value is obtained for all frequencies. If the stiffness exists ($k_{notch} > 0$), a resonance peak appears in the accelerance response and inertance varies near the natural frequency. The natural frequency approximates to zero for very high inertance or very small stiffness values. However, even small stiffness values could lead to resonance regions at relatively higher frequencies for small inertance values. Therefore, the analysis of the effect of the flexure notch becomes important since the inerter device in this design study also requires the ability to produce small inertance values obtained from the optimisation results.

The most influential geometric parameter on the stiffness is the thickness of the notch t. The stiffness of the notch for the design parameters given in Table 5.6 was determined as 5020.3 N/m for the thickness of 0.5 mm. The effect of the notch stiffness on the inertance of 0.030 kg was shown by changing only the thickness of the notch and taking the other parameters constant. Substituting the notch stiffness found from Equation 5.20 into Equation 5.21, the relative inertance values of the spring-inerter arrangement in Figure 5.14b for different notch thicknesses are presented in Figure 5.15.

As it can be observed from Figure 5.15, the thickness of the notch of 0.1mm provides constant inertance after almost 50 Hz and thus, the pivoted-bar with the flexural hinges

Table 5.6 Design parameters of the semi-circular notches and theoretical prediction of the total stiffness of four notches connected. The total stiffness k_{notch} is determined from the distance between the pivots l_a and the rotational stiffness k_θ of one notch.

E (GPa)	w (mm)	t (mm)	R (mm)	l_a (mm)	k_θ (Nm/rad)	k_{notch} (N/m)
70	5	0.5	4.75	40	2.008	5020.3
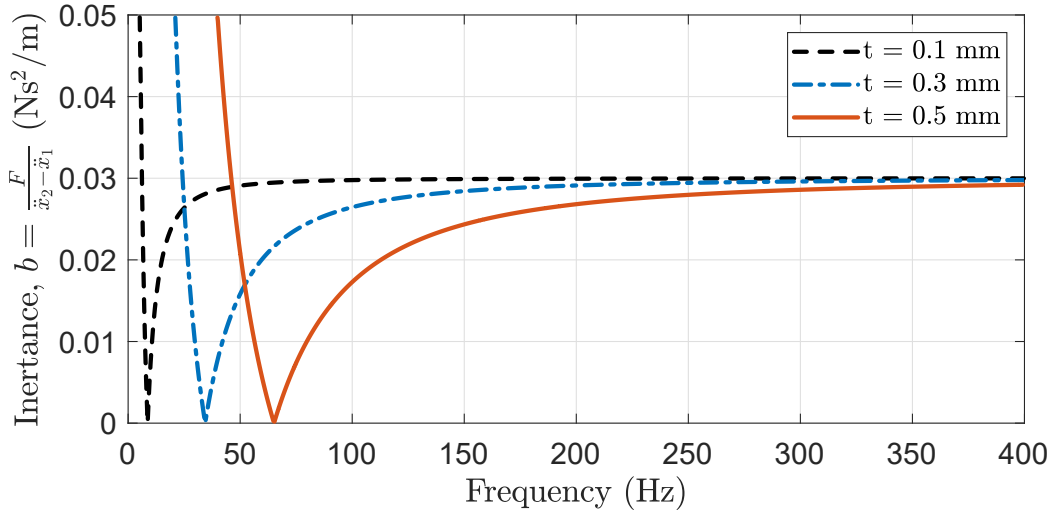
Figure 5.15 The effect of the thickness of the notch on the relative inertance performance of the spring-inerter arrangement in Figure 5.14b obtained from Equation 5.21 for constant inertance $b = 0.030$ kg. The result was shown for the thicknesses of 0.1 mm, 0.3 mm and 0.5 mm.

acts as a pure inerter with constant inertance. With increasing thickness, frequency band where constant inertance is obtained shifts to higher frequencies as the stiffness of the notch and thus, the natural frequency of the pivoted-bar system increases. The working frequency of the absorber for the milling operation is determined as $100 - 200$ Hz as it will be discussed in Chapter 6. It is reasonable to choose the thickness of the notch as 0.1 mm as it provides constant inertance along with the working frequency band. However, the prototype of the inerter was manufactured with a notch thickness of 0.5 mm due to manufacturing limitations. This leads to a different inertance value from the targeted (optimal) inertance in the frequency band of $100 - 200$ Hz and reduces the performance of the absorber. However, this difference can be easily amended by

fine tuning the inertance through additional lumped masses, and the performance loss is then componsated for as will be shown in Chapter 6.

5.4.4   Fatigue analysis

Notch hinges have been frequently used as compliant mechanisms, for especially where precision motion is needed. However, one of the major issues that could limit their usage under cycloid loading, such as milling operations, is their fatigue strength. This can be especially problematic for milling operations where the excitation (or chatter) frequencies can reach relatively high frequencies. Under dynamic loading with high frequencies, the completion of the reduced fatigue life cycle can be very short. For instance, it takes less than an hour to complete 1 million cycles for a dynamic loading frequency of 300 Hz. Fatigue life cycle defines the life of the passive absorber device as fatigue failure of the notch hinges causes the malfunction of the inerter device and consequently, the passive absorber. Therefore, the fatigue life cycle of the notch hinges is discussed in this section.

The details of the fatigue analysis are given in Appendix D. Here, only the important points to improve the fatigue life are listed as following:

- One of the most important design parameters that define the fatigue life of the notch hinge is the notch thickness. The fatigue life can be improved by decreasing the notch thickness. However, having a very small notch thickness is mostly defined by the manufacturing capability.

- Choosing a different material affects the fatigue life. There is no doubt that the most influential parameters are the material parameters, specifically both Young's

modulus E and fatigue strength S_f. Fatigue strength could be increased to levels as high as $500 - 800$ MPa with the use of steel alloys, instead of aluminium alloy. However, stiffness of the notch also increases with increasing Young's modulus, which leads to resonance region at high frequencies as discussed in Section 5.4.3.

- Increasing the radius of notch R improves the fatigue life by decreasing the maximum stress occurring at the notch. Increasing R also decreases the stiffness of the notch. However, a high radius of notch could increase the overall height and length of the flexural hinge.

- Manufacturing process applied can also improve the fatigue life by increasing the surface roughness reduction factor as explained in Appendix D. Improving surface roughness by improving the manufacturing technology provides increase in the fatigue life as well.

With the analysis of the fatigue life cycle, the design studies of the inerter is completed. The following section will present the implementation of the damping.

5.5 Implementation of damping

After having presented the inerter design, another critical component in terms of manufacturing is the damping element. As the passive device focuses on the small-scale small-amplitude application, the damper design should be compatible with this requirement and work with the inerter device presented in the previous section. For this reason, a silicone gel material is employed for the damping. It is applicable to small sizes and easy to implement. Moreover, the silicone gel has damping elastic characteristics that can be used as the stiffness element. The gel, by showing both the

damping and elastic properties, enables the physical realisation of the spring-damping arrangement compactly without needing a separate spring. This section first discusses the specification of the gel. Secondly, it presents the design of the gel damper and finally, test results for the performance evaluation of the gel are presented.

The gel damper is modelled with complex stiffness, assuming that the gel's mechanical properties are independent of frequency. A hysteretic damping term is assumed in the complex stiffness model. It has been shown in Section 5.3 that using complex stiffness instead of a spring-viscous damping arrangement provides identical performance in the frequency domain. The silicone gel utilised in the damper is based on polyorganosiloxanes (called Magic Power Gel, from Raytech) and obtained from a mixture of two liquids. Depending on the mixing ratio, the gel shows different damping and elastic characteristics. The hysteretic damping (loss factor) and elastic (Young's Modulus) behaviour of the silicon gel were tested under different temperatures and different dynamic strains at room temperature in [287]. It was found that the loss factor and Young's modulus of the gel is independent of the temperature and the dynamic strain. It was also presented in [287] how to obtain loss factors and Young's Modulus of the gel for the mixing ratios of 1:1 and 1:2. The mixing ratio for desired mechanical properties by using linear interpolation was determined. The same method was followed to obtain the desired loss factor and Young's Modulus here.

After mixing two liquids to prepare the gel damper, a vacuum pump extracted the air bubbles in the mixture. Then, the mixture in liquid form was poured into the gap in the gel damper. It waited until the mixture takes the non-fluid gel form. The silicone gel with a mixing ratio of 1:1.1 was applied to two sides between the base and the sliding plate as shown in Figure 5.16a.

The gel on both sides works on the shear plane and thus, noting that the shear modulus equals $G = \frac{\tau_{xy}}{\gamma_{xy}} = \frac{E}{2(1+\nu)}$, the stiffness of the gel damper can be calculated as:

$$k = \frac{EA}{(1+\nu)d} \tag{5.22}$$

where E is Young's modulus corresponding to 1:1.1 mixing ratio, A is the area of the gel, d is the thickness of one layer of the gel and ν is the Poisson's ratio, which is assumed 0.5 [288]. Equation 5.22 shows that the stiffness of the gel damper can be adjusted by setting the area and the thickness of the gel. The gel damper with two identical gel layers with an area of 35x45 mm^2 and a thickness of 3 mm on both sides was manufactured as shown in Figure 5.16b.
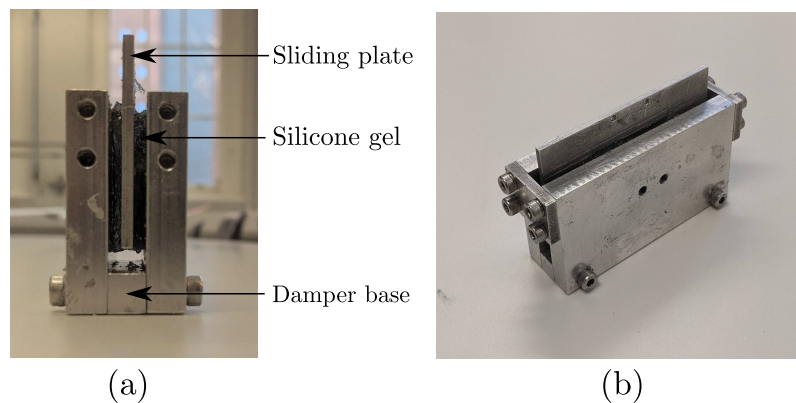
Figure 5.16 Manufactured gel damper consisting of a sliding plate, two layers of silicone gel and damper base as shown in (a). Isometric view of the gel damper is shown in (b).

In order to measure and evaluate the frequency-dependency of the mechanical properties of the gel under the working frequencies (100-150 Hz as presented in Chapter 6), an impulse hammer test was applied to the gel damper. It was fixed from the damper base and a small aluminium block was added to the sliding part to enable the connection of the accelerometer. The natural frequency of the gel damper was increased by adding a mass as the effect of the loss factor and the gel's stiffness becomes more apparent around resonance. Experiments of three cases: no additional mass added, the total

mass was increased by 11 gram and 28 gram, were conducted. The impulse hammer was applied by hitting the small aluminium block. The accelerance of the gel damper is written as:

$$\frac{\ddot{x}}{F} = \frac{-\omega^2}{k_i(1+j\eta) - m\omega^2}$$

(5.23)

where k_i and η are the stiffness and the loss factor of the gel, ω is the forcing frequency and m is the total mass of the sliding plate, aluminium block and the accelerometer, which is 38.5 grams. The loss factor and the stiffness of the gel were found by fitting k_i and η in Equation 5.23 to the experimental curve for known mass values m. It is known that the experimental curve obeys Equation 5.23. Only unknown parameters in Equation 5.23 are properties of the gel k_i and η. These values were obtained by applying the least-squares fitting in Matlab.

The mechanical properties of the gel that provide the experimental curves are given in Table 5.7. The experimental results in comparison with the numerical simulation using the corresponding mechanical properties are presented in Figure 5.17a-c, respectively. They are also compared with the average values of the loss factors and the stiffness obtained from three cases.

Table 5.7 Loss factor and the stiffness for the gel

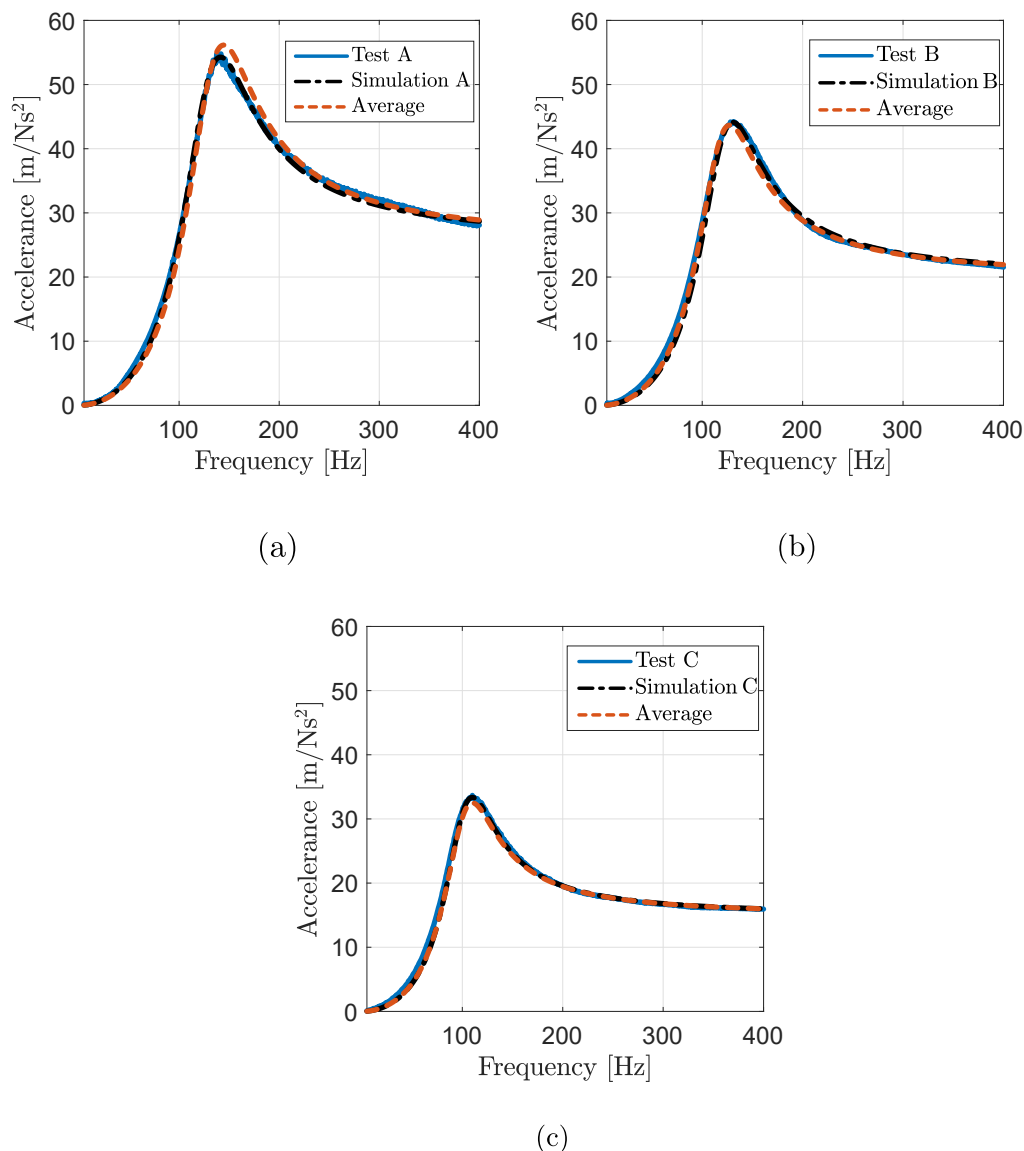|	Total mass, m (gram)	Natural frequency, ω_n (Hz)	Loss factor, η	Stiffness, k_i (kN/m)
Test A (Fig. 5.17a)	38.5	110	0.545	23.4
Test B (Fig. 5.17b)	49.5	130	0.515	26.3
Test C (Fig. 5.17c)	66.5	141	0.505	25.3
Average	–	–	0.5217	25.0

(a)

(b)

(c)

Figure 5.17 Three experimental cases with different total masses to determinate the loss factor and the stiffness of the gel damper where each experimental result (solid blue line) was compared with the simulation result obtained using Equation 5.23 for the mechanical properties in Table 5.7. The average result (orange dashed line) was obtained using the averages of mechanical properties presented in Table 5.7.

It was observed that there is no significant change in the stiffness and the loss factor of the gel between 100 Hz and 150 Hz, which are the working frequency of the absorber. Therefore, the average values of the loss factors and stiffnesses obtained from the three

experiments were accepted as the dynamic properties of the gel damper. As a result, the loss factor and the stiffness were determined as 0.5217 and 25 kN/m.

5.6 Final design of the absorber

The designs of the inerter device and the gel damper, which provides the stiffness and the hysteretic damper, were already discussed. As for the outer spring, a notch type linear spring was employed. According to design studies presented above, each absorber component was manufactured and the assembly was completed. The prototype of the D2 manufactured is demonstrated in Figure 5.18.
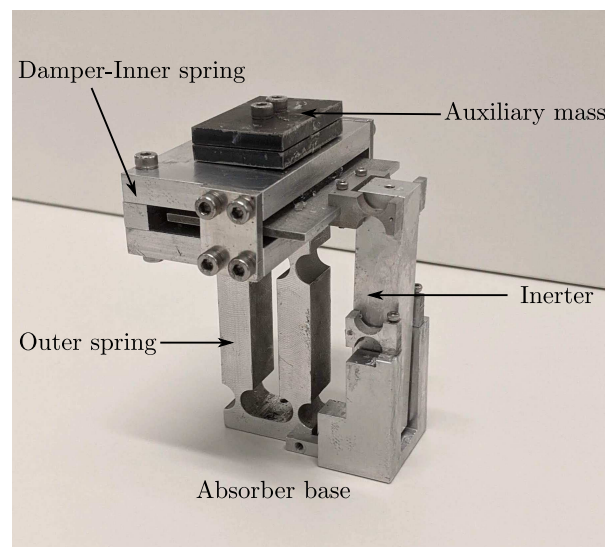
Figure 5.18 The manufactured prototype of D2 after its assembly

The mass of the base of the gel damper is accounted for by the auxiliary mass. In order to obtain the mass ratio, an additional mass is mounted on the gel damper. The total auxiliary mass becomes the sum of the mass of the gel damper and the additional mass. The prototype is mounted on the machining system from the absorber base. The prototype manufactured device relates to the updated mechanical model in Figure

5.5: Specifically, the gel damper is connected in series to the inerter while the outer spring is connected in parallel to the series-connected inerter-gel damper arrangement. The mass of the sliding plate acting between the layers of the gel, as demonstrated in Figure 5.16a is an isolated mass that cannot be counted towards the auxiliary mass nor the mass of the machining system. Therefore, its mass of 0.026 kg creates the parasitic mass effect. Even a very small mass of the sliding mass will act as the parasitic mass due to small inertance as discussed in Section 5.2. Hence, complete elimination of the parasitic mass effect caused by the sliding plate is difficult.

Although the inerter design can have steady inertance for thin notch thickness of the living hinges, this was not possible due to the manufacturing limitations. It was shown that the notch stiffness affects the inertance. This effect is presented in the equations of motion in Appendix E, and it will be utilised to obtain the optimal equivalent inertance in the optimisation in the next chapter.

The prototype requires an area of 50 mm x 65 mm on the base for the connection. It has a total length of 100 mm and its width reaches a maximum 90 mm in the damper. It can be directly mounted to a host structure in the same way as a classical TMD. Most importantly, it is possible to manufacture an even smaller version of the proposed design to apply the inerter-based absorber into smaller applications.

5.7   Discussion

A design study of the physical realisation of L2 in Chapter 4 was presented in this chapter. The application of such an absorber into a milling operation requires small-scale absorbers as milling operations generally has limited spaces for the passive control

device application and small inertance as the optimal inertance obtained in Chapter 4 is very small for small mass ratios. In order to succeed in these objectives, the mechanical model of L2 was evolved to D2 in Figure 5.5 by updating the model with the parasitic mass and the hysteretic damping. Section 5.2 investigated the parasitic mass effect and concluded that the elimination of the parasitic mass effect was challenging even with rigorous design of the absorber due to small inertance. This was shown with a numerical example considering a machining system with the main mass of 10 kg and the damping of 0.023. Optimal inertance for this system was found as 55.8 gram, which is very small. Even the mass of a very small connection component of the absorber can be $5 - 10\%$ of the inertance and this leads to $5 - 40\%$ performance loss as shown in Figure 5.3. For small modal mass for the primary system, the performance loss becomes even more deteriorated. This numerical example is important because it is a very close example to the milling operation case for the experimental verification, as presented in Chapter 6.

The compact design of the gel damper by providing stiffness and damping through the silicone gel was also important as it eliminates the need for a separate spring for the inner stiffness. After including the parasitic mass and the complex stiffness, D2 provided an identical performance improvement in the frequency domain as for the idealised L2. However, the performance analysis in the time domain has not been evaluated. The time domain results of L2, D1 and D2 may contain some differences but only the performance in the frequency domain was found sufficient for the chatter stability assessment.

Different pivoted-bar arrangements were investigated using a generic pivoted-bar model where the position of the pivots and a pair of additional lumped masses attached to two ends of the bar can be set differently. The mass of the inerter $(m_{bar} + 2m)$ was

always included in the analysis. When considering that the absorber is connected to the host structure whose mass is guaranteed to be much larger than the mass of the inerter due to optimal dimensionless parameters obtained, it was shown that the pivoted-bar in Figure 5.11d acts as inerter. For this, three important remarks could be highlighted: one of two pivots must be positioned at the centre of the mass of the pivoted-bar and additional lumped mass. Secondly, additional lumped masses attached to the end of the pivoted-bar must be equal if fine tuning requires. Finally, the inerter must be attached to the host structure from the pivot at the centre of mass. Otherwise, the mass of the inerter increases the parasitic mass. This design of the inerter was specifically proposed for small inertance. The distance between the pivots l_a was set as maximum as possible to keep the inertance small. Furthermore, it is reasonable to keep l_a small by amplifying the rotational inertia of the bar.

One of the novelties in the proposed design of the inerter is the fine tuning property by simply adding two equal masses to the ends of the pivoted-bar. In that way, the minor adjustment of the inertance becomes possible without significant structural modification of the pivoted-bar. Fine tuning is also helpful to eliminate or alleviate the detuning effects stemming from uncertainties of the other components in the system. In the design, the mass of the pivoted-bar (m_{bar}) and the distance between the pivots l_a were considered as the main design parameters and the use of the additional lumped masses (m_b and m_c) was considered as the secondary design parameter used for fine tuning. The experimental inertance given in Figure 5.13 showed fluctuations from the intended inertance as the additional lumped mass were increased. Moreover, excessive use of the additional mass could decrease the natural frequency of the second mode of the pivoted-bar and flexural hinge system such that its resonance region could prevent constant inertance in the working frequency band. Therefore, care should be taken if

using of excessive additional lumped masses since it could deteriorate the performance of the design.

The absorber was considered to be utilised for relatively small-scale small-amplitude applications such as milling operations. Therefore, semi-circular notches as flexural hinges were used to eliminate the friction that is possibly problematic. However, employment of the flexural hinges due to the stiffness of the notch causes a resonance region that prevents constant inertance for a frequency band. Therefore, it is important that the resonance region of the pivoted-bar should be avoided in the working frequency band of the absorber as much as possible. Having small inertance easily increases the natural frequency with even small stiffness of the notch. It was shown that the thickness of the notch should be as small as 0.1 mm to have the inerter generating constant inertance above 50 Hz. However, due to manufacturing limitations, the prototype was manufactured with thickness of 0.5 mm. It is therefore expected that the prototype leads to differences in inertance from the intended inertance values at $100 - 150$ Hz. These differences could cause performance loss in the stability of the milling operation as the inertance obtained from the inerter is different from the optimal inertance that gives the best performance. It is possible to amend the performance loss by using the fine tuning of the inerter as it will be presented in Chapter 6. The performance loss is because the pivoted-bar acts an inerter connected in parallel to a spring due to high notch stiffness (or equally low inertance) rather than a pure inerter. A pivoted-bar with high notch stiffness can also be used for a simple realisation of a parallel-connected spring-inerter arrangement.

The silicone gel employed provided the damping and stiffness properties. It was assumed that the gel properties are frequency-independent and they were tested for only the working frequency range, $100 - 150$ Hz. It was observed that the mechanical

properties were mainly stable. The sliding plate of the gel damper causes the parasitic mass effect. Although it can be possible to reduce the sliding plate's mass, it is very difficult to be completely avoided due to small inertance.

Another novelty presented in this chapter is that the final design of the absorber given in Figure 5.18 is directly applicable to the host structure in the manner of a classical TMD. Unlike the other practical applications in the literature, this design of D2 requires no need for grounded connection of the absorber or its deployment between two parts of the host structure. The absorber can be built even in a smaller size than the prototype if the application requires it.

5.8   Summary

This chapter aimed to design the physical realisation of L2 for the experimental verification of its performance improvement in a milling operation. Design studies showed that it is reasonable to have the D2 rather than idealised L2 considering the parasitic mass effect and the implementation of the damping. The silicone gel applied the damping, which was modelled with a complex stiffness consisting of a stiffness element and the loss factor. Numerical simulations showed that D2 and L2 have an identical performance, so the modal update in D2 leads to no performance loss in milling operation stability.

A pivoted-bar with flexural hinges was employed as the inerter. One novelty presented was that the pivoted-bar proposed could generate very small inertance considering its attachment to a host structure as a part of localised addition. The second novelty in the design of the inerter was that the design allowed small adjustment of the inertance

without the need for significant structural modification by simply adding two equal masses to the ends of the pivoted bar. The fatigue analysis and the effect of the stiffness of the semi-circular notch hinges employed as flexural hinges in the design to eliminate friction and backlash were also investigated.

Finally, the physical design of D2 was presented by assembling the inerter with the gel damper and a notch type linear spring. It was a novel feature that the design of D2 did not need to have a grounded connection or the placement between two parts of the host structure. It enabled direct application between the host structure and the auxiliary mass, similar to implementing a classical TMD. A prototype of the D2 design was manufactured.

Chapter 6

Experimental Verification

6.1 Introduction

This chapter presents experimental verification of the performance of the prototype of the inerter-based absorber. The focus is chatter suppression in milling operations by improving the real part response of the system. To verify this, the dynamic behaviour of the prototype is first explored using impact hammer tests in the laboratory condition. Later, performance is examined under real milling conditions by conducting cutting tests. Moreover, the vibration suppression capability of the prototype is also examined by setting the mass ratio and the inertance during the impact tests. This is particularly straightforward because the prototype allows adjustment of its inertance by simply adding equal lumped masses at the ends of the inerter bar. This is also beneficial for fine tuning the design parameters that could be required due to structural uncertainties induced by both primary and control systems.

Section 6.2 presents the experimental setup for the impact tests and their results with the consideration of the vibration suppression case. Milling tests, including the experimental setup, results and discussion, are presented in Section 6.3. Finally, Section 6.4 summarises the chapter.

6.2   Preliminary impact test

The effectiveness of the prototype was first evaluated with a vibration suppression case and the investigation was further continued applying a series of impact hammer tests for different auxiliary masses and inertance values.

An aluminium workpiece attached to a compliant mechanism was considered in the experiments as shown in Figure 6.1. The compliant mechanism was designed to have one flexible mode in the horizontal x direction and it was assumed rigid enough in the other directions. In order to identify the dynamic properties, the structure was fixed from the bottom of the compliant mechanism and the modal tests of the structure with and without the prototype were conducted. In the impact hammer tests, the impact hammer Dytran 5800B2 was applied to the aluminium block in parallel to the flexible mode and the acceleration of the structure was recorded from the same direction using the accelerometer PCB 353B18. For all experimental tests in the laboratory, LMS Test.Lab. was used for the data acquisition as well as processing data.

The first modal test was conducted to identify the modal parameters of the uncontrolled host structure without attaching the prototype. The natural frequency of the flexible mode of the structure, modal mass and structural damping were found as 117.3 Hz, 10.7 kg and 2.3%, respectively. Next, a series of modal tests were utilised, as presented

below, for the vibration suppression case and evidence that the prototype is operating as expected.

6.2.1 Optimal design parameters for vibration suppression

According to the modal parameters, optimal design parameters in D2 were determined for vibration suppression and chatter stability cases considering the notch stiffness. The SaDE algorithm was utilised for the optimisation of the objective function. For the vibration suppression of the structure, H_∞ optimisation was conducted to minimise the maximum amplitude of the FRF and therefore, the objective function evaluated is written:

$$J_{vs} = max\Big(|G(j\omega)|\Big) \tag{6.1}$$

where $|G(j\omega)|$ is the amplitude of the FRF of the system and full expression in given in Appendix E. The objective function is optimised to minimise the objective value.

The optimal design parameters were first obtained when neglecting the notch stiffness ($k_{notch} = 0$) where a constant inertance is produced at each frequency. The stiffness in the notches prevents the inerter from generating constant inertance in the resonance region as discussed in Section 5.4.3. Although this effect is avoidable for an effective working frequency band, the notch thickness of 0.5 mm does not allows this in these experimental cases due to manufacturing limitations. Therefore, an equivalent optimal inertance value was determined accounting for the spring-inerter arrangement instead of only an inerter element in the optimisation process. Though the notch stiffness was theoretically calculated as 5020.3 N/m, the estimation for the actual stiffness value was around 9000 N/m because of manufacturing errors and possible stress stiffening effect (due to assembly conditions and load of inerter bar and added masses). Thus,
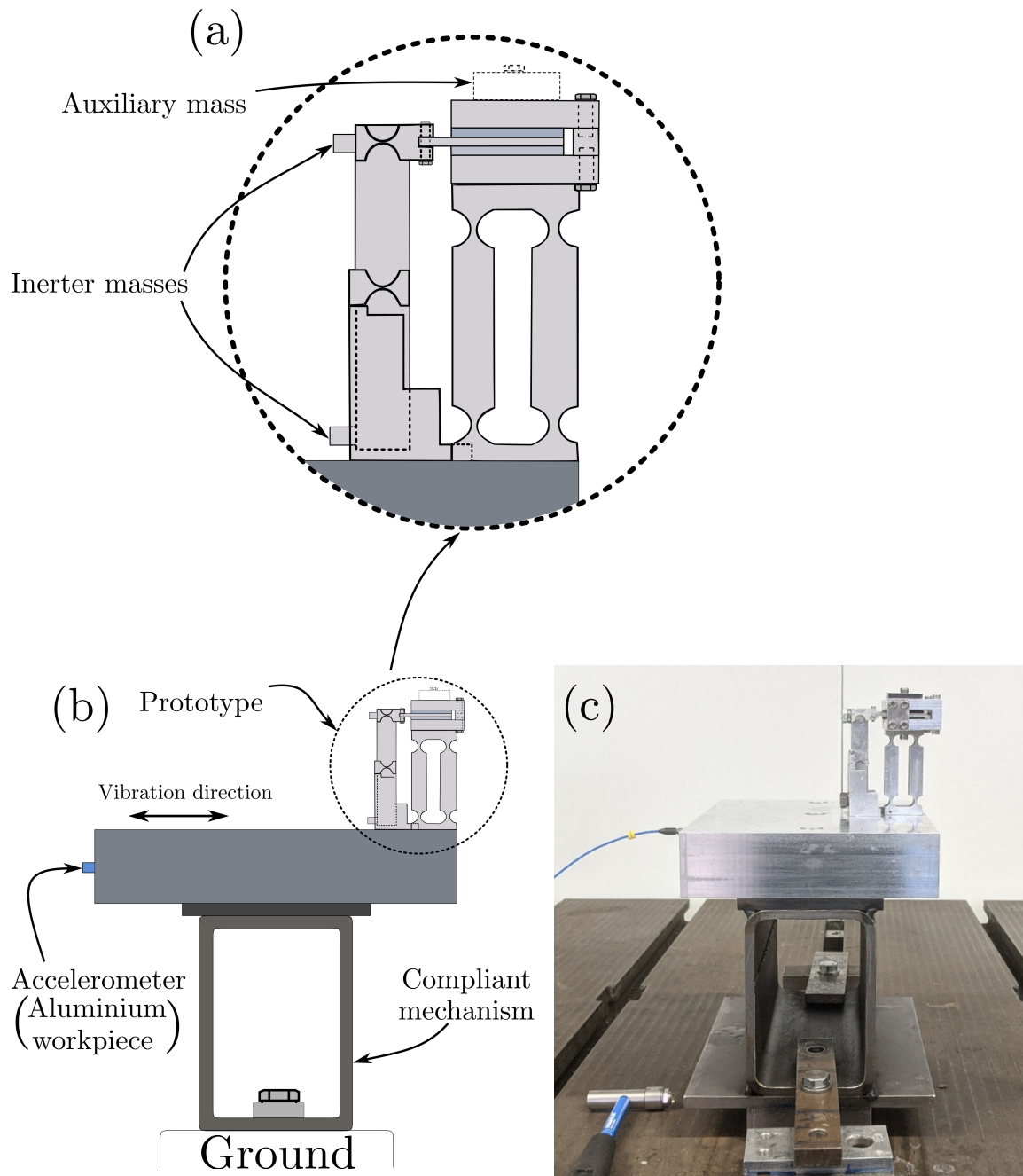
Figure 6.1 Experimental setup of the structure with the prototype for the impact hammer test: the illustrations of (a) the prototype in detail and (b) the whole setup, and (c) an image of the experimental setup.

the equivalent optimal inertance values were found for notch stiffness values of 5020.3 N/m and 9000 N/m, restricting all design parameters except the inertance to their optimal values.

The optimal design parameters obtained for $\mu = 0.045$ and $\beta = 0.054$ are presented in Table 6.1. The parasitic mass effect in the controlled structure is induced by the mass of the sliding plate moving in the gel damper. It is worth reiterating that β is the ratio of the parasitic mass to auxiliary mass and it was determined for the mass of the sliding plate of 26 gram. Table 6.1 also presents the maximum amplitude H_{max} observed in the frequency response for each set of design parameters. The actual value of each control element in the experiment in the prototype: the outer spring k_o was found as 251.89 kN/m, the stiffness k_i and the loss factor η of the gel damper were identified as 24.97 kN/m and 0.5217, respectively.

Table 6.1 Optimal design parameters for H_∞ optimisation determined by performing SaDE for the notch stiffness of 0, 5020.3 N/m and 9000 N/m. H_{max} represents the maximum amplitude obtained in the FRF from numerical optimisation.

	k_o (kN/m)	k_i (kN/m)	η	b (kg)	H_{max} (m/N)
D2 ($k_{notch} = 0$)	254.51	24.84	0.5114	0.032	7.52 x 10^{-7}
D2 ($k_{notch} = 5020.3$ N/m)	254.51*	24.84*	0.5114*	0.043	7.69 x 10^{-7}
D2 ($k_{notch} = 9000$ N/m)	254.51*	24.84*	0.5114*	0.052	7.86 x 10^{-7}

*constrained parameters

6.2.2 Experimental result for vibration suppression

The prototype was attached to the top surface of the aluminium workpiece as shown in Figure 6.1. Both glue and screw connections were utilised to ensure the rigidity of the connection between the bottom side of the prototype and the top side of the workpiece. The inertance of the inerter was set to the optimal inertance of 0.052
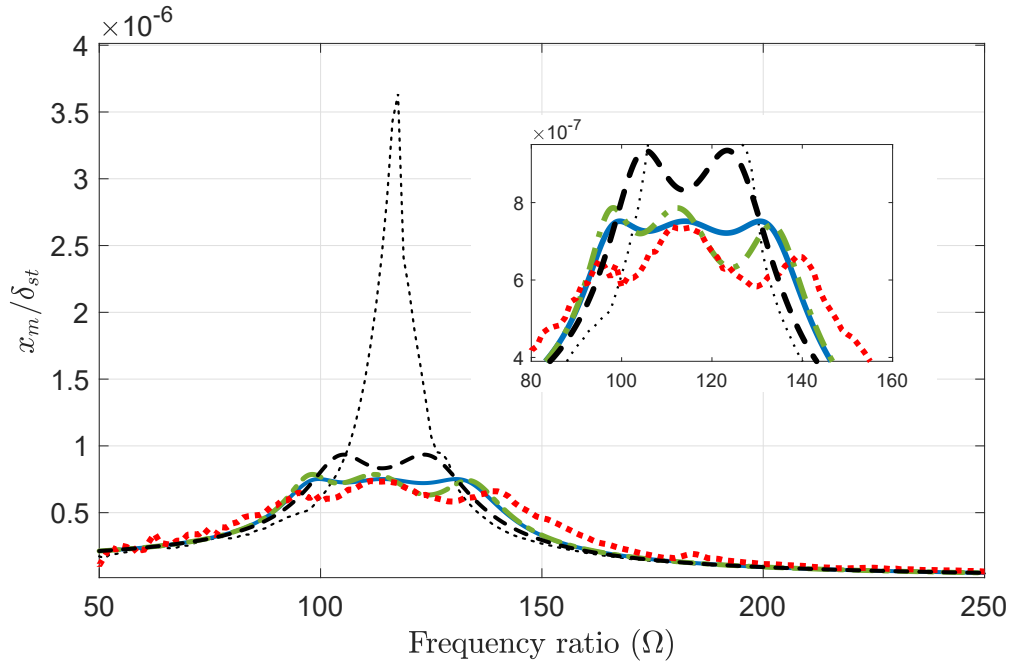
Figure 6.2 Experimental results of the structure with the prototype with $\mu = 0.045$ and $\beta = 0.054$ in comparison with the experimental result of the uncontrolled host structure, and the numerical simulations of D2 for $k_{notch} = 0$ and $k_{notch} = 9000$ N/m with the design parameters presented in Table 6.2 and a classical TMD. (⋯⋯) Uncontrolled structure (experiment), (- - -) TMD (simulation), (——) IDVA-D2 with $k_{notch} = 0$ (simulation), (-·-·-) IDVA-D2 with $k_{notch} = 9000$ N/m (simulation), (·····) prototype (experiment).

kg for $k_{notch} = 9000$ N/m by adding equal masses to the end of the inerter bar as illustrated in Figure 6.1a. For this setup, the impact hammer test was conducted for the vibration suppression case. The resulting FRF is presented in Figure 6.2 compared to uncontrolled experimental result, TMD, and numerical simulations for the IDVA. In the comparison, the TMD was numerically optimised for the same mass ratio considering the structural damping. The inertial effect of the parasitic mass was neglected since no significant contribution of the parasitic mass to the performance is observed if the parameters are tuned optimally.

Figure 6.2 shows that the prototype achieved 79.7% vibration suppression by decreasing the peak value of 36.34 x10^{-7} m/N to 7.37 x 10^{-7} m/N as is very close to numerical simulation. With this result, the prototype has improved the TMD performance (numerically obtained) by almost 21.2%, as observed in the figure. The notch stiffness of 5020.3 N/m and 9000 N/m caused only slight reduction in the suppression performance by 2.3% and 4.5%, respectively, as presented in Table 6.1. This was achieved thanks to the adjustment of the inertance. It must be noted that the reduction in the performance due to the notch stiffness can be further recovered if the constraints are removed on the design parameters (marked with an asterisk in Table 6.1). The absorber's performance, even with the notch stiffness of 9000 N/m as in the experiment, can be accomplished as very close to the performance with zero notch stiffness.

6.2.3 Exploratory modal tests

The dynamic behaviour of the structure controlled by the prototype was further explored applying a number of modal tests where the inertance and auxiliary mass values vary. The aim of these test is to ensure that the prototype acts as the IDVA D2 by showing that the controlled structure reflects the expected dynamic responses for the change in the design parameters. The modal tests were conducted for three auxiliary mass values of 0.365 kg, 0.480 kg and 0.530 kg, and four inertance values of 0.020 kg, 0.030 kg, 0.043 kg and 0.054 kg.

The magnitudes of the FRFs are presented in Figures 6.3. Since the chatter stability is proportional to the real part responses, they are also presented in Figure 6.4. The experimental results were compared with the numerical simulations obtained for the notch stiffness of $k_{notch} = 9000$ N/m and the actual values of the components identified

where the outer spring $k_o = 251.89$ kN/m, the gel damper's stiffness of $k_i = 24.97$ kN/m, and the loss factor of 0.5217. The results will be discussed in the following section.

6.2.4 Discussion

The experimental result showed that the prototype could effectively suppress the vibration by performing better than a classical TMD. Furthermore, the IDVA was physically applied without need for a grounded connection or deployment between two parts of the structure. To the author's knowledge, this was the first experimental study using an IDVA as a localised addition similar to a classical TMD in such a small scale application.

Another important and novel feature was that the inerter enabled the adjustment of the inertance by simply attaching additional small masses. This was especially beneficial for fine tuning after the inerter device was built. It was shown that although the design parameters were optimised, neglecting the notch stiffness, the inerter device was capable of capturing comparable performance by increasing the inertance. The fine tuning with adjustable inertance would be possibly used to compensate detuning effect due to uncertainties in other control elements such that it was used for the notch stiffness in the experiment. The vibration suppression performance could be further improved by re-optimising all design parameters without the constraints. However, this would require the re-manufacturing of components other than the inerter where it was easy to adjust inertance.
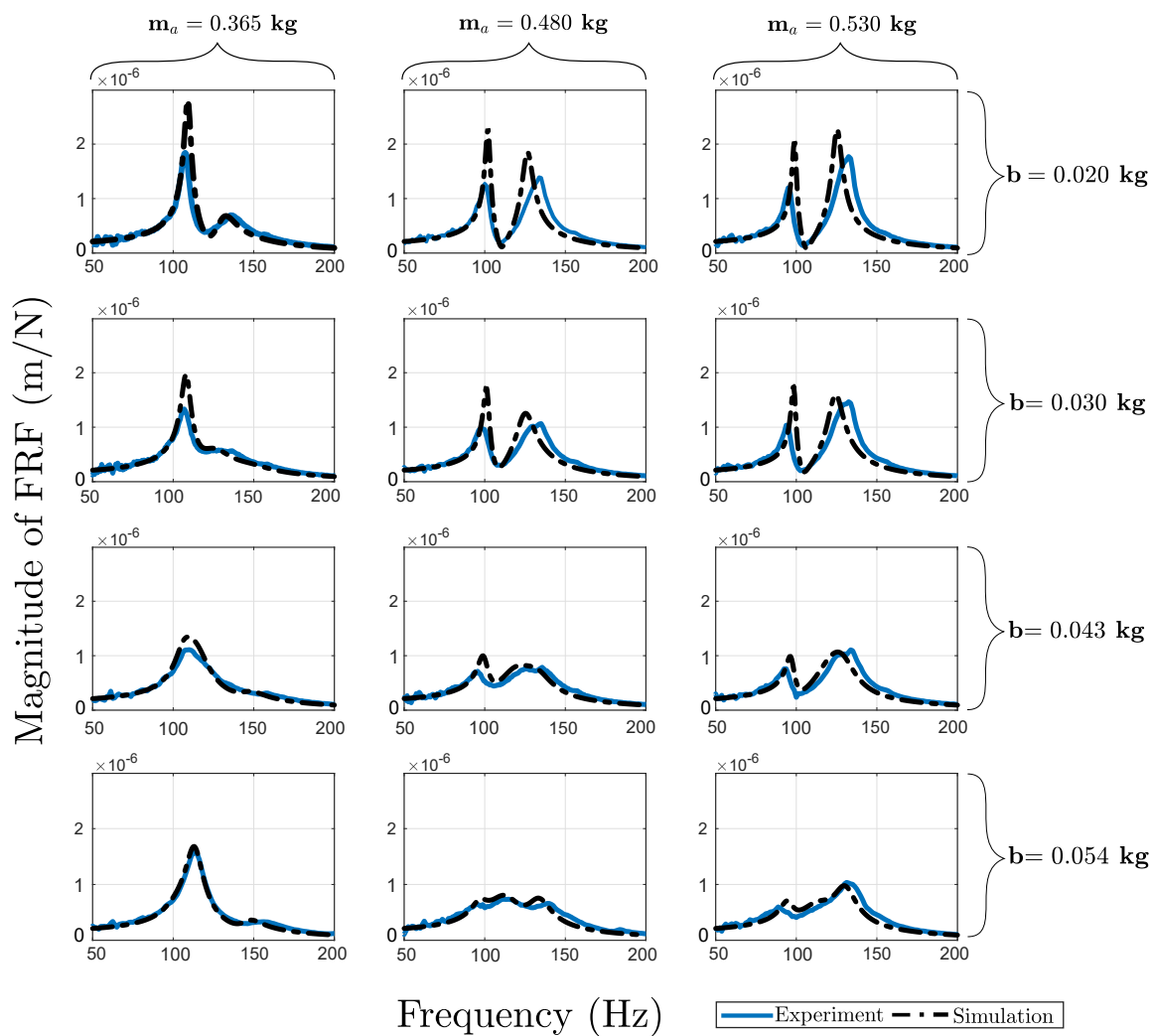
Figure 6.3 Magnitude of the FRFs obtained from the modal tests for different auxiliary masses and inertance values. The numerical simulations consider the actual values of the components. Auxiliary masses of 0.365 kg, 0.480 kg and 0.530 kg (column from left to right, respectively), and inertance of 0.020 kg, 0.030 kg, 0.043 kg and 0.054 kg (row from top to bottom) are presented.
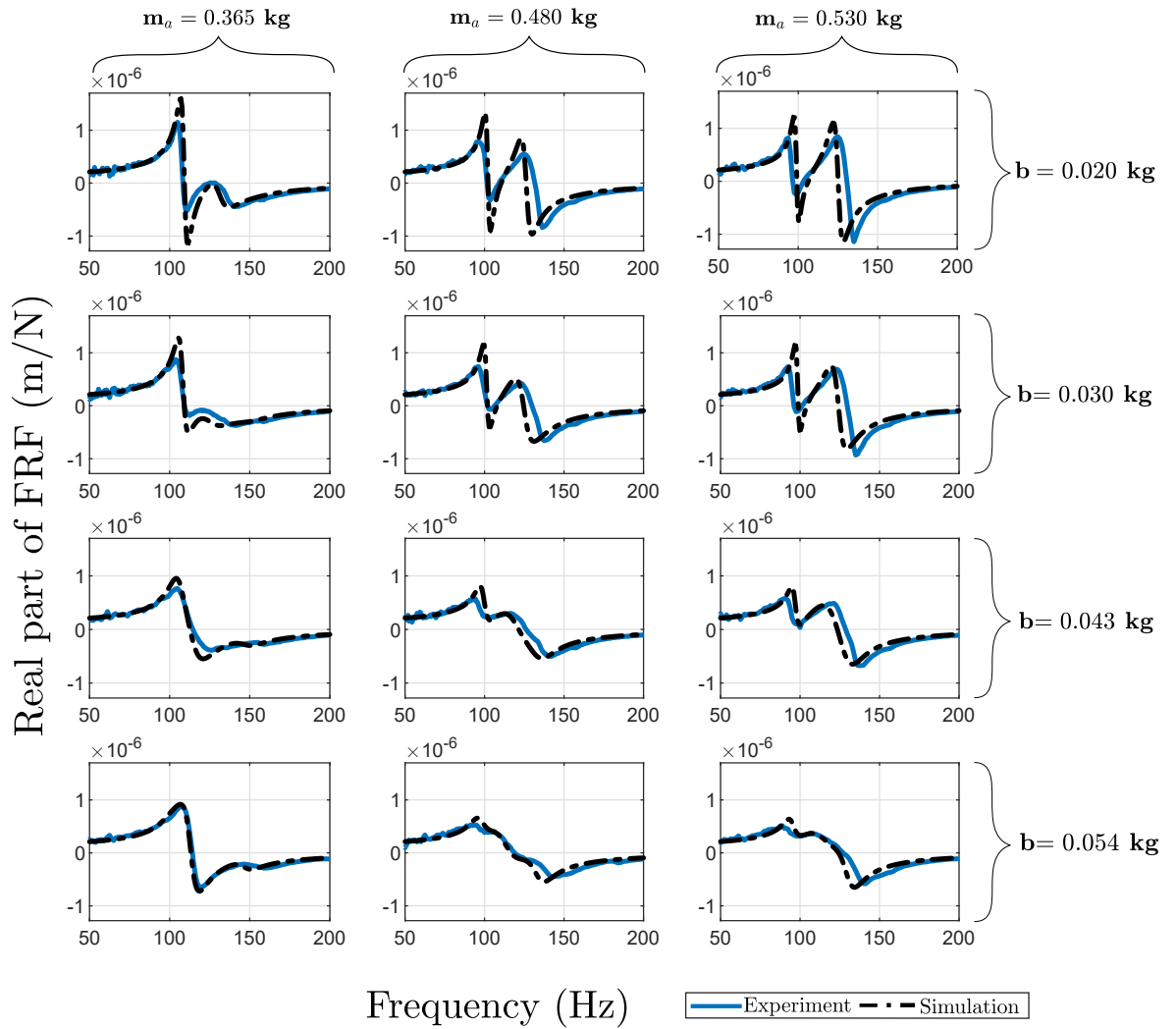
Figure 6.4 Real parts of the FRFs obtained from the modal tests for different auxiliary masses and inertance values. The numerical simulations consider the actual values of the components. Auxiliary masses of 0.365 kg, 0.480 kg and 0.530 kg (column from left to right, respectively), and inertance of 0.020 kg, 0.030 kg, 0.043 kg and 0.054 kg (row from top to bottom) are presented.

Further investigation conducted by several modal tests indicated that the changes in the inertance and auxiliary mass were well reflected in the dynamic responses of the prototype as given in Figures 6.3 and 6.4. Simulation results obtained for $k_{notch} = 9000$ N/m for especially smaller inertance (0.020 kg) exhibit relatively large deviation compared to higher inertances. Using the theoretically obtained notch stiffness of 5020.3 N/m in the numerical simulation provides a better match for this inertance value. This can be attributed to the fact that increasing the load due to additional masses in the inerter bar also increases the stiffness because of a stress stiffening effect in the notch hinges.

Most of the experimental results in Figures 6.3 and 6.4 were consistently lower in magnitude compared to the numerical analyses. The reason for these lower magnitudes could be the additional damping introduced in several points of the structure. The living hinges and the connection between the prototype and the workpiece might have led to extra damping. Also, the damping property of the gel damper was tested for a complete horizontal motion of the sliding plate between the gel. However, the sliding plate was not able to move in a complete horizontal direction due to the imperfection in the assembly. Most importantly, clamping conditions of the workpiece to the worktable could introduce additional damping to the main system which leads to lower magnitudes.

In the modal tests, the real part responses of the prototype have also shown promising results in terms of chatter stability. The chatter stability performance of the prototype under actual cutting conditions will be evaluated in the following section.

6.3   Milling stability experiments

The chatter stability performance of the prototype is experimentally examined through milling tests. The aluminium workpiece (Al 7075-T6) is fixed to the table in the CNC machine and modal tests are conducted to determine the optimal design parameters through a similar optimisation procedure as in the vibration suppression case. The cutting stiffnesses that are required for the stability prediction of the stability analysis were identified. Finally, the cutting tests are conducted to validate the absolute stability improvement. The details of the experimental process will be explained below.

6.3.1   Identification of the cutting coefficients

Identification of the cutting stiffnesses was made from milling tests. For this, a 40x20x150 aluminium alloy block, which was the same material as the workpiece: Al 7075-T6, was directly attached to the dynamometer Kistler Type 9257B to measure the cutting forces in x and y directions. The cutting forces obtained from a half-immersion down milling operation were evaluated to estimate the cutting stiffness values of the material. The cutting tool with the diameter of 16 mm and 30° constant helix angle was utilised for the axial depth of cut of 1 mm, constant feed rate of 0.04 mm at 1500 rpm spindle speed.

The cutting force results indicated that the runout existed in the cut. Therefore, the cutting coefficients were determined using time-domain simulation [274], instead of using cutting forces for different feed rates [275]. Considering the tool runout, the tangential and radial cutting coefficients K_t and K_n were estimated as 660 N/mm^2 and 180 N/mm^2, respectively. Time-domain simulation obtained with these cutting

coefficients and the experimental cutting forces in both directions are presented in Figure 6.5. The steady-state portion in the time-domain simulation is compared with the experimental results. The time lag between the two results in Figure 6.5 is manually adjusted so it is arbitrary.
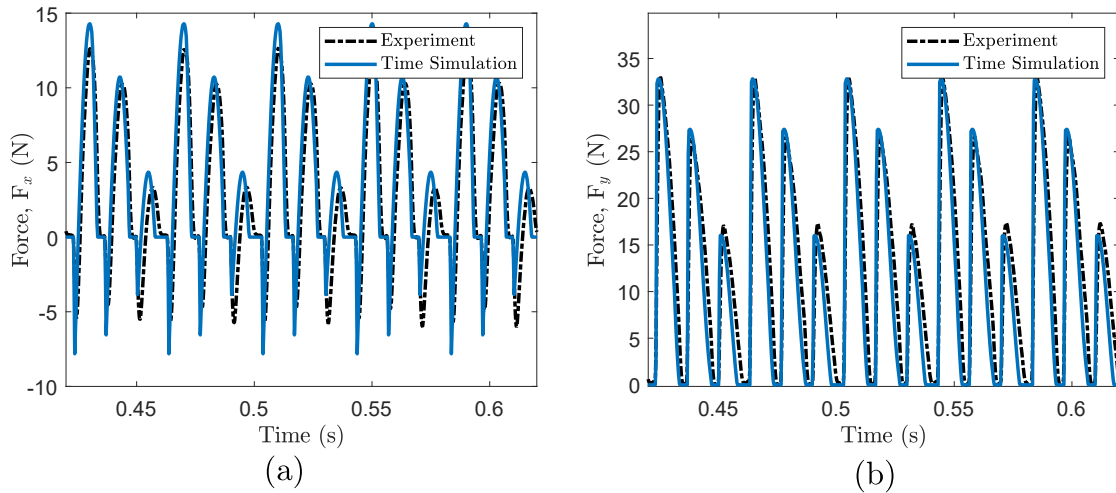

Figure 6.5 Cutting forces obtained in the x (a) and y (b) directions by the dynamometer for half immersion down milling with 1 mm axial depth of cut at 1500 rpm. The experimental results are in comparison with time domain simulation.
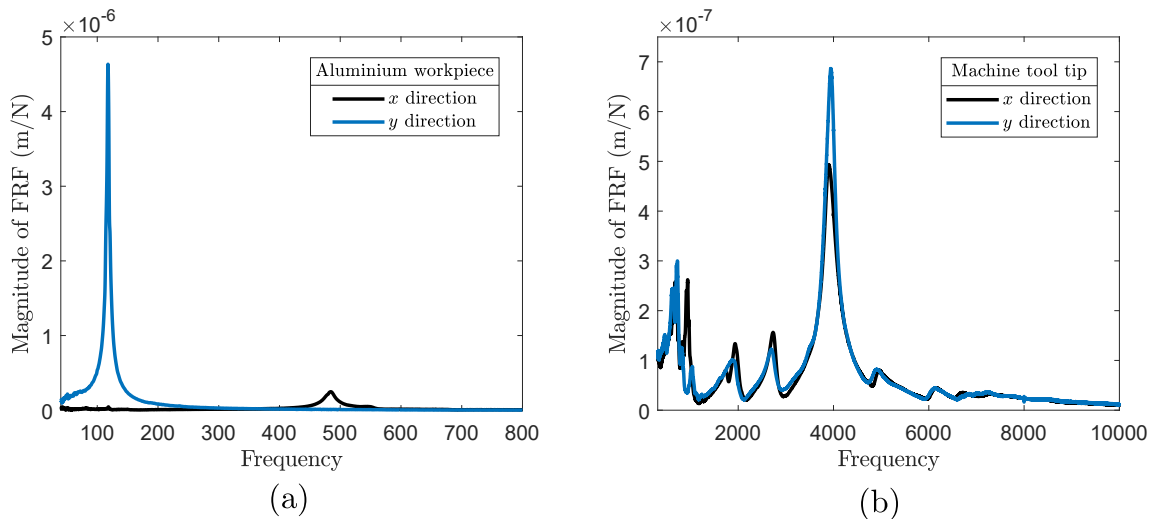
Figure 6.6 Frequency responses obtained by the impact hammer tests from (a) the aluminium workpiece and (b) the tip of the machine tip.

6.3.2 Optimal design parameters for chatter stability

The impact hammer test identified the dynamic properties of the aluminium workpiece. The modal tests were conducted for the workpiece with the prototype as well as the tip of the end mill in both horizontal directions (x and y) to assure that the dominant mode in the machining system is the horizontal y direction of the workpiece as designated. The results showed that other modes were adequately far away as shown in Figure 6.6 so that the milling system could be considered as an SDOF and the dominant mode can be assumed to be the only cause of the chatter instability. For the most flexible mode, the natural frequency, modal mass and the structural damping were obtained as 118 Hz, 10.7 kg and 1.9%, respectively. The possible reason for the slight change in the natural frequency and the damping ratio between tests in the CNC machine and the laboratory, where the previous impact tests are conducted, is the clamping conditions that were provided with different clamping equipment in the two tests.

The chatter stability performance depends on the real part of the SDOF structure transfer function $G(j\omega)$. For the experimental verification, the chatter stability improvement was considered as the absolute stability border (a_{lim}). Also, only down milling operations were conducted in the milling trials. As a result, the chatter stability performance of the system depends on the most negative real part as explained. Hence, the objective function can be expressed as

$$J_{cs} = -max\Big(\big|\mathfrak{Re}(G(j\omega))\big|\Big) \tag{6.2}$$

where $\mathfrak{Re}(G(j\omega)) < 0$ is considered. By assigning a negative sign into Equation 6.2, the objective function can be optimised to maximise the objective value.

Table 6.2 Optimal design parameters for the most negative real part of the FRFs determined by performing SaDE for the notch stiffnesses of 0 and 9000 N/m. $\mathfrak{Re}(\mathrm{H})_{min}$ represents for the most negative value of the real part in the FRF obtained from numerical optimisation.

	k_o (kN/m)	k_i (kN/m)	η	b (kg)	$\mathfrak{Re}(\mathrm{H})_{min}$ (m/N)
D2 ($k_{notch} = 0$)	273.10	22.39	0.4557	0.013	-3.33×10^{-7}
D2 ($k_{notch} = 9$ kN/m)	268.93	25.80	0.6087	0.038	-3.36×10^{-7}
D2 ($k_{notch} = 9$ kN/m)	251.89*	24.97*	0.5217*	0.038	-3.72×10^{-7}

*constrained parameters

Considering the mass ratio of $\mu = 0.037$ and $\beta = 0.066$ (for a parasitic mass of 0.026 kg due to the sliding plate), the optimal design parameters were determined for both notch stiffnesses of zero and 9000 N/m as presented in Table 6.2. Considering the differences between the optimal values for $k_{notch} = 9000$ N/m and the actual values of the control elements manufactured, the optimal inertance was also determined by constraining all parameters but the inertance to their actual values.

The real part of the response for each case obtained from numerical simulation is illustrated in Figure 6.7a compared to the uncontrolled case (black dotted line) and a classical TMD (black dashed line). In comparison, the TMD was numerically optimised for the same mass ratio considering the structural damping in the main system. Possible performances can be commented on from the real part responses. The unconstrained optimal design parameters regardless of whether the notch stiffness is zero (green solid line) or 9000 N/m (orange dash-dotted line) provides considerable improvement compared to a classical TMD by increasing the real part responses from 4.32 x 10^{-7} m/N to -3.33 x 10^{-7} m/N and -3.36 x 10^{-7} m/N, respectively. When the actual values of the control elements are considered (blue dash-dotted line), the performance reduces because of the detuning effect. However, significant stability improvement (16.1% considering the absolute stability limit) compared to TMD performance is achievable

only by adjusting the inertance. The most negative real part of the experimental FRF was measured -3.65 x 10^{-7} m/N, which indicated slightly better performance than the numerical simulation (-3.72 x 10^{-7} m/N).

Figure 6.7b presents the experimental results of the real part of the frequency response (solid red line) compared to uncontrolled structure, TMD and the expected response (blue dash-dotted line). Using these FRFs, the stability lobe diagrams obtained are presented in Figure 6.8. According to these stability limits, a classical TMD can already improve the absolute stability limit (a_{lim}) from 0.76 mm to 3.85 mm. The expected FRF has improved the absolute limit to 4.46 mm. It is worth pointing out that although this limit was 4.87 mm in theory, it has been reduced due to the actual values of the control elements. Finally, the stability limit was estimated from the measured FRF as 4.51 mm. The validation was made through milling tests.

6.3.3   Milling tests

6.3.3.1   Experimental method

The aluminium block fixed to the table of the CNC machine and the experimental setup is presented in Figure 6.9. The prototype was attached to the workpiece to control the vibration in the most flexible mode, which was the y direction of the workpiece. The vibration of the workpiece in the y direction was measured by the accelerometer PCB353B18 from the side of the workpiece. One revolution of the spindle speed was identified through a hall effect sensor attached to the spindle facing the tool holder at a proximity. The change in the sensor's voltage due to two slots on the tool holder was
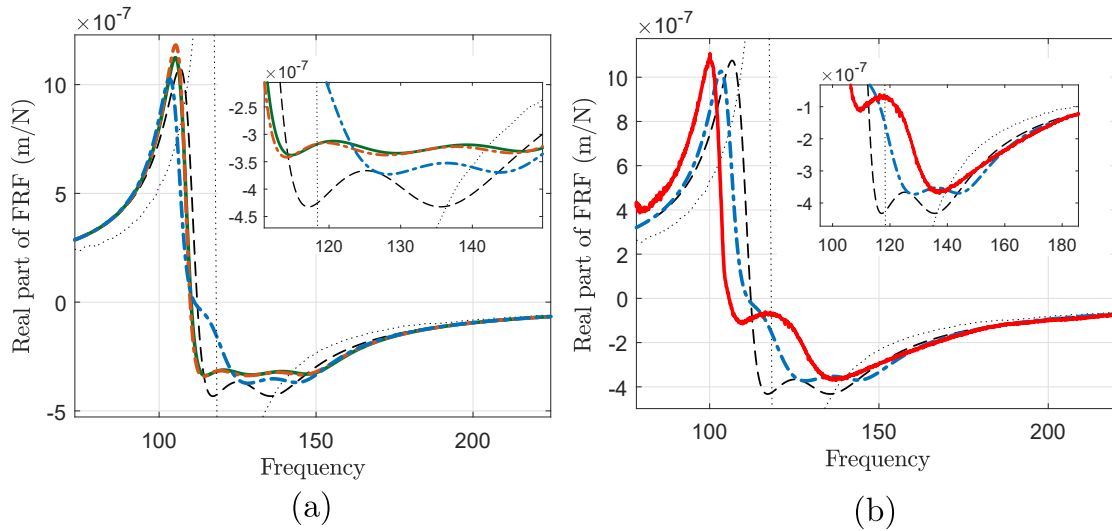
Figure 6.7 Real part of the FRFs obtained from the numerical simulations using the design parameters in Table 6.2 in (a). The real part response obtained from the impact hammer test is in comparison with the real part responses of the uncontrolled structure, numerically obtained TMD and IDVA-D2 obtained for the optimal design parameters for the actual values of the components in (b). $\cdots$ Uncontrolled structure, (- - -) TMD, (——) IDVA-D2 optimised for $k_{notch} = 0$, (-·-·-) IDVA-D2 optimised for $k_{notch} = 9000N/m$, (-·-·-) IDVA-D2 optimised for $k_{notch} = 9000N/m$ constraining parameters to the actual values of the components, and (——) experiment.
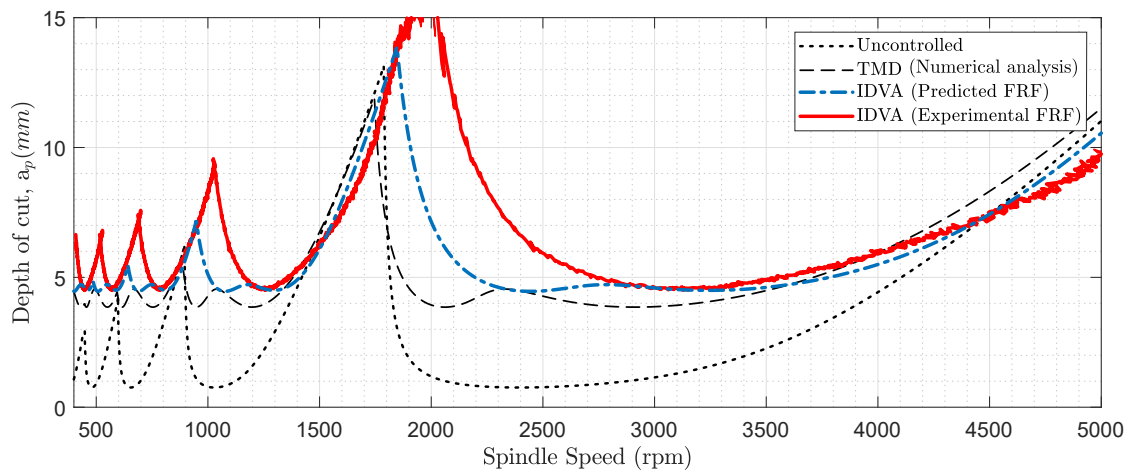
Figure 6.8 Stability lobe diagrams obtained from the real part of the FRF in Figure 6.7 including the experimental FRF

recorded during the rotation of the spindle. The NI DAQ USB-4431 acquired both data.
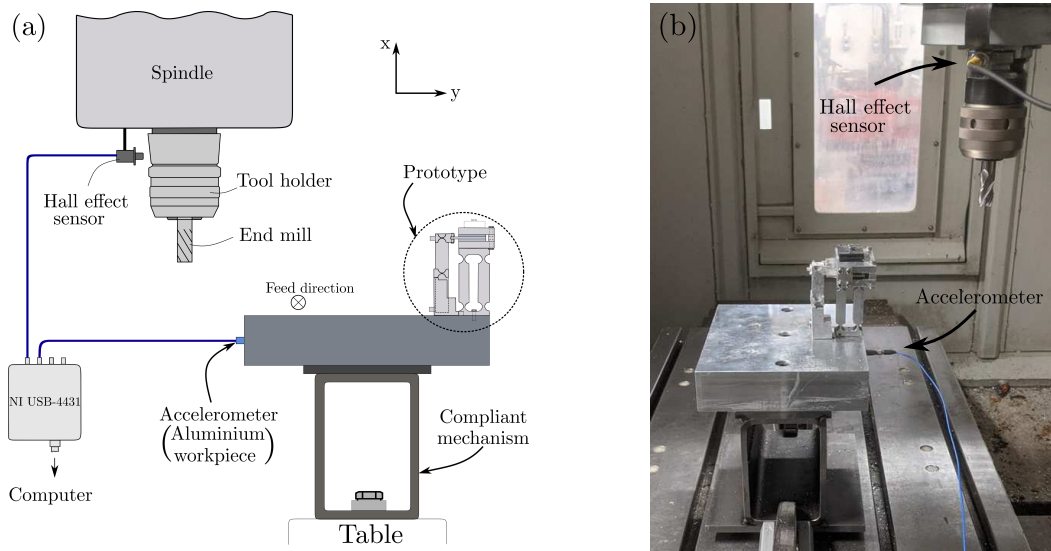
Figure 6.9 Experimental setup of the milling test: (a) an illustration of the setup showing the locations of the accelerometer and the hall effect sensor, and (b) an image of the setup.

The properties of the cutting tool and the cutting parameters of the down milling for all cuts are given in Table 6.3. The dimensions of the workpiece were the length of 250 mm, the width of 200 mm and the height of 50 mm. The cutting operations were conducted from only one side opposite the location of the prototype. Each cut was made for constant 50 mm length and 8 mm radial immersion of the cutting tool while the axial depth of cut was set for each cut. The feed direction of the end mill was into the page as shown in Figure 6.9. The maximum material removal from the workpiece was set to not exceed the change of the natural frequency of the uncontrolled structure more than 1% by considering the formula of the natural frequency:

$$1 < \sqrt{\frac{M}{M - \Delta M}} < 1.01 \tag{6.3}$$

where M and ΔM are the modal mass of the uncontrolled structure and the mass of the removal material. Consequently, the maximum material removal was calculated 0.210 kg per workpiece.

Table 6.3 Milling parameters for cutting tests

Tool diameter	16 mm
Radial immersion	8 mm
Number of teeth	4
Helix angle	30° (constant)
Feed per tooth	0.04 mm

6.3.3.2   Chatter detection methods

The FFT spectrum and once per revolution sampling are two methods that have been frequently utilised for chatter detection. In a milling operation with non-zero runout, the measured signal is expected to be periodic at the tooth passing frequency, $f_{tp} = N_t N/60$ (where N and N_t are the spindle speed in the unit of rev/min and the number of teeth, respectively) and its harmonics. If runout exists in a milling operation, the measured signal also involves the spindle rotation frequency, $f_s = N/60$, and its harmonics [289]. Any frequency other than these in the frequency response indicates chatter [289, 290]. Hence, the detection of the onset chatter can be made by taking the FFT spectrum.

The once per revolution sampling technique is based on the synchronised sampled signal in stable cutting [291, 292]. This method was introduced by Davies et al. [291] with a Poincaré map showing the $x-$ and $y-$directions motions of tool sampled once per revolution. The tool is located almost the same position in each revolution in steady-state conditions for a stable cut. Thus, after initial transient motion, the sample point repeats for each revolution of the spindle in a stable cut while it shows variations

in the case of chatter. This can be observed as synchronised data points in a stable cut or distributed data points in chatter scenarios, in the time domain output of the signal sampled once per revolution. Alternatively, this technique can be visualised with a Poincaré map whose the $x-$ and $y-$axes indicates the current and previous motions of the tool. In the maps, a small cluster of the data points indicates a synchronised motion and thus stable cut, while a distributed cluster is the indicator of chatter.

The FFT spectrum and once per revolution sampling were employed to detect the chatter for the cutting tests in this thesis. Both techniques were applied after the completion of each cut as an out-of-process technique and acceleration of the workpiece was used as the measured signal. The two visualisations methods, time-domain plot and Poincaré map were utilised for once per revolution sampling.

6.3.4   Results

The aim was to verify the absolute stability of the structure with the prototype considering only the first lobe in the milling tests. The stability border was first experimentally verified for the spindle speed of 2800 rpm with the depth of cut starting from 3 mm to 5 mm. Later, cuts were extended for the lower and upper spindle speeds from 2400 rpm to 4200 rpm as shown in Figure 6.10. The location of the stability pocket was verified with the cuts at 2200 rpm. Stable cut examples A(2200 rpm, 7 mm) and B(3400 rpm, 4.6 mm), chatter example C(3400 rpm, 5 mm) are presented in Figure 6.11. Data points sampled once per revolution in Figure 6.11 verify stable cutting operations for A(2200 rpm, 7 mm) and B(3400 rpm, 4.6 mm) as they indicate synchronised data points. The Poincaré map regarding these cuts shows a tight cluster of data points. Also, only the tooth passing frequencies, spindle rotation frequencies,

their harmonics are observed in the FFT spectrum regarding these cuts. Unlike stable cuts A(2200 rpm, 7 mm) and B(3400 rpm, 4.6 mm), the cut C(3400 rpm, 5 mm) has a distributed (unsynchronised) data point in the time domain plot and the Poincaré map, which the evidence of the occurrence of chatter. The chatter frequency also appears in the FFT spectrum.

Also, the stability of the uncontrolled and the controlled structures was compared for 2800 rpm. As it can be seen in Figure 6.12, the stable cut observed with 0.8 mm depth of cut D(2800 rpm, 0.8 mm) turns into an unstable cut by increasing the depth of cut to 1.2 mm E(2800 rpm, 1.2 mm) for the uncontrolled structure. In the controlled case for the same spindle speed, the stable cut was achieved until 4.4 mm depth of cut (F(2800 rpm, 3 mm) and G(2800 rpm, 4.4 rpm)). The chatter occurred for 4.8 mm H(2800 rpm, 4.8 mm). Like in Figure 6.11, the evidence of chatter in Figure 6.12 can be observed from once per revolution and the FFT spectrum for the cuts E(2800 rpm, 1.2 mm) for the uncontrolled structure and H(2800 rpm, 4.8 mm) for the controlled structure. It can be clearly seen from the figure that the chatter occurring for depth of cut of 1.2 mm for uncontrolled structure was suppressed with the attachment of the prototype as the results for depth of cuts of 3 mm and 4.4 mm for the controlled structure suggested. All experimental results regarding the cuts presented in Figure 6.10 are given in Appendix F. The results will be discussed in the following section.
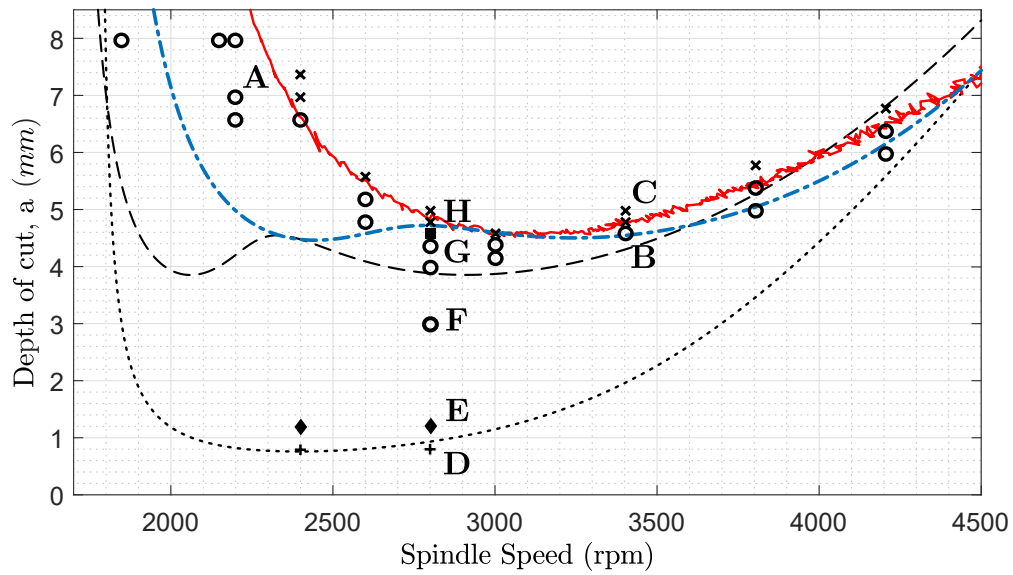
Figure 6.10 Stability lobe diagrams with the experimental cuts. (······) Uncontrolled, (- - -) TMD, (-·-·-) IDVA(predicted FRF), (——) IDVA(experimental FRF), (+) stable cut (uncontrolled), (♦) chatter (uncontrolled), (◦) stable cut (controlled), (■) marginal cut (controlled), (×) chatter (Controlled).

6.3.5   Discussion

From the experimental results, three key points could be remarked on. First of all, the milling tests were verified that the prototype can effectively operate and provide a very close performance to the stability limit obtained from the experimental FRF from the impact hammer test. This indicates that the prototype's dynamic behaviour was not affected from the actual cutting conditions in stable cuts. This was important in terms of the applicability of the design for the milling operations.

Chatter in the milling test was detected applying both once per revolution sampling and the FFT, as presented in Figures 6.11 and 6.12. Once per revolution sampling is based on the synchronised data points, which was observed as data points aligned in a straight line in time domain plot or a tight cluster of data points in the Poincaré
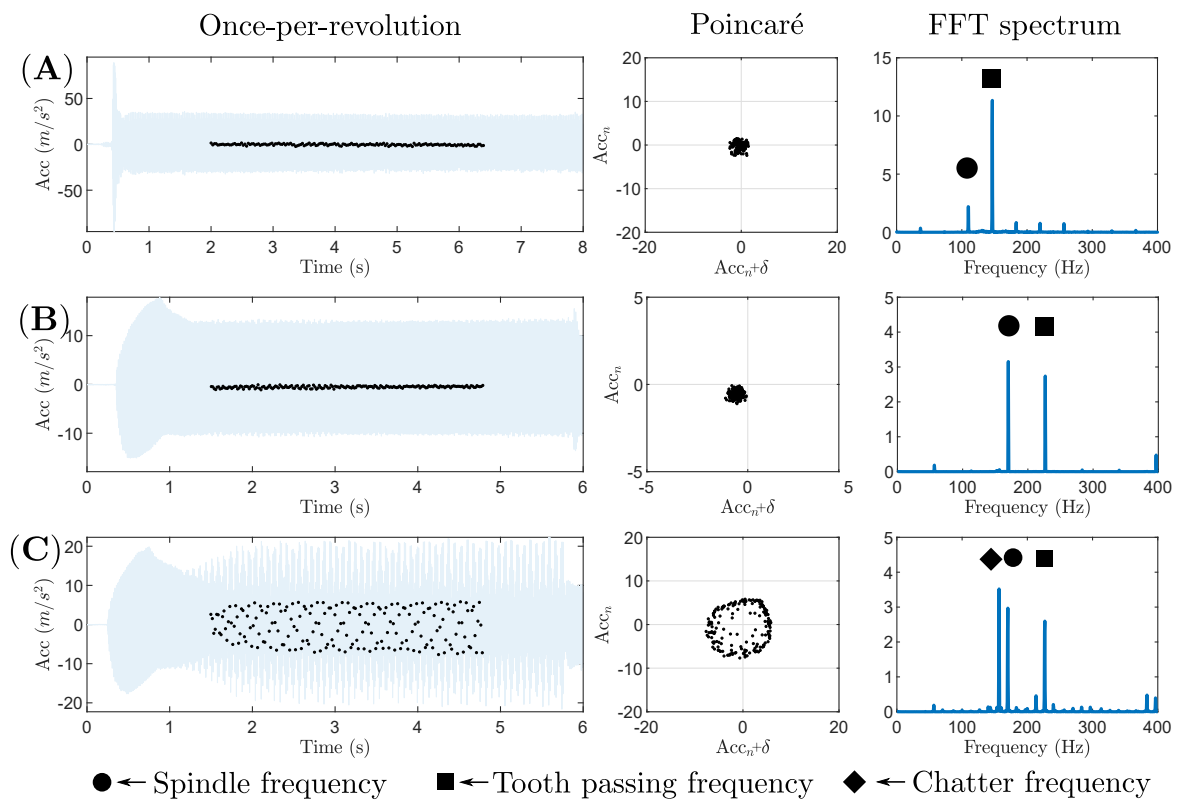
Figure 6.11 Once per revolution samples, the Poincaré maps and the FFT spectrums for chosen cuts: stable cut A(2200 rpm, 7 mm), stable cut B(3400 rpm, 4.6 mm), and chatter C(3400 rpm, 5 mm).
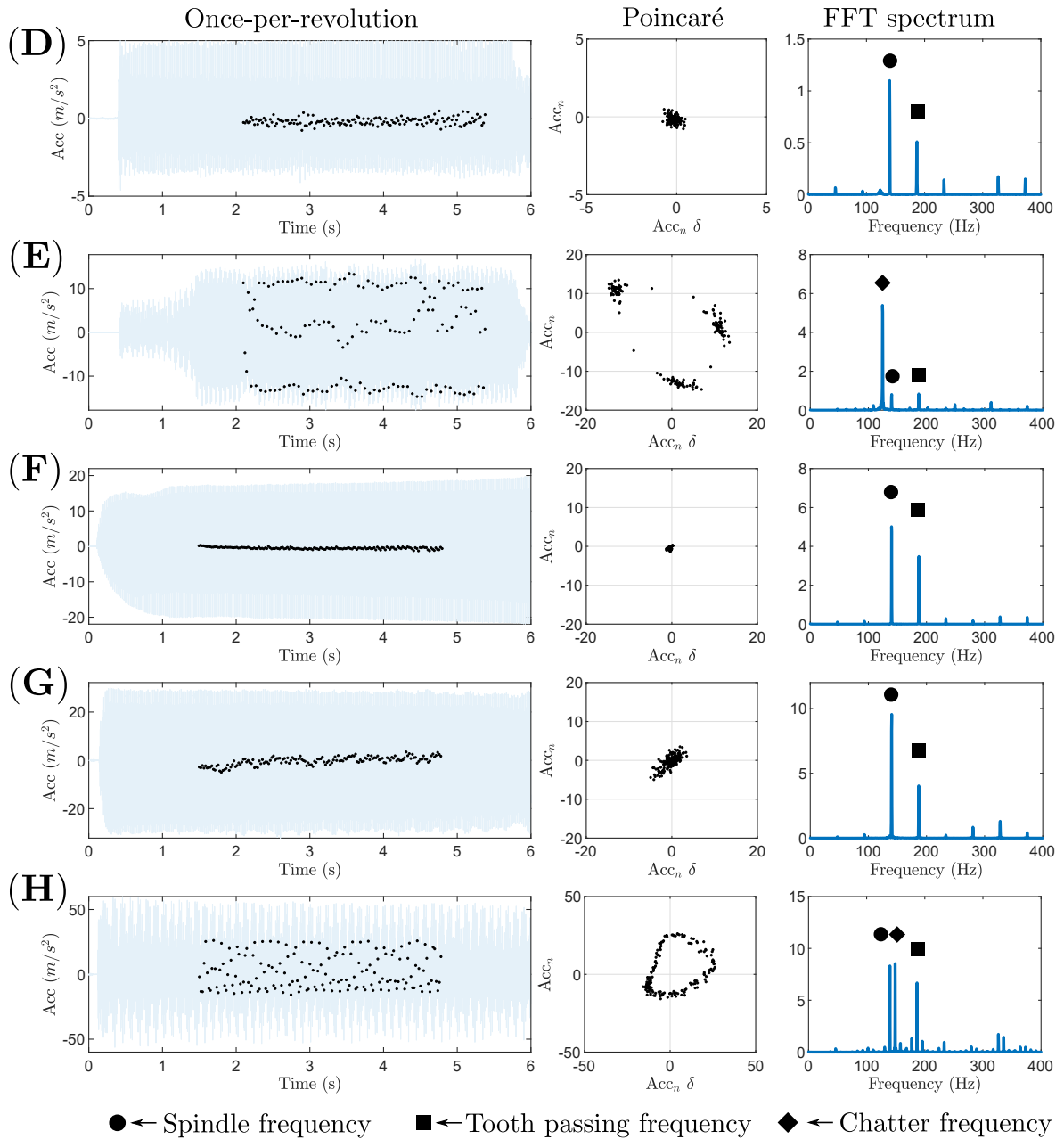
Figure 6.12 Once per revolution samples, the Poincaré maps and the FFT spectrums showing different axial depth of cut at 2800 rpm for uncontrolled and controlled cases. Uncontrolled structure: stable cut D(2800 rpm, 0.8 mm) and stable cut E(2800 rpm, 1.2 mm), and controlled structure: stable cut F(2800 rpm, 3 mm), stable cut G(2800 rpm, 4.4 mm) and chatter H(2800 rpm, 4.8 mm).

map in the case of a stable cut. The FFT spectrum of stable cut involved only the tooth passing frequency, the spindle rotation frequency (due to the existing runout in the tool) and their harmonics. In the case of chatter, unsynchronised data points in the time domain plot and large elliptic-shaped clusters in the Poincaré map were monitored. The chatter was also verified with the additional peak in the FFT spectrum other than the peaks appearing in the stable cut. The second important point is that the prototype was designed to improve the absolute stability and achieved the limited critical depth of cut of 4.4 mm, which is close to the numerical simulation obtained for the actual values of the control elements (blue dash-dotted line in Figure 6.10). This result improved the absolute stability by 14.3% compared to a classical TMD performance. This improvement was close to the simulation result obtained by using the actual design parameters (16.1%), as presented in Table 6.2. However, further improvement is possible by up to 28.6% with accurate actual design parameters as indicated in the simulation result. It is also worth noting that the amplitude of the acceleration in the first 6 seconds in the chatter cut E(2800 rpm, 1.2 mm) was lower than the amplitude in the stable cut G(2800 rpm, 4.4 rpm). However, the actual danger was the unstable behaviour of the cut E as the vibration would grow in time and become detrimental. On the other hand, the cut G would not show an increase in the vibration as it was a stable cut.

Finally, though the minimisation of the most negative real part of the response was achieved and the absolute stability limit was improved as expected, the negative real part showed a deviation from the numerical simulation between $120 - 135$ Hz. This led to an extra stable region in the stability pocket between especially $2000 - 2500$ rpm in the stability lobe diagram. Similar deviations were also observed in the exploratory modal tests in Figure 6.4.

It should also be noted that the excessive vibration in the case of chatter in the experiments was detrimental to the connection between the workpiece and the prototype. Therefore, the tests of the higher depth of cut with chatter were limited. These excessive vibrations could lead to breakage of the notch hinges due to uncontrolled higher rotation. Adding a stopper that limits to the rotation of the inerter bar after a certain level can be considered in the future to protect the notch hinges.

6.4   Summary

This chapter investigated experimental verification of the inerter-based absorber design through the prototype. The prototype was first tested, considering the vibration suppression case. It was shown that it could effectively suppress the vibration as expected. Then, further investigation was conducted with a series of modal tests where different inertances and auxiliary masses were considered. Both the magnitude and the real part of the FRFs obtained from the tests exhibited similar dynamic responses to the numerical simulations. These results presented the proof of the design concept proposed in Chapter 5.

The prototype was later examined under actual cutting conditions. Although the mass ratio was chosen to have optimal design parameters as close as possible to the actual design parameters, there were still differences between the actual and optimal design parameters. As setting the inertance was straightforward, the optimal inertance was optimised considering the actual values of the control elements. Despite the loss in the optimal performance, the impact hammer test result indicated 16% improvement

compared to the TMD. Similar improvement was also validated through the milling tests and it was shown that the prototype could effectively improve the chatter stability.

Chapter 7

Conclusions

7.1 Summary of thesis

Chapter 2 presented the literature review of both machining chatter stability and the inerter applications. In the part on machining chatter stability, the methods for stability prediction, including the ZOA and more advanced methods such as SDM and MFA, were reviewed. Later, the techniques to avoid and mitigate chatter were presented with a focus on passive methods. In the part of inerter after giving the initial works related to inerter, different realisations of the inerter device were presented. Three well-known inerter-based layouts (TID, TMDI and TVMD) and IDVA were evaluated with their applications.

Chapter 3 introduced the theoretical background of the milling stability analysis. The chapter explained the basic regenerative chatter mechanism with a simplified cutting operation where a single-point continuous cut was conducted in a turning operation.

The stability analysis was then extended to milling operation where the cutting occurs intermittently via a rotating cutting tool. The stability analysis of milling was presented using ZOA where the time-varying dynamic cutting coefficient due to rotating cutting tool is averaged to a constant term (zeroth order) of the Fourier series. The concept of the stability lobe diagram was also introduced in this chapter.

Chapter 4 numerically evaluated four different inerter-based layouts attached to an SDOF milling system as a localised addition. The layouts examined in this chapter were chosen from simple arrangements consisting of two springs, one inerter and one damper, by considering the physical realisation for experimental verification. After having presented the transfer function of each layout, the stability analysis was conducted by mostly evaluating the real part of the FRF. The main focus in the stability evaluation was the absolute stability, but also the stability enhancement in the stability pocket was examined. Moreover, the global sensitivity analysis of the design parameters of the best three layouts was made via Sobol's method. One of the objectives of the thesis was achieved in this chapter by numerically evaluating the performance of four different layouts of inerter-based passive control devices as localised additions in milling. All layouts investigated showed performance increment in milling stability.

Chapter 5 involved design studies considering the physical realisation of one of the layouts. It was shown that there were different factors to prevent achieving an ideal layout, as presented in Chapter 4. First, the parasitic mass effect, which was shown to be inevitable in real structures due to the mass of the components, was included and analysed to assess its effect on the performance of the layout. Using a gel damper, the realisation of the damping mechanism and the realisation of the inner spring in the layout was accomplished in a relatively simple way. Therefore, the effect of hysteretic damping behaviour of the gel on the effect of the performance was examined. A

small-scale small-amplitude inerter device with living hinges was also developed to apply the passive device into a milling operation. Finally, the effect of the stiffness of the living hinges on the inertance was shown at the working frequency near the resonance region of the inerter device with living hinges. As the developed inerter allowed the adjustment of the inertance by simply adding equal masses to the end of the inerter bar, the stiffness effect of the living hinges could be compensated for by an equivalent optimal inertance value. To achieve this, the stiffness of the living hinge was included in the mathematical model to optimise the design parameters in the experimental verifications. The importance of the fatigue analysis of the living hinges was also highlighted in this chapter since the living hinges were expected to be exposed to high frequency loading in milling applications. Employing the inerter device developed, the physical realisation of the layout with the above-mentioned modal updates was presented and the prototype was manufactured. Two objectives were met in this chapter by having developed an inerter device applicable to milling operations and by having designed an inerter-based passive control device that can be applied as a localised addition in a similar way to a classical TMD.

Chapter 6 demonstrated the experimental verification of the dynamic behaviour of the prototype and the improvement of the milling stability. Several modal tests for different inertances and auxiliary masses were conducted to validate whether the prototype reflects the dynamic behaviour obtained from the numerical simulations. The capability of vibration suppression of the prototype was also tested in one of the modal tests. Finally, the prototype attached to a workpiece with one flexible mode was tested through milling tests. Thus, the functionality of the prototype and the stability improvement was tested under actual cutting conditions. The chapter fulfilled two more objectives by testing the prototype's dynamic behaviour and validating the

functionality and the stability improvement of the proposed device under real cutting conditions.

Conclusions and contributions to knowledge will be discussed in the following section.

7.2   Conclusions and original contributions

Several conclusions from this research are drawn as follows:

- All four IDVAs tested can improve the absolute stability limit of milling compared to a classical TMD while the Layouts L1, L2 and L4 provide significant increments in the absolute stability. For the Layouts L1, L2 and L4, the performance improvement was generally more than 20% for almost all cases tested and it reached the maximum up to 40% for low structural damping and high mass ratios.

- The benefit of the use of an inerter in these layouts was limited for the first stability pocket enhancement. Comparing the TMD and IDVA whose design parameters are tuned for the same purpose considering the same mass ratio, no significant improvement was observed in terms of maximising of the deepest possible lobe. The only benefit of using an IDVA in this scenario was to broaden the spindle speed band for a higher stable depth of cut.

- The global sensitivity analysis has shown that the most sensitive parameter to the absolute stability limit is the outer spring k_o regardless of layouts. This analysis was important because it showed the element to which the most care

should be taken to avoid the performance loss due to the deviation of the actual parameters from the optimal ones.

- Optimal design parameters obtained via SaDE showed that the optimal inertance is tiny for the IDVAs with the best performances for small mass ratios. This primarily requires attention to be paid to the parasitic mass effect that becomes apparent even with small values and the design of the inerter device capable of producing such small inertance.

- Physical realisation of the idealised L2 for a small mass ratio is difficult due to parasitic mass effect. However, it has been presented that including the parasitic mass effect in the model and replacing the viscous damping with the hysteretic damping did not lead to performance loss. The IDVA with the parasitic mass and the hysteretic damping (IDVA-D2) provided an identical performance to the idealised IDVA-L2.

- A prominent feature of the new design of the inerter device is that it allows adjusting the inertance for fine tuning by simply adding equal lumped masses to both end of the inerter bar. The benefit of this feature was presented in the experimental study of the vibration case, where the possible performance loss due to notch stiffness was compensated for by adjusting the inertance. The inerter device, which was designed as an ad hoc solution for the localised addition, can produce small inertance in practice. However, for application with higher inertance, the design in Figure 5.11a with small l_a, which is similar to living-hinge inerter in [207] but with adjustable inertance, is suggested.

- Fatigue life analysis and the effect of the stiffness of the living-hinges have shown that implementation of the living-hinges with smaller notch thickness is beneficial in increasing the fatigue life cycle and reducing the effect of the notch stiffness.

- The proposed design of the IDVA functions as an inerter-based absorber. This was tested through the modal tests considering different combinations of the auxiliary mass and inertance. The absolute stability improvement was also verified with milling tests, albeit some reduction in the improvement due to deviation between the optimal design parameters and their actual values. It was also noted that the experimental stability limits showed an extra stable region in the pocket stability compared to numerical stability analysis. This was due to deviation in the experimental frequency response in the real part of the system transfer function. However, the experimental results of the cutting test matched well with the stability limit created using the experimental FRF of the workpiece controlled by the prototype. This indicates that the prototype shows similar performance to the modal test under actual cutting conditions for stable cuts. However, excessive vibration for unstable cuts beyond the stability limit can be a challenging issue to maintain healthy connection of the prototype to the workpiece.

The major contributions of the research to knowledge are outlined as follows:

- Chatter stability performance of using inerters in machining operation has been evaluated for the first time. Although Wang et al. [5] presented some advantages of utilising inerters for vibration suppression for milling machines with experiments, their approach did not include the consideration of the regenerative chatter mechanism and the stability analysis. In this thesis, the vibration problem in milling operation has been approached as a chatter stability problem and the analyses have been conducted in this direction.

- The design parameters of the TMD and IDVAs have been numerically tuned for the enhancement of the stability pocket, unlike traditional tuning methods of Sims [108] and Den Hartog [107]. Even the TMD improved the largest stable point in the stability border, albeit for a narrow spindle speed band. Optimising the parameters to enhance the stability lobe diagram can be beneficial for the cut conducted in the stability pocket range.

- A mechanical small-scale inerter device with adjustable inertance has been developed. The adjustment is as simple as attaching additional masses to the inerter bar and it can be used for fine tuning the inertance.

- A new absorber design for the physical realisation of the layout consisting of two springs, one inerter and one damper has been proposed. The new design is applicable in a similar manner to a classical TMD without the need for a grounded connection or deployment between two components of the host structure. Therefore, it provides a potentially more versatile solution for chatter as well as vibration absorption problems.

- Finally, the absolute stability improvement has been experimentally validated through milling tests. This was the first experimental study of the inerter that considers chatter stability in milling as presented in the literature of the machining community.

To date, these contributions to knowledge have been disseminated via three conference papers, along with a journal paper that is currently under review. These publications are listed in Appendix G

7.3   Discussion and future works

There are some limitations for the use of inerter and the absorber presented in this study. Firstly, the absorber was designed for the workpiece and it cannot be applied to the rotating tool. Secondly, the rotation of the inerter is allowed to a certain angle. The high rotational angle of the inerter reduces the fatigue life of the absorber. Moreover, the inerter does not show a linear behaviour due to the violation of the small-angle approximation applied in the design study. Lastly, the absorber can act only in one direction so the chatter suppression provided by the absorber is limited to SDOF systems.

The analysis and experiments have shown that there is an effect of the notch stiffness on the inertance. The notch stiffness in practice was higher than the theoretical estimation. Possible reasons for this were noted as the manufacturing errors and the stress stiffening effect. Even though this increase in stiffness might be problematic in practice, the performance loss can be compensated for by adjusting the inertance. Indeed, the effect of the stiffness would be almost entirely eliminated with very thin notch thickness. However, this was limited to manufacturing technology. Although the notch stiffness is undesirable to achieve a pure inerter, it did not significantly reduce its effect in practice. The use of designated notch stiffness can be promising to realise an inerter-spring arrangement. The analysis of this has remained as future work. In the case of zero stiffness in the notch, the pivoted-bar acts as a pure inerter whilst it becomes a cantilever beam acting as a spring in the case of elimination of the notch completely. These two marginal cases of the pivoted-bar present a transition from an inerter to a spring element. Applying a continuum mechanics, the pivoted-bar can be designated as an inerter-spring arrangement with desired inertance and stiffness.

Fatigue analysis showed that higher notch thickness leads to a reduction in fatigue life due to increasing stress. This analysis was presented theoretically. However, as the experimental part of this project was considered the proof of concept of the absorber design, the fatigue analysis results have not been experimentally verified. In future work, this verification can easily be provided with an experiment setup where the notch is exposed to a controlled cyclic load and the number of fatigue life cycles is recorded.

The scale of the application in this project was small compared to other experimental studies in the literature regarding inerter. The design concept is promising for even much smaller applications. However, this also needs experimental verification with a smaller prototype. The monolithic design of the whole absorber is possibly more beneficial in terms of performance and application, although its manufacture might be more challenging. The application of a much smaller prototype with a monolithic design can be considered as another future work. For this, a similar workpiece with a smaller modal mass can be employed, and additive manufacturing might be considered for the manufacturing of the monolithic design, albeit with cost implications.

In numerical evaluations, the enhancement of the stable region in the stability pocket was examined but was not experimentally tested. The experimental verification of this enhancement for both TMD and IDVA has remained in future work. Implementing this kind of verification requires a new prototype with the optimal design parameters addressing this objective. Then, the similar verification process presented in Chapter 6 can be considered to show its effectiveness. Also, the experimental verifications of the prototype used in this thesis can be extended to milling tests with low radial immersions, which has not been considered in this project.

Appendix A

Expressions for dimensionless transfer functions

$$A_{L1} = -2\delta\alpha^2\gamma^2\Omega^2\zeta_a + 2\alpha^2\gamma^4\zeta_a - 2\alpha^2\gamma^2\Omega^2\zeta_a - 2\gamma^2\Omega^2\zeta_a + 2\Omega^4\zeta_a$$

$$B_{L1} = \delta\alpha^2\gamma^3\Omega - \delta\alpha^2\gamma\Omega^3$$

$$C_{L1} = 2\delta\alpha^2\gamma^2\Omega^4\mu\zeta_a + 2\delta\alpha^2\gamma^2\Omega^4\zeta_a - 2\alpha^2\gamma^4\Omega^2\mu\zeta_a - 2\alpha^2\gamma^4\Omega^2\zeta_a + 2\alpha^2\gamma^2\Omega^4\zeta_a - 2\delta\alpha^2\gamma^2\Omega^2\zeta_a$$
$$+ 2\gamma^2\Omega^4\mu\zeta_a + 2\alpha^2\gamma^4\zeta_a - 2\alpha^2\gamma^2\Omega^2\zeta_a + 2\gamma^2\Omega^4\zeta_a - 2\Omega^6\zeta_a - 2\gamma^2\Omega^2\zeta_a + 2\Omega^4\zeta_a$$

$$D_{L1} = -\delta\alpha^2\gamma^3\Omega^3\mu - \delta\alpha^2\gamma^3\Omega^3 + \delta\alpha^2\gamma\Omega^5 + \delta\alpha^2\gamma^3\Omega - \delta\alpha^2\gamma\Omega^3$$

$$A_{L2} = -\delta^2\alpha^2\gamma^2\Omega^2 + \delta\alpha^2\gamma^4 - \delta\alpha^2\gamma^2\Omega^2 - \delta\gamma^2\Omega^2 + \delta\Omega^4$$

$$B_{L2} = -2\delta\gamma\Omega^3\zeta_a + 2\gamma^3\Omega\zeta_a - 2\gamma\Omega^3\zeta_a$$

$$C_{L2} = \delta^2\alpha^2\gamma^2\Omega^4\mu + \delta^2\alpha^2\gamma^2\Omega^4 - \delta\alpha^2\gamma^4\Omega^2\mu - \delta\alpha^2\gamma^4\Omega^2 + \delta\alpha^2\gamma^2\Omega^4 - \delta^2\alpha^2\gamma^2\Omega^2$$
$$+ \delta\gamma^2\Omega^4\mu + \delta\alpha^2\gamma^4 - \delta\alpha^2\gamma^2\Omega^2 + \delta\gamma^2\Omega^4 - \delta\Omega^6 - \delta\gamma^2\Omega^2 + \delta\Omega^4$$

$$D_{L2} = 2\delta\gamma\Omega^5\mu\zeta_a + 2\delta\gamma\Omega^5\zeta_a - 2\gamma^3\Omega^3\mu\zeta_a - 2\gamma^3\Omega^3\zeta_a + 2\gamma\Omega^5\zeta_a - 2\delta\gamma\Omega^3\zeta_a + 2\gamma^3\Omega\zeta_a - 2\gamma\Omega^3\zeta_a$$

$$A_{L3} = \delta\alpha^2\gamma^4 - \delta\alpha^2\gamma^2\Omega^2 - \delta\gamma^2\Omega^2 + \delta\Omega^4$$

$$B_{L3} = 2\delta\alpha^2\gamma^3\Omega\zeta_a - 2\delta\gamma\Omega^3\zeta_a + 2\gamma^3\Omega\zeta_a - 2\gamma\Omega^3\zeta_a$$

$$C_{L3} = -\delta\alpha^2\gamma^4\Omega^2\mu - \delta\alpha^2\gamma^4\Omega^2 + \delta\alpha^2\gamma^2\Omega^4 + \delta\gamma^2\Omega^4\mu + \delta\alpha^2\gamma^4 - \delta\alpha^2\gamma^2\Omega^2 + \delta\gamma^2\Omega^4$$
$$- \delta\Omega^6 - \delta\gamma^2\Omega^2 + \delta\Omega^4$$

$$D_{L3} = -2\delta\alpha^2\gamma^3\Omega^3\mu\zeta_a - 2\delta\alpha^2\gamma^3\Omega^3\zeta_a + 2\delta\gamma\Omega^5\mu\zeta_a + 2\delta\alpha^2\gamma^3\Omega\zeta_a + 2\delta\gamma\Omega^5\zeta_a - 2\gamma^3\Omega^3\mu\zeta_a$$
$$- 2\gamma^3\Omega^3\zeta_a + 2\gamma\Omega^5\zeta_a - 2\delta\gamma\Omega^3\zeta_a + 2\gamma^3\Omega\zeta_a - 2\gamma\Omega^3\zeta_a$$

$$A_{L4} = -\delta^2\alpha^2\gamma^2\Omega^2 + \delta\alpha^2\gamma^4 - \delta\alpha^2\gamma^2\Omega^2 - \delta\gamma^2\Omega^2 + \delta\Omega^4$$

$$B_{L4} = 2\delta\alpha^2\gamma^3\Omega\zeta_a + 2\gamma^3\Omega\zeta_a - 2\gamma\Omega^3\zeta_a$$

$$C_{L4} = \delta^2\alpha^2\gamma^2\Omega^4\mu + \delta^2\alpha^2\gamma^2\Omega^4 - \delta\alpha^2\gamma^4\Omega^2\mu - \delta\alpha^2\gamma^4\Omega^2 + \delta\alpha^2\gamma^2\Omega^4 - \delta^2\alpha^2\gamma^2\Omega^2$$

$$+ \delta\gamma^2\Omega^4\mu + \delta\alpha^2\gamma^4 - \delta\alpha^2\gamma^2\Omega^2 + \delta\gamma^2\Omega^4 - \delta\Omega^6 - \delta\gamma^2\Omega^2 + \delta\Omega^4$$

$$D_{L4} = -2\delta\alpha^2\gamma^3\Omega^3\mu\zeta_a - 2\delta\alpha^2\gamma^3\Omega^3\zeta_a + 2\delta\alpha^2\gamma^3\Omega\zeta_a - 2\gamma^3\Omega^3\mu\zeta_a - 2\gamma^3\Omega^3\zeta_a + 2\gamma\Omega^5\zeta_a$$

$$+ 2\gamma^3\Omega\zeta_a - 2\gamma\Omega^3\zeta_a$$

Appendix B

Fixed-point technique for IDVAs

Five the damping-ratio-invariant fixed points have been identified for each layout as shown in Figures B.1a, B.2a, B.3a, and B.4. All fixed points are called P1-P5 from left to right. In the fixed-point technique, analytical expressions that give the optimal design parameters are analytically obtained. However, although the analytical solutions for the fixed point frequencies were obtained, further implementation of the technique could not be taken due to the extensive number of terms stemming from the roots of the cubic equation. Therefore, substituting the fixed point frequencies into the function, giving the real values of the transfer function, could not be succeeded. The fixed points were numerically taken equal instead in order to evaluate the possible use of the fixed points.

Considering only equal real troughs for $\zeta_m = 0$, the design parameters (γ, δ, and α) except the damping ratio ζ_a were optimised to make some of the fixed points equal. Two cases where the four fixed points from P2 to P5 and the three fixed points from P3 to P5 are taken equal were examined. After finding the optimal values for the three

design parameters γ, δ, and α, the optimal damping ratio was obtained by considering the maximisation of the most negative real part value as the optimisation objective. The results for both cases for the Layouts L1, L2 and L4 are presented in Figures B.1b-c, B.2b-c, and B.3b-c, respectively. The results are also compared with the TMD tuned with Sims' method [108] in Figures B.1d, B.2d, and B.3d.

The results showed that using the fixed-point technique, applied by taking three and four fixed points equal in this study provided very limited improvement compared to the TMD. The numerical optimisation applied without considering the fixed points (indicated with the legend 'H$_\infty$') presented a better performance than the fixed-point technique. The result of the Layout L3 is not presented since the fixed-point technique as it was applied in this study showed no improvement compared to the TMD. Therefore, only the existence of the fixed points is demonstrated in Figure B.4.
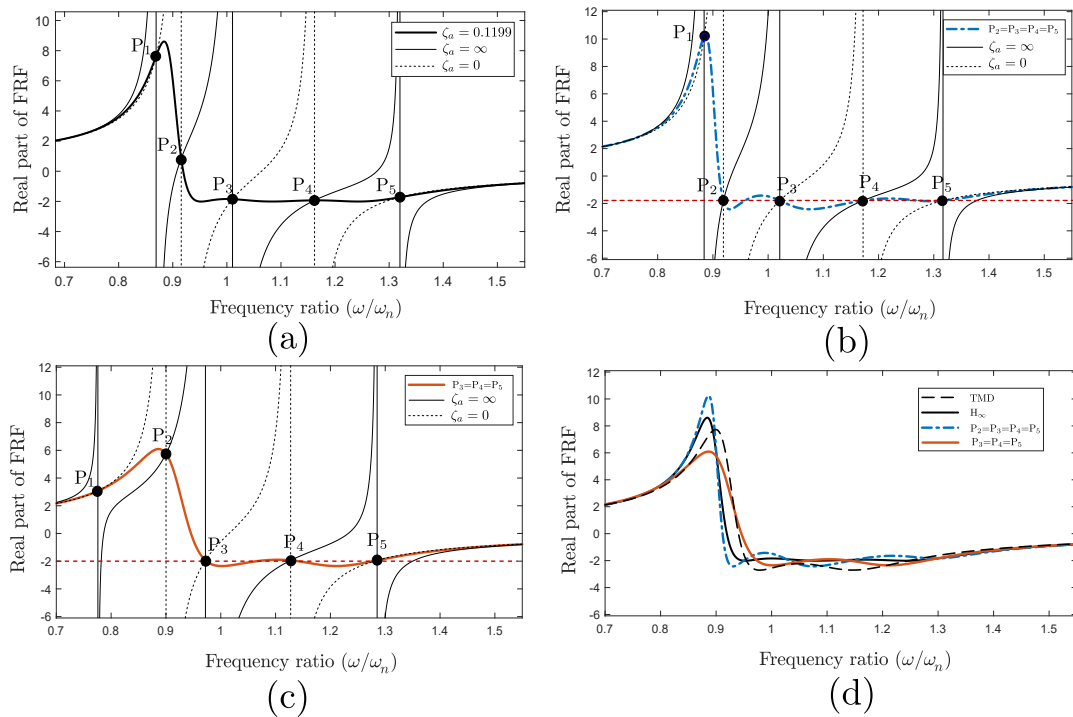
Figure B.1 Fixed-point technique for the Layout L1 where (a) indicates the fixed points. The fixed-point techniques are apply for four equal fixed points from P2 to P5 in (b) and three equal fixed points from P3 to P5 in (c). The results are compared with the TMD tuned with Sims' method [108].
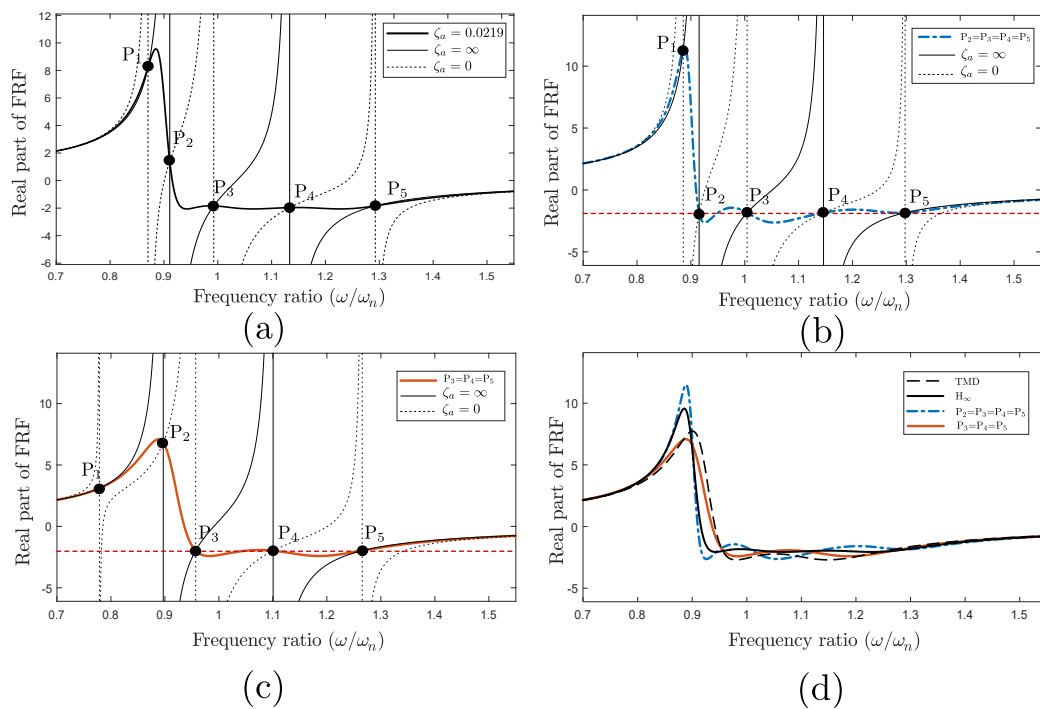
Figure B.2 Fixed-point technique for the Layout L2 where (a) indicates the fixed points. The fixed-point techniques are apply for four equal fixed points from P2 to P5 in (b) and three equal fixed points from P3 to P5 in (c). The results are compared with the TMD tuned with Sims' method [108].
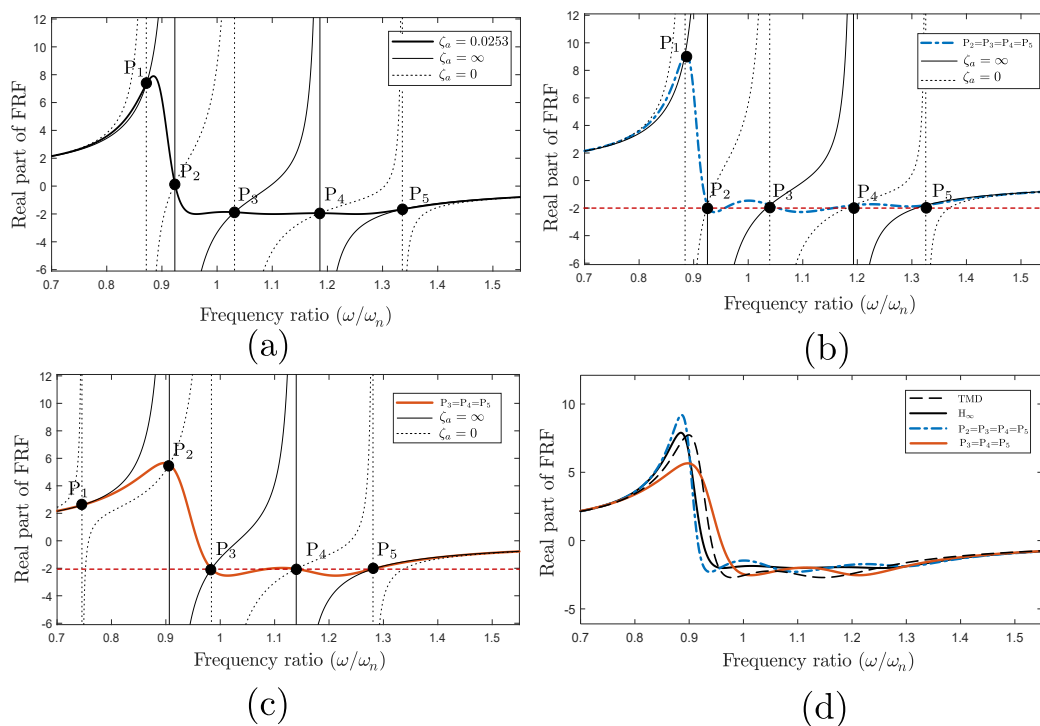
Figure B.3 Fixed-point technique for the Layout L4 where (a) indicates the fixed points. The fixed-point techniques are apply for four equal fixed points from P2 to P5 in (b) and three equal fixed points from P3 to P5 in (c). The results are compared with the TMD tuned with Sims' method [108].
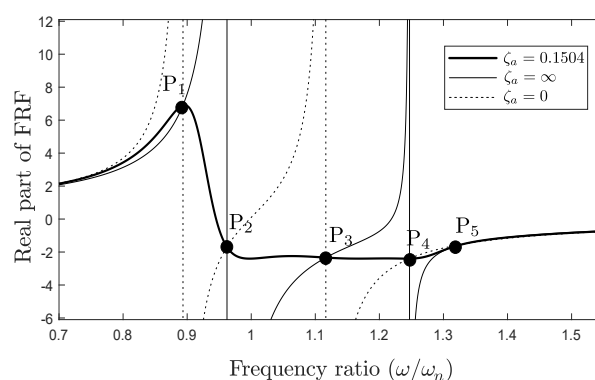
Figure B.4 Fixed points for the Layout L3

Appendix C

SaDE convergences for absolute stability

The objective values in each generation are presented in Figure C.1. The results were obtained for each layout by performing SaDE multiple times.
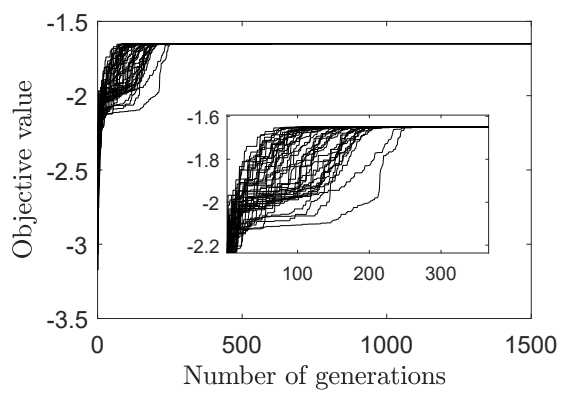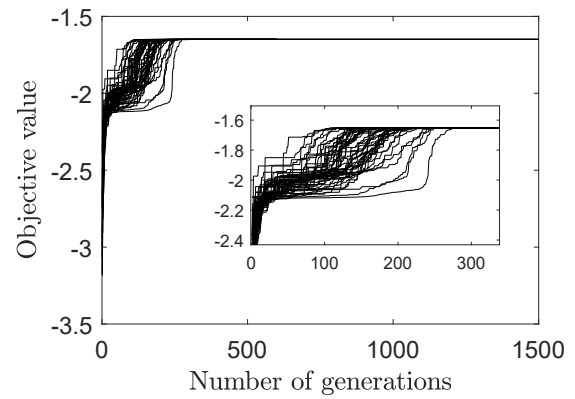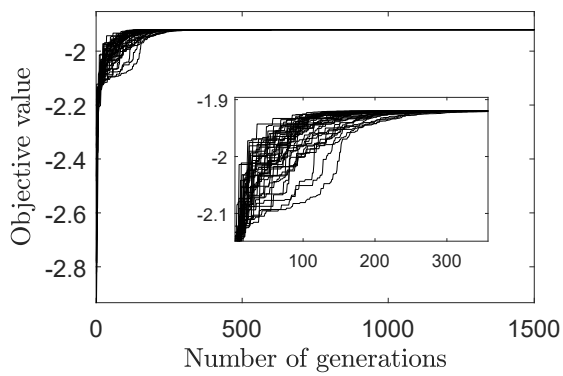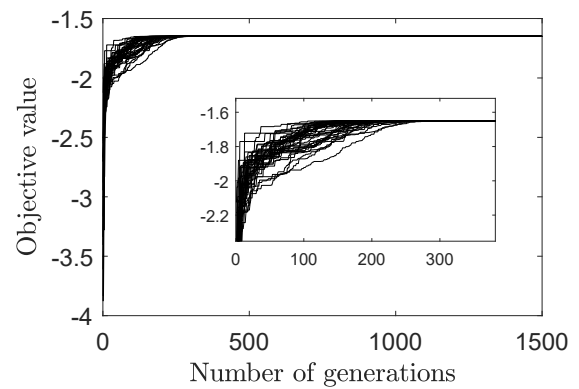
Figure C.1 Convergence studies for SaDe for each layout.

Appendix D

Fatigue analysis

A schematic view of the flexural hinge is already given in Figure 5.14a. The maximum stress occurs in the thinnest section of the notch due to the rotation of the pivoted-bar. The angle of rotation depends on the distance between the pivots and the relative displacement of two pivots (terminals) as stated in Equation 5.11. The bending stress at the notch is directly proportional to the rotational angle of the notch while it is inversely proportional to the thickness of the notch t. The maximum allowable thickness of a notch for maximum angular rotation is predicted by Smith [286] for safe operation:

$$t_{max} = \frac{9\pi^2 R}{16K_t^2 E^2} \left(\frac{\sigma_y}{\theta_{max}} \right)^2, \tag{D.1}$$

where R, E, σ_y and θ_{max} are the radius of the notch in Figure 5.14a, Young's Modulus of the material, the yield stress of the material, and the maximum angle of rotation of the notch hinge, respectively. K_t is the stress concentration factor, which is:

$$K_t = (1 + \beta_n)^{9/20}, \tag{D.2}$$

where β_n is a dimensionless parameter, which is $\beta_n = \frac{t}{2R}$. Equation D.1 is accurate providing that $0 < \beta_n < 2.3$, which is met through the design study. Equation D.1 can be modified to determine the maximum stress at the notch for given thickness and the radius of the notch is found to be

$$\sigma_{max} = \sqrt{\frac{16K_t^2 E^2 t}{9\pi^2 R}} \theta \qquad (D.3)$$

where the θ indicates the angular rotation of the notch hinge. The maximum amplitude of the angular rotation, $\theta_{max}(\omega)$, in the frequency domain should be chosen in order to obtain the maximum stress over all working frequencies.

It can be observed from Equation D.3 that the maximum stress observed at the notch increases with increasing thickness of the notch and angle of rotation. For a safe operation under static loading, the maximum stress observed at the notch should be smaller than the material's yield stress. For a safe operation under dynamic loading, the maximum stress at the notch should be smaller than the fatigue strength of the notch hinge, which depends on the material, the loading conditions, geometry of the flexure hinge, and the manufacturing technology.

The fatigue strength of a material is reduced by some factors stemming from a notched structure, the surface effect due to manufacturing process and thermal effects [286, 293, 294]. Irregularities in the geometry of a structure such as a notch or a hole lead to a concentration in the stress flow near the irregularity and reduce the strength of the material by stress concentration factor K_t. However, it was reported that using the stress concentration factor leads to an inaccurate estimation of the fatigue strength as the stress concentration factor is determined considering static loading [294]. The stress concentration is updated with the notch sensitivity and the

effective stress concentration is used in the fatigue analysis. Finally, the effect of the surface roughness is introduced by the surface roughness reduction factor, which is highly dependent on the manufacturing process applied [293]. Thermal effects which reduce the fatigue strength are assumed as negligible.

The endurance limit is generally defined as the stress value for which a material can resist a very high number of cycles without failure. Even though there is no endurance limit for some materials such as aluminium, the endurance limit can be typically expected to be of the order of 100-500 million cycles [286]. The relation between the ultimate tensile strength and bending fatigue strength for 100 million cycles of aluminium alloy can be written as stated in [293]:

$$S_{fb} \approx \begin{cases} 0.4 S_U & for \quad S_U \geq 325 \; MPa, \\ 130 \; MPa & for \quad S_U \leq 325 \; MPa \end{cases} \tag{D.4}$$

where S_U is the ultimate tensile strength of the material. The relationship in Equation D.4 is also coherent with the endurance limit (assumed 500 million cycles) for aluminium alloy given in [295]. Therefore, it is reasonable to determine the fatigue strength for aluminium alloy for an endurance limit of 100-500 million cycles. According to the supplier's specification sheet of Aluminium Alloy 6082-T6, the material's ultimate tensile strength is $S_U = 340$ MPa. Thus, the bending fatigue stress can be assumed as $S_{fb} = 130$ MPa. This value is valid only for dynamic loading with zero mean stress ($\sigma_{max} = \sigma_{min}$). If the mean stress of the dynamic loading is non-zero, the permissible stress amplitude can be given by the Goodman criteria [296, 286, 293]:

$$S_a = S_f(1 - \frac{\sigma_m}{S_U}) \tag{D.5}$$

where if $\sigma_m = 0$ or $\sigma_m \ll S_U$, S_a equals S_f.

The permissible stress amplitude in Equation D.5 is only valid for very smooth parts without geometric irregularities such as notches. The stress concentration factor K_t due to a notch is already given in Equation D.2. However, it is an overestimated factor for the dynamic loading. Hence, the effective stress concentration factor K_e is introduced as [294, 293, 296]

$$1 \leq K_e = \frac{S_{f,Unnotched}}{S_{f,Notched}} \leq K_t \tag{D.6}$$

and K_e is determined utilising the notch sensitivity:

$$q = \frac{K_e - 1}{K_t - 1} \tag{D.7}$$

The average notch sensitivities q for steel and aluminium alloy materials presented with a chart depending on the radius of the notch R in [294] are given in Figure D.1.
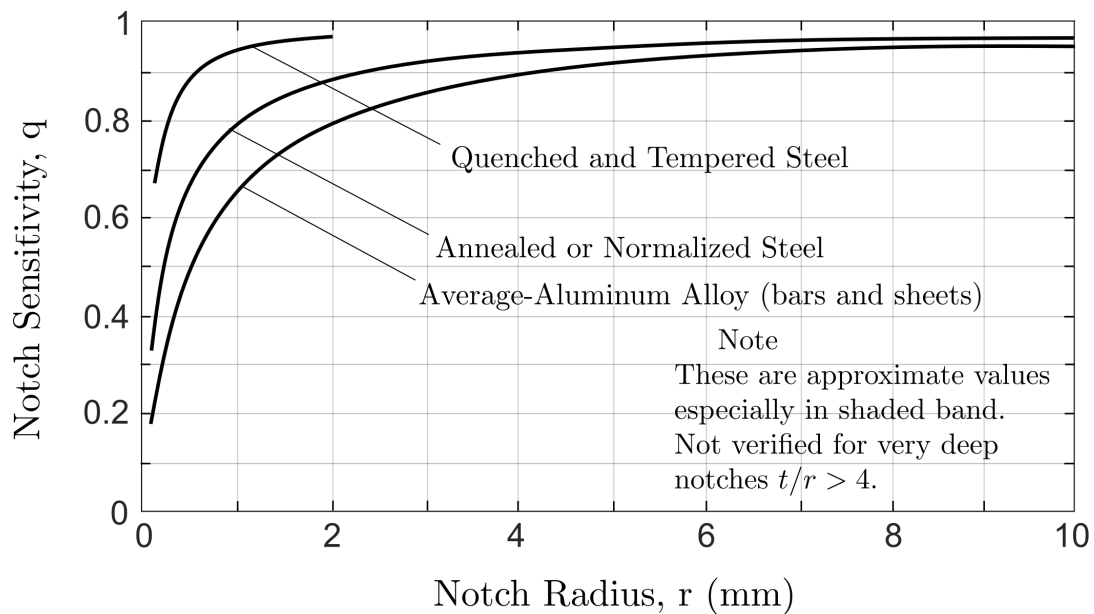
Figure D.1 Average notch sensitivities q for steel and aluminium alloy with notch radius R as stated in [294].

The manufacturing method also affects on the fatigue strength as it defines the surface quality and surface roughness. Increasing surface roughness leads to a reduction in the fatigue strength as it escalates the crack propagation. The reduction is defined by the surface roughness reduction factor κ. The notch hinges were manufactured applying electric discharged wire erosion. Therefore, it is reasonable to take a surface reduction factor of $\kappa = 0.75$ for electrical discharge machined aluminium alloy part as discussed in [293].

The permissible stress amplitude yields with the inclusion of the reduction factors considering the Goodman criteria:

$$S_a = \frac{\kappa S_f}{K_e}\left(1 - \frac{\sigma_m}{S_U/K_t}\right), \tag{D.8}$$

where σ_m is the mean stress and reduction factors: the stress concentration factor K_t, the effective stress concentration factor K_e, and the surface roughness reduction factor κ.

The fatigue analysis for a notch hinge was conducted for the parameters given in Table 5.6. The effect of the change in the thickness of the notch was examined for two notch thicknesses: 0.1 mm and 0.5 mm. The notch sensitivity was taken to be 0.91 for the constant radius of the notch of 4.75 mm for aluminium alloy from Figure D.1. The stress concentration factor K_t and the effective stress concentration factor K_e were determined from Equation D.2 and Equation D.7, respectively, for the thickness of the notch. The fatigue performance of the notch hinges with the different thicknesses was evaluated with the safety factor, which is expressed as the ratio of the allowable stress

amplitude to the maximum stress observed at the notch:

$$\text{Safety Factor} = \frac{S_a}{\sigma_{max}}. \tag{D.9}$$

The safety factors for both zero mean stress ($\sigma_m = 0$) and the mean stress of 50 MPa are demonstrated in Figure D.2. It is safe to operate the flexure hinges for the values of the safety factor larger than 1. Safety factors are determined for the relative displacements between two terminals (pivots) of the inerter. For the relative displacements with a safety factor higher than 1, the fatigue life cycle is expected to be between $100 - 500$ million cycles.
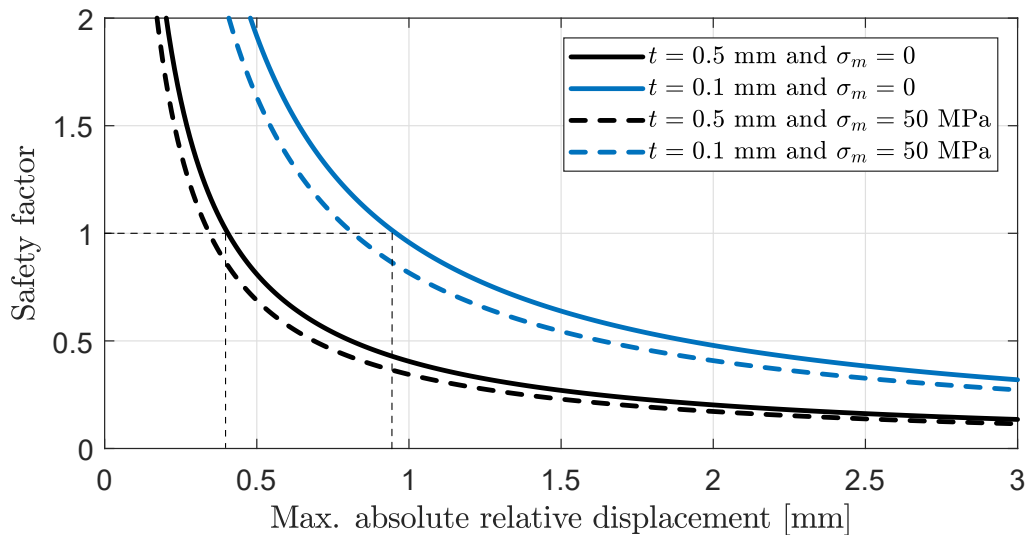
Figure D.2 Fatigue life analysis of the flexural hinge for notch thicknesses of 0.1 mm and 0.5 mm was made considering zero mean stress ($\sigma_m = 0$) and mean stress of 50 MPa (dashed lines). Safety factors are determined for relative displacement between two terminals of the inerter. A safety factor larger than 1 indicates that the flexural hinges can operate more than 100 million cycles.

Flexural hinges with notch thickness of 0.5 mm are expected to operate safely for at least 100 million cycles under relative displacement of the terminals of the inerter of 410 μm, assuming no mean stress and distance between the pivots $l_a = 40$ mm. This relative displacement value could be smaller if mean stress exists (e.g. due to

pre-stress caused by assembly). In this analysis, only the effect of thickness of notch was presented and it was shown that choosing small thickness improves the fatigue life cycle. It is also possible to improve the fatigue life by changing the other design parameters of the notch:

- Choosing a different material affects the fatigue life. There is no doubt that the most influential parameters are the material parameters, specifically both Young's modulus E and fatigue strength S_f. Fatigue strength could be increased at as high levels as $500 - 800$ MPa with the use of steel alloys. However, stiffness of the notch also increases with increasing Young's modulus, which leads to resonance region at high frequencies as discussed in Section 5.4.3

- Increasing the radius of notch R improves the fatigue life by decreasing the maximum stress occurring at the notch (as given in Equation D.3) albeit slightly increasing in notch sensitivity q. Increasing R also decreases the stiffness of the notch. However, a high radius of notch could increase the overall height and length of the flexural hinge.

- Manufacturing process applied can also improve the fatigue life by increasing the surface roughness. In this analysis, an estimated surface reduction factor κ of 0.75 was used. This corresponds 25% reduction in the permissible stress amplitude. Therefore, improving surface roughness by improving the manufacturing technology applied can increase the fatigue life as well.

Appendix E

Equations of motion of IDVA-D2 with notch stiffness

The mechanical model of IDVA-D2 with the notch stiffness is illustrated in Figure E.1. The equations of motion of the updated mechanical model with the complex stiffness is written as

$$
\begin{aligned}
M\ddot{x}_m(t) + C\dot{x}_m(t) + Kx_m(t) - b\big(\ddot{x}_p(t) - \ddot{x}_m(t)\big) - k_{notch}\big(x_p(t) - x_m(t)\big) - k_o\big(x_a(t) - x_m(t)\big) &= F(t), \\
m_p\ddot{x}_p(t) + b\big(\ddot{x}_p(t) - \ddot{x}_m(t)\big) + k_{notch}\big(x_p(t) - x_m(t)\big) - k_i\big(1 + j\eta\big)\big(x_a(t) - x_p(t)\big) &= 0, \\
m_a\ddot{x}_a(t) + k_o\big(x_a(t) - x_m(t)\big) + k_i\big(1 + j\eta\big)(x_a(t) - x_p(t)) &= 0.
\end{aligned}
\tag{E.1}
$$

where k_{notch} is the notch stiffness.
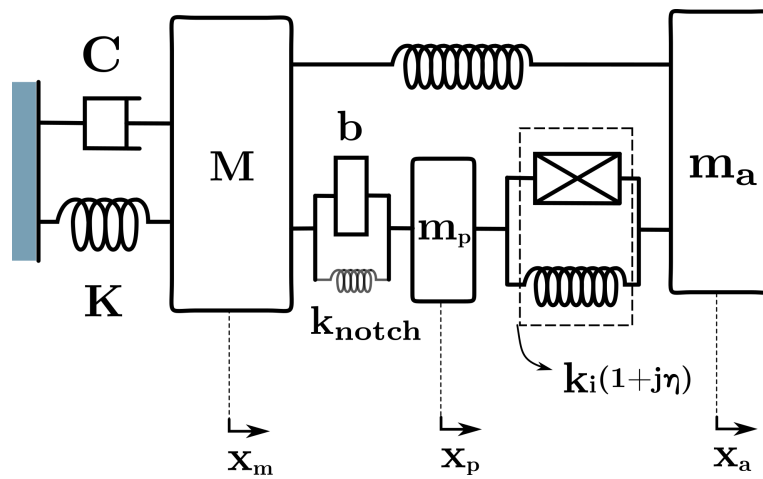
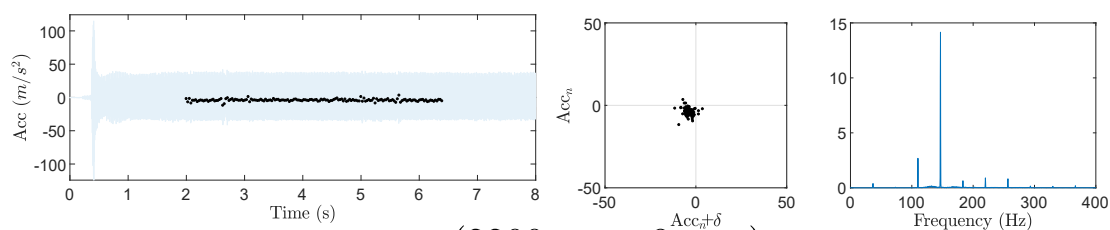Figure E.1 IDVA-D2 with the notch stiffness.
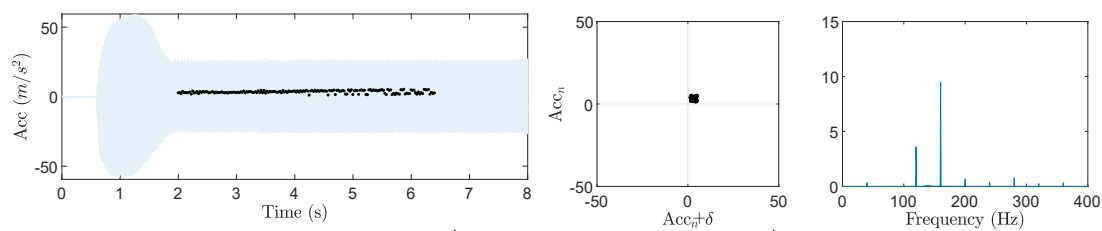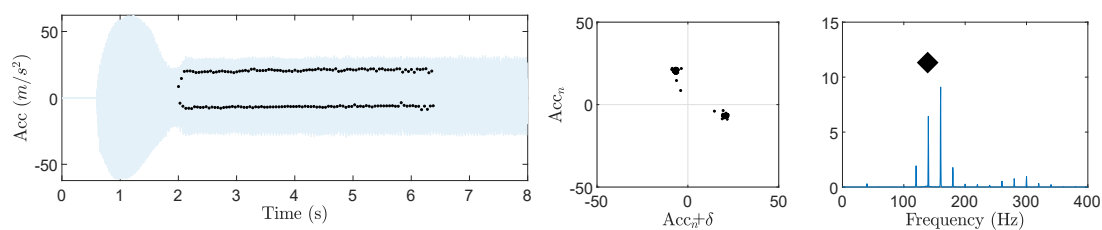
Appendix F

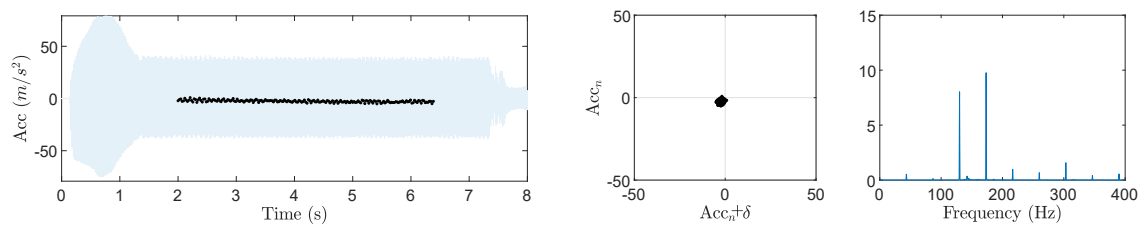# Milling test results
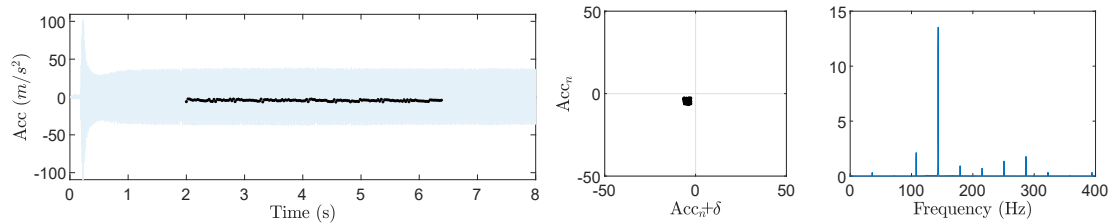
(2150 rpm, 8 mm)
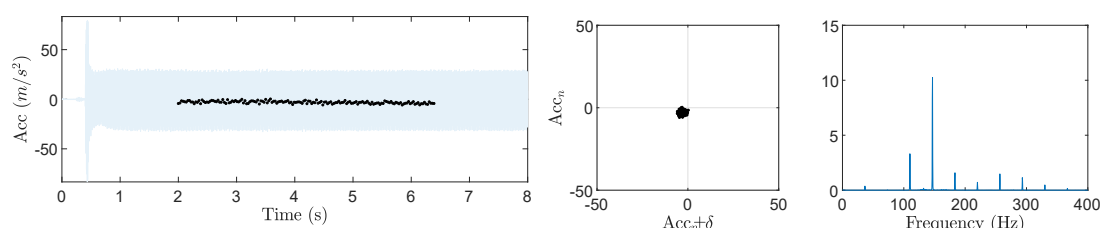
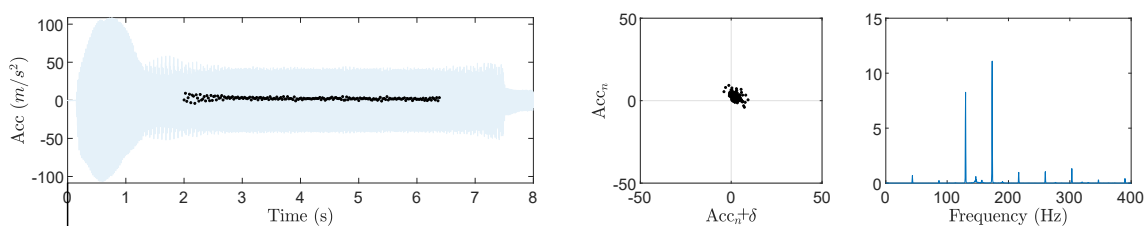(2200 rpm, 6.6 mm)
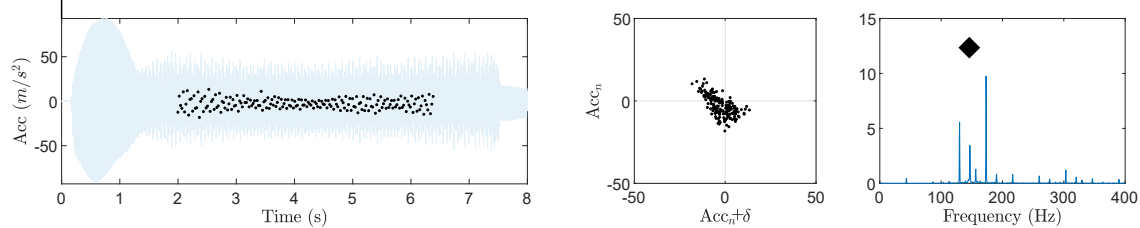
(2200 rpm, 8 mm)
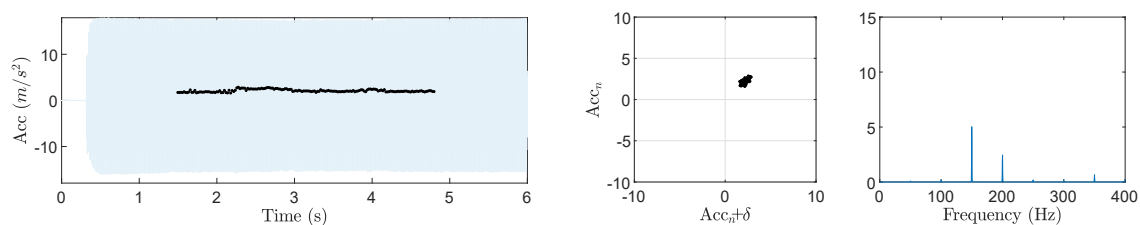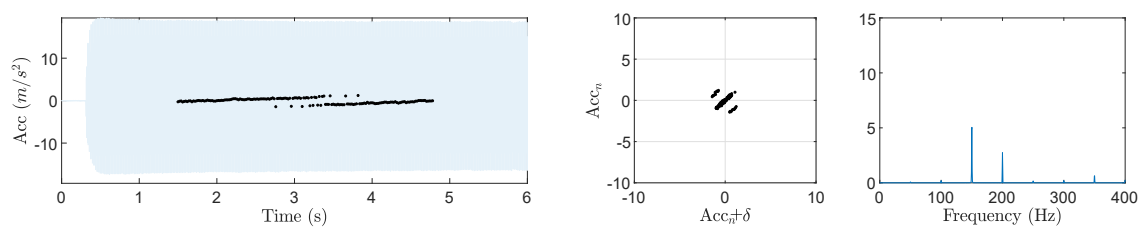
(2400 rpm, 6.4 mm)

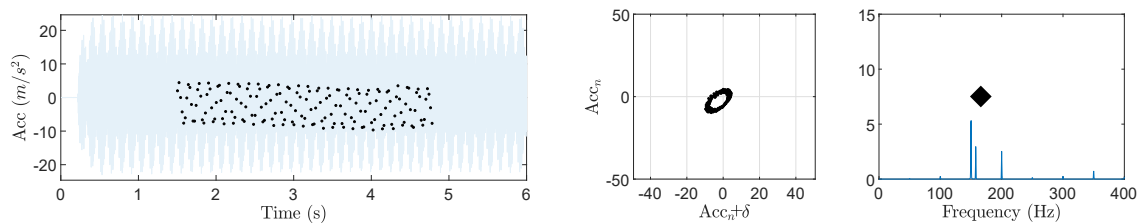(2400 rpm, 7mm)

(2600 rpm, 4.6 mm)
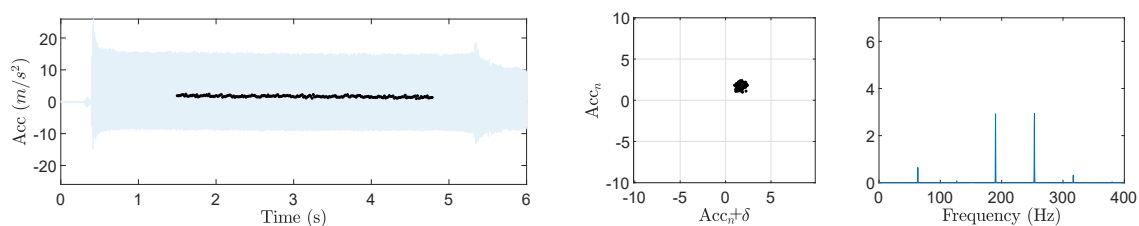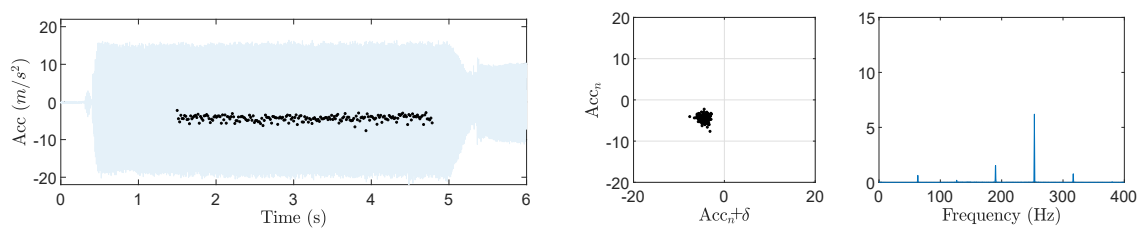
(2600 rpm, 5.2 mm)

(2600 rpm, 5.6 mm)

(3000 rpm, 4.2 mm)

(3000 rpm, 4.4 mm)

(3000 rpm, 4.6 mm)

(3800 rpm, 5 mm)

(3800 rpm, 5.4 mm)
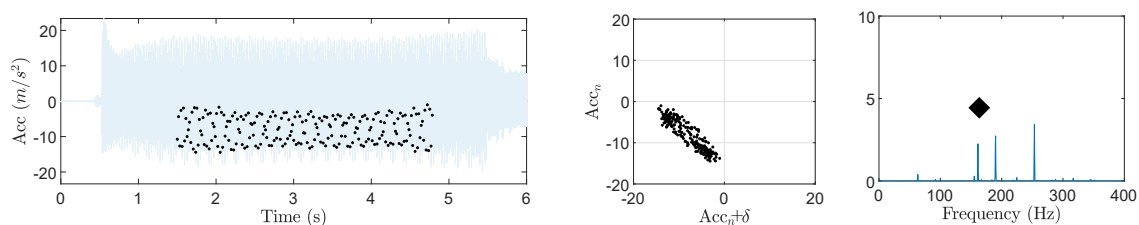
(3800 rpm, 5.8 mm)
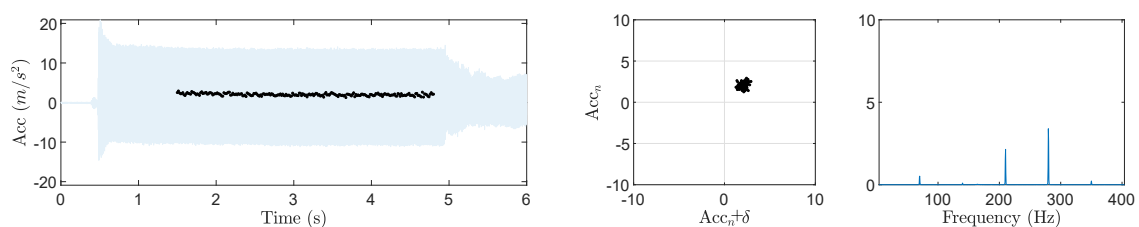
(4200 rpm, 6 mm)
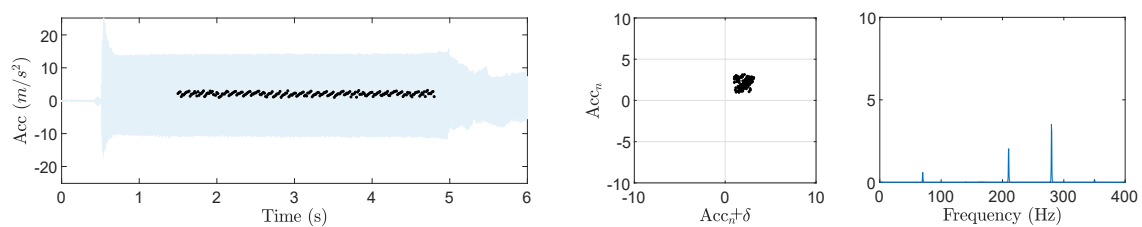
(4200 rpm, 6.4 mm)
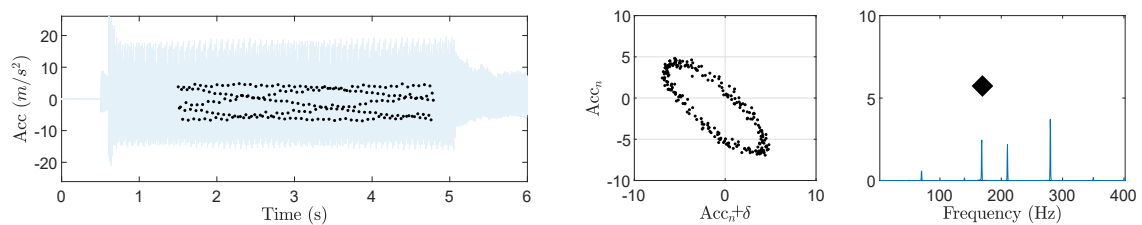
(4200 rpm, 6.8 mm)

Appendix G

Research papers

1. H. Dogan, N. D. Sims, and D. J. Wagg. Design, testing and analysis of a pivoted-bar inerter device used as a vibration absorber. *Mechanical Systems and Signal Processing, 2021.* (Submitted)

2. H. Dogan, N. D. Sims, and D. J. Wagg. Investigation of the inerter-based dynamic vibration absorber for machining chatter suppression. *IOP Cong. Series: Journal of Physics: Conf. Series*, 1264(2019)012030, 2019.

3. H. Dogan, N. D. Sims, and D. J. Wagg. Design and implementation of TID for vibration suppression. *Conference proceeding at ISMA*, 2020.

4. H. Dogan, N. D. Sims, and D. J. Wagg. The effects of parasitic mass on the performance of inerter-based dynamic vibration absorbers. *EURODYN 2020 XI International Conference on Structural Dynamics*, Athens, Greece, 22-24 June 2020.

References

[1] J. Munoa, X. Beudaert, Z. Dombovari, Y. Altintas, E. Budak, C. Brecher, and G. Stepan. Chatter suppression techniques in metal cutting. *CIRP Annals*, 65(2):785–808, 2016.

[2] S. A. Tobias and W. Fishwick. Theory of regenerative machine tool chatter. *The Engineer*, 1958.

[3] J. Tlusty and M. Polacek. The stability of machine tools against self-excited vibrations in machining. *International Research in Production Engineering*, pages 465–474, 1963.

[4] M. C. Smith. Synthesis of mechanical networks: The inerter. *IEEE Transactions on Automatic Control*, 47(10):1648–1662, 2002.

[5] F. C. Wang, C. H. Lee, and R. Q. Zheng. Benefits of the inerter in vibration suppression of a milling machine. *Journal of the Franklin Institute*, 356(14):7689–7703, 2019.

[6] D. J. Mead. *Passive vibration control*. Wiley, 1999.

[7] M. E. Merchant. Twentieth century evolution of machining in the united states - an interpretative review. *Sadhana - Academy Proceedings in Engineering Sciences*, 28(5):867–874, 2003.

[8] F. W. Taylor. *On the art of cutting metals*. The American Society of Mechanical Engineers, 1907.

[9] M. E. Merchant. Basic mechanics of the metal-cutting process. *Journal of Applied Mechanics*, 11(3):A168–A175, 1944.

[10] M. E. Merchant. Mechanics of the metal cutting process. I. Orthogonal cutting and a type 2 chip. *Journal of Applied Physics*, 16(5):267–275, 1945.

[11] M. E. Merchant. Mechanics of the metal cutting process. II. Plasticity conditions in orthogonal cutting. *Journal of Applied Physics*, 16:318–324, 1945.

[12] H. Ernst. Physics of metal cutting. *Machining of Metals*, page 24, 1938.

[13] R. Sridhar, R. E. Hohn, and G. W. Long. A General Formulation of the Milling Process Equation. *Journal of Engineering for Industry*, 90(2):317–324, 1968.

[14] R. Sridhar, R.E. Hohn, and G.W. Long. A stability algorithm for the general milling process. *Journal of Engineering for Industry*, 90(2):330–334, 1968.

[15] R. E. Hohn, R. Sridhar, and G. W. Long. A stability algorithm for a special case of the milling process. *Journal of Engineering for Industry*, 90(2):325–329, 1968.

[16] Y. Altintas and E. Budak. Analytical prediction of stability lobes in milling. *Annals of the CIRP*, 44(1):357–362, 1995.

[17] E. Budak and Y. Altintas. Analytical prediction of chatter stability in milling — Part I : General formulation. *Journal Of Dynamic Systems Measurement And Control*, 120:22–30, 1998.

[18] E. Budak and Y. Altintas. Analytical prediction of chatter stability in milling - Part II: Application of the general formulation to common milling systems. *Journal Of Dynamic Systems Measurement And Control*, 120:31–36, 1998.

[19] Y. Altintas. Analytical prediction of three dimensional chatter stability in milling. *JSME International Journal*, 44(3):717–723, 2001.

[20] S. D. Merdol and Y. Altintas. Multi frequency solution of chatter stability for low immersion milling. *Journal of Manufacturing Science and Engineering*, 126:459–466, 2004.

[21] T. Insperger and G. Stépán. Stability of the milling process. *Periodica Polytechnica Mechanical Engineering*, 44(1):47–57, 2000.

[22] T. Insperger and G. Stépán. Semi-discretization method for delayed systems. *International Journal for Numerical Methods in Engineering*, 55:503–518, 2002.

[23] T. Insperger and G. Stépán. Vibration frequencies in high-speed milling processes or a positive answer to davies, pratt, dutterer and burns. *Journal of Manufacturing Science and Engineering*, 126:481–487, 2004.

[24] T. Insperger and G. Stépán. Updated semi-discretization method for periodic delay-differential equations with discrete delay. *International Journal for Numerical Methods in Engineering*, 61:117–141, 2004.

[25] R. N. Arnold. The mechanism of tool vibration in the cutting of steel. Technical report, 1946.

[26] R. S. Hahn. Metal-cutting chatter and its elimination. *Transactions of the ASME*, 75:1073–1080, 1953.

[27] S. Doi and S. Kato. Chatter vibration of lathe tools. *Transactions of the ASME*, 78:1127–1134, 1956.

[28] H. E. Merritt. Theory of self-excited machine-tool clatter. *Journal of Engineering for Industry*, pages 447–454, 1965.

[29] R. L. Kegg. Cutting dynamics in machine tool chatter. *Journal of Engineering for Industry*, pages 464–470, 1965.

[30] T. Insperger and G. Stépán. *Semi-discretization for time-delay systems: stability and engineering applications.* Springer, 2011.

[31] F. Koenigsberger and J. Tlusty. *Machine tool structures: volume I.* Pergamon Press, 1967.

[32] Oplitz H. Chatter behaviour of heavy machine tools. Technical report, 1968.

[33] H. Opitz and F. Bernardi. Investigation and calculation of the chatter behaviour of lathes and milling machines. 18:335–343, 1970.

[34] J. Tlusty and F. Ismail. Basic non-linearity in machining chatter. *CIRP Annals*, 30(1):299–304, 1981.

[35] J. Tlusty, W. Zaton, and F. Ismail. Stability lobes in milling. *CIRP Annals*, 32(1):309–313, 1983.

[36] J. Tlusty and F. Ismail. Special aspects of chatter in milling. *Journal of Vibration, Acoustics, Stress, and Reliability in Design*, 105:24–32, 1983.

[37] J. Tlusty. Dynamics of high-speed milling. *Journal of Engineering for Industry*, 108:59–67, 1986.

[38] Y. Altintas, D. Montgomery, and E. Budak. Dynamic peripheral milling of flexible structures. *Journal of Engineering for Industry*, 114:137–145, 1992.

[39] S. Smith and J. Tlusty. Efficient simulation programs for chatter in milling. *CIRP Annals*, 42(1):463–466, 1993.

[40] I. Minis and R. Yanushevski. A new theoretical approach for the prediction of machine tool chatter in milling. *Journal of Engineering for Industry*, 115:1–8, 1993.

[41] Y. Altintas, S. Engin, and E. Budak. Analytical stability prediction and design of variable pitch cutters. *Journal of Manufacturing Science and Engineering*, pages 173–178.

[42] E. Budak. An analytical design method for milling cutters with nonconstant pitch to increase stability, part I: Theory. *Journal of Manufacturing Science and Engineering, Transactions of the ASME*, 125(1):29–34, 2003.

[43] Y. Altintaş, E. Shamoto, P. Lee, and E. Budak. Analytical prediction of stability lobes in ball end milling. *Journal of Manufacturing Science and Engineering*, 121:586–592, 1999.

[44] M. A. Davies, J. R. Pratt, B. S. Dutterer, and T. J. Burns. Stability of low radial immersion milling. *CIRP Annals*, 49(1):37–40, 2000.

[45] M. A. Davies, J. R. Pratt, B. Dutterer, and T. J. Burns. Stability prediction for low radial immersion milling. *Journal of Manufacturing Science and Engineering*, 124:217–225, 2002.

[46] P. V. Bayly, B. P. Mann, D. A. Peters, T. L. Schmitz, G. Stepan, and T. Insperger. Effects of radial immersion and cutting direction on chatter instability in end-milling. In *Proceedings of IMECE2002, ASME International Mechanical Engineering Congress and Exposition*, pages 1–13, 2002.

[47] P. V. Bayly, J. E. Halley, B. P. Mann, and M. A. Davies. Stability of interrupted cutting by temporal finite element analysis. *Journal of Manufacturing Science and Engineering*, 125:220–225, 2003.

[48] J. Gradišek, M. Kalveram, T. Insperger, K. Weinert, G. Stépán, E. Govekar, and I. Grabec. On stability prediction for milling. *International Journal of Machine Tools and Manufacture*, 45:769–781, 2005.

[49] T. Insperger, G. Stépán, and J. Turi. On the higher-order semi-discretizations for periodic delayed systems. *Journal of Sound and Vibration*, 313:334–341, 2008.

[50] T. Insperger and J. Muñoa. Unstable islands in the stability chart of milling processes due to the helix angle. In *CIRP 2nd International Internationl Conference on High Performance Cutting*, 2006.

[51] N. D. Sims, B. Mann, and S. Huyanan. Analytical prediction of chatter stability for variable pitch and variable helix milling tools. *Journal of Sound and Vibration*, 317(3-5):664–686, 2008.

[52] G. Stepan, D. Hajdu, A. Iglesias, D. Takacs, and Z. Dombovari. Ultimate capability of variable pitch milling cutters. *CIRP Annals*, 67(1):373–376, 2018.

[53] D. Bachrathy and G. Stepan. Improved prediction of stability lobes with extended multi frequency solution. *CIRP Annals*, 62(1):411–414, 2013.

[54] E. A. Butcher, H. Ma, E. Bueler, V. Averina, and Z. Szabo. Stability of linear time-periodic delay-differential equations via Chebyshev polynomials. *International Journal for Numerical Methods in Engineering*, 59(7):895–922, 2004.

[55] E. A. Butcher, O. A. Bobrenkov, E. Bueler, and P. Nindujarla. Analysis of milling stability by the chebyshev collocation method: Algorithm and optimal stable immersion levels. *Journal of Computational and Nonlinear Dynamics*, 4(3):1–12, 2009.

[56] Y. Ding, L. Zhu, X. Zhang, and H. Ding. A full-discretization method for prediction of milling stability. *International Journal of Machine Tools and Manufacture*, 50(5):502–509, 2010.

[57] Y. Ding, L. Zhu, X. Zhang, and H. Ding. Second-order full-discretization method for milling stability prediction. *International Journal of Machine Tools and Manufacture*, 50(10):926–932, 2010.

[58] C. G. Ozoegwu, S. N. Omenyi, and S. M. Ofochebe. Hyper-third order full-discretization methods in milling stability prediction. *International Journal of Machine Tools and Manufacture*, 92:1–9, 2015.

[59] O. Tuysuz and Y. Altintas. Analytical modeling of process damping in machining. *Journal of Manufacturing Science and Engineering*, 141(6):1–16, 2019.

[60] B. Denkena, R. Grabowski, A. Krödel, and L. Ellersiek. Time-domain simulation of milling processes including process damping. *CIRP Journal of Manufacturing Science and Technology*, 30:149–156, 2020.

[61] Y. Ji, X. Wang, Z. Liu, H. Wang, L. Jiao, L. Zhang, and T. Huang. Milling stability prediction with simultaneously considering the multiple factors coupling effects—regenerative effect, mode coupling, and process damping. *The International Journal of Advanced Manufacturing Technology*, 97:2509–2527, 2018.

[62] Z. Li, S. Jiang, and Y. Sun. Chatter stability and surface location error predictions in milling with mode coupling and process damping. *Proceedings of the Institution of Mechanical Engineers, Part B: Journal of Engineering Manufacture*, 233(3):686–698, 2017.

[63] S. Smith and J. Tlusty. Update on high-speed milling dynamics. *Journal of Engineering for Industry*, pages 142–149.

[64] S. Smith and J. Tlusty. Stabilizing chatter by automatic spindle speed regulation. *CIRP Annals*, pages 433–436.

[65] S. Smith and T. Delio. Sensor-based chatter detection and avoidance by spindle speed selection. *Journal of Dynamic Systems, Measurement and Control*, 114(3):486–492, 1992.

[66] Y. S. Tarng and T. C. Li. The change of spindle speed for the avoidance of chatter in end milling. *Journal of Materials Processing Technology*, 41:227–236, 1994.

[67] Y. S. Tarng, Y. W. Hseih, and T. C. Li. Automatic selection of spindle speed for suppression of regenerative chatter in turning. *International Journal of Advanced Manufacturing Technology*, 11:12–17, 1996.

[68] J. S. Sexton and B. J. Stone. The stability of machining with continuously varying spindle speed. *CIRP Annals - Manufacturing Technology*, 27:321–326, 1978.

[69] S. Jayaram, S. G. Kapoor, and R. E. Devor. Analytical stabilty analysis of variable spindle speed machining. *Journal of Manufacturing Science and Engineering*, 122(3):391–397, 2000.

[70] S. Sastry, S. G. Kapoor, and R. E. DeVor. Floquet theory based approach for stability analysis of the variable speed face-milling process. *Journal of Manufacturing Science and Engineering, Transactions of the ASME*, 124(1):10–17, 2002.

[71] T. Insperger, T. L. Schmitz, T. J. Burns, and G. Stépán. Comparison of analytical and numerical simulations for variable spindle speed turning. In *Proceedings of the ASME 2003 International Mechanical Engineering Congress and Exposition*, pages 41–47, 2003.

[72] S. Seguy, T. Insperger, L. Arnaud, G. Dessein, and G. Peigné. On the stability of high-speed milling with spindle speed variation. *International Journal of Advanced Manufacturing Technology*, 48:883–895, 2010.

[73] I. Bediaga, M. Zatarain, J. Muñoa, and R. Lizarralde. Application of continuous spindle speed variation for chatter avoidance in roughing milling. *Proceedings of the Institution of Mechanical Engineers, Part B: Journal of Engineering Manufacture*, 225(5):631–640, 2011.

[74] A. Otto, G. Kehl, M. Mayer, and G. Radons. Stability analysis of machining with spindle speed variation. *Advanced Materials Research*, 223:600–609, 2011.

[75] S. C. Lin, R. E. DeVor, and S. G. Kapoor. The effects of variable speed cutting on vibration control in face milling. *Journal of Manufacturing Science and Engineering*, 112(1):1–11, 1990.

[76] Y. Altintas and P. K. Chan. In-process detection and suppression of chatter in milling. *International Journal of Machine Tools and Manufacture*, 32(3):329–347, 1992.

[77] M. Zatarain, I. Bediaga, J. Muñoa, and R. Lizarralde. Stability of milling processes with continuous spindle speed variation: Analysis in the frequency and time domains, and experimental correlation. *CIRP Annals*, 57(1):379–384, 2008.

[78] A. Yilmaz, E. Al-Regib, and J. Ni. Machine tool chatter suppression by multi-level random spindle speed variation. *Journal of Manufacturing Science and Engineering, Transactions of the ASME*, 124(2):208–216, 2002.

[79] I. Bediaga, J. Muñoa, J. Hernández, and L. N. López de Lacalle. An automatic spindle speed selection strategy to obtain stability in high-speed milling. *International Journal of Machine Tools and Manufacture*, 49:384–394, 2009.

[80] E. Al-Regib, J. Ni, and S. Lee. Programming spindle speed variation for machine tool chatter suppression. *International Journal of Machine Tools and Manufacture*, 43(12):1229–1240, 2003.

[81] J. Slavicek. The effect of irregular tooth pitch on stability of milling. In *6th MTDR Conference, Manchester*, 1965.

[82] A. Iglesias, Z. Dombovari, G. Gonzalez, J. Munoa, and G. Stepan. Optimum selection of variable pitch for chatter suppression in face milling operations. *Materials*, 12(1), 2018.

[83] P. Doolan, M. . Phadke, and S. M. Wu. Computer design of a vibration-free face-milling cutter. *Journal of Engineering for Industry*, (3):925–930, 1975.

[84] J. Tlusty, F. Ismail, and W. Zaton. Use of special milling cutters against chatter. In *NAMRC11*, pages 408–415, 1983.

[85] E. Budak. An analytical design method for milling cutters with nonconstant pitch to increase stability, part 2: Application. *Journal of Manufacturing Science and Engineering, Transactions of the ASME*, 125(1):35–38, 2003.

[86] E. Budak. Improving productivity and part quality in milling of titanium based impellers by chatter suppression and force control. *CIRP Annals*, 49(1):31–36, 2000.

[87] T. Insperger and G. Stépán. Updated semi-discretization method for periodic delay-differential equations with discrete delay. *International Journal for Numerical Methods in Engineering*, 61(1):117–141, 2004.

[88] B. R. Patel, B. P. Mann, and K. A. Young. Uncharted islands of chatter instability in milling. *International Journal of Machine Tools and Manufacture*, 48(1):124–134, 2008.

[89] A. Comak and E. Budak. Modeling dynamics and stability of variable pitch and helix milling tools for development of a design method to maximize chatter stability. *Precision Engineering*, 47:459–468, 2017.

[90] S. Turner, D. Merdol, Y. Altintas, and K. Ridgway. Modelling of the stability of variable helix end mills. *International Journal of Machine Tools and Manufacture*, 47(9):1410–1416, 2007.

[91] G. Jin, Q. Zhang, H. Qi, and B. Yan. A frequency-domain solution for efficient stability prediction of variable helix cutters milling. *Proceedings of the Institution of Mechanical Engineers, Part C: Journal of Mechanical Engineering Science*, 228(15):2702–2710, 2014.

[92] A. Otto and G. Radons. Frequency domain stability analysis of milling processes with variable helix tools. In *Nineth International Conference on High Speed Machining*, volume 1, 2012.

[93] N. D. Sims. Multi-frequency Chatter Analysis Using the Shift Theorem. *Procedia IUTAM*, 22:3–9, 2017.

[94] A. R. Yusoff and N. D. Sims. Optimisation of variable helix tool geometry for regenerative chatter mitigation. *International Journal of Machine Tools and Manufacture*, 51(2):133–141, 2011.

[95] Z. Dombovari and G. Stepan. The effect of helix angle variation on milling stability. *Journal of Manufacturing Science and Engineering, Transactions of the ASME*, 134(5), 2012.

[96] S. Kato, E. Marui, and H. Kurita. Some considerations on prevention of chatter vibration in boring operations. *Journal of Manufacturing Science and Engineering*, 91(3):717–728, 1969.

[97] G. Gubanov. Broadband pneumatic mass damper for the elimination of workpiece vibrations. *Journal of Manufacturing Science and Technology*, 30:184–194, 2020.

[98] S. Ema and E. Marui. Damping characteristics of an impact damper and its application. *International Journal of Machine Tools and Manufacture*, 36(3):293–306, 1996.

[99] S. Ema and E. Marui. Suppression of chatter vibration of boring tools using impact dampers. *International Journal of Machine Tools and Manufacture*, 40(8):1141–1156, 2000.

[100] E. Marui, S. Ema, M. Hashimoto, and Y. Wakasawa. Plate insertion as a means to improve the damping capacity of a cutting tool system. *International Journal of Machine Tools and Manufacture*, 38(10-11):1209–1220, 1998.

[101] J. C. Ziegert, C. Stanislaus, T. L. Schmitz, and R. Sterling. Enhanced damping in long slender end mills. *Journal of Manufacturing Processes*, 8(1), 2006.

[102] E. Edhi and T. Hoshi. Stabilization of high frequency chatter vibration in fine boring by friction damper. *Precision Engineering*, 25(3):224–234, 2001.

[103] K. Seto and N. Tominari. Effect of a aariable stiffness-type dynamic damper on machine tools with long overhung ram. *Bulletin of the JSME*, 19(137):1270–1277, 1976.

[104] K. J. Liu and K. E. Rouch. Optimal passive vibration control of cutting process stability in milling. *Journal of Materials Processing Technology*, 28(1-2):285–294, 1991.

[105] E. I. Rivin and H. Kang. Enhancement of dynamic stability of cantilever tooling structures. *International Journal of Machine Tools and Manufacture*, 32(4):539–561, 1992.

[106] Y. S. Tarng, J. Y. Kao, and E. C. Lee. Chatter suppression in turning operations with a tuned vibration absorber. *Journal of Materials Processing Technology*, 105(1-2):55–60, 2000.

[107] J. P. Den Hartog. *Mechanical vibrations.* McGraw-Hill, New York, 1956.

[108] N. D. Sims. Vibration absorbers for chatter suppression: A new analytical tuning methodology. *Journal of Sound and Vibration*, 301(3-5):592–607, 2007.

[109] H. Moradi, F. Bakhtiari-Nejad, and M. R. Movahhedy. Tuneable vibration absorber design to suppress vibrations: An application in boring manufacturing process. *Journal of Sound and Vibration*, 318(1-2):93–108, 2008.

[110] M. H. Miguélez, L. Rubio, J. A. Loya, and J. Fernández-Sáez. Improvement of chatter stability in boring operations with passive vibration absorbers. *International Journal of Mechanical Sciences*, 52(10):1376–1384, 2010.

[111] L. Rubio, J. A. Loya, M. H. Miguélez, and J. Fernández-Sáez. Optimization of passive vibration absorbers to reduce chatter in boring. *Mechanical Systems and Signal Processing*, 41(1-2):691–704, 2013.

[112] A. Yadav, D. Talaviya, A. Bansal, and M. Law. Design of chatter-resistant damped boring bars using a receptance coupling approach. *Journal of Manufacturing and Materials Processing*, 4(2), 2020.

[113] W. Ma, J. Yu, Y. Yang, and Y. Wang. Optimization and tuning of passive tuned mass damper embedded in milling tool for chatter mitigation. *Journal of Manufacturing and Materials Processing*, 5(1):2, 2020.

[114] K. J. Kim and J. Y. Ha. Suppression of machine tool chatter using a viscoelastic dynamic damper. *Journal of Manufacturing Science and Engineering*, 109(1):58–65, 1987.

[115] A. Rashid and C. M. Nicolescu. Design and implementation of tuned viscoelastic dampers for vibration control in milling. *International Journal of Machine Tools and Manufacture*, 48(9):1036–1053, 2008.

[116] J. Saffury and E. Altus. Optimized chatter resistance of viscoelastic turning bars. *Journal of Sound and Vibration*, 324(1-2):26–39, 2009.

[117] Y. Yang, J. Muñoa, and Y. Altintas. Optimization of multiple tuned mass dampers to suppress machine tool chatter. *International Journal of Machine Tools and Manufacture*, 50(9):834–842, 2010.

[118] Y. Nakano, H. Takahara, and E. Kondo. Countermeasure against chatter in end milling operations using multiple dynamic absorbers. *Journal of Sound and Vibration*, 332(6):1626–1638, 2013.

[119] M. Wang, T. Zan, Y. Yang, and R. Fei. Design and implementation of nonlinear TMD for chatter suppression: An application in turning processes. *International Journal of Machine Tools and Manufacture*, 50(5):474–479, 2010.

[120] M. Wang. Feasibility study of nonlinear tuned mass damper for machining chatter suppression. *Journal of Sound and Vibration*, 330(9):1917–1930, 2011.

[121] G. Habib, G. Kerschen, and G. Stepan. Chatter mitigation using the nonlinear tuned vibration absorber. *International Journal of Non-Linear Mechanics*, 91:103–112, 2017.

[122] Y. Yang, W. Dai, and Q. Liu. Design and implementation of two-degree-of-freedom tuned mass damper in milling vibration mitigation. *Journal of Sound and Vibration*, 335:78–88, 2014.

[123] Y. Yang, W. Dai, and Q. Liu. Design and machining application of a two-DOF magnetic tuned mass damper. *International Journal of Advanced Manufacturing Technology*, 89(5-8):1635–1643, 2017.

[124] Y. Yang, D. Xu, and Q. Liu. Milling vibration attenuation by eddy current damping. *International Journal Advanced Manufacturing Technology*, 81:445–454, 2015.

[125] Y. Yang, R. Xie, and Q. Liu. Design of a passive damper with tunable stiffness and its application in thin-walled part milling. *International Journal of Advanced Manufacturing Technology*, 89:2713–2720, 2017.

[126] H. Yuan, M. Wan, Y. Yang, and W. H. Zhang. A tunable passive damper for suppressing chatters in thin-wall milling by considering the varying modal parameters of the workpiece. *International Journal of Advanced Manufacturing Technology*, 104(9-12):4605–4616, 2019.

[127] H. Yuan, M. Wan, and Y. Yang. Design of a tunable mass damper for mitigating vibrations in milling of cylindrical parts. *Chinese Journal of Aeronautics*, 32(3), 2019.

[128] Z. Zhang, H. Li, G. Meng, and S. Ren. Milling chatter suppression in viscous fluid: A feasibility study. *International Journal of Machine Tools and Manufacture*, 120:20–26, 2017.

[129] Z. Zhang, H. Li, X. Liu, W. Zhang, and G. Meng. Chatter mitigation for the milling of thin-walled workpiece. *International Journal of Mechanical Sciences*, 138-139:262–271, 2018.

[130] M. A. Butt, Y. Yang, X. Pei, and Q. Liu. Five-axis milling vibration attenuation of freeform thin-walled part by eddy current damping. *Precision Engineering*, 51:682–690, 2018.

[131] J. Fei, B. Lin, S. Yan, M. Ding, J. Xiao, J. Zhang, X. Zhang, C. Ji, and T. Sui. Chatter mitigation using moving damper. *Journal of Sound and Vibration*, 410:49–63, 2017.

[132] M. Wan, W. Q. Gao, J. Feng, and W. H. Zhang. On improving chatter stability of thin-wall milling by prestressing. *Journal of Materials Processing Technology*, 264:32–44, 2019.

[133] J. Munoa, M. Sanz-Calle, Z. Dombovari, A. Iglesias, J. Pena-Barrio, and G. Stepan. Tuneable clamping table for chatter avoidance in thin-walled part milling. *CIRP Annals*, 69(1):313–316, 2020.

[134] J. Munoa, A. Iglesias, A. Olarra, Z. Dombovari, M. Zatarain, and G. Stepan. Design of self-tuneable mass damper for modular fixturing systems. *CIRP Annals*, 65(1):389–392, 2016.

[135] J. Burtscher and journal = CIRP Annals number = 1 pages = 397–400 title = Adaptive tuned mass damper with variable mass for chatter avoidance volume = 66 year = 2017 Fleischer, J.

[136] Y. Z. Lei. Use of the electrorheological technoque for chatter control. In *International Conference on Intelligent Manufacturing*, volume 2620, pages 762–766, 1995.

[137] T. Aoyama and I. Inasaki. Application of electrorheological fluid dampers to machine tool elements. *CIRP Annals*, 46(1), 1997.

[138] M. Wang and R. Fei. Chatter suppression based on nonlinear vibration characteristic of electrorheological fluids. *International Journal of Machine Tools and Manufacture*, 39(12):1925–1934, 1999.

[139] G. Park, M. T. Bement, D. A. Hartman, R. E. Smith, and C. R. Farrar. The use of active materials for machining processes: A review. *International Journal of Machine Tools and Manufacture*, 47(15):2189–2206, 2007.

[140] Y. Zhou and Y. L. Zhang. Optimal design of a shear magnetorheological damper for turning vibration suppression. *Smart Materials and Structures*, 22(9), 2013.

[141] Y. Zhang, N. M. Wereley, W. Hu, M. Hong, and W. Zhang. Magnetic circuit analyses and turning chatter suppression based on a squeeze-mode magnetorheological damping turning tool. *Shock and Vibration*, 2015, 2015.

[142] R. Kishore, S. K. Choudhury, and K. Orra. On-line control of machine tool vibration in turning operation using electro-magneto rheological damper. *Journal of Manufacturing Processes*, 31:187–198, 2018.

[143] A. Som, D. H. Kim, and H. Son. Semiactive magnetorheological damper for high aspect ratio boring process. *IEEE/ASME Transactions on Mechatronics*, 20(5):2575–2582, 2015.

[144] J. Ma, D. Zhang, B. Wu, M. Luo, and Y. Liu. Stability improvement and vibration suppression of the thin-walled workpiece in milling process via magnetorheological fluid flexible fixture. *International Journal of Advanced Manufacturing Technology*, 88(5-8):1231–1242, 2017.

[145] D. Segalman and J. Redmond. Chatter suppression through variable impedance and smart fluids, 1996.

[146] D. Mei, T. Kong, A. J. Shih, and Z. Chen. Magnetorheological fluid-controlled boring bar for chatter suppression. *Journal of Materials Processing Technology*, 209(4):1861–1870, 2009.

[147] D. Mei, Z. Yao, T. Kong, and Z. Chen. Parameter optimization of time-varying stiffness method for chatter suppression based on magnetorheological fluid-controlled boring bar. *International Journal of Advanced Manufacturing Technology*, 46(9-12):1071–1083, 2010.

[148] R. G. Klein and C. L. Nachtigal. The apllication of active control to improve boring bar performance. *Journal of Dynamic Systems, Measurement, and Control*, 97(2):179–183, 1975.

[149] R.G. Klein and C. L. Nachtigal. A theoretical basis for the active control of a boring bar operation. *Journal of Dynamic Systems, and Measurement and Control*, 97(2):172–178, 1975.

[150] D. J. Glaser and C. L. Nachtigal. Development of a hydraulic chambered, actively controlled boring bar. *Journal of Manufacturing Science and Engineering*, 101(3):362–368, 1979.

[151] H. Tanaka, F. Obata, T. Matsubara, and H. Mizumoto. Active chatter suppression of slender boring bar using piezoelectric actuators. *JSME International Journal*, 37(3):601–606, 1994.

[152] Sanjiv G. Tewani, Keith E. Rouch, and Bruce L. Walcott. A study of cutting process stability of a boring bar with active dynamic absorber. *International Journal of Machine Tools and Manufacture*, 35(1):91–108, 1995.

[153] J. R. Pratt and A. H. Nayfeh. Chatter control and stability analysis of a cantilever boring bar under regenerative cutting conditions. *Philosophical Transactions of the Royal Society A: Mathematical, Physical and Engineering Sciences*, 359(1781):759–792, 2001.

[154] J. L. Dohner, J. P. Lauffer, T. D. Hinnerichs, N. Shankar, M. Regelbrugge, C. M. Kwan, R. Xu, B. Winterbauer, and K. Bridger. Mitigation of chatter instabilities in milling by active structural control. *Journal of Sound and Vibration*, 269(1-2):197–211, 2004.

[155] J. Monnin, F. Kuster, and K. Wegener. Optimal control for chatter mitigation in milling-Part 1: Modeling and control design. *Control Engineering Practice*, 24(1):156–166, 2014.

[156] J. Monnin, F. Kuster, and K. Wegener. Optimal control for chatter mitigation in milling-Part 2: Experimental validation. *Control Engineering Practice*, 24(1):167–175, 2014.

[157] C. Wang, X. Zhang, H. Cao, X. Chen, and J. Xiang. Milling stability prediction and adaptive chatter suppression considering helix angle and bending. *International Journal of Advanced Manufacturing Technology*, 95:3665–3677, 2018.

[158] D. Li, H. Cao, X. Zhang, X. Chen, and R. Yan. Model predictive control based active chatter control in milling process. *Mechanical Systems and Signal Processing*, 128:266–281, 2019.

[159] F. Shi, H. Cao, X. Zhang, and X. Chen. A chatter mitigation technique in milling based on H -ADDPMS and piezoelectric stack actuators. *International Journal of Advanced Manufacturing Technology*, 101(9-12):2233–2248, 2019.

[160] X. Zhang, C. Wang, J. Liu, R. Yan, H. Cao, and X. Chen. Robust active control based milling chatter suppression with perturbation model via piezoelectric stack actuators. *Mechanical Systems and Signal Processing*, 120:808–835, 2019.

[161] C. Wang, X. Zhang, Y. Liu, H. Cao, and X. Chen. Stiffness variation method for milling chatter suppression via piezoelectric stack actuators. *International Journal of Machine Tools and Manufacture*, 124(28):53–66, 2018.

[162] C. Wang, X. Zhang, J. Liu, R. Yan, H. Cao, and X. Chen. Multi harmonic and random stiffness excitation for milling chatter suppression. *Mechanical Systems and Signal Processing*, 120(1):777–792, 2019.

[163] D. Li, H. Cao, J. Liu, X. Zhang, and X. Chen. Milling chatter control based on asymmetric stiffness. *International Journal of Machine Tools and Manufacture*, 147:103458, 2019.

[164] J. Kyung and C. Lee. Controller design for a magnetically suspended milling spindle based on chatter stability analysis. *JSME International Journal Series C Mechanical Systems, Machine Elements and Manufacturing*, 46(2):416–422, 2003.

[165] M. Chen and C. R. Knospe. Control approaches to the suppression of machining chatter using active magnetic bearings. *IEEE Transactions on Control Systems Technology*, 15(2):220–232, 2007.

[166] N. Van de Wouw, N. J. M. Van Dijk, A. Schiffler, H. Nijmeijer, and E. Abele. Experimental validation of robust chatter control for high-speed milling processes. *Springer International Publishing*, pages 315–331, 2017.

[167] Y. Wu, H. T. Zhang, T. Huang, G. Ren, and H. Ding. Robust chatter mitigation control for low radial immersion machining processes. *IEEE Transactions on Automation Science and Engineering*, 15(4):1972–1979, 2018.

[168] T. Huang, Z. Chen, H. T. Zhang, and H. Ding. Active control of an active magnetic bearings supported spindle for chatter suppression in milling process. *Journal of Dynamic Systems, Measurement and Control, Transactions of the ASME*, 137(11), 2015.

[169] N. Van de Dijk, N. Van de Wouw, E. Doppenberg, H. Oosterling, and H. Nijmeijer. Chatter control in the high-speed milling process using μ-synthesis. *Proceedings of the 2010 American Control Conference*, (2010):6121–6126, 2010.

[170] N. J.M. Van Dijk, N. Van De Wouw, E. J. J. Doppenberg, Han A. J. Oosterling, and H. Nijmeijer. Robust active chatter control in the high-speed milling process. *IEEE Transactions on Control Systems Technology*, 20(4):901–917, 2012.

[171] N. Van de Wouw, N. J. M. Van Dijk, A. Schiffler, H. Nijmeijer, and E. Abele. Experimental validation of robust chatter control for high-speed milling processes. In *Time Delay Systems*, pages 315–331. 2017.

[172] W. Bickel, K. M. Litwinski, and B. Denkena. Increase of process stabiliyt with innovative spindle drives. In *New Production Technologies in Aerospace Industry*, pages 145–151, 2014.

[173] S. Wan, X. Li, W. Su, J. Yuan, J. Hong, and X. Jin. Active damping of milling chatter vibration via a novel spindle system with an integrated electromagnetic actuator. *Precision Engineering*, 57:203–210, 2019.

[174] S. Wan, X. Li, W. Su, J. Yuan, and J. Hong. Active chatter suppression for milling process with sliding mode control and electromagnetic actuator. *Mechanical Systems and Signal Processing*, 136, 2020.

[175] S. Huyanan and N. D. Sims. Vibration control strategies for proof-mass actuators. *Journal of Vibration and Control*, 13(12):1785–1806, 2007.

[176] S. Huyanan. *An Active Vibration Absorber for Chatter Reduction in Machining.* PhD thesis, 2007.

[177] X. Beudaert, K. Erkorkmaz, and J. Munoa. Portable damping system for chatter suppression on flexible workpieces. *CIRP Annals*, 68(1):423–426, 2019.

[178] Y. Zhang and N. D. Sims. Milling workpiece chatter avoidance using piezoelectric active damping: A feasibility study. *Smart Materials and Structures*, 14(6), 2005.

[179] C. Brecher, D. Manoharan, U. Ladra, and H. G. Köpken. Chatter suppression with an active workpiece holder. *Production Engineering*, 4(2):239–245, 2010.

[180] L. Sallese, G. Innocenti, N. Grossi, A. Scippa, R. Flores, M. Basso, and G. Campatelli. Mitigation of chatter instabilities in milling using an active fixture with a novel control strategy. *International Journal of Advanced Manufacturing Technology*, 89(9-12):2771–2787, 2017.

[181] A. Rashid and C. Nicolescu. Active vibration control in palletised workholding system for milling. *International Journal of Machine Tools and Manufacture*, 46(12-13):1626–1636, 2006.

[182] A. Parus, B. Powałka, K. Marchelek, S. Domek, and M. Hoffmann. Active vibration control in milling flexible workpieces. *Journal of Vibration and Control*, 19(7):1103–1120, 2013.

[183] B. Chung, S. Smith, and J. Tlusty. Active damping of structural modes in high-speed machine tools. *Journal of Vibration and Control*, 3:279–295, 1997.

[184] C. Brecher, A. Schulz, and M. Weck. Electrohydraulic active damping system. *CIRP Annals*, 54(1):389–392, 2005.

[185] J. Munoa, I. Mancisidor, N. Loix, L. G. Uriarte, R. Barcena, and M. Zatarain. Chatter suppression in ram type travelling column milling machines using a biaxial inertial actuator. *CIRP Annals Technology*, 62:407–410, 2013.

[186] M. F. Zaeh, R. Kleinwort, P. Fagerer, and Y. Altintas. Automatic tuning of active vibration control systems using inertial actuators. *CIRP Annals*, 66(1):365–368, 2017.

[187] Hermann Frahm. Device for damping bibrations of bodies, *US Patent Office* US989958A, 1909.

[188] J. Ormondroyd and J. P. Den Hartog. The theory of the dynamic vibration absorber. *Journal of Applied Mechanics*, 50:9–22, 1928.

[189] M. C. Smith. The inerter: A retrospective. *Annual Review of Control, Robotics, and Autonomous Systems*, 3(1):361–391, 2020.

[190] A. Okumura. The gyro-mass inerter, *Japan patent koukai* h09-177875, 1997.

[191] H. Kuroda, F. Arima, K. Baba, and Y. Inoue. Principles and characteristics of viscous damping devices (gyro-damper), the damping forces which are highly amplified by converting the axial movement to rotary one. In *12WCEE*, 2000.

[192] K. Saito, K. Yogo, Y. Sugimura, S. Nakaminami, and K. Park. Application of rotary inertia to displacement reduction for vibration control system. In *13th World Conference on Earthquake Engineering*, 2004.

[193] D. J. Wagg. A review of the mechanical inerter : historical context , physical realisations and nonlinear applications. *Nonlinear Dynamics*, 2021.

[194] W. M. Kuhnert, P. J. P. Gonçalves, D. F. Ledezma-Ramirez, and M. J. Brennan. Inerter-like devices used for vibration isolation: A historical perspective. *Journal of the Franklin Institute*, 358(1):1070–1086, 2021.

[195] C. Papageorgiou, N. E. Houghton, and M. C. Smith. Experimental testing and analysis of inerter devices. *Journal of Dynamic Systems, Measurement and Control, Transactions of the ASME*, 131(1):1–11, 2009.

[196] M. C. Smith and F. C. Wang. Performance benefits in passive vehicle suspensions employing inerters. *Vehicle System Dynamics*, 42(4):235–257, 2004.

[197] R. Wang, X. Meng, D. Shi, X. Zhang, Y. Chen, and L. Chen. Design and test of vehicle suspension system with inerters. *Proceedings of the Institution of Mechanical Engineers, Part C: Journal of Mechanical Engineering Science*, 228(15):2684–2689, 2014.

[198] K. Ikago, K. Saito, and N. Inoue. Seismic control of single-degree-of-freedom structure using tuned viscous mass damper. *Earthquake Engineering and Structural Dynamics*, 41:453–474, 2012.

[199] F. C. Wang and W. J. Su. Impact of inerter nonlinearities on vehicle suspension control. *Vehicle System Dynamics*, 46(7):575–595, 2008.

[200] A. Gonzalez-Buelga, I. F. Lazar, J. Z. Jiang, S. A. Neild, and D. J. Inman. Assessing the effect of nonlinearities on the performance of a tuned inerter damper. *Structural Control and Health Monitoring*, 24(3):1–17, 2017.

[201] R. Tuluie. Fluid inerter, *European Patent Office* EP2528757A1, 2010.

[202] B. J. Gartner and M. Smith. Damping and inertial hydraulic device, *US Patent Office* US20130037362A1, 2011.

[203] M. C. Smith, Neil E. Houghton, P. J. G. Long, and A. R. Glover. Force-controlling hydraulic device, *US Patent Office* US20120199428A1, 2012.

[204] S. J. Swift, M. C. Smith, A. R. Glover, C. Papageorgiou, B. Gartner, and N. E. Houghton. Design and modelling of a fluid inerter. *International Journal of Control*, 86(11):2035–2051, 2013.

[205] D. De Domenico, P. Deastra, G. Ricciardi, N. D. Sims, and D. J. Wagg. Novel fluid inerter based tuned mass dampers for optimised structural control of base-isolated buildings. *Journal of the Franklin Institute*, 356(14), 2018.

[206] X. Liu, B. Titurus, and J. Z. Jiang. Generalisable model development for fluid-inerter integrated damping devices. *Mechanism and Machine Theory*, 137:1–22, 2019.

[207] E. D. A. John and D. J. Wagg. Design and testing of a frictionless mechanical inerter device using living-hinges. *Journal of the Franklin Institute*, 356(14):7650–7668, 2019.

[208] W. G. Flannelly. Dynamic antiresonant vibration isolator, *US Patent Office* US3322379A, 1967.

[209] F. C. Wang, M. F. Hong, and T. C. Lin. Designing and testing a hydraulic inerter. *Journal of Mechanical Engineering Science*, 225(1):66–72, 2010.

[210] S. Y. Zhang, H. Yuan, J. Z. Jiang, S. Neild, and W. X. Ren. Realising embedded stiffness in hydraulic implementations of stiffness-damping-inertance configurations. *Journal of Vibration and Control*, page 107754632110337, 2021.

[211] X. L. Zhang, Q. Gao, and J. Nie. The mem-inerter: A new mechanical element with memory. *Advances in Mechanical Engineering*, 10(6):2018, 2018.

[212] C. Málaga-Chuquitaype, C. Menendez-Vicente, and R. Thiers-Moggia. Experimental and numerical assessment of the seismic response of steel structures with clutched inerters. *Soil Dynamics and Earthquake Engineering*, 121:200–211, 2019.

[213] M. Tipuric, D. Wagg, and N. D. Sims. Magnetorheological bypass valve design for a semi-active inerter. *Active and Passive Smart Structures and Integrated Systems XII*, (March):55, 2019.

[214] F. C. Wang and H. A. Chan. Vehicle suspensions with a mechatronic network strut. *Vehicle System Dynamics*, 49(5):811–830, 2011.

[215] Y. Hu, M. Z. Q. Chen, and Z. Shu. Passive vehicle suspensions employing inerters with multiple performance requirements. *Journal of Sound and Vibration*, 333(8):2212–2225, 2014.

[216] Y. Shen, L. Chen, X. Yang, D. Shi, and J. Yang. Improved design of dynamic vibration absorber by using the inerter and its application in vehicle suspension. *Journal of Sound and Vibration*, 361:148–158, 2015.

[217] Y. Hu and M. Z. Q. Chen. Low-complexity passive vehicle suspension design based on element-number-restricted networks and low-order admittance networks. *Journal of Dynamic Systems, Measurement and Control*, 140(10), 2018.

[218] Y. Shen, J. Z. Jiang, S. A. Neild, and L. Chen. Vehicle vibration suppression using an inerter-based mechatronic device. *Proceedings of the Institution of Mechanical Engineers, Part D: Journal of Automobile Engineering*, 234(10-11):2592–2601, 2020.

[219] C. Papageorgiou, O. G. Lockwood, N. E. Houghton, and M. C. Smith. Experimental testing and modelling of a passive mechanical steering compensator for high-performance motorcycles. In *2007 European Control Conference*, pages 3592–3599, 2007.

[220] J. Z. Jiang, M. C. Smith, and N. E. Houghton. Experimental testing and modelling of a mechanical steering compensator. In *Communications, Control, and Signal Processing, ISCCSP 2008*, pages 249–254, 2008.

[221] J. Z. Jiang, A. Z. Maramoros-Sanchez, R. M. Goodall, and M. C. Smith. Passive suspension incorporating inerters for railway vehicles. *Vehicle System Dynamics*, 50:263–276, 2012.

[222] F. C. Wang, M. R. Hsieh, and H. J. Chen. Stability and performance analysis of a full-train system with inerters. *Vehicle System Dynamics*, 50(4):545–571, 2012.

[223] J. Z. Jiang, A. Z. Matamoros-Sanchez, A. Zolotas, R. M. Goodall, and M. C. Smith. Passive suspensions for ride quality improvement of two-axle railway vehicles. *Proceedings of the Institution of Mechanical Engineers, Part F: Journal of Rail and Rapid Transit*, 229(3):315–329, 2015.

[224] Y. Li, J. Z. Jiang, and S. Neild. Inerter-based configurations for main-landing-gear shimmy suppression. *Journal of Aircraft*, 54(2):684–693, 2017.

[225] Y. Li, J. Z. Jiang, S. A. Neild, and H. Wang. Optimal inerter-based shock–strut configurations for landing-gear touchdown performance. *Journal of Aircraft*, 54(5):1901–1909, 2017.

[226] I. F. Lazar, S. A. Neild, and D. J. Wagg. Using an inerter-based device for structural vibration suppression. *Earthquake Engineering and Structural Dynamics*, 43(8):1129–1147, 2014.

[227] A. Giaralis and L. Marian. Use of inerter devices for weight reduction of tuned mass-dampers for seismic protection of multi-story building: the tuned mass-damper-interter (TMDI). (April 2016):97991G, 2016.

[228] D. Pietrosanti, M. De Angelis, and M. Basili. Optimal design and performance evaluation of systems with Tuned Mass Damper Inerter (TMDI). *Earthquake Engineering and Structural Dynamics*, 46(8):1367–1388, 2017.

[229] D. De Domenico and G. Ricciardi. Optimal design and seismic performance of tuned mass damper inerter (TMDI) for structures with nonlinear base isolation systems. *Earthquake Engineering and Structural Dynamics*, 47(12):2539–2560, 2018.

[230] Y. Hu, J. Wang, M. Z. Q. Chen, Z. Li, and Y. Sun. Load mitigation for a barge-type floating off shore wind turbine via inerter-based passive structural control. *Engineering Structures*, 177(15):198–209, 2018.

[231] R. Zhang, Z. Zhao, and K. Dai. Seismic response mitigation of a wind turbine tower using a tuned parallel inerter mass system. *Engineering Structures*, 180:29–39, 2019.

[232] I. F. Lazar, S. A. Neild, and D. J. Wagg. Vibration suppression of cables using tuned inerter dampers. *Engineering Structures*, 122(1):62–71, 2016.

[233] L. Sun, D. Hong, and L. Chen. Cables interconnected with tuned inerter damper for vibration mitigation. *Engineering Structures*, 151(15):57–67, 2017.

[234] J. Luo, J. H. G. Macdonald, and J. Z. Jiang. Identification of optimum cable vibration absorbers using fixed-sized-inerter layouts. *Mechanism and Machine Theory*, 140:292–304, 2019.

[235] M. Z. Q. Chen, Y. Hu, L. Huang, and G. Chen. Influence of inerter on natural frequencies of vibration systems. *Journal of Sound and Vibration*, 333:1874–1887, 2014.

[236] Y. Hu, M. Z. Q. Chen, and M. C. Smith. Natural frequency assignment for mass-chain systems with inerters. *Mechanical Systems and Signal Processing*, 108:126–139, 2018.

[237] J. Z. Jiang and M. C. Smith. Regular positive-real functions and five-element network synthesis for electrical and mechanical networks. *IEEE Transactions on Automatic Control*, 56(6):1275–1290, 2011.

[238] J. Z. Jiang, S. Y. Zhang, and S. A. Neild. Passive vibration control: a structure–immittance approach. *Proc. R. Soc. A*, 473(2201), 2017.

[239] Y. Y. Li, S. Y. Zhang, J. Z. Jiang, and S. Neild. Identification of beneficial mass-included inerter-based vibration suppression configurations. *Journal of the Franklin Institute*, 356(14), 2019.

[240] K. Wang and M. Z. Q. Chen. Passive mechanical realizations of bicubic impedances with no more than five elements for inter-based control design, year = 2021. *Journal of the Franklin Institute*, 358(10).

[241] A. Radu, I. F. Lazar, and S. A. Neild. Performance-based seismic design of tuned inerter dampers. *Structural Control Health Monitoring*, 26(5), 2019.

[242] W. Shen, A. Niyitangamahoro, Z. Feng, and H. Zhu. Tuned inerter dampers for civil structures subjected to earthquake ground motions: optimum design and seismic performance. *Engineering Structures*, 198(1), 2019.

[243] D. De Domenico, N. Impollonia, and G. Ricciardi. Soil-dependent optimum design of a new passive vibration control system combining seismic base isolation with tuned inerter damper. *Soil Dynamics and Earthquake Engineering*, 105:37–53, 2018.

[244] H. Zuo, K. Bi, H. Hao, and R. Ma. Influences of ground motion parameters and structural damping on the optimum design of inerter-based tuned mass dampers. *Engineering Structures*, 227, 2021.

[245] L. Marian and A. Giaralis. Optimal design of a novel tuned mass-damper-inerter (TMDI) passive vibration control configuration for stochastically support-excited structural systems. *Probabilistic Engineering Mechanics*, 38:156–164, 2014.

[246] L Marian and A Giaralis. The tuned mass-damper-inerter for harmonic vibrations suppression , attached mass reduction , and energy harvesting. *Smart Structures and Systems*, 19(6):665–678, 2017.

[247] A. Giaralis and A. A. Taflanidis. Optimal tuned mass-damper-inerter (TMDI) design for seismically excited MDOF structures with model uncertainties based on reliability criteria. *Structural Control and Health Monitoring*, 25(2):1–22, 2018.

[248] A. D. Matteo, C. Masnata, and A. Pirrotta. Simplified analytical solution for the optimal design of Tuned Mass Damper Inerter for base isolated structures. *Mechanical Systems and Signal Processing*, 134, 2019.

[249] Z. Wang and A. Giaralis. Enhanced motion control performance of the tuned mass damper inerter through primary structure shaping. *Structural Control and Health Monitoring*, 28(8), 2021.

[250] A. Giaralis, M. Asce, and F. Petrini. Wind-induced vibration mitigation in tall buildings using the tuned mass-damper-inerter. *J. Struct. Eng.*, 143(9), 2017.

[251] J Dai, Z. D. Xu, and P. P. Gai. Tuned mass-damper-inerter control of wind-induced vibration of flexible structures based on inerter location. *Engineering Structures*, 199, 2019.

[252] K. Xu, K. Bi, Q. Han, X. Li, and X. Du. Using tuned mass damper inerter to mitigate vortex-induced vibration of long-span bridges: Analytical study. *Engineering Structures*, 182:101–111, 2019.

[253] M. De Angelis, A. Giaralis, F. Petrini, and D. Pietrosanti. Optimal tuning and assessment of inertial dampers with grounded inerter for vibration control of seismically excited base-isolated systems. *Engineering Structures*, 196, 2019.

[254] P. Deastra, D. Wagg, N. Sims, and M. Akbar. Tuned inerter dampers with linear hysteretic damping. *Earthquake Engineering and Structural Dynamics*, 49(12):1216–1235, 2020.

[255] C. Pan, R. Zhang, H. Luo, C. Li, and H. Shen. Demand-based optimal design of oscillator with parallel-layout viscous inerter damper. *Structural Control and Health Monitoring*, 25(1):1–15, 2018.

[256] C. Pan and R. Zhang. Design of structure with inerter system based on stochastic response mitigation ratio. *Structural Control and Health Monitoring*, 25(6):1–21, 2018.

[257] Y. Hu, M. Z. Q. Chen, Z. Shu, and L. Huang. Analysis and optimisation for inerter-based isolators via fixed-point theory and algebraic solution. *Journal of Sound and Vibration*, 346:17–36, 2015.

[258] R. Zhang, Z. Zhao, C. Pan, K. Ikago, and S. Xue. Damping enhancement principle of inerter system. *Structural Control and Health Monitoring*, 27(5):1–21, 2020.

[259] Y. Hu and Michael Z. Q. Chen. Performance evaluation for inerter-based dynamic vibration absorbers. *International Journal of Mechanical Sciences*, 99:297–307, 2015.

[260] E. Barredo, A. Blanco, J. Colín, V. M. Penagos, A. Abúndez, L. G. Vela, V. Meza, R. H. Cruz, and J. Mayén. Closed-form solutions for the optimal design of inerter-based dynamic vibration absorbers. *International Journal of Mechanical Sciences*, 144:41–53, 2018.

[261] A. Javidialesaadi and N. E. Wierschem. Optimal design of rotational inertial double tuned mass dampers under random excitation. *Engineering Structures*, 165:412–421, 2018.

[262] Y. Hu, J. Wang, M. Z. Q. Chen, Z. Li, and Y. Sun. Load mitigation for a barge-type floating off shore wind turbine via inerter- based passive structural control. *Engineering Structures*, 177(15):198–209, 2018.

[263] A. Javidialesaadi and N. E. Wierschem. Three-element vibration absorber–inerter for passive control of single-degree-of-freedom structures. *Journal of Vibration and Acoustics*, 140(6):1–11, 2018.

[264] X. Wang, X. Liu, Y. Shan, Y. Shen, and T. He. Analysis and optimization of the novelinerter-based dynamic vibration absorbers. *IEEE Access*, 6:33169–33182, 2018.

[265] S. Zhou, C. Jean-Mistral, and S. Chesne. Optimal design of an inerter-based dynamic vibration absorber connected to ground. *Journal of Vibration and Acoustics*, 141(5):1–11, 2019.

[266] E. Barredo, J. G. Mendoza Larios, J. Colín, J. Mayén, A. A. Flores-Hernández, and M. Arias-Montiel. A novel high-performance passive non-traditional inerter-based dynamic vibration absorber. *Journal of Sound and Vibration*, 485, 2020.

[267] X. Wang, T. He, Y. Shen, Y. Shan, and X. Liu. Parameters optimization and performance evaluation for the novel inerter-based dynamic vibration absorbers with negative stiffness. *Journal of Sound and Vibration*, 463(3), 2019.

[268] E. Barredo, L. Gilberto, J. May, J. Mayen, and Flores-Hernandez A. A. Innovative negative-stiffness inerter-based mechanical networks. *International Journal of Mechanical Sciences*, 205, 2021.

[269] Y. W. Zhang, Y. N. Lu, W. Zhang, Y. Y. Teng, H. X. Yang, T. Z. Yang, and L. Q. Chen. Nonlinear energy sink with inerter. *Mechanical Systems and Signal Processing*, 125:52–64, 2019.

[270] A. Javidialesaadi and N. E. Wierschem. An inerter-enhanced nonlinear energy sink. *Mechanical Systems and Signal Processing*, 129, 2019.

[271] X. Hua, Y. Tai, Z. Huang, and Z. Chen. Optimal design and performance evaluation of novel hysteretic friction tuned inerter damper for vibration isolation systems. *Structural Control and Health Monitoring*, 28(8), 2020.

[272] F. D. H. Moraes, M. Silveira, and Gonçalves. On the dynamics of a vibration isolator with geometrically nonlinear inerter. *Nonlinear Dynamics*, 93:1325–1340, 2018.

[273] J. Yang, J. Z. Jiang, and S. A. Neild. Dynamic analysis and performance evaluation of nonlinear inerter-based vibration isolators. *Nonlinear Dynamics*, 99:1823–1839, 2020.

[274] T. L. Schmitz and S. K. Smith. *Machining dynamics: Frequency response to improved productivity.* Springer, 2nd edition, 2019.

[275] Y. Altintas. *Manufacturing automation: Metal cutting mechanics, machine tool vibrations, and CNC design.* Cambridge University Press, 2 edition, 2012.

[276] A. Sabanovic and K. Ohnishi. Chapter5: Interactions and constraints. In *Motion Control Systems*, pages 175–232. John Wiley & Sons.

[277] R. Storn and K. Price. Differential evolution - a simple and effivcient heuristic for global optimization over continuous spaces. *Journal of Global Optimization*, 11:341–359, 1997.

[278] A. K. Qin, V. L. Huang, and P. N. Suganthan. Self-adaptive differential evolution algorithm for numerical optimization. *IEEE Communications Magazine*, 13(2):398–417, 2009.

[279] K. Worden and G. Manson. On the identification of hysteretic systems. Part I: Fitness landscapes and evolutionary identification. *Mechanical Systems and Signal Processing*, 29:201–212, 2012.

[280] M. D. McKay, R. J. Beckman, and W. J. Conover. Comparison of three methods for selecting values of input variables in the analysis of output from a computer code. *Technometrics*, 21(2):239–245, 1979.

[281] A. Saltelli, M. Ratto, T. Andres, F. Campolongo, J Cariboni, D. Gatelli, M. Saisana, and S. Tarantola. *Global sensitivity analysis.* John Wiley $ Sons, 2008.

[282] A. Saltelli, S. Tarantola, F. Campolongo, and M. Ratto. *Sensitivity analysis in practice.* John Wiley $ Sons, 2004.

[283] T. Homma and A. Saltelli. Importance measures in global sensitivity analysis of nonlinear models. *Reliability Engineering and System Safety*, 52(1):1–17, 1996.

[284] I. M. Sobol. Sensitivity estimates for nonlinear mathematical models. *Mathematical Modelling and Computational Experiments*, 1(4):407–414, 1993.

[285] M. Z.Q. Chen, C. Papageorgiou, F. Scheibe, F. C. Wang, and M. Smith. The missing mechanical circuit element. *IEEE Circuits and Systems Magazine*, 9(1):10–26, 2009.

[286] S. T. Smith. *Flexures: Elements of elastic mechanisms.* CRC Press, 1st edition, 2000.

[287] A. Almagirby, J. A. Rongong, and M. J. Carré. The development of a new artificial model of a finger for assessing transmitted vibrations. *Journal of the Mechanical Behavior of Biomedical Materials*, 78:20–27, 2018.

[288] D. N. Tasron. *Understanding the tribological interactions between plantar skin and sock textiles through the development of biofidelic test-beds.* PhD thesis, 2017.

[289] T. Insperger, B. P. Mann, T. Surmann, and G. Stépán. On the chatter frequencies of milling processes with runout. *International Journal of Machine Tools and Manufacture*, 48(10):1081–1089, 2008.

[290] T. Insperger, G. Stépán, P. V. Bayly, and B. P. Mann. Multiple chatter frequencies in milling processes. *Journal of Sound and Vibration*, 262:333–345, 2003.

[291] M Davies, J. R. Prattl, A. J. Schaut, and J. B. Bryan. On the dynamics of high-speed milling with long, slender endmills. *CIRP Annals*, 47(1):55–60, 1998.

[292] T. L. Schmitz. Chatter recognition by a statistical evaluation of the synchronously sampled audio signal. *Journal of Sound and Vibration*, 262(3):721–730, 2003.

[293] F. Dirksen, M. Anselmann, T. I. Zohdi, and R. Lammering. Incorporation of flexural hinge fatigue-life cycle criteria into the topological design of compliant small-scale devices. *Precision Engineering*, 37(3):531–541, 2013.

[294] W. D. Pilkey. *Peterson's stress concentration factors.* Wiley, 2nd edition, 1997.

[295] H. E. Boyer. *Atlas of datigue curves.* ASM International, 1986.

[296] J. Schijve. *Fatigue of structures and materials.* Springer, 2nd edition, 2009.